A Multiscale Investigation of the Fatigue Behavior of Additively Manufactured Nickel Superalloys

by

Mohammad Soleimani Dodaran

A dissertation submitted to the Graduate Faculty of
Auburn University
in partial fulfillment of the
requirements for the Degree of
Doctor of Philosophy

Auburn, Alabama
December 11, 2021

Additive Manufacturing, Ni Superalloy, Crystal Plasticity, Molecular Dynamics, Density Functional Theory, Fatigue

Approved by

Shuai Shao, Chair, Associate Professor Mechanical Engineering

Nima Shamsaei, Professor Mechanical Engineering
Jeffrey C. Suhling, Professor Mechanical Engineering
Vinamra Agrawal, Assistant Professor Aerospace Engineering

Abstract

Fatigue as the most frequent mode of failure among mechanical systems has been the focus of a large part of the research community. Modern manufacturing technologies are developed to address the need for complex geometries of parts used in industrial applications and reduce the associated cost of manufacturing and post manufacturing processes. Additively manufactured parts, due to their surface roughness and volumetric defects, are very sensitive to cyclic loading. Fatigue of AM parts, due to their complexity, has brought multiple disciplines such as mechanical engineering, materials science, and physics together. Various materials have been developed to suit specific purposes and withstand extreme conditions. With the advancement of numerical models and computational capabilities, the deformation mechanisms that are involved in the process leading to fracture have been investigated at multiple length scales. In this dissertation, a comprehensive numerical multiscale investigation of phenomena affecting the fatigue performance of additively manufactured metallic materials, specifically nickel superalloys, has been conducted. At a lower length scale, the intrinsic properties of the material, such as fault energies, are calculated in the disordered solid solution matrix and the ordered strengthening precipitates using density functional theory. The operation of persistent slip bands formed during cyclic loading is studied using molecular dynamics to further understand the parameters affecting dislocation glide. The energetic properties and strength of metal/metal and metal/ceramic interfaces as an important microstructural feature are studied in detail. Mechanisms responsible for deformations at such locations are illustrated. At the continuum level, crystal plasticity analysis is done to understand the effect of the surface hard coating applied to the parts and components to suppress the formation of surface extrusions and prevent the formation of cracks. Lastly, a crystal

plasticity hardening model has been proposed that can capture a location-dependent slip resistance evolution. The formation of persistent slip bands and strain localizations as a result of cyclic deformation is studied. Using this model, the initiation behavior of cracks within the material is investigated in detail.

Acknowledgments

I would like to thank my esteemed supervisor, Dr. Shuai Shao, for his invaluable supervision, support, and tutelage during the course of my PhD study. Additionally, I would like to express gratitude to Dr. Nima Shamsaei for his intellectual support, which was really influential in shaping my experiment methods and critiquing my results. I also thank Drs. Jeffrey C. Suhling and Vinamra Agrawal from Auburn University as well as Drs. Dorel Moldovan, Shengmin Guo, and Wenjin Meng from Louisiana State University for their mentorship. I would like to thank my friends, lab mates, colleagues, and the research team at NCAME for the cherished time spent together in the lab and in social settings. My appreciation also goes out to my family and friends for their encouragement and support all through my studies. I also gratefully acknowledge support from the U.S. National Science Foundation and the U.S. Department of Energy.

Table of content

List of Tables

List of Figures

CHAPTER 1 INTRODUCTION

Around ten thousand years ago, after two and a half million years of struggle with wood and stone as the major sources of structural material, in the near east and China, humans started to use gold, silver, copper, and tin as alternatives to make tools and weapons. It didn't take long until they realized that the combination of different materials would result in interesting and desired properties that would suite specific purposes. Among the first instances of making alloys, one can mention the development of bronze, which was a combination of tin and copper. Since then, an ongoing effort has been devoted to the exploration of possibilities for new alloys.

It was by the beginning of the twentieth century that the "rustless" steels were developed by the combination of chromium and iron. This helped with the manufacturing of the airplane engines and many other metal parts and components. The hydrodynamic limitations of the propellers led to the development of jet engines whose key components operate in much harsher conditions, i.e., higher temperatures and more corrosive environments. Thus, the need for materials that are capable of maintaining their strength while they are operating at temperatures above half of their melting temperature motivated the development of a new group of alloys generally called superalloys. Nickel, as one of the most abundant elements found on earth, has been tried in the development of new alloys[1]. Nowadays, the application of nickel superalloys in many key industries such as power plants, petroleum industries, aviation and the health sector is greater than ever.

Various methods are used to increase the mechanical, thermal, and corrosion resistance of the parts that are made of superalloys and being used in high temperature and corrosive environments. In the precipitation hardened alloys by promoting the formation of thermally stable precipitates (i.e., γ' phase) the operating temperature of the alloys are increased. Addition of

alloying elements such as chromium can increase the corrosion resistance of Ni superalloys. For instance, the addition of Cr to IN-738 has led to the development of IN-939, which can be used in slightly higher temperatures and more corrosive environments. Manufacturing of the parts in the form of a single crystal has resulted in better mechanical performance at higher temperatures due to the removal of grain boundaries. This way, the creep resistance at elevated temperatures is reduced. Application of active cooling systems such as micro-channel heat exchangers that run through the material can also increase the operating temperature of the part. In addition, different types of coating can be deposited on the part surface to further increase the resistance of the material to temperature. Ceramic thermal barrier coatings can be applied onto the surface or a metallic interlayer can be deposited such that when they are exposed to higher temperatures, they form a so-called "thermally grown oxide layer" that can further increase the operating temperature of the material.

Alongside the advancement of materials, the reliability of the structures was constantly improved by better informed design practices. Amongst various mechanical failure modes, more than half of the failures are due to the fatigue failure mode. Thus, special attention is always drawn to failures due to fatigue loading. Prevention of failure due to fatigue is specifically challenging because, in many cases, the loading amplitude is well below the yield strength of the material. In reality, parts and components are subjected to a varying load amplitude. However, in experimental settings, application of constant loading amplitude is sometimes considered to simplify the problem.

Usually, fatigue has been considered in two different regimes based on the number of cycles to failure, i.e., low-cycle and high-cycle fatigue. A classical definition of low cycle fatigue is when the number of cycles to failure is below $10^{3\text{-}4}$, whereas higher numbers of cycles up to 10^{7}

are called a high cycle regime. In some textbooks, a very high cycle fatigue regime is also defined for life above 10^7cycles. More accurately, the definition of low/high cycle fatigue must be regarded as the dominancy of plastic/elastic strain in each cycle [2]. Furthermore, the life of a part or component can be divided into different stages, namely crack initiation, crack propagation and final fracture, in any of the regimes mentioned before. However, one should note that the importance of each stage is not equal in different regimes. In the case of low cycle fatigue, a bigger portion of the total life will be associated with the propagation of fatigue cracks that are be formed within the first few cycles because of the large applied loads. In contrast, in high-cycle fatigue, initiation of the fatigue crack will take place over a larger fraction of the total life. Thus, not long after the crack initiation, final fracture happens and may result in catastrophic failures.

Mechanical responses of metals and alloys under cyclic loading have entertained many curious minds. It was the similarities in the cyclic mechanical responses of different metals in single crystal form that raised many questions. As shown in Fig. 1, initially, the stress response of the material under cyclic loading increases as the amplitude of the excitation increases [3]. Next, there is a plateau in the stress response. Afterwards, with a further increase in the plastic strain amplitude, the stress response will rise again. This behavior was observed for different materials, such as nickel, copper, gold, and silver. The answer to this problem was not clear until the dislocation microstructure of the cyclically loaded specimen was investigated in detail.

Prior to the point that technological advancement has made it possible to investigate such problems, Ewing and Humfrey were among the pioneers who performed cyclic loading in the form of constant amplitude stress cycles on rectangular cross-section specimens made of Swedish iron. One surface of the rods was polished, and stress had been applied by bending [4]. As a result of cyclic loading, they observed what they later called "surface markings" appearing on the material

surface. A few novel and interesting observations were made by a series of tests performed under different loading amplitudes. First, they realized the correlation between the loading amplitude and the number of surface markings. As the loading amplitude increases, the number of markings increases as well. The appearance of the new slip lines and widening of the existing ones was due to the continuation of cyclic loading was their second observation. Finally, they realized that the fatigue crack forms at these surface markings in individual grains and that it grows by the joining of cracks from multiple grains. Later on, this was confirmed by many other studies [5]. It was the observations of Thompson et al. that made others believe permanent changes in the material at the location of surface markings were happening [6]. This was concluded based on the reappearance of slip markings after they were removed by polishing at the same location where they initially occurred on the specimen surface. Also, for the first time, the term "persistent slip band" was used by them to describe the observed phenomenon. Ever since, understanding the dislocation microstructure within the fatigued specimen and a framework that can be used to model the formation of extrusion and intrusions on the specimen surface have been the focus of many studies.

Dislocation arrangement of the material in single crystal form under cyclic loading was studied by many [7–13]. Gradual changes in the dislocation structure were investigated by Hancock and Grosskreutz [7]. It was shown that the formation of dislocation dipoles and multipoles results in increase in the dislocation density and a fatigue specific dislocation configuration generally referred to as “loop patches”. Formation of vein structures and loop patches were also described to minimize elastic strain energy stored in the material in the work of others [8,9,14]. Increase in the dislocation density within such structure was suggested to be the reason behind the initial rapid hardening behavior of certain materials. However, a maximum dislocation density was suggested as a result of balance between simultaneous multiplication and

annihilation of dislocations [15]. Hardening of the material will continue up to the point that plastic deformation can no longer be accommodated by the motion of screw dislocation between the neighboring veins [16]. Consequent instability of the vein structure will result in the annihilation of the dislocations within the bundles and formation of the PSBs where the plastic deformation will be localized by the motion of screw dislocations confined by the dislocation walls. Following the initial hardening stage, saturation stresses were justified by the activation of PSBs. A clear image of the mechanisms governing the formation of PSBs was a critical step forward in understanding the fatigue phenomena, however, explaining the distinguishing key characteristics of PSBs formed in different materials such as differences in activation stress or morphological aspects, i.e., surface protrusions and PSB heights were/are open questions that require further investigation. In this dissertation using Molecular dynamics simulations the operating stress of PSBs and the parameters affecting that are investigated thoroughly.

The correlation between various parameters such as amplitude of loading, strain rate, chemical composition, and temperature with characteristics of PSB are studied in the literature [13,16,17]. It was suggested to be the nature of slip being planar or wavy that controls the PSB width [16]. Higher equilibrium distance between partial dislocations in face centered cubic materials with lower stacking fault energy results in slip with planar nature. This is because of the higher activation energy of the cross slip in such materials. In contrast, wavy slip is common in materials with high stacking fault energy. In this dissertation, a numerical scheme is presented that enables the calculation of stacking fault energy (SFE) in multicomponent alloys. Furthermore, in ordered phases anti phase boundary (APB) energy affects the irreversibility of the dislocation motion, thus, calculation of its value must be of high importance. Combining cluster expansion

method, along with Monte Carlo metropolis algorithm, the APB energy of the precipitates forming in Ni-bases superalloys are being calculated.

Formation of point defects in the fatigued specimen was noticed by the changes in electrical resistivity [18]. These point defects were formed by the annihilation of vacancy type dipoles within the PSB where the plastic shear strain is confined and is two orders of magnitude larger than matrix [10,19]. Annihilation either happens at the wall or within the channel by the edge or screw dipoles, respectively. One should note that vacancy formation was observed at temperatures as low as ~ 4 K [20]. However, to compensate for the annihilated dislocations and maintain the plastic deformation throughout the PSB, nucleation of new dislocations happens at the wall and provides a steady state condition. Significant increase in the density of point defect will result in a rapid increase of the PSB volume. This has been manifested by the abrupt change of the surface profile at the PSB-surface intersection[20]. In addition to the formed extrusion over the whole width of the PSB, random nature of the slip irreversibility will result in the continuous growth of the local intrusions and extrusions at the PSB-surface intersection[15,21].

Multiple method are used to delay the formation of surface extrusions and relieve the extrusions made on the surface. Application of compressive residual stress to the part surface can help reduce the stress amplitude acting on the part and consequently improve the fatigue resistance of the part. However, application of such stresses using shot/cavity pinning are not possible for all geometries. Intermediate surface polishing is another method that can be used to prevent the initiation of fatigue crack from the part surface. One should note that, using this method the interruption made in service is a significant drawback. Application of surface hard coating that can suppress the formation of surface protrusions is a method that has been extensively used for the parts that are undergoing cyclic loading[22]. Considerations regarding the magnitude of the

applied load, material chosen for the coating, and the thickness of the coating layer must be made to obtain an optimum solution for the crack initiation problem. In this dissertation the interaction of surface hard coating and PSBs are studied using crystal plasticity method. The efficacy of coating thickness in the suppression of the plastic strain as well as development of normal and shear stresses at the coating substrate interface are investigated in details.

Due to the complex geometries of the parts and difficulties of the surface machining, additive manufacturing technique can be used as an alternative to reduce the need for post processing. Also, manufacturing of multiple component into an integral part can reduce the need for assembly and the final cost. However, the existence of volumetric defects such as gas entrapped pores, lack of fusions, and key holes that are proven to be detrimental to the mechanical performance of the parts cannot be avoided. Thus, the synergistic effect of defects and microstructure on the initiation of fatigue crack in additively manufactured Ni superalloy must be taken into account. In this dissertation, proposing a local crystal plasticity hardening model, the effect of grain size and orientation on the formation of slip bands and initiation of fatigue cracks from PSB-matrix interface and grain boundaries are studied. Overall, consideration of competing mechanisms in the formation of the fatigue cracks require great amount of microstructural details to be taken into account. This renders multiscale numerical investigation scheme, specifically crystal plasticity, a strong toll for studying the fatigue in additively manufactures superalloys.

Figures

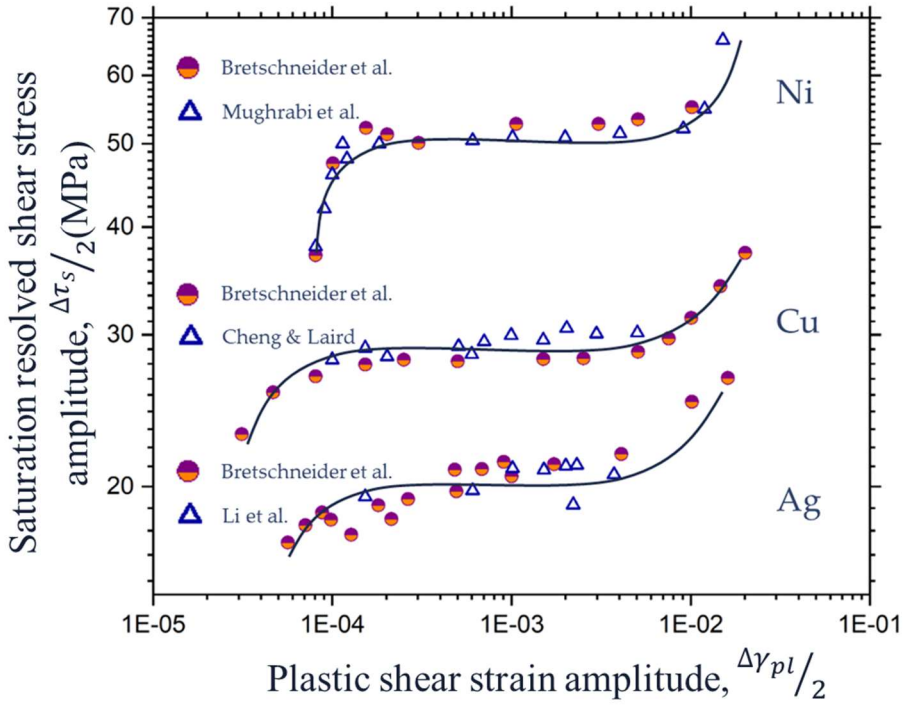

Figure 1. 1 Saturation stress versus plastic shear strain amplitude for different materials under cyclic loading. Figure is generated using data from [3].

CHAPTER 2 CRITICAL OPERATING STRESS OF PERSISTENT SLIP BANDS IN Cu

2.1. Abstract

This work elucidates the dependence of operating stress of persistent slip bands (PSB) on the channel width and wall dislocation density. Using Cu as a model system and molecular dynamics as the main investigative tool, a new length scale effect, namely the wall dislocation spacing, is provided to enhance theoretical understanding of PSBs. It is discovered that the operation of PSB is a thermally activated event in which operating stress is inversely related to the wall dislocation spacing, strain rate and temperature. Leveraging the existing framework of confined layer slip in nanoscale metallic multilayers and classical nucleation theory, a mathematical model describing the rate- and temperature- dependent PSB operating stress is proposed.

Keywords: Persistent Slip Bands; Metal Fatigue; Molecular Dynamics

2.2. Introduction

Fatigue damage accounts for 90% of all engineering failures [23,24]. In modern engineering applications, such as in high-speed trains and turbine engines, operating frequencies of the structural components range from thousands to tens of thousands revolutions per minute. The desired fatigue life these components easily resides in the high cycle (HCF, ~10^6 cycles) or very high cycle fatigue (VHCF, ~10^9 cycles) regime. During HCF or VHCF, the majority (~ 90%) of materials' fatigue life is typically spent in the initiation phase and/or early propagation phase of the fatigue cracks [25]. Localized microstructural developments during this stage, such as the operation and formation of persistent slip bands (PSB), has been shown to dictate the materials' cyclic stress-strain behavior as well as fatigue life [9,24,26,27].

The fatigue life under the HCF or VHCF regime can generally be divided into several phases (Fig. 1a) according to the cyclic hardening/softening behavior, as well as the microstructural evolution. Within the initial 10-100 cycles of loading, dislocations rapidly multiply via the Frank-Read type multiplication mechanisms leading to increased dislocation density and a rapid increase in cyclic stress (*Phase I*). Above certain threshold dislocation density, the dynamic recovery of dislocations activates, enabled by the annihilation of screw dislocations, which can easily cross-slip (*Phase II*). Remaining dislocations, most of which are edge in character and have identical burgers vectors, form bundles of dipolar vein structures and are most immobile (Fig. 1b and inset). A few mobile screw dislocations remain and interconnect neighboring veins (Fig. 1b). The motion of these screw dislocations accommodates the plastic deformation and deposits more edge dislocations onto the veins. Recovery of dislocations in Phase II results in a slightly reduced hardening rate (Fig. 1a).

At a certain critical stress level, veins collapse into dislocation walls (Fig. 1c) due to the annihilation between edge dislocations within the veins [8,27–29]. A possible mechanism for such annihilation is ascribed to the cutting action of from dislocations on either a secondary or tertiary slip systems (insets of Fig. 1). These dislocation walls have much higher dislocation density and a regular structure with a well-defined spacing. The collective entity of dislocation walls and the channels in between are commonly referred to as the PSB. The spacing between the walls has been shown to depend on the critical annihilation spacing between the screw runners [30,31] (temperature dependent) and is typically around 1 micron or below [26,29]. The smallest reported spacing has been shown to be as low as 180 nm [32]. Runner screw dislocations exist between the dislocation walls (Fig. 1c). The formation of the periodic wall structure increases the size of the channel in which the runner dislocations propagate —compared to the case of vein structures— thereby localizing the deformation within the PSB. The formation of PSBs also leads to the cyclic saturation and the gradual softening behavior in *Phase III* (Fig. 1a). In the latest phase of the cyclic deformation (*Phase IV*), a secondary hardening of varying degree may develop if, for instance, cyclic phase transformation is present [33,34]. The continuous operation of PSBs lead to the formation of surface and/or internal cracks; substantial fatigue damage enters the fatigue crack propagation stage and eventual fracture soon follows [35]. Similar stage-wise life evolution has also been captured by recent fatigue experiments with surface temperature monitoring via infra-red cameras [36–39].

Over the years, renewed interest, from both theoretical as well as experimental perspectives, has been devoted to the mechanisms governing the materials' cyclic deformation behavior [8,27–31,40]. Accordingly, numerous theoretical models, including the Mughrabi's composite model [11] and Brown's "bowing and passing" (B-P) model [41], have been proposed

to predict the cyclic saturation strengths of metals. The former model, by assuming a strong geometrical constraint by the matrix, mainly considers the long-range stress field caused by the edge dislocations deposited on the dislocation walls. The B-P model postulates that the stress response of the PSB is dominated by the stress required to bow a screw dislocation in between two dislocation walls as well as the stress required to pass through two adjacent dislocations within the same channel (hence the name "bowing and passing"). The B-P model, with several recent revisits [30,31], performs reasonably well when predicting the saturation strengths of materials with various stacking fault energies, especially when the effect of temperatures is involved.

These models typically assume that the dislocation walls are featureless, planar entities that are semi-permeable to the motion of dislocations. However, this assumption may be inadequate as localized inhomogeneous stress fields exist near the dislocation walls and the wall dislocation density may affect the interaction energy between the runner dislocations and the dislocation walls. In this work, using molecular dynamics simulations performed on a Cu model system, we study the behavior of the runner screw dislocations as a function of the geometric characteristics of PSBs, including the wall spacing and the dislocation density within the walls. We investigate the maximum shear stress that a structure can sustain before it destabilizes. We also show that, in addition to the dislocation wall spacing and the distance between the runner screw dislocations, a third factor—dislocation wall density—also affects the activation stress.

2.3. Methodology of atomistic simulations

In this work, we use molecular dynamics (MD) to characterize the behavior of PSB in FCC Cu. Simulations were performed using the parallel atomistic simulator LAMMPS [42,43]. Cu is chosen as the prototype material due to the abundance of experimental data available in the literature and well-developed atomic potentials [44]. The interatomic interaction is described

using the semi-empirical, embedded atom method (EAM) potentials which are known to reliably reproduce properties of the point, line, and surface defects [44,45]. To investigate the stability of dislocation walls and the activity of screw runner dislocation in the PSB channels, two different geometrical types of models were made. All models have the same crystallographic orientation: x//$[1\bar{1}0]$, y//[111], z//$[\bar{1}\bar{1}2]$ and the slip plane is (111) perpendicular to *y*- direction. The computation cells in relation to a typical PSB structure is shown in Fig. 2. Complying with the finding in Ref. [9], the dislocation walls are modeled as an array of four opposing pure tilt boundaries. Perfect dislocations are inserted into the perfect FCC lattices using the Barnett-Lothe solution [46] for an anisotropic displacement field of a dislocation. The dislocation line is parallel to the *z*- axis in all cases. Each perfect dislocation has a Burgers vector of *a*/2<110>, where *a* for Cu is 3.615 Å [44]. The perfect dislocations immediately dissociate during relaxation. All computational cells are subjected to the strain-controlled loading of ε_{yx}, by applying corresponding displacements along the direction of the Burgers vector.

To find the maximum shear stress that can be sustained by a dislocation wall, Type-1 geometry of computational cells is used (Fig. 2). Each model has full periodic boundary conditions and includes four edge dislocations, with the distance between dislocations (*h*) differing for each model, ranging from 25 to 200 Å in the y direction. Due to periodicity, the width of the channel (*w*) equals to the width of the cell in *x*- direction, ranging from about 31 nm to 220 nm. The maximum channel size is larger than the smallest channel size observed in the experiments (180 nm) [32]. The *z*- direction was chosen to be small (~9 Å) in order to reduce the sizes of the simulation cells.

To quantify the mobility of the runner dislocations as a function PSB geometry, such as *h* and *w*, the Type-2 geometry of computational cells is used (Fig. 2, the runner dislocation is visible).

The cell is periodic in the *x*- and *y*- directions, with fixed boundary conditions in *z*. Since the screw dislocations propagate in the *z*- direction, these models were much larger, around 600 Å, in the *z* direction. The height of the cells is around 200 Å, while the vertical distance (*h*) between dislocations ranged from 30 to 50 Å. The width in x direction also changed between 105 and 240 Å in order to observe the changes in activation stress with both wall dislocation spacing (*h*) and channel width (*w*). This dimension is smaller than what has been observed in the experiments, nevertheless, it is sufficient to capture the trend by which one of PSB's key characteristics, i.e. its activation stress, varies with *h* and *w*. Fixed boundary conditions are applied in the *z*-direction of Type-2 cells, by fixing the outside layer of the atomic models, no more than 10 Å thick. The total number of atoms in these cells ranges from 10 to 29 million atoms.

Residual stresses arise as a result of the insertion of dislocations. During the relaxation process, the relative positions of dislocations shift in search of a minimum energy configuration given the constraint of the current shape of the simulation boxes. The relative motion of dislocations yields an overall shear strain, which, if not relieved, leads to a residual stress. For Type-2 cells this residual stress is not a concern as the critical operating stresses of the PSBs constructed in this work are well above its magnitude (will be shown in the forthcoming sections). For Type-1 cells, before the evaluation of the critical shear stress, all structures are relieved of such residual shear stresses by iteratively applying small shear deformations.

2.4. Results and Discussion

2.4.1. Mechanical stability of dislocation walls

For Cu, the backbone structure of dislocation walls comprises four layers of tilt boundaries [9]. Realistically, the dislocation walls in a PSB also contain ~90% of "debris", which typically represents the dislocation loops of the primary or secondary Burgers vectors. This debris serves

as an effective dislocation pinning point, increasing the mechanical stability of the walls. For simplicity, this study treats each dislocation wall as an aggregation of four alternating tilt boundaries (Fig. 2). A schematic illustration of such a structure is given in the inset of Fig. 3, where the faint dashed lines represent the tilt walls. Note that the sign of the dislocations alternative in each adjacent walls, hence the net Burger vector of the dislocation walls in PSB is zero. In such a simplify wall model utilized in MD, the associated stability is hinged upon the elastic interaction within each dislocation dipoles. To establish a point of reference, the critical shear stresses (τ_c) that the tilt boundary-based dislocation walls can sustain are assessed as a function of the vertical dislocation spacing by both MD simulations and analytical models (Fig. 3).

MD simulations in this regard have been performed using the Type-1 cells as shown in Fig. 2 at two different temperatures (25 K and 300 K) and two different strain rates (10^7 /s and 10^8 /s). A power law-like decay is observed in the $\tau_c - h$ relations. This is expected as the stress field of a dislocation varies inversely as functions of distance. It is also apparent that while increasing temperature reduces τ_c at lower h, its effect is harder to discern at higher h. Indeed the difference in τ_c induced by temperature is still within the error bands. The decreasing strain rate appears to reduce τ_c (compare the hollow circle and triangle with the solid circles and triangles in Fig. 3). However, within the time scale of MD simulations, such a change in τ_c appears insignificant.

As the difference in strain rates between MD simulations (>10^7 /s) conventional fatigue experiments (~ 10^0 /s) is vast, further assessment on the effects of strain rate is necessary. To this end, τ_c has been calculated using classical isotropic linear elastic solutions of dislocations [47], including the interaction force for infinitely long and parallel dislocations [48]. The interaction

force felt by these dislocations from a surrounding dislocation can, therefore, be estimated by [47,48]

$$\frac{F_R}{L} = \frac{G}{2\pi R}(\boldsymbol{b}_1 \cdot \boldsymbol{\xi})(\boldsymbol{b}_2 \cdot \boldsymbol{\xi}) + \frac{G}{2\pi(1-\nu)R}[(\boldsymbol{b}_1 \times \boldsymbol{\xi}) \cdot (\boldsymbol{b}_2 \times \boldsymbol{\xi})] \quad (1a)$$

$$\frac{F_\theta}{L} = \frac{G}{2\pi(1-\nu)R^3}\{(\boldsymbol{b}_1 \cdot \boldsymbol{R})[(\boldsymbol{b}_2 \times \boldsymbol{R}) \cdot \boldsymbol{\xi}] + (\boldsymbol{b}_2 \cdot \boldsymbol{R})[(\boldsymbol{b}_1 \times \boldsymbol{R}) \cdot \boldsymbol{\xi}]\} \quad (1b)$$

where $\frac{F_R}{L}$ and $\frac{F_\theta}{L}$ are the magnitude of the per-unit-length interaction force along the radial (R) and tangential (θ) directions in the cylindrical coordinate, respectively; G (taking 45 GPa for Cu) and ν (taking 0.33 for Cu) are the elastic constants under the isotropic assumptions; $\mathbf{b}_i$, $\mathbf{R}$, $\boldsymbol{\xi}$ are the Burgers vectors, relative positions and line sense of the pair of dislocations. Following the Taylor's approach [49], it is assumed that the interaction within individual dipoles governs critical stress of the dislocation walls. Two scenarios are considered: (1) all dislocations in the wall structure are perfect dislocations; (2) all perfect dislocations have dissociated into Shockley partials with an equilibrium separation distance of 30 Å. The results from these analyses have been shown in Fig. 3 as dashed and solid lines. The predictions made by MD simulations in this regard do not deviate significantly from the theoretical estimations. This indicates that the elastic interactions within dislocation dipoles might not suffer a strong rate sensitivity.

2.4.2. Critical operating stress of PSB

The critical operating stress of PSB determines the cyclic stress amplitude of a fatigue specimen under the saturated conditions. Prevailing models of PSBs, as discussed in the introduction, having accounted for the long-range stresses within the channels [11], the stress required for screw dislocations to pass each other, and stress needed to "bow" screw dislocation within the channels [30,41]. However, one important factor, i.e. the short-range interaction

between the runner dislocation with the wall dislocations, has not been explicitly accounted for. In this section, we assess operating stress of PSBs using MD simulations. In a formal sense, we assess the effect of runner-wall interaction as a function of dislocation density in the walls.

For this purpose, simulation cells of Type-2 (shown in Fig. 2) are used. At fixed strain rates (10^7 and 10^8 /s), shear strains (ε_{xy}) are applied. The resulting shear stress (τ_{xy}) are monitored. The position of the central portion (between the dash-dotted lines in Fig. 4a) of the runner dislocation, is also monitored. Typical evolution of the velocity – stress relation is shown in Fig. 4b, the direction of such evolution is marked by an arrow. In all simulations of this type, stresses required to activate the screw dislocation is well above 200 MPa. For this reason, the initial shear stresses of the models are not relaxed. As shown in Fig. 4b, below a critical stress, the velocity of the screw dislocation is approximately zero. When the critical stress is reached, the velocity increases and, due to the inertia effect, the velocity maintains a relatively high value even though the applied stress is substantially relaxed by the motion of this screw dislocation. The maximum velocity of the dislocation is around 1200 ~ 1400 m/s, consistent with prior studies using the same EAM potential [50]. This implies that, within the length of 600Å (z dimension of the Type-2 cells structures), the screw dislocations have sufficient room to propagate relatively freely. We expect that the effect of the fixed boundary condition in z direction to be minimal, if any. It also noted that an increase in the dislocation velocity is witnessed even when the stress appears to be decreasing. This phenomenon has to do with the "strain-controlled" nature of the simulations and the stress inhomogeneity in the simulation cell. The motion of the dislocation loop, the loop-wall interaction, and the local rearrangement of the wall structure due to the interaction all lead to sudden relaxations of the average stress in the simulation cell. This could happen even while central dislocation segment (shown in Fig. 4a) is still accelerating under local residual stresses.

The maximum stress measured from the velocity – stress curves is then taken as the estimation of the PSBs' operating stress.

Measured operating stress of the PSBs (τ_{PSB}) is shown by the data markers (circles, squares and triangles) in Fig. 5. Error bars represent the data scatter encountered in the measurement of the maximum stress from velocity – stress curves (such as ones shown in Fig. 4b). It is evident that, in general, the operating stress of PSB increases as the width of the channel (w) decreases. This is expected since, similar to the operation of a Frank-Read Source, the stress required to bow a dislocation within the channel is inversely related to the channel width. This effect can already be captured by the existing "Bowing and Passing" models.

Interestingly, it is also noted that an apparent decreasing trend of τ_{PSB} exists with increasing w. This may originate from the short-range interaction between the screw runner dislocation with the wall dislocations, which may be stronger (weaker) if the dislocation density in the walls is higher (lower). This can be better illustrated by plotting the stress field around/at a dislocation wall comprising tilt boundaries. Fig. 6 visualizes the distribution of σ_{xx} and τ_{xy} near perfect edge dislocations walls according to classical analytical solutions (given in Appendix A) with isotropic assumptions. It is evident that at smaller (larger) dislocation spacing (h), the overall magnitude of stresses in and near the dislocation wall structure (excluding the dislocation core regions) is noticeably higher. The stronger elastic field of dislocation walls with higher dislocation density may substantially increase stress required to operate the PSB. In other words, the deposition of edge dislocations due to the propagation of the screw runner dislocations is more difficult for PSBs with higher wall dislocation density.

Realizing the similarity between the operation of PSB and the plastic deformation in nanoscale multilayered composites (NMC) [51], a refined mathematical framework that predict

the yield stress of the latter may be adopted herein to describe the operating stress of PSB as a function of both channel width (w) and wall dislocation density (controlled via h). According to the refined confined layer slip (RCLS) model [51], the applied shear stress required to propagate a gliding hair pin dislocation is given as

$$\tau_{RCLS} = \frac{Gb}{8\pi h'}\left(\frac{4-\nu}{1-\nu}\right)\left[\ln\frac{\alpha h'}{b}\right] - \frac{f}{h} + \frac{C}{\lambda}. \quad (2)$$

As laid out by the terms on the right-hand side of the Eqn. 2, three major contributions to the flow stress of a NMC are considered, namely (1) increase in the total dislocation line energy and self-interaction energy due to the motion of the screw runner dislocation, i.e. line tension, (2) an elastic interface stress that may assist/oppose the applied stress, and (3) an additional stress arising from the interaction between the gliding dislocation with the interface dislocations. In Eqn. 2, G and ν are the shear modulus and Poisson's ratio, h' is the thickness of the individual layers measured parallel to the glide plane, α is the dislocation core cutoff parameter, b is the magnitude of the Burger vector of the gliding dislocation, h is the individual layer thickness of the NMC, f/h measures the magnitude of the interface stress, $C = Gb/(1-\nu)$ and λ is the mean interfacial dislocation spacing.

The three contributions to the flow stress of NMC are also present in the case of the PSBs. The first contribution, i.e. the effect of line tension, is inherent to the propagation of screw dislocations within the channels of PSB and has been accounted for in Browns bowing and passing model and its subsequent revisions [30,41]. The second contribution [52], i.e. the elastic interface stress, is missing in PSBs due to the lack of interphase boundaries. Nevertheless, a counterpart of it, namely the long-range stress field developed within the dislocation channels, exists in PSBs. As was shown by Mughrabi [11], due to the rigid geometric constraints imposed by the

surrounding material, the collective motion of dislocations within the PSBs give rise to a "back stress" that opposes the applied stress. This stress (τ_{LR}) has been shown to be a constant value for a given material. The last contribution, as demonstrated in the foregoing text, is clearly present in PSB. Accordingly, in correspondence to Eqn. 2, the operation stress of PSB can be written as the following:

$$\tau_{PSB} = \frac{Gb}{8\pi w}\left(\frac{4-\nu}{1-\nu}\right)\left[\ln\frac{\alpha w}{b}\right] + \tau_{LR} + \frac{\beta C}{h} + \tau_{pass}, \quad (3)$$

where β is a constant that accounts for the difference in stress contribution between interfacial dislocations and tilt boundary dislocations, and τ_{pass} is the critical passing stress for neighboring screw dislocations in the same dislocation channel. The latter has been well accounted for in recent literature [30,41] and won't be investigated in this work.

Apparent strain rate sensitivity has also been observed in our simulations (compare Figs. 5a and 5b). Granted, the operation of PSB or Frank-Read sources alike are not hugely impacted by strain rate [53] compared to nucleation events, the motion of dislocations, in general, are thermally activated. Disparities in strain rates between MD simulations and experiments, demands careful evaluation of strain rate effect. In addition, modern material life assessment relies upon fatigue tests with increasing test frequencies. Fatigue testing platforms running at 20kHz is already a common practice [54], test frequencies in the MHz regime is required for MEMS devices. Such a range in the testing frequency corresponds to a strain rate varying from 10^0 /s up to 10^5 /s, and can significantly affect the mechanical response of materials. The strain rate effect on τ_{PSB} demands careful assessment.

Treating the motion of the screw dislocations in PSBs as a thermally activated event, the plastic strain rate, $\dot{\varepsilon}$, and the τ_{PSB} can be related as [55]:

$$\dot{\varepsilon}^p = \dot{\varepsilon}_0^p \exp\left(-\frac{Q^* - \tau_{PSB}\widehat{\Omega}}{kT}\right), \quad (4)$$

assuming a linear relation between the activation energy and the mean applied stress, i.e. $\Delta Q = Q^* - \tau_{PSB}\widehat{\Omega}$, where $\widehat{\Omega}$ is the activation volume. In Eqn. 4, *k* and *T* are Boltzmann's constant and absolute temperature, $\dot{\varepsilon}_0^p$ is a rate constant. $\dot{\varepsilon}_0^p$ is considered as "a limiting plastic strain rate" assuming that all attempts at moving the screw dislocation (at Debye frequency of Cu) has succeeded and have propagated through the represented volume, yielding a characteristic plastic strain, i.e. $\dot{\varepsilon}_0^p = \upsilon_D \varepsilon^p$. Rearranging Eqn. 4 results in:

$$\tau_{PSB}\left(T, \dot{\varepsilon}_0^p\right) = \frac{Q^*}{\widehat{\Omega}} - \frac{kT}{\widehat{\Omega}} \ln \frac{\dot{\varepsilon}_0^p}{\dot{\varepsilon}^p}. \quad (5)$$

The term $Q^*/\widehat{\Omega}$ has the unit of stress and is typical interpreted as an athermal activation stress [53,55], the contribution of temperature and strain rate only appear in the second term on the right hand side. Realizing this, the $Q^*/\widehat{\Omega}$ term can be replaced by an athermal variant of Eqn. 3, resulting in a temperature and strain rate dependent PSB operating stress:

$$\tau_{PSB}\left(T, \dot{\varepsilon}_0^p\right) = \frac{Gb}{8\pi w}\left(\frac{4-\nu}{1-\nu}\right)\left[\ln\frac{\alpha w}{b}\right] + \tau_{LR} + \frac{\beta C}{h} - \frac{kT}{\widehat{\Omega}} \ln \frac{\dot{\varepsilon}_0^p}{\dot{\varepsilon}^p} + \tau_{pass}\left(T, \dot{\varepsilon}_0^p\right). \quad (6)$$

The term $kT/\widehat{\Omega} \ln \dot{\varepsilon}_0^p/\dot{\varepsilon}^p$, alone, produces the effect of strain rate. By fitting $\Delta\tau_{PSB} = kT/\widehat{\Omega} \ln 10^8/\dot{\varepsilon}^p - kT/\widehat{\Omega} \ln 10^7/\dot{\varepsilon}^p$ into the data shown in Fig. 5, the activation volume can be determined as a linear function of w, i.e. $\widehat{\Omega} = 0.0021w + 1.3058$, where $\widehat{\Omega}$ has a unit of b^3 and w has a unit of Å. The activation volume, by definition, is the work conjugate of the applied stress in the activation process. Note that the work is written as $\tau_{PSB}\widehat{\Omega}$. Intuitively, the activation volume is simply the area swept by the dislocation loop times the Burgers vector before the loop becomes critical. Consequently, the activation volume is related to the width of the dislocation channel (*w*).

Using the parameters shown in Table 1, data shown in Fig. 5 can be represented by Eqn. 6 (see the solid, dashed and dash-dotted lines in Fig. 5).

As shown in Fig. 5, Eqn. 6 has good agreement with data corresponding to h = 30 Å and 50 Å. The model, however, appears to underestimate the data for h = 40 Å. In fact, it appears from Fig. 5 that the difference in PSB operating stress between the cases of h = 30 Å and h = 40 Å is smaller than that between cases of h = 40 Å and h = 50 Å, while Eqn. 6 predicts otherwise. Here, it is important to note that Eqn. 6 predicts a mean operating stress of PSBs, while the actual operating stress may fluctuate depending on the relative positioning between the runner screw dislocation with the wall dislocations (refer to Fig. 7). As shown in Fig. 6, the stress field near a dislocation wall is heterogeneous. Close inspection on the atomistic configurations reveals that the relative positioning between the runner dislocation and wall dislocations is similar for cases h = 30 Å and h = 40 Å — minimum distance ($h_{\min}$ in Fig. 7) in y- direction is around 6 Å. For the case of h = 50 Å, this $h_{\min}$ is around 12 Å. This is likely the reason for such a "disagreement" between Eqn. 6 and data for h = 40 Å. At such small h values afforded in MD simulations, scattering of data induced by the inconsistencies in the relative positioning of dislocations is sometimes unavoidable. After all, the distance between two parallel and adjacent {111} planes is $d_{\{111\}}$ = 2.087 Å. Dictated by the simplified, tilt-boundary based dislocation wall model, the space allowable for the positioning of a screw runner dislocation is $h/2 - 2d_{\{111\}}$. At h = 30 Å this space is 10.8 Å (5.2 $d_{\{111\}}$), while at h = 40 Å this space is 15.8 Å (7.6 $d_{\{111\}}$). The careful control of the $h_{\min}$ becomes challenging in this case. It can be argued that, if a sufficient number of MD simulations can be run, the averaged results can be well predicted by Eqn. 6.

2.5. Conclusions

In this work, molecular dynamics simulations have been performed on single crystalline Cu to elucidate the dependence of operating stress of persistent slip bands on the wall dislocation density and the channel width. Consistent with prior studies, the operating stress was found to be inversely dependent on the channel width. Interestingly, it was also shown that the operating stress is inversely related to the wall dislocation spacing. Adopting the existing framework of confined layer slip in nanoscale metallic multilayers, a mathematical model describing the rate- and temperature- dependent operating stress of persistent slip bands are proposed.

Tables

Table 2. 1 Parameters in Eqn. 6 used to represent data shown in Fig. 5.

G	ν	b	α	β	τ_{LR}	$\dot{\varepsilon}_0^p$
45 GPa	0.33	2.556 Å	2	0.023	167 MPa	8.13 × 10 /s

Figures

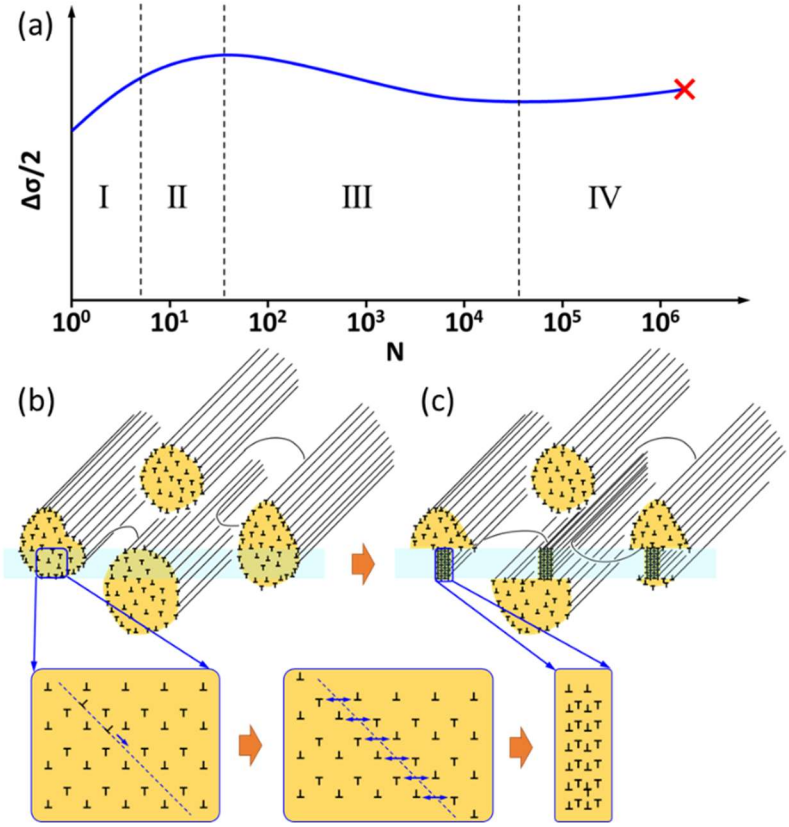

Figure 2. 1 Schematic illustration of the formation of persistent slip bands from vein structures by means of dislocation annihilation. (a) A typical evolution of cyclic stress range during the fatigue life of a metallic material. (b)-(c) The formation of PSBs from vein structures. A possible mechanism has been given in the insets.

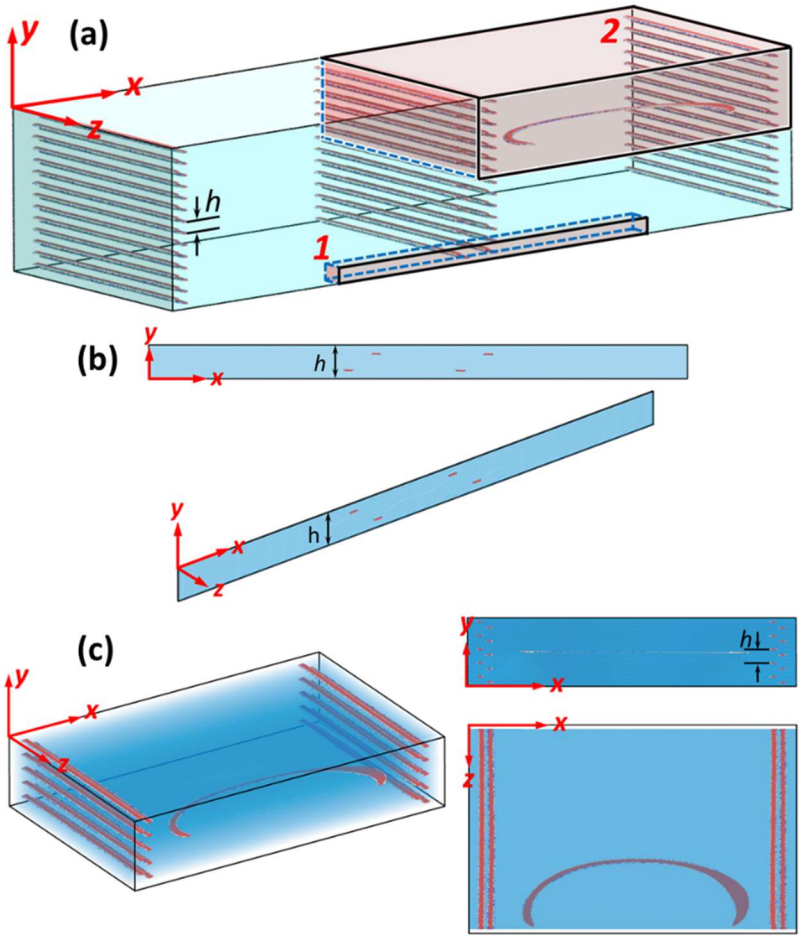

Figure 2. 2 (a) Simulation cell geometries in relation to the wall structures in a PSB. (b) Frontal (along – *z* axis) and orthographic views of Type-1 cell geometry. (c) Orthographic, frontal (along – z axis) and top views of the Type-2 cell geometry. The dislocation configuration shown in the Type-2 geometry correspond to early stage of loading. The visualization technique is common neighbor analysis [56], where the red atoms represent ones in stacking fault structures.

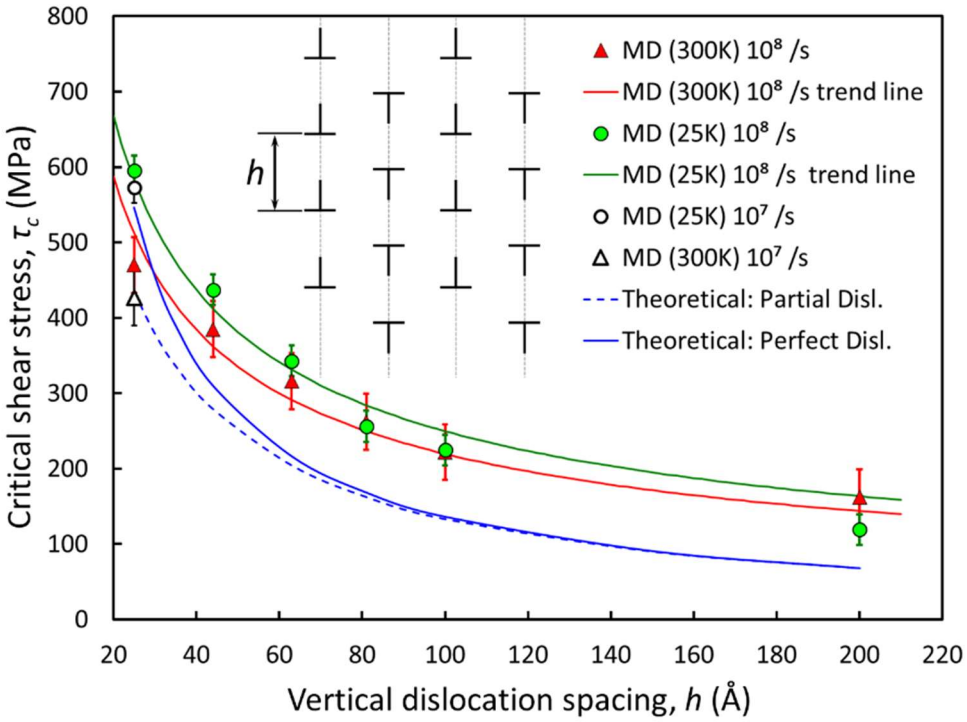

Figure 2. 3 Critical shear stress of dislocation walls as functions of varying vertical dislocation spacing. Error bars signify the standard deviation in the positive and negative directions. The associated scatter originate from the thermos fluctuation captured by MD simulations.

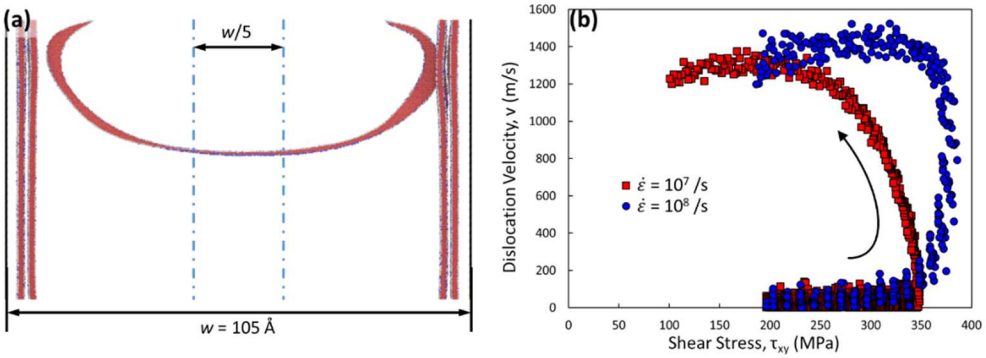

Figure 2. 4 Result from a typical case of PSB simulation, with w = 105 Å and vertical dislocation spacing of 30 Å. (a) The plan view of the atomistic configuration of dislocations on the x-z plane. Atoms are color-coded according to common neighbor analysis [56]. Atoms in an FCC lattice are not shown, red atoms represent HCP structure. Due to the high degree of distortion in the dislocation cores, the lattice type of a few atoms is not recognized or falsely recognized as BCC structure. The black vertical lines denote the periodic boundaries in the *x*-direction. (b) The obtained dislocation velocity vs shear stress data under two different strain rates.

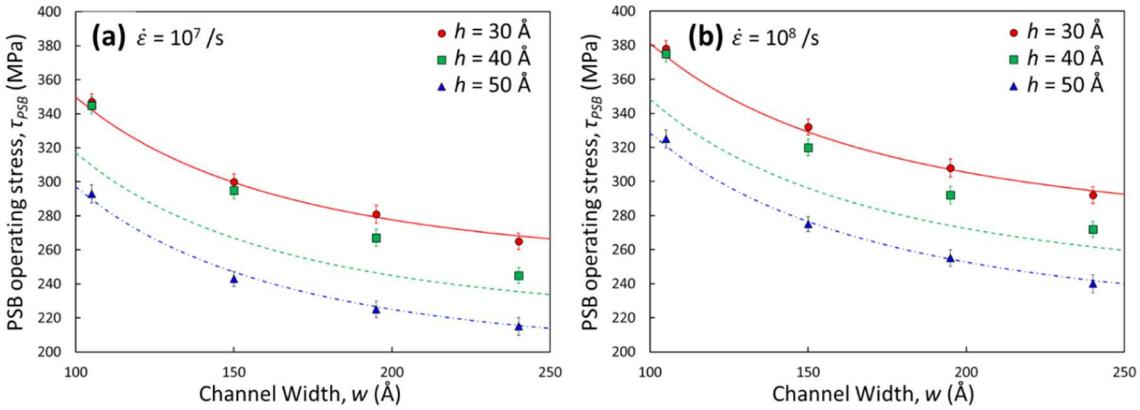

Figure 2. 5 Operating stress of PSBs as functions of varying channel width (w). Three levels of dislocation wall dislocation density have been considered, reflected as three values of h, i.e. 30, 40 and 50 Å. Definition of h is shown in Fig. 2. (a) and (b) show data acquired at two different strain rates, i.e. 10^7 and 10^8 /s. Lines represent the fit from the proposed rate-sensitive model.

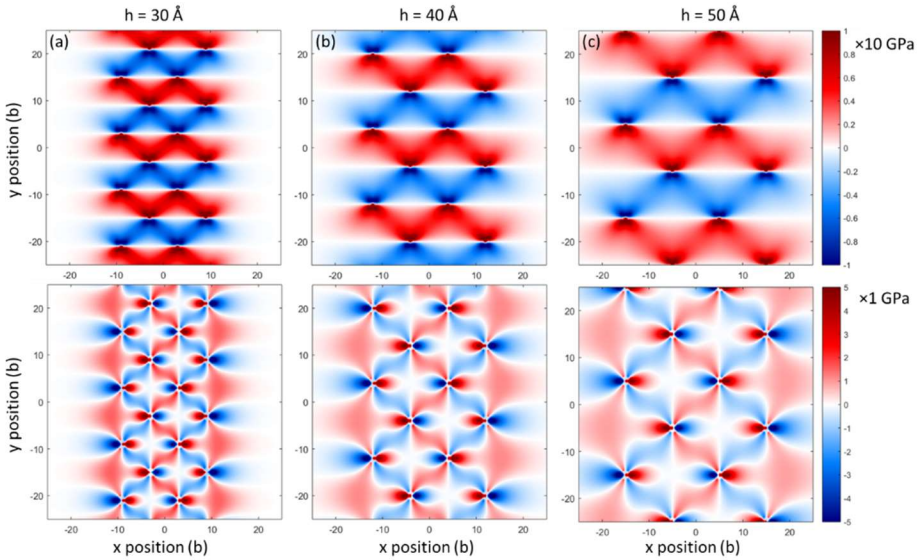

Figure 2. 6 Stress field near and in a dislocation wall comprising four alternating tilt boundaries. (a), (b) and (c) show, respectively, distribution of σ_{xx} stress in the x-y plane for the cases of h = 30 Å, 40 Å and 50 Å. (d), (e) and (f) show distribution of τ_{xy} stress in the x-y plane for the cases of h = 30 Å, 40 Å and 50 Å. The distance units are in the magnitude of the Burgers vector of perfect dislocations in Cu (i.e. b = 2.556 Å) for convenience.

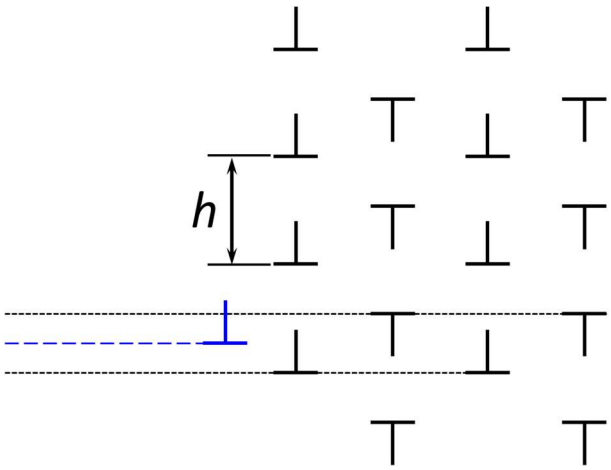

Figure 2. 7 Relative positioning of the edge dislocation deposited by the screw runner dislocation and the wall dislocations.

CHAPTER 3 A THEORETICAL CALCULATION OF STACKING FAULT ENERGY OF NI ALLOYS: THE EFFECTS OF TEMPERATURE AND COMPOSITION

3.1. Abstract

Combining cluster expansion (CE) method with one dimensional axial Ising model, this work investigated the effects of alloying elements and configurational variations due to temperature on the stacking fault energy (SFE) of FCC Ni binary alloys. Ensembles of large numbers of atomistic structures, each with more than ~400 atoms, were generated to consider sufficient long-range chemical disorder and temperature effects due to configurational entropy. A Monte Carlo Metropolis algorithm was used to generate these structures, whose energies were then evaluated based on the effective cluster interactions obtained from CE. As a baseline, this work had shown the SFE of pure Ni and Al to be 127 mJ/m^2 and 137 mJ/m^2, respectively, which agreed with the experimental values of 125 mJ/m^2 and 150 mJ/m^2 reported in the literature. Additions of Al, Ti, Cr and Co to pure Ni were found to decrease the SFE to different extents. Although temperature does not strongly influence the SFE of the FCC Ni-Al and Ni-Cr binary alloys, it can lead to significant changes to the SFE of the FCC Ni-Ti and Ni-Co alloys. While effects of temperature and composition on SFE observed in this work were calculated from binary Ni alloys, the general trends are nonetheless expected to be valid in the γ phase of multicomponent Ni superalloys.

Keywords: Ni superalloys; Stacking fault energy; Cluster expansion; Density functional theory; One dimensional axial Ising model

3.2. Introduction

Ni superalloys, owing to their exceptional thermal-mechanical properties at elevated temperatures and in corrosive environments, find applications under extreme conditions, such as ones encountered in gas turbines and power plants [57–60]. The alloys' superior high-temperature strength is primarily ascribed to a solid solution strengthened FCC matrix (γ) that can also be strengthened by γ' and/or γ" intermetallic precipitates. The γ' precipitates have an $L1_2$ ordered lattice structure and are typically coherent with the γ matrix. The existence of Nb and Fe are believed to result in precipitation of another ordered phase, with $D0_{22}$ lattice structure, known as γ" which is typically disk-shaped [61,62]. The γ" is also coherent with the γ matrix but is at a significantly larger lattice mismatch— ~3.0% or ~0.5% depending on the crystallographic orientation [63].

Other phases, such as topologically close packed phases and various forms of carbides, are observed mostly at grain boundaries. These phases do not significantly contribute to the strength of the material, but can prevent grain boundary sliding and improve the creep properties of the alloy [64]. While the precipitates impede the gliding motion of dislocations and are primarily responsible for the strengthening in Ni superalloys, the more compliant γ matrix accommodates plasticity better and is more susceptible to plasticity induced damage [65]. As is well known, a strong influencing factor for plasticity occurring in the γ phase is the stacking fault energy (SFE) [66,67].

In FCC crystals, a perfect dislocation dissociates into Shockley partials, bounding a stacking fault, to reduce the dislocation line energy. The width of the stacking fault is determined by the energy balance between the repelling partial dislocations and the fault's excess energy. The equilibrium distance between the Shockley partials is therefore given as:

$$d_{eq} = \frac{Gb^2}{\gamma_{SFE}} f \quad (1)$$

where d_{eq} is the equilibrium distance of the Shockley partials, G is the shear modulus, b is the magnitude of the Burgers vectors of the partials, γ_{SFE} is the SFE, and f is a geometrical factor that depends on the dislocations' character [47,68]. Using this relation, transmission electron microscopy is typically used to measure the SFE by measuring the separation distance between a partial dislocation pair [69,70].

Applied stress, temperature, and SFE dictate the activation of different mechanisms occurring during slip, such as cross slip and climb [71–73]. Cross slip can happen via the Friedel-Escaig (FE) mechanism [74–76], in which an extended core will constrict locally and dissociate again onto another slip plane [77]. Accordingly, the reduction in the SFE will increase the energy barrier for the cross slip. Similarly, dissociation of perfect dislocations into Shockley partials also results in the reduction of climb-rate as constriction is required prior to the climb of a dislocation. Indeed, Argon et al., using a hard-sphere model, demonstrated that the climb velocity of an extended jog is reduced as the SFE is reduced [78]. Experimental results also indicate that higher SFEs lead to higher creep rates [79–81] in dislocation creep regime, indicating the positive influence of SFE on the dislocation climb rate.

SFE is strongly influenced by local chemistry [82]. The complex chemical composition of the Ni superalloys makes it difficult to account for the effect of all atomic species in numerical calculations. For instance, both molecular dynamics (MD) simulations and density functional theory (DFT) had been used to evaluate SFE using the supercell approach or the axial Ising model (AIM) [83–86]. The supercell approach calculates the SFE by comparing the total energies of perfect and faulted structures. However, the main drawback of MD had been the lack of accurate

interatomic potentials that can represent multiple atomic species. On the other hand, DFT calculations, although capable of modeling the interactions among multiple atomic species, are computationally limited. In addition, the interaction between different chemical species with the stacking fault tends to strongly influence the results of the calculations [87]. Direct DFT calculations with the supercell approach had been performed with only a few tens of atoms [84]. As a result, increasing the number of the random configurations (each containing 24 atoms) from 4 to 25 have led to a change in SFE by 20-30 mJ/m^2.

In contrast to the supercell approach, the AIM is regarded as a "non-local" method and does not explicitly consider the location of a specific stacking fault. When combined with DFT, it can produce more reliable, "averaged" SFE values [84,88,89]. However, due to DFT's inherent limitation in the computational length scale, the effect of chemical disordering in the alloys still cannot be properly accounted for. To this end, statistical mechanical models, such as the cluster expansion (CE) method, may help overcome the length scale barriers of DFT. Indeed, the DFT + CE framework had been successfully applied to investigate the effects of temperature and composition on the antiphase boundary energy in Ni superalloys [1,90].

In this work, a combination of DFT, cluster expansion (CE), and AIM have been used to determine the SFE of FCC $Ni_xM_{(1-x)}$ alloys (M = Al, Ti, Cr, and Co) in a temperature range that is likely to be encountered by Ni superalloys during service. The results shed light into the general effects of solutes and configurational variations due to temperature on the SFE of Ni superalloys. With the effective cluster interactions determined by CE, the chemical disordering effect was captured by calculating the energies of 1000+ randomized atomistic configurations per composition—each of such configurations contained more than ~400 atoms. For each composition, three different crystal structures, namely FCC, HCP, and double hexagonal close-

packed (DHCP), were considered to formally establish the second nearest-neighbor AIM. In what follows, the temperature effects on the SFE originating from configurational entropy is referred to as the "configurational temperature effect". This article first explains the utilized methodology and describes the investigated material system in Section 2. Section 3 presents the main findings of this study and discusses the effect of solutes, configurational temperature effect, and their synergy on the SFE of Ni binary alloys. Finally, the conclusions are drawn in Section 4.

3.3. Methodology and Computational Details

Using AIM combined with CE and Monte Carlo (MC) sampling, the SFE of binary FCC $Ni_xM_{(1-x)}$ alloys are calculated at a range of temperatures. Since the service temperature of most Ni superalloys are generally below 1100 K, it has been selected as the maximum temperature in the current study. Due to their high mechanical strengths and good corrosion resistance, many Ni superalloys are also used in the room temperatures. Therefore, the temperatures considered in this study are 300K, 700K, and 1100K. The approach, as summarized in the Graphical Abstract, include: (1) parameterization of the interaction between dissimilar atoms in an alloying environment using CE and DFT calculations in FCC, HCP, and DHCP lattices; (2) calculation of average per atom energies of the randomized atomistic configurations under three parent lattice structures at each composition; and (3) calculation of SFE at each composition using AIM. This section provides details regarding each part of the procedure, including the AIM, CE, and DFT.

3.3.1. Axial Ising Model (AIM)

AIM approach is adopted in this work to overcome the shortcomings of the supercell approach with DFT calculations, i.e. the undesired interactions between a stacking fault and its periodic images. Within the supercell approach, if the effects of such interactions are to be minimized, the number of atoms within the cell would have to be increased, and—if the random

nature of the solid solution is to be captured—it will likely exceed the capability of the DFT method (100~200 atoms).

In these cases, energy parametrization seems to be a viable alternative. Indeed, the AIM, which was adapted from the generalized Ising model, has been utilized to parametrize energies of atomic structures composed of periodic stacking of atomic layers [88,89,91,92]. In this method, a spin parameter, S_i, taking the values ±1, will be assigned to each layer based on the stacking of the next layer. For instance, in an FCC structure, if layer i+1 conforms to the perfect stacking sequence, S_i will be +1. Otherwise, S_i will be assigned -1. As an example, the spin parameters assigned to a stacking such as, …ABCBC…, would be shown in up/down spin notation as ↑↑↓↑↑, and the corresponding spin parameters would be 1, 1, -1, 1, 1. Having defined the spin parameters, the energy of an atomic stack can be calculated as:

$$E = J_0 - J_1 \sum_i S_i S_{i+1} - J_2 \sum_i S_i S_{i+2} - J_3 \sum_i S_i S_{i+3} - \cdots \quad (2)$$

where J_i are the interaction coefficients having the units of energy, which can be obtained by equating Eq. 2 to the calculated energy of atomic stacks using numerical methods such as DFT and solving the corresponding linear systems of equations. The number of solvable interaction coefficients, J_i, depends on the available number of atomic stacks with known energies. The values of the interaction coefficients measure how strongly a particular atomic layer interacts with its neighbors, i.e. J_0 indicates self-interaction, J_1 indicates nearest-neighbor interaction, J_2 indicates second nearest-neighbor interaction, etc.

Theoretical works have shown that the second-order expression considering the interaction of next-nearest neighbors within AIM model is accurate enough to parametrize the energy of atomic stacks [93,94]. This work, therefore, only considers J_i where $i \leq 2$. The energy per layer of

the stack in each of the parent lattices is (here the lower case e is used to denote the per layer energy):

$$e_{ABC} = J_0 - J_1 - J_2 - O(J_3) + \cdots$$

$$e_{AB} = J_0 + J_1 - J_2 + O(J_3) + \cdots \quad (3)$$

$$e_{ABCB} = J_0 + J_2 + O(J_3) \ldots$$

Solving Eq. 3, one can obtain the interaction coefficients. Isolating a single fault within the structure by increasing the number of layers to infinity, the SFE can be calculated by subtracting the energy polynomials as:

$$E_{ISF} - E_{FCC} = \gamma_{ISF} A_{ISF} = 4J_1 + 4J_2 \quad (4)$$

where A_{ISF} is the area of the stacking fault, E_{ISF} and E_{FCC} are the total energies of structures containing only one intrinsic stacking fault (ISF) and no stacking fault, respectively. For any compositions listed in Table 1, three different stacking sequences, namely ABC (FCC), AB (HCP), and ABCB (DHCP) (shown in Fig. 1), have been considered to calculate the interaction coefficients appearing in Eq. 2. Substituting Eq. 3 into Eq. 4, the intrinsic SFE can also be calculated by directly substituting the per layer, energy of these three stacking sequences, i.e.

$$\gamma_{ISF} A_{ISF} = e_{AB} + 2e_{ABCB} - 3e_{ABC} \quad (5)$$

Each term appearing in Eq. 5 are the mean values obtained by averaging the per atom (normalized to the case of one atom per layer) energies of over 1000 variations in the atomic configurations, constructed by MC sampling scheme and evaluated by CE method.

3.3.2. Cluster Expansion (CE)

Energies of the atomic stacks used to solve for the interaction coefficients in Eq. 2 are obtained using the CE method [95] via the ATAT toolkit developed by van de Walle et al. [96]. For each composition, ~1000 randomized configurations/clusters of atoms representing alloying elements in a disordered solid solution are considered and their mean energy value obtained. These small atomic clusters are periodic and typically contain no more than ~10 atoms (such as the schematic representations and the actual geometries shown in the top and middle rows of Fig. 2) [97]. In CE formalism, any configuration dependent function, including energy, can be expressed using orthogonal cluster functions ($\varphi_{\alpha s}$) and the so-called effective cluster interactions ($K_{\alpha s}$) i.e.

$$E(\sigma) = \sum_{\alpha} \sum_{s} K_{\alpha s}\, \varphi_{\alpha s}(\sigma), \tag{6}$$

where α is the designation used for each cluster of atoms and s is the order of the orthogonal polynomial used to describe the cluster functions [95,98,99]. The effective cluster interactions ($K_{\alpha s}$) can be fitted to the energies of small atomic clusters obtained from DFT calculations (such as the ones shown in Fig. 2). The accuracy of the CE, is measured by cross-validation (CV) score:

$$CV = \sqrt{\frac{1}{n}\sum_{i=1}^{n}\left(E_i - \hat{E}_i\right)^2} \tag{7}$$

where n is the total number of structures used to obtain the cluster interaction coefficients, E_i is the energy of the cluster i using DFT calculation, and $\hat{E}_i$ is the energy obtained by CE using all the structures except for cluster i to calculate the interaction coefficients.

As SFE is sensitive to the local chemistry, the chemical disorder effect on the SFE can only be considered when enough structures are generated and their mean energy value obtained. For this purpose, starting from an initial structure, MC sampling is performed with the Metropolis algorithm to swap atoms within the lattice structure. Note that the MC "randomization" is needed

as structures with lower energies are more probable to occur [100]. Starting with the initial atomistic configuration as the reference structure, if the new structure generated has lower energy, i.e. $\Delta E = E_1 - E_0 < 0$, the new cluster will be accepted as a new reference configuration. Otherwise, a temperature-dependent probability, $\exp\left(-{}^{\Delta E}/_{k_b T}\right)$, will be assigned for the acceptance of the new configuration. Here, k_b is the Boltzmann constant, and T is the temperature in the units of Kelvin. At any given composition and temperature, configurational variations in the atomic structures generated by the aforementioned procedure may induce fluctuations in the SFE, which can be estimated based on the standard deviation (SD) of the energies of these structures under each parent lattice. According to Eq. 5, an upper bound estimation of the SD of γ_{ISF} can be calculated as:

$$SD(\gamma_{ISF}) = 1/A_{ISF}\,[SD(e_{AB}) + 2 \times SD(e_{ABCB}) + 3 \times SD(e_{ABC})] \quad (8)$$

where $SD(\gamma_{ISF})$ accounts for the natural fluctuation in the SFE due to configurational entropy, $SD(e_{AB})$, $SD(e_{ABC})$, and $SD(e_{ABCB})$ are the SDs of the per-atom energies of the HCP, FCC, and DHCP structures generated by MC, respectively. As shown, the SDs of the per-atom energies of all lattice structures superimpose constructively in the calculation of $SD(\gamma_{ISF})$.

Since Eq. 5 is extremely sensitive to error, correction factors based on the difference in the energies obtained from DFT and CE performed on pure systems are considered for each element type. Note that the correction factors for a specific material vary by the change of the parent lattice.

The advantages of using CE method over conventional direct DFT to calculate the energy of an atomic structure are twofold. First, many more different configurations can be calculated using CE, which incorporates the effect of chemical disorder. Second, since CE can calculate much

larger atomic clusters, much more dilute solid solutions can be accessed (compare 1 solute atom in a 10-atom cluster vs. 1 solute atom in a 400-atom cluster).

3.3.3. Correlating CE of Different Parent Lattices

Within CE, the calculated per-atom energy of material with parent lattice-type β is presented as

$$E_{\beta}^{CE} = \sum_{i=1}^{n} x_i \, E_i^{pure} + \Delta E_{inter} \quad (9)$$

where the sum is taken over all atom types that exist in the configuration, x_i is the concentration of atom type i, E_i^{pure} is the per-atom energy of atom i in the pure limit, and ΔE_{inter} is the interaction energy of dissimilar atoms within the configuration. Although the CE produces energies of atomistic configurations with relatively good accuracy (CV is below 0.020 eV/atom for all cases), when performed on different parent lattices, it may give rise to small systematic errors that may accumulate due to the form of Eq. 5. As such, the energy terms used in Eq. 5 are obtained from Eq. 9 and adjusted based on a correction factor.

The correction factors are obtained in the limit of pure materials using the per atoms energies acquired from DFT calculations ($E_i^{DFT-pure}$) as a reference, i.e.

$$C_{Cor.} = \frac{E_i^{DFT-pure}}{E_i^{pure}} . \quad (10)$$

Thus, the final form of the calculated energy for parent lattice-type β that will be substituted in Eq. 5 is calculated as:

$$E_{\beta} = \sum_{i=1}^{n} C_{cor.} E_i^{pure} x_i + \Delta E_{inter} \quad (11)$$

Note that in Eq. 11, ΔE_{inter} is a mean value evaluated based on 1000 or more atomic configurations. In addition, ΔE_{inter} is solely due to the configurational variations induced by finite temperatures – vibrational entropic effects [101] are not included.

3.3.4. Density Functional Theory

To obtain the energies of the atomic clusters (such as ones shown in the bottom row of Fig. 2) for CE, first-principle calculations based on DFT as implemented in Quantum Espresso package has been performed. These small atomic clusters are periodic and typically contain no more than ~10 atoms (such as the schematic representations and the actual geometries shown in the top and middle rows of Fig. 2) [97]. The pseudopotentials have been obtained from the standard solid state pseudopotential (SSSP) repository [102]. The combined effect of nuclei and core electrons with the valence electrons is incorporated using the projector augmented wave (PAW) method for Al, while ultrasoft pseudopotentials are used for the rest of elements, i.e Ni, Ti, Cr, and Co. The Perdew-Burke-Ernzerhof parametrized form of the generalized gradient approximation for the true exchange and correlation functional is used in self-consistent calculations [103]. A plain wave basis with 35 Ry (476 eV) energy cutoff is used to expand the wave functions. For the integration over the Brillion zone, the Monkhorst-Pack scheme has been used for k-point sampling with the k-point density of 0.02-0.03 Å in the reciprocal space. Necessary spin polarization is used whenever the clusters contain magnetic elements such as Ni, Cr, and Co. The energy convergence criterion for self-consistent energy calculation is 10^{-7} Ry. To verify the accuracy of the pseudopotentials used, the lattice parameters and the elastic constants of the pure elements were calculated and compared to data available in literature. The results of such comparison were provided in the authors' earlier work [1]. For all three parent lattices, i.e. FCC, HCP, and DHCP, the volumetric relaxation is performed while keeping the ions fixed and maintaining the lattice

symmetry. This technique has proven to yield results in good agreement with the experiments, since chemical disorder was shown to have more influence on the SFE [1,84].

3.4. Results and Discussion

3.4.1. SFE of Pure FCC Crystals from DFT

To establish a baseline and confidence in the methodology adopted in this study, the SFEs of pure Ni and Al crystals are first calculated using DFT combined with AIM and compared with the literature. Since there is no chemical disorder effect in the case of pure crystals, direct DFT calculations are used to obtain energies of the three parent lattices, including FCC, HCP, and DHCP. Computational details regarding DFT calculations are similar to what has been mentioned in Section 2.4. Ground state lattice structures are acquired by fitting the Murnaghan equation of state to a series of structures, with varying cell parameters [104]. The equilibrium lattice parameters of the FCC structures are also obtained from this procedure and are used to calculate the per atom area on the {111} lattice planes. Resulting SFE of pure Ni and Al are presented in Table 2 along with the data available in the literature. The calculated SFE value in this study for Ni is 127.37 mJ/m^2, and for Al this value is 137.44 mJ/m^2, respectively, which resides well within the reported ranges by both experimental and numerical studies. For instance, Carter et al. have measured the equilibrium distance of a dissociated edge dislocation using weak beam transmission electron microscopy (TEM) and obtained the SFE of Ni to be within the range 120-130 mJ/m^2 [69]. Experimentally measured intrinsic SFE of Al is reported to be 135 ± 20 mJ/m^2 [105].

Next, to calculate the correction factors introduced in Eq. 11, the per-atom energies of prototypical FCC, HCP, and DHCP lattices for other elements considered in this study, i.e. Ti, Cr, and Co, are calculated using DFT as well. Accordingly, the determined correction factors ($C_{Cor.}$) are included in Table 3.

3.4.2. Multicomponent CE Parameterization

Compositional range for each binary alloy (1-*x* for $Ni_xM_{(1-x)}$, where M = Al, Ti, Cr, or Co) is decided such that only the disordered FCC solid solution forms throughout. Therefore, the range of compositions selected for CE of all parent lattices should cover the compositions investigated here. Based on the binary phase diagram of Ni-Al [106] starting from 300 K up to 1100 K, the solubility of Al linearly increase from 7.5 at. % to ~15 at. %. The excess Al dissolved into the Ni matrix above the mentioned threshold will form the ordered $L1_2$ γ' phase. Since the lattice structure of the γ' phase exactly matches that of the FCC parent lattice, the resulting energy values obtained from CE are still valid as a measure of the complex stacking fault energy [107]. On the other hand, Ni matrix can hold a maximum amount of ~15 at. % of Ti at 1300 K. Lower temperatures at this composition or excess Ti solute addition to the system will result in precipitation of the Ni_3Ti compound [108]. The equilibrium lattice structure of this phase is hexagonal $D0_{24}$ [109]. Consequently, the CE performed using FCC parent lattice is no longer applicable to this phase. Therefore, the maximum concentration of Ti is limited to ~15 at. %.

For Cr and Co, based on the phase diagram, in order to have a single-phase solid solution compatible with the FCC lattice structure, a maximum of 45 at. % and 75 at. % percent solute can be added, respectively [110–112]. Note that above the Co's transition temperature (from HCP to FCC) Ni and Co are infinitely soluble. However, to avoid the formation of HCP phases at room temperature, the solute concentration is limited to 75 at. %. As listed in Table 1 for all the solute elements, multiple equally spaced compositional intervals are designed to capture the solute effect on the SFE. For all compositions listed above, the configuration-dependent energies are obtained using the multicomponent CE with correction factors applied (see Eq. 11).

Details regarding the multicomponent CE performed in this study are included in Table 4. In all three cases, a minimum of 25 at. % Ni is defined as the constraint by which the clusters are generated, and effective cluster interactions are obtained. As shown, all three CEs are resulting in energy values that are close to the exact energy values, evidenced by the cross-validation score of 0.0114, 0.0163 and 0.0189 meV/atom are obtained for the HCP, FCC and DHCP parent lattices, respectively. Using MC metropolis algorithm, a minimum of 1000 structures are generated and calculated for each parent lattice types and at each composition, reaching a convergence of the mean energy. In all cases, convergence is ensured within a threshold of 1 meV/atom. Typical convergence behavior of 15 at. % Al within the Ni matrix is shown in Fig. 3.

3.4.3. SFE of Binary Alloys at Room Temperature

The variation of SFE due to solute changes in binary alloys are measured by $\Delta\gamma_{ISF}$ – a relative SFE with respect to that of the pure Ni (127 mJ/m^2, see Table 2). The effect of solute concentration on the SFE of binary Ni-Al alloy at room temperature has been presented in Fig. 4(a) and compared to the values reported in the literature. As reported in the literature, with the increase of Al concentration up to ~10 at. %, the SFE significantly drops—as low as 60 mJ/m^2 (50% of the reference value) [113]. The energy drop calculated in this study is almost linear with the increase in Al concentration and agrees well with the reported experimental results. Note that the experimentally measured value of SFE for pure Ni in Fig. 4(a) is obtained from Hirth and Lothe and the results for alloyed metal by Al addition are taken from the study of Beeston et al. [47,113]. A similar descending trend was also reported by Nie et al. using MD, although the present work was able to capture the trend shown in the experiment more accurately [86]. Al concentrations beyond 15% lead to a drastic increase in SFE. This trend, although not reported in the literature,

does seem intuitive as the Al concentration of 25% corresponds to the formation of Ni_3Al compound, which has a very high complex stacking fault energy of ~230 mJ/m^2 [107].

On the other hand, this study indicated that the increase in Co content also decreases the SFE of the binary Ni-Co alloy at room temperature. Delehouzee et al. have experimentally measured the stacking fault density of multiple binary solid solutions and reported that the stacking fault density measured from alloy filings using X-ray diffraction analysis is inversely related to the SFE [114]. Using this relation, one can estimate the SFE of a $Ni_xM_{(1-x)}$ alloy based on its stacking fault density relative to the SFE and the stacking fault density of pure Ni. This procedure has shown a pronounced drop in SFE of binary Ni-Co alloys (red dashed line with hollow circles in Fig. 4(b)), which in a good agreement with the present study. The experimental measurement from Koster et al. [115] by weak beam TEM is also in qualitative agreement with this study, although they reported a more significant rate of decline of SFE at the Co concentration of 55%~70%. As shown in Fig. 4(b), the discrepancy among the experimental data in the literature appears to have increased as the solute concentration decreases. The discrepancy is ~20 mJ/m^2 among these results at ~55 at. % Co concentration.

The comparison of results from multiple numerical studies on the effect of solute concentration on the SFE of Ni-Co binary alloys are also plotted in Fig. 4(b) [84,86,116]. Chandran et al. utilized a similar AIM based approach to capture the effect of alloying elements on the SFE of binary alloys, although they used direct DFT calculations within the framework of AIM. The computational cost of direct DFT calculations limits the total number of atomistic configurations that can be considered to account for the chemical disorder. In their study, an ensemble containing 30 different configurations was used at each composition. Data produced by Chandran et al. (green solid triangles in Fig. 4(b)) qualitatively agrees with this study and the experimental results,

although relatively large scatter exists. The results from the MD calculations by Nie et al. [86], however, appear to overestimate the SFE compared to the experimental results—at 70 at. % Co concentration, the difference in SFE is ~20 mJ/m^2.

The effects Ti and Cr solution in room temperature SFE of the Ni-Ti and Ni-Cr binary alloys are presented in Figs 4(c) and 4(d) and were compared to the limited data in the literature. The present study suggests that both Ti and Cr reduces the SFE, which is in general agreement with the literature. Specially, within 15%, the predicted reducing effect of Ti (~120 mJ/m^2) is more significant than that of Cr in the same concentration range. The literature data on the effect of Ti, although limited, appear to agree fairly well (see Fig. 4(c)) [114,117]. The present work slightly underestimates Ti's reducing effect on SFE. As for Cr, although all literature data consistently suggested that Cr reduces SFE of the Ni based binary alloys, significant scatter exists (Fig. 4(d)) [114,117,118]. The present work's prediction agrees well with the one made by Li et al. [89,118] at Cr at. % below 30%. Nevertheless, the overall effect of Cr predicted by this work is in a reasonable agreement with the experimental measurement by Delehouzee et al [114]. The reducing effect of Cr were also highlighted in the theoretical calculation of ternary alloys using first principle calculations [89].

3.4.4. Synergy of Solute Content and Configurational Temperature Effects on the SFE of Binary Alloys

The complete data set obtained from this study showing the combined solute atom concentration and configurational temperature effects on the SFE of the Ni-base binary FCC alloys (measured by the relative SFE, i.e., $\Delta\gamma_{ISF}$) is presented below. The temperature effects captured in this work only arise from the temperature-dependent configurational entropy and do not

incorporate the vibrational entropy [119]. As shown in Fig. 5(a), the temperature does not significantly influence the SFE value of Ni-Al alloy. As the concentration of Al increases (up to 15 at. %) the SFE experiences a relative decrease of ~125 mJ/m^2 (see Fig. 5(a)), effectively dropping to 0 on the absolute scale. Further increase in solute concentration increases the SFE. This increasing trend, as discussed in Section 3.3, is somewhat echoed by the experimental data available in the literature that the complex SFE of the Ni_3Al (25% of Al) phase is ~235 mJ/m^2, which is significantly higher than that of the pure Ni or any of the FCC Ni-Al alloys [107,113]. Since Ni_3Al is a thermally stable compound and, as was shown by Dodaran et al. [1], no configurational variations were expected even at elevated temperatures (up to 1100K), this trend of SFE variation of Ni-Al alloy beyond 15 at. % Al is expected to be valid at different temperatures [107,113].

Variation in the SFE of binary Ni-Co system is presented in Fig. 5(b). At room temperature (300K), the SFE rapidly decreases with the increasing Co concentration. However, at elevated temperatures, the SFE exhibited a slight increasing then decreasing trend. Overall, the Co concentration does not seem to affect the SFE of the FCC Ni-Co alloy when the configurational entropic effects of higher temperatures (700K and 1100K) are considered in the calculations. In the case of the Ni-Co alloy, the temperature appears to strongly influence the SFE. No data, to the best knowledge of the authors, is available in the literature on the SFE of Ni-Co alloys at elevated temperatures. However, the decrease in SFE at room temperature obtained in this study is in perfect agreement with the existing numerical and experimental investigations [84,114,115], as was discussed in Section 3.3.

As shown in Fig. 5(c), the increase in the concentration of Ti significantly decreases the SFE, while the increase in temperature has a similar effect, i.e., increase in temperature from 300

K to 1100K tends to decrease the SFE as a result of change in configurational entropy. Note that the effect of solute concentration is far more pronounced than that of the configurational temperature effect. Overall, the introduction of 15 at. % Ti solute decreases the SFE by 150±50 mJ/m^2 relative to pure Ni. The Cr concentration and configurational temperature effects on the variation of SFE of the FCC Ni-Cr is shown in Fig. 5(d). As an overall behavior across all temperatures, when Cr is introduced to pure Ni, the change in SFE is not significant up to ~25 at. %. However, the further increase in the concentration of Cr tends to decrease the SFE to a maximum of ~200 mJ/m^2 relative to pure Ni. It is worth noting that the configurational temperature effect is most significant when the Cr concentration is ~25%.

Fluctuations in the SFE ($SD(\gamma_{ISF})$) due to the configurational variations in the atomic structures generated by MC, as calculated using Eq. 8, are shown in Fig. 5 as error bars. As shown, in most cases $SD(\gamma_{ISF})$ increases with increasing temperature. This is expected since, as mentioned in Section 2.2, the temperature dependent probability assigned for the acceptance of new structures within the MC scheme will increase as the temperature increases, leading to larger configurational variation. Due to the same reason, for thermally stable, ordered compounds such as Ni_3Al, the $SD(\gamma_{ISF})$ is expected to be smaller than disordered alloys. Indeed, this is evident in Fig. 5(a) where the fluctuation in the SFE at 25 at. % Al is considerably smaller than other compositions at all temperatures. Similarly, the $SD(\gamma_{ISF})$ for pure Ni is always zero since the configurational entropy is zero.

3.5. Conclusions

In this work, the axial Ising model (AIM) is combined with density functional theory calculations (DFT) and cluster expansion (CE) to investigate the solute concentration and configurational temperature effects on the stacking fault energy (SFE) of binary Ni alloys. The

effect of the chemical disorder has been incorporated by evaluating the energies of a minimum of 3000 atomistic structures for each composition using the Monte Carlo (MC) sampling scheme. The CE method is used to calculate the energy of all the structures constructed by MC. The following conclusions can be drawn:

1) Across the entire temperature range of 300 K-1100 K, an increase in Al concentration first decreases and then increases the SFE, while configurational temperature effects on SFE are negligible.
2) An increase in solute concentration in binary FCC $Ni_xTi_{(1-x)}$ alloy significantly decreases the SFE. Variation of SFE is not significant up to 15 at. % of Ti while further increase in solute concentration decreases the SFE significantly. Configurational variations due to temperature effects further reduces the SFE.
3) An increase in Cr concentration decreases the SFE, while configurational variations due to temperatures does not have a clear and pronounced influence.
4) The addition of Co reduces the SFE of the Ni-Co alloy at room temperature, while not significantly influencing SFE at elevated temperatures.

Tables

Table 3. 1 Compositional ranges of the binary $Ni_xM_{(1-x)}$ alloys considered in the present work and the solubility of various elements in Ni.

Alloying element	**Solute Concentration at. %**					**Solubility @700 K at. %**	**Solubility @1100 K at. %**
Al	5	10	15	20	25	11	15
Ti	5	10	15	---	---	~7	12
Cr	9	18	27	36	45	36	47
Co	15	30	45	60	75	100	100

Table 3. 2 SFE of pure Ni and Al.

Al	γ_{SF} ($^{mJ}/_{m^2}$)	Ref	Ni	γ_{SF} ($^{mJ}/_{m^2}$)	Ref
This study	137.44		This study	127.37	
Exp.	280±50	[120]	Exp.	125	[47]
	135±20	[105]		214	[121]
	166	[122]		120-130	[69]
	150±40	[123]		128	[122]
Sim.	144 (MD)	[86]	Sim.	134 (MD)	[124]
	158 (DFT)	[125]		137 (MD)	[126]
	124 (MD)	[127]		125 (MD)	[128]
	124 (DFT)	[129]		110 (DFT)	[130]
	130 (DFT)	[131]		133 (DFT)	[132]
	146 (DFT)	[128]		127 (DFT)	[132]
	164 (DFT)	[133]		129 (MD)	[134]
	203±77 (DFT)	[135]		262 (DFT)	[136]

Table 3. 3 Per atom energies obtained from DFT, predicted by CE, and correction factors obtained for different lattice structures to be used in the AIM.

	FCC			HCP			DHCP		
	DFT (eV/atom)	CE (eV/atom)	$C_{Cor.}$	DFT (eV/atom)	CE (eV/atom)	$C_{Cor.}$	DFT (eV/atom)	CE (eV/atom)	$C_{Cor.}$
Ni	-4670.232	-4670.254	0.9999953	-4670.217	-4670.223	0.9999986	-4670.222	-4670.261	0.9999916
Al	-537.4697	-537.2719	1.0003681	-537.433	-537.2068	1.0004217	-537.457	-537.3557	1.0001895
Ti	-1622.432	-1622.437	1.0000527	-1622.461	-1622.393	1.000011	-1622.441	-1622.328	1.0001154
Cr	-2387.312	-2387.324	1.0000105	-2387.264	-2387.216	0.9999895	-2387.299	-2387.408	1.0000547
Co	-4061.093	-4061.075	1.0000042	-4061.097	-4061.041	1.0000137	-4061.094	-4061.166	0.9999823

Table 3. 4 Number of relaxed structures and cross validation scores for CE performed for the current study.

Structure	Number of clusters relaxed by DFT	Cross validation score (eV/atom)
HCP	1689	0.0114866
FCC	1669	0.0163439
DHCP	1725	0.0189006

Figures

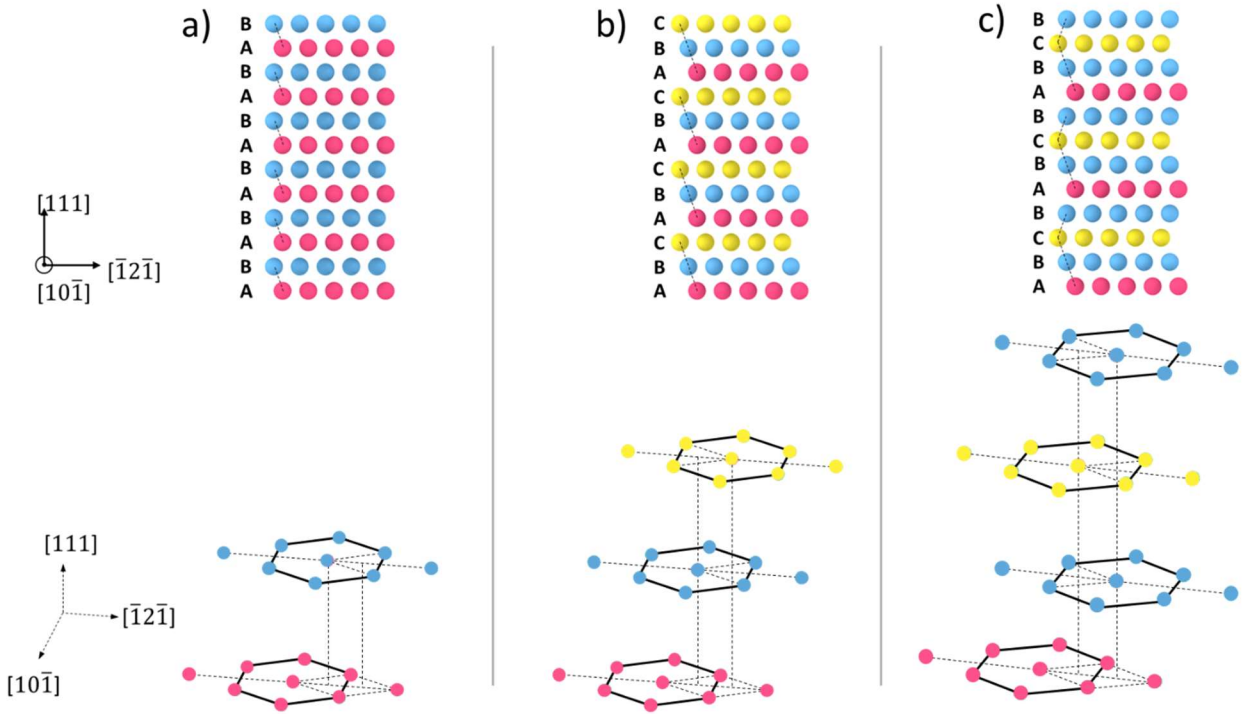

Figure 3. 1 Different stacking along <111> direction, used in Axial Ising model: a) HCP, b) FCC, and c) DHCP.

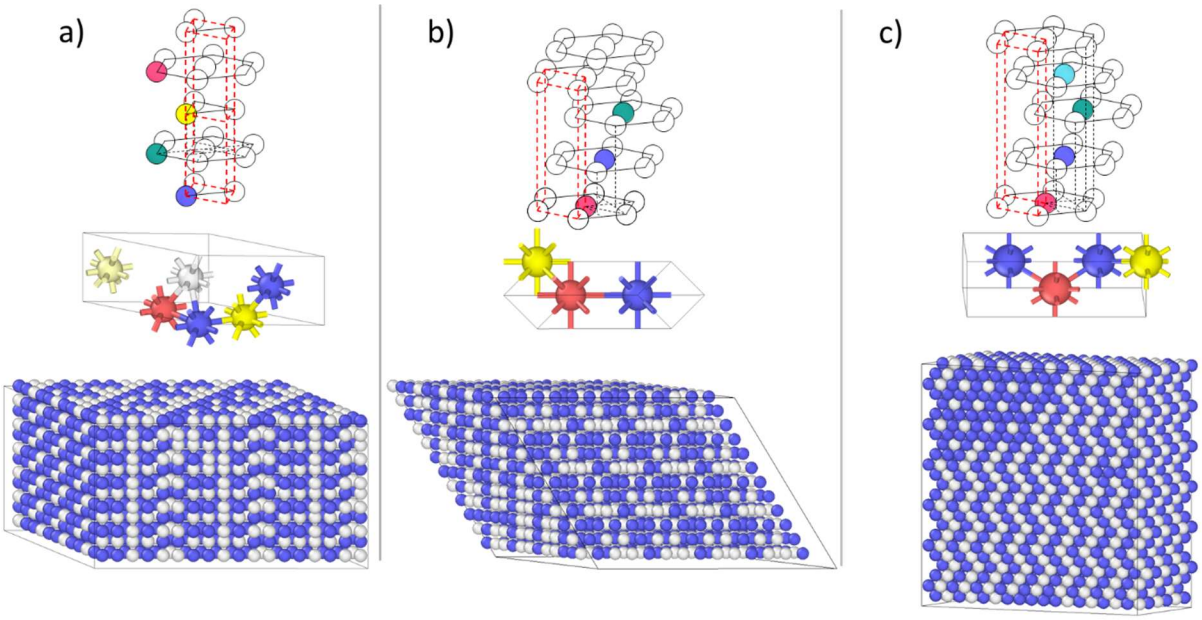

Figure 3. 2 Top and middle rows: schematic representation vs actual geometries of supercells relaxed by DFT calculations for different parent lattices: a) HCP, b) FCC, and c) DHCP. Bottom row: actual supercells whose energies are calculated by cluster expansion (CE).

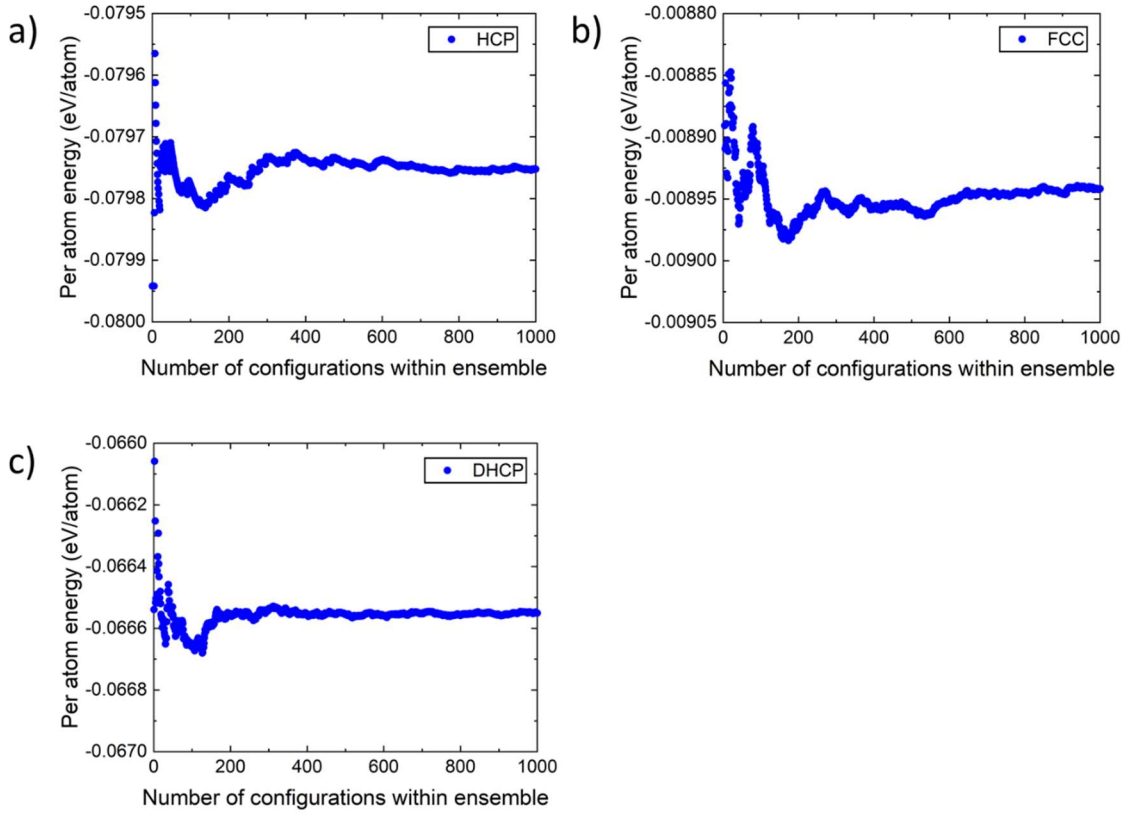

Figure 3. 3 Typical convergence behavior (using 15 at. % Al in Ni for instance) of the mean per atom energies with respect to the number of configurations generated by MC for three parent lattice types: a) HCP, b) FCC, and c) DHCP.

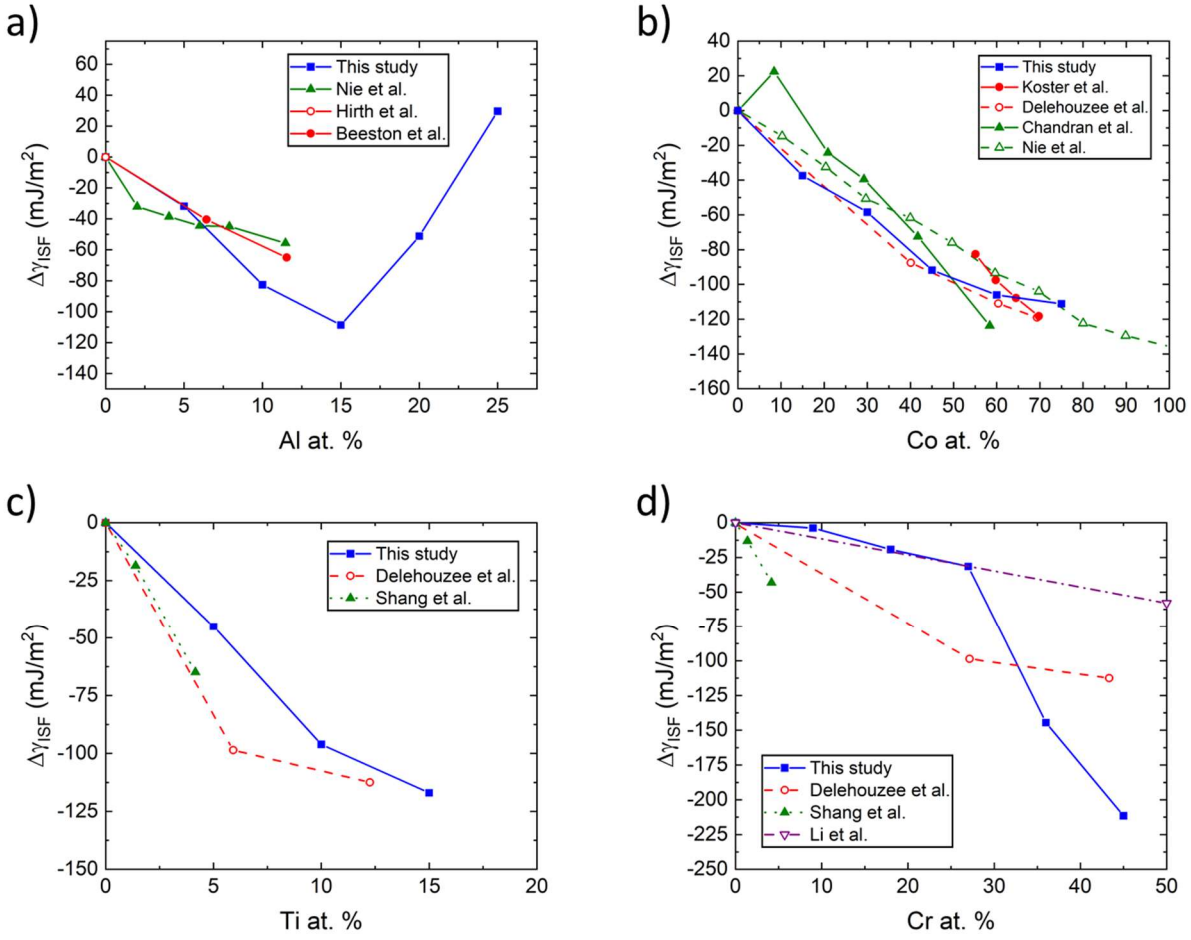

Figure 3. 4 Variation in SFE (ΔγISF with the SFE of pure Ni as reference) as a result of change in solute concentration for a) NixAl(1-x), b) NixCo(1-x), c) NixTi(1-x), and d) NixCr(1-x) alloys.

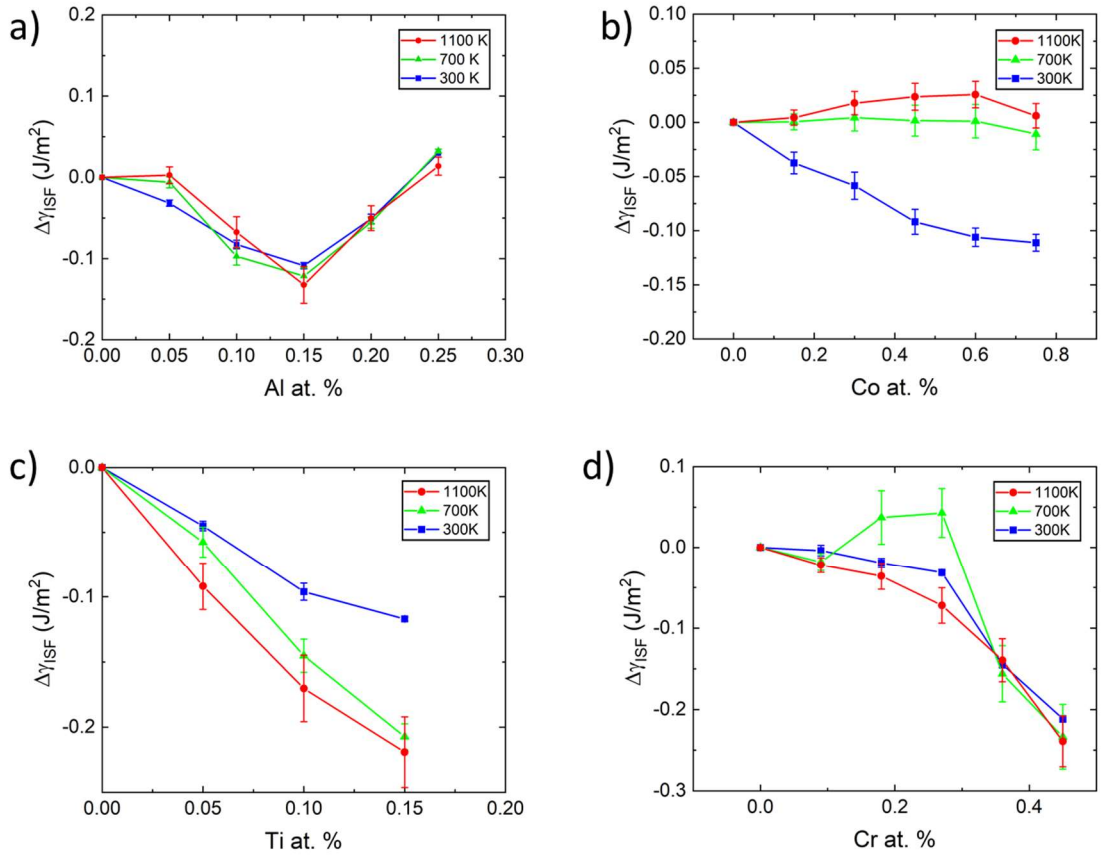

Figure 3. 5 Synergistic effect of temperature and solute concentration on the SFE (ΔγISF with the SFE of pure Ni as reference) of NixM(1-x) alloys with M being a) Al, b) Co, c) Ti, and d) Cr.

CHAPTER 4 EFFECT OF ALLOYING ELEMENTS ON THE γ' ANTIPHASE BOUNDARY ENERGY IN Ni-BASE SUPERALLOYS

4.1. Abstract

Mechanical and fatigue performance of γ-γ' Ni-base superalloys are strongly affected by the antiphase boundary energy (APBE) of the γ' precipitates which, in turn, is dictated by the alloy's composition. Due to the multicomponent character of these alloys, establishing composition-APBE relationships are challenging, even though the qualitative effect of individual solutes on the APBE may be known. This work attempts to utilize density functional theory-based cluster expansion calculations to systematically assess the effect of composition on the APBE of the γ' phases in Ni-base superalloys. We aim to elucidate the influence of not only one single element but also multiple coexisting alloying elements on the γ' APBE. By explicit consideration of configurational disorder via Monte Carlo sampling, the effect of temperature on the APBE has also been analyzed. This work reveals that (1) effects of individual solute element M on the APBE energy obtained in an isolated, ternary condition (i.e. in $Ni_{3-x}Al_{1-y}M_{x+y}$) does not directly translate to a multi-solute case and that (2) the mutual synergistic interactions among different solute elements are not negligible. Based on the present results, an empirical master equation that predicts the APBE based on the composition of the γ' phases has been obtained.

Keywords: Ni-base superalloys; alloy design; antiphase boundary energy; $L1_2$ structure; cluster expansion; density functional theory

4.2. Introduction

Ni-base superalloys generally have excellent high-temperature strength, creep rupture resistance and corrosion resistance, and have been widely adopted as key components in the mid-high temperature regions of gas-turbine engines. These alloys typically comprise a γ (FCC) matrix phase, strengthened by either γ' (A_3B type of an ordered L12 structure, e.g. Ni_3Al) or γ" (an ordered body-centered tetragonal) coherent precipitates. The strengthening effect of the precipitates derives from two origins. First, the ordered lattice structures of the γ' and γ" phases inhibit the motion of dislocations, as the passing of a perfect dislocation from the γ phase to the γ' and γ" phases leads to the formation of antiphase boundaries (APB). Second, the lattice mismatch between the γ matrix and γ' or γ" precipitates induces long-range coherency stresses which further inhibits the motion of incoming dislocations. The lattice mismatch between γ and γ' is sensitive on the exact alloying composition (such as additions of Cr, Co, Ti or Mo), but is generally very small, around ~ ±0.2% [137–139]. The γ-γ'-γ" alloys generally offer better mechanical strengths over the γ-γ' alloys due to the additional strengthening effects offered by the lattice distortions surrounding the coherent γ" phase (a mismatch of ~3%) [140]. However, the γ" phase is unstable under temperatures above 650 ˚C and decomposes to a δ (orthorhombic DO_a) phase, which deteriorates the overall strength of the three-phased alloys [141–143]. On the other hand, the γ' phase displays a remarkable "stress anomaly" as a function of temperature in the intermediate temperature range (~300K to ~900K) [144], whereby the critical resolved shear stress (CRSS) increases as a function of the temperature. For these reasons, γ-γ' alloys are still preferred in the high-temperature regions of the gas turbines. The γ-γ' alloys are the focus of the present paper.

Under normal service conditions, modern rotating machinery's components are exposed to cyclic loading (such as vibration and rotating-bending, etc.) at low amplitudes and relatively high

loading frequency. These constitute high cycle fatigue (HCF, $N_f > 10^6$) and even very high cycle fatigue (VHCF, $N_f \approx 10^9$) conditions. Under the HCF and VHCF conditions, macroscopic plastic deformation is vanishingly small, as reflected by the almost linear hysteresis response. Thus, macroscopic plastic yielding does not occur. Instead, localized plastic deformation occurs due to elastic incompatibilities among grains and local stress risers [54,145]. The cyclic plastic deformations are typically achieved by the simple to- and fro- motion of dislocations, resulting in little dislocation multiplication and cyclic hardening/softening [26,40,146]. The accumulation of fatigue damage is largely associated with the screw dislocations, whose motion is likely to generate irreversible cyclic deformation, due to interruptive events such as cross-slip [26,145]. The extent of cyclic slip reversibility is dependent on the superalloys' composition, to which the occurrence of these interruptive events is sensitive.

In the FCC γ phase, perfect dislocations always dissociate into Shockley partials. Cross-slip of a perfect screw dislocation requires the temporary recombination of the partials, whose rate is positively correlated to the stacking fault energy (SFE) and, in turn, composition. In the $L1_2$ γ' phase, perfect screw dislocations exist in pairs, separated by ribbons of either APB or superlattice stacking faults (SSF).

When a perfect FCC dislocation enters the γ' precipitate, an APB is created on its wake until it is removal by a closely-spaced trailing perfect FCC dislocation. These dislocation-APB-dislocation defects are referred to as the super-dislocations in the γ' precipitates, with each dislocation being named as superpartial dislocations. The magnitude of the strengthening by γ' precipitates is closely related to the magnitude of APB energy (APBE), which is an important parameter in precipitation strengthening theories (PST) [147–154].

Extensive experimental evidence indicates the (111) type slip with a screw-APB-screw configuration is predominant in the "stress anomaly" regime [155]. The screw-APB-screw defects are referred to as the superscrew dislocations, while each perfect screw dislocation is referred to as superpartial dislocations. The mutual elastic interaction between the superpartials generates an interaction force component perpendicular to their slip plane, providing a driving force for their cross-slip. Due to this reason, the slip of screw dislocations in γ' is rarely planar and has a natural propensity to undergo the (111) to (100) type of cross-slip. The tendency of these cross-slip events is related to APBE.

A typical (111)-(100) cross-slip mechanism in the γ' phase is illustrated in Fig. 1. Each superpartial (SP in Fig. 1) dislocation dissociates into two Shockley partial (ShP in Fig. 1) dislocations separated by complex stacking faults (CSF) according to the reaction:

$$a[1\bar{1}0] \rightarrow \frac{a}{2}[1\bar{1}0] + \frac{a}{2}[1\bar{1}0] \rightarrow \frac{a}{6}[1\bar{2}1] + \frac{a}{6}[2\bar{1}\bar{1}] + \frac{a}{6}[1\bar{2}1] + \frac{a}{6}[2\bar{1}\bar{1}]. \quad (1)$$

The products of Reaction (1) correspond to the Burgers vectors of ShP *a*, ShP *b*, ShP *c*, and ShP *d*, respectively (Fig. 1(a)). Subjected to the mutual elastic interaction between SP 1 and SP 2, SP 2 dislocation feels both the tangential ($\boldsymbol{F}_{\theta}^{1\rightarrow 2}$) and the radial force ($\boldsymbol{F}_{r}^{1\rightarrow 2}$) originating from SP 1 (Fig. 1(b)). The resultant force drives the cross-slip of SP2 onto a (001) plane (Fig. 1(c)) [156,157]. The superpartial dislocations then re-dissociate into Shockley partials (Fig. 1(d)). Upon the onset of a reversed loading, the SP 2 dislocation (ShP *c* and ShP *d*) now travels back along a different path (Fig. 1(e)). The mechanism depicted in Fig. 1 leads to irreversible slip as the trajectory of a superpartial dislocation (SP 2) altered during its to-and-fro motion. If the mechanism represents the behavior of small screw segments of a larger dislocation loop, then such motion would lead to

an increase in dislocation density due to the increase in the edge dislocation length (edge dislocations cannot cross-slip).

The width of the APB ribbons depends on the competition between the repulsion between SP 1 and SP 2 and the surface tension in the APB. Lower APBE, therefore, leads to wider APB ribbons shown in Fig. 1(a) & (b), and vice versa. If the APBE is low, then the tangential force component generated by the interaction between SP 1 and SP 2 may lead to a significantly reduced cross-slip rate. Therefore, APBE strongly affects the cross-slip based motion of the super screw dislocations and plays a central role in the accumulation of fatigue damage in Ni-base superalloys. Lower APBE is thus favored to reduce the damage accumulation for Ni-base alloys under cyclic loading. This is echoed by experimental findings on γ-γ' alloys [137,158,159].

In Ni-base superalloys, the APBE can be tuned by adjusting the relative fractions of the alloying elements (can be to 10 species) [160–163]. Although understanding the precise effect of each alloying element on the overall APBE in the γ' phase of a commercial alloy is highly desirable, obtaining such knowledge has been proved to be challenging for both experiments and numerical calculations. In experiments, the APBE can be obtained indirectly via the measurement of the spacing between superpartials via weak-beam transmission electron microscopy [144,155,164], which is associated with large systematic errors. In simulations, molecular dynamic (MD) using interatomic embedded atom method (EAM) potentials has been employed to study the planar faults, including APB and stacking faults, in pure Ni_3Al [165]. The stable fault energies and the energy landscape on various fault planes have been measured. The major drawback of MD is that describing the interatomic interaction among multiple atom types is challenging and requires a specifically parameterized interatomic potential that is tuned for a very narrow purpose [166,167]. Although attempts of direct density functional theory (DFT) calculations have been

made for this purpose [168], addressing the long-range disordering effects of the alloys is challenging due to the limitations in the size of DFT simulation cells.

In this work, we utilize the cluster expansion method combined with DFT calculation and Monte-Carlo (MC) sampling to assess the effect of composition on the (111) APBE of both an idealized Ni_3Al γ' phase and the γ' phase in a commercial alloy—Inconel 939. This article is organized as follows: in Section 2, a background is given on prevailing numerical methods available for the calculation of APBE in ordered γ' phases; in Section 3 the computational details of this work is provided; in Section 4, effects of compositional variation and temperature changes on the relative APBE of ternary and multicomponent γ' phases are provided; finally, conclusions are drawn in Section 5.

4.3. Background

Several methods have been utilized to calculate the APBE of $L1_2$ structures, taking into account the atomic disordering due to alloying. These methods include

(1) direct, "brute-force" DFT calculations;

(2) *ab initio* calculation with the coherent potential approximation (CPA);

(3) cluster expansion (CE) based method; and

(4) one dimensional-long periodic structure (1D-LPS) method.

Methods (1)-(3) all share a common supercell approach, where the APBE is calculated based on the energy differences between two supercells (atomistic structures)—one with APB and one without. Between these two structures, the energy difference is assumed to be solely due to presence of defect, and the APBE can be expressed as

$$\gamma_{APB} = \frac{E_{APB} - E_{pris}}{A} \quad (2)$$

where γ_{APB} is the defect formation energy per unit area, E_{APB} is the total energy of the structure with APB, E_{pris} is that of the pristine one, and A is the area of the defect in the computational cells. This has been the central idea for the calculation of the formation energies of generalized planar defects, including stacking fault energy [84], heterophase interface energy [169], and grain boundary energy [170]. This type of bi-crystal setup has been not only useful for these boundary energy calculations, but also in studies where the deformation at boundaries is focused [171,172].

Method (1) constitutes calculating the total energies of the pristine structure and the structure with APB [173–175]. A typical representation of the computational cells is given in Fig. 2(a) [174]. To consider the effect of alloying, the supercells are typically randomly mixed—in the form of substitutional atoms—with a third atomic species [174]. The mole fraction of the alloying element corresponds to the number of the solute atoms divided by the total number of atoms in the computational cell. As typical DFT calculations can only consider a few tens of atoms (well below 100), this method cannot probe the effect of dilute solutes (mole fractions below a few %). In addition, the positions of the solute atoms relative to the APB affect the APBE. Indeed, it is energetically preferred for solute atoms to segregate at or near the APB according to experimental observations [175]. The APBE of an alloyed $L1_2$ structure is, in fact, a mean-field quantity, where the effects due to the randomly positioned solutes are "averaged". To address this, current direct approaches typically perform large number of calculations on randomized atomistic configurations to obtain the averaged energies of the pristine and APB structures, which is computationally expensive [84,176]. In addition, the length scale of DFT is typically limited to a few tens of angstroms, which, with the application of periodic boundary conditions, imposes an unphysical spatial periodicity.

Method (2) addresses the configurational disorder introduced by the solute atoms using ab-initio calculations based on the coherent potential approximation (CPA) [161]. The essential idea is to replace the randomly positioned atoms in a lattice structure with an effective medium (Fig. 2(b)), whose parameters can be solved self consistently [176]. Typical approaches using this method describe potential field around atoms using exact muffin-tin orbital (EMTO) [176] approximation and solves the Schrödinger equation using the Green's function method, as opposed to the Hamiltonian formalism commonly adopted by prevailing DFT calculations. According to the combined EMTO-CPA approach, the Green's function (g) and the alloy potential (P_{alloy}) that characterizes the real alloy can be replaced by a site-independent coherent potential $\tilde{P}$ and a coherent Green's function $\tilde{g}$. The Green's function of individual atomic species, g_i, weight-averaged by their mole fraction m_i, is used to calculate the coherent Green's function that describes the system of random atomic configuration, i.e. $\tilde{g} = \sum_i m_i g_i$. With this method, the calculation of the APBE of an $L1_2$ phase at any given alloy composition would simply require *ab initio* calculations of the total energies of two effective atomistic structures with and without the APB. Method (2), as a mean-field technique, avoids the statistical nature of the problem, therefore cannot address the effect of temperature on APBE, which includes both configurational and vibrational contributions (phonon related).

The cluster expansion (CE) based methods (Method (3)), when combined with both DFT calculations and MC sampling, can address satisfactorily the effects of alloying elements and temperature on the APBE. The energy of a multicomponent alloy can be defined by the cluster expansion method introduced by Sanchez et al [95]. Essentially, CE expresses the configuration-dependent energy of the atomistic configuration an alloy by first abstracting the alloy's atomic structure into a lattice model, then expressing the energy into a polynomial form of the occupation

states (spins) [90,177], see (Fig. 2(c)). The coefficients in the polynomial form are acquired by considering the energies of a large quantity of small periodic atomic clusters obtained from DFT calculations. Once the CE has been performed, energy of relatively large atomistic structures, containing at least thousands of atoms, can be efficiently calculated. Aided by MC sampling, the total energy of thousands of atomistic structures with randomized atomic positioning, with and without APBs, can be calculated [99]. This enables one to produce enough configurational variation for an accurate assessment of the average APBE. Thus, the APBE in the γ' phase can be accurately measured with the disordered alloying elements properly accounted for [178].

Method (4) represents another class of approaches that evaluate the planar fault energies, including stacking fault energy and APBE, using a one dimensional Ising (1DI) based models [179–182]. 1DI model describes the configurational energy of local stacking sequence of an infinite stack of atomic monolayers—also referred to as polytypes—by perfect ($S_i = +1$) and faulty ($S_i = -1$) and parametrize the energy of the stack according to [88]

$$E = J_0 - J_1 \sum_i S_i S_{i+1} - J_2 \sum_i S_i S_{i+2} - J_3 \sum_i S_i S_{i+3} - \cdots \quad (3)$$

where J_n are the interaction coefficients between the stacking of nearest neighbors (J_1), second nearest neighbors (J_2), etc. The one-dimensional long period structures (1D-LPS) method can be considered as an extension of the 1DI model to the case of APB in $L1_2$ structures. According to this method, the energy difference of a structure containing several APBs from the reference, APB-free structure, can be expressed as the following [182]:

$$E_S - E_{L1_2} = \frac{1}{N}\sum_i \left(\sigma_i + \frac{1}{2}\right) E_{APB} + \frac{1}{N}\sum_{j>i} I_{j-i} \left(\sigma_i + \frac{1}{2}\right)\left(\sigma_j + \frac{1}{2}\right) + \frac{1}{N}\sum_{j>i>k} H_{i-k,j-i} \left(\sigma_i + \frac{1}{2}\right)\left(\sigma_j + \frac{1}{2}\right)\left(\sigma_k + \frac{1}{2}\right) \quad (4)$$

where E_S is the per-atom energy of the structure containing the APB, $E_{L_{12}}$ is the per atom energy of reference structure, N is periodicity in which the APB occurs (i.e. one APB per N $L1_2$ cell), E_{APB} is the per-atom energy contribution of a single APB, σ_i is the corresponding occupation number defined based on the presence of APB i.e. $\sigma_i = 1/2$ when the APB is present and $\sigma_i = -1/2$ when the APB is not present. I_n and $H_{m,n}$ are the pair and three-body interaction coefficient, respectively. Therefore, energies of base $L1_2$ structure, as well as its derived atomistic structures by periodically adding APBs, can be calculated using DFT, which can then be used to fit with Eq. 4 to obtain necessary coefficients, including the E_{APB}, to obtain the APBE. For instance, the $D0_{22}$ and $D0_{23}$ are derived from the $L1_2$ structure, by introducing one {100} APB every one and two $L1_2$ cubes, respectively (Fig. 2(c)) [182]. Like Method (1), the disordering effect of the solute atoms requires performing large number of DFT calculations using atomistic configurations with randomized solute distributions. Due to this reason, Method (4) shares the drawback of Method (1) being computationally expensive.

4.4. Methodology

Based on the overview of the prevailing simulation methodologies in the foregoing section, the CE based methods are appealing as they can explicitly address the statistical nature of the solute-APB interaction and account for the effect of temperature through configurational variations. As was discussed by Sluiter et al., the vibrational contribution to APBE is small compared to the configurational contribution [183]. Using CE combined with DFT and MC, we study the effect of composition and temperature on the {111} APBE of Inconel 939. APB on the {111} plane is considered in this work due to their importance in the alloys cyclic deformation mechanisms in all temperature ranges [184]. CE is performed using ATAT toolkit [98] which relies on the ab initio total-energy calculation on small and simple clusters of atoms.

Under the formalism of CE [95], the energy of an arbitrary atomistic configuration can be expressed by a polynomial of the energies of its composing atomic clusters. The energy of each atomic cluster is proportional to the product of an orthogonal cluster function $\varphi(\sigma)$ and an interaction energy coefficient K. Mathematically, the total energy is written as

$$E(\sigma) = \sum_{\alpha} \sum_{s} K_{\alpha s}\, \varphi_{\alpha s}(\sigma), \tag{5}$$

where $\varphi_{\alpha s}(\sigma)$ are the orthogonal cluster functions, $K_{\alpha s}$ are the interaction energy coefficients among all clusters (also referred to as effective cluster interaction, ECI), α is a designation of the atomic clusters, and s is the order of the orthogonal polynomials with which the atomic clusters (cluster functions) are expressed. This suggests that, if the energies of a finite number of strategically chosen atomic structures can be provided, e.g. from DFT calculations, then Eq. 5 can be fitted with a given number of $K_{\alpha s}$. In a sense, CE extracts the interaction among atoms and attempts to predict the energy of unknown atomistic configurations.

The accuracy of a CE can be defined based on a cross-validation score, i.e.

$$CV = \sqrt{\frac{1}{n}\sum_{i=1}^{n}\left(E_i - \hat{E}_i\right)^2} \tag{6}$$

where n is the total number of structures used for fitting, E_i and $\hat{E}_i$ are the calculated (e.g. using DFT) energy of structure i and predicted value of the energy by CE, respectively [99,177]. In this work, all cross-validation scores are below 35 meV/atom.

DFT calculations were performed to obtain the total energies of small, periodic atomistic structures and provide input to CE. Pseudopotentials from the Standard Solid State Pseudopotentials (SSSP) [102] were selected and their accuracy in predicting the lattice and elastic constants was verified. Resulting values of lattice parameter and elastic moduli have been

compared with results from experiments and/or similar DFT calculations, as shown in Table 1. For these verifications, the wave function energy cutoff used is 35 Ry (476 eV), and the k points mesh grid used is 11×11×11 for primitive cells with dimensions of ~2.5 × ~2.5 × ~2.5 $Å^3$. Accordingly, in the DFT calculations for CE, k- point meshes are created for computational cells in such a way that a total of 1000 integration points are distributed as uniformly as possible within the Brillouin zone. Although APBE is sensitive to the local (~ several Å) mole fraction of alloying elements, the APBE of the alloy is a mean field quantity and is "averaged" over a long range (tens of nm or above). Therefore, in this study, atoms are assumed to reside at perfect $L1_2$ lattice points, even with the presence of multiple alloying elements. The effect of local, atomic-scale lattice distortions on the APBE is assumed to be small and is neglected. Indeed, experiments revealed that distortions in the first nearest neighbor distance induced by alloying elements in Ni are less than 3.6%, while that in the second nearest neighbor distance is less than 1% [185]. Only long-range lattice distortion effect, i.e. lattice dilation or contraction, is considered. Accordingly, in the present set of DFT calculations, only volumetric relaxations of the computational cells are performed, ionic relaxations are prohibited. Similar assumptions have been made in other studies in the literature and have yielded satisfactory results [174]. The soundness of our assumption will also be verified in Section 4 when the results of our calculations are compared with existing literature.

Once the CE is performed and the ECIs acquired, the energies of atomistic structures much larger than those considered in DFT calculations can be obtained. Using the Thermo-Calc software [186], a series of compositional ranges for all atomic types are determined, ensuring that throughout these ranges, no more than 5% of phases other than γ and γ' exist. Corresponding to the compositional ranges, Table 2 lists the number of atoms (given in parentheses) for each species present in the atomistic structures. To calculate APBE, atomistic structures containing 2160 atoms

are created, duplicated along [111] and shifted to create {111} APBs (Fig. 3), and energy differences due to this operation measured. The dimensions of these duplicated structures along the crystallographic directions $[10\bar{1}]$, $[01\bar{1}]$, and [111] are 29.94 Å, 29.94 Å, and 72.89 Å respectively (see Fig. 3). Structures of this size eliminate the interaction between the APBs from neighboring periodic cells, enable slight changes in the composition, and allow for the probing of dilute solutions. To compare, in the supercell approach which requires direct DFT calculations, the supercells only contain ~50 atoms [168].

The effect of the randomness in the distribution of solute atoms is addressed by MC sampling technique. In this work, MC sampling uses the metropolis algorithm and generates a minimum of 2500 different atomistic configurations at each composition. For compositions that converges slowly, as many as 6000 configurations are created. Whenever the spatial configuration changes, the energy of the structure can be determined using the ECIs. Starting from any given structure, the next attempted structure is randomly generated following the approach outlined in Ref. [100]. If the new structure has less energy compared to the current one, the new structure will automatically be accepted. Otherwise, a probability $\exp(-\beta\Delta E)$, where ΔE is the energy difference between the structures, will be assigned for the acceptance of the new structure [99]. This has been done for multiple temperatures ranging from 300 K to 1300 K with 200 K intervals.

4.5. Results and discussion

In order to establish a baseline on the APBE of the ordered $L1_2$ precipitate, we first look into the case of a binary Ni_3Al alloy. Then, we investigate the isolated cases of single solute addition to the Ni_3Al structure resulting in ternary γ' phases. Lastly, multicomponent cases representative of the variants of the Inconel 939 alloy, whose base composition is shown in Table 3 [187], are studied. A total of five separate CE listed in Table 4 are performed. The results of

these studies—APBE—are presented as relative values (i.e. $\Delta\gamma_{APB}$) with respect to that of pure Ni_3Al for each case. Since a different CE is used for each ternary and multicomponent alloy case, a specific reference point of pure Ni_3Al APBE should be calculated using the corresponding CE. Note that although systematic errors exist in the DFT calculations as well as in CE, a significant portion of which can be canceled via the calculation of $\Delta\gamma_{APB}$. The concept of error cancelation can be rationalized by realizing the fact that the errors of the same origins in energy calculation exists in both the Ni_3Al reference point as well as target composition. Additional related discussions can be found in Refs. [99,162].

4.5.1. APBE of pure Ni3Al γ' phase

The APBE of pure Ni_3Al is first calculated based on a binary CE with the cross-validation score of 7.85 meV/atom—about a quarter of the typical reported values of ~30 meV/atom [99,162]. ECIs are obtained by the volumetric relaxation of 95 different clusters. In a computational cell of Ni_3Al containing 4320 atoms, an APBE of 320.737 mJ/m^2 was obtained. The APBE of pure Ni_3Al and off-stoichiometry Ni_3Al reported in the literature is provided in Table 4. It is noted that although the APBE reported in this work significantly overestimates the experimental measurements (~195 mJ/m^2), it largely agrees with other theoretical calculations, including both DFT and CE. It is also noted from Table 4 that several DFT based studies reported two APBE for pure Ni3Al, a higher and a lower estimation, that correspond to idealized and fully-relaxed conditions. For the calculations performed in the idealized condition, all atoms in atomistic structure containing the APB still reside in a perfect FCC parent lattice. This condition is also inherent to all CE based approaches. However, the atomistic structure constructed from this pure geometrical consideration does not coincide with the true ground energy state. Indeed, a gamma-surface analysis revealed that minimum energy stacking in the APB deviates from a perfect FCC

stacking [188]. Therefore, the in-plane atomic arrangement at the APB predicted by calculations performed under the "fully-relaxed" condition tend to approach the realistic, experimental conditions. This is likely the origin of the discrepancy in APBE of pure Ni_3Al between the present work and the experiments.

However, it is also worth noting that the validity of the DFT calculations based on fully-relaxed condition may be debatable as the APBs always appear as ribbons in the γ' phase and are always constrained by the surrounding media. Although lattice relaxations parallel to the APB may be permitted, the out-of-plane relaxation is inhibited. Indeed, in the case of CSF ribbons embedded in a γ' phase, little changes (if any) in the {111} interplanar spacing parallel to APB can be resolved by high resolution (transmission electron microscopy) TEM imaging (see Fig. 3(d) of Ref. [189]).

Nevertheless, the goal of the present study is to assess the influence of composition and temperature on the APBE. It is expected that the systematic errors in the absolute APBE observed in this work exist in all calculations of APBE and, when the relative APBE $\Delta\gamma_{APB}$ is calculated, cancel to a large extent. Indeed, using DFT calculations, Crudden et al. [163] captured the effect of Ti addition on the $\Delta\gamma_{APB}$ which agreed with the experiments, even though they conducted their calculations under the idealized condition and reported a APBE value for pure Ni_3Al of 310 mJ/m^2.

4.5.2. Composition and temperature effects on APBE for ternary γ' phase

For the ternary cases, the mixture of excessive third elements into the base Ni_3Al can result in the decomposition of the γ' phase. To ensure that the APBE obtained from MC-based calculations are valid, the stability of the γ' phase due to the introduction of solutes is first investigated using Thermo-Calc software with the TCNI8 database [186]. Figure 4 shows the mole fraction of γ' phase as a function of composition, which is given by the mole fraction of Al

and the solute element. These solutes are all of the substitutional type [190]. It can be observed from Fig. 4 that the solutes prefer to form substitutes on certain atomic sites over others. As a guide to the eye, the red dashed lines correspond to the compositions in which the solute atoms only replace the Al atoms. Compositions above the diagonal lines correspond to substitutions of both Al and Ni by the solutes. The horizontal line of 25% of Al correspond to the substitution of Ni atoms. Compositions below the diagonal lines correspond to Al% + Solute% below 25% and suggest replacement of Al sites by Ni atoms. In the case of Ti (Fig. 4(a)), the coincidence (or near-coincidence) between the field of 100% γ' and the dashed line suggests that the solute atoms prefer to replace aluminum atoms, which is in agreement with the literature [161,190]. In the cases of Cr and Mo, similar preferences can be observed (Figs. 4(b) & (d)). However, in the literature, the agreement on such preferences has not been well established [190–195]. In the case of Co, Fig. 4(c) suggests that the solute atoms simultaneously replace Al and Ni at an approximate ratio of 1:7 (green dashed line), giving strong preference to Ni sites. This is in qualitative agreement with the literature, although the latter suggests an exclusive preference of Co replacing Ni in γ' phase [190]. According to these observations the exact compositions of the ternary γ' alloys investigated in this work are shown in Table 5. As shown, the site preference is given to only Al for the cases of Ti, Cr, and Mo, whereas the site preference is given to only Ni for the case of Co.

The effect of the solutes, including Ti, Cr, Co, and Mo, on the APBE is shown in Fig. 5. Note that CEs performed for these cases led to slightly different APBE for pure Ni_3Al as shown in Table 4. Even though this is the case, these energies are still in agreement with the literature [174,196–204]. The systematic errors associated with these energies are expected to be canceled to a large extent when $\Delta\gamma_{APB}$ is calculated, as will be shown later when the result of this work is compared to the literature.

Effect of Ti: For the case of Ti, eight different compositions ranging from 1% to 15% of Ti are considered (Fig. 5(a)). An increase in the amount of Ti results in a substantial increase in APBE. For low Ti fraction of 1%, the increase in APBE at room temperature is as low as 6 mJ/m^2. This value increases as Ti fraction increases and it is as high as 140 mJ/m^2 at 15% of Ti. At each composition, an increase in temperature slightly reduces the value of $\Delta\gamma_{APB}$. For instance, an increase in temperature from room temperature to 1300 K leads to only a reduction of around 15 mJ/m^2. A comparison between the results of this work (for the case of Ti solutes at 300K) and the literature has been provided in Fig. 6(a). Sun et al. [162] have studied the effect of both Ti and Hf impurities on the APBE of Ni_3Al. For 1 % and 10 % of Ti, they have reported a $\Delta\gamma_{APB}$ of 10 and 65 mJ/m^2, respectively, agreeing well with the present study. The agreement is also a testament of the soundness of the assumption made in this work that the effect of atomic-scale lattice distortion can be neglected. In Sun et al., similar reducing effect of temperature on $\Delta\gamma_{APB}$ has been witnessed. Wider compositional range, starting from pure Ni_3Al to a complete substitution of Al by Ti has been studied by Chandran et al. [174]. However, care should be taken when interpreting their results in the limit of complete Ti substitution of Al, as the stable phase for Ni_3Ti is $D0_{24}$, a hexagonal structure, instead of $L1_2$ [109]. In their study, using the reference {111} APBE of 315 mJ/m^2, the $\Delta\gamma_{APB}$ at 0 K is close to 300 mJ/m^2 for 15 % Ti. The increasing effect on the APBE due to Ti addition into Ni_3Al γ' has also been reported by Raynor et al. using precipitation strengthening theories [205]. It is also worth to note that part of results presented by Chandran et al. are based on "full-cell relaxation" which yields APBs in a stress-free state and inter planar spacing at APB distinct from the γ' phase. As discussed at the beginning This assumption might not be realistic as the APBs always appear as ribbons in the γ' phase and are always constrained by the surrounding media.

Further, increase in the APBE by addition of Ti to Ni_3Al has also been reported by several other work, including Vamsi et al. [206], Gorbatov et al. [161], and Crudden et al. [163] (Fig. 6(a)). The present work showed qualitative agreement with their results. Although the present work underestimates the experimental $\Delta\gamma_{APB}$ value reported by Kawabata et al. [207] at 10% Ti, it agrees well with the experimental measurement by Korner et al. [208].

Effect of Cr: A maximum of 9% Cr can be added to Ni_3Al before a new phase starts to appear. Seven different composition ranging from 0.1-9 % have been studied (Fig. 5(b)). At all temperatures, the presence of Cr reduces the APBE of the γ' phase (reflected by negative values of $\Delta\gamma_{APB}$) and this reducing effect appears to be more significant at higher mole fractions. Like the case of Ti, increasing temperature seems to decrease the APBE. The temperature-induced reduction is more pronounced at temperatures above 800 K. Compared to the case of Ti (a maximum of $\Delta\gamma_{APB}$ = 140 mJ/m^2), the magnitude of reduction achieved by addition of Cr is merely 70 mJ/m^2. The findings of this work (at 300K) have been compared to the literature in Fig. 6(b). In qualitative agreement with the present work, Crudden et al. [163] have also shown—using DFT calculations—that Cr reduces the overall APBE in the γ' phase. However, the magnitude of reduction predicted by Crudden et al. ($\Delta\gamma_{APB}$ of −15 mJ/m^2 at Cr fraction of 9%) is significantly less than that by the present work ($\Delta\gamma_{APB}$ of −33 mJ/m^2 at Cr fraction of 9%) [163]. In contrast, Gorbatov et al., using CPA method (Method 2 introduced in Section 2), suggested that the APBE initially increases as a function of increasing Cr content, then drastically decreases beyond 5% of Cr [161].

Effect of Co: Co fraction ranging from 1% to 23%—a total of 6 compositions—has been assessed (see results presented in Fig. 5(c)). Similar to Cr, Co also tends to decrease the APBE. For Co fractions smaller than 10 %, the reduction in APBE is very small and does not exceed 1.5

mJ/m^2. The decreasing effect appears to be stronger at Co fractions above 10%. Also similar to the previous cases, temperature rises tend to reduce the APBE. At room temperature, the maximum reduction in APBE is only ~20 mJ/m^2 (at Co fraction of 23%), while at 1300 K this reduction becomes ~50 mJ/m^2. Employing CPA method (Method 2 as introduced in Section 2), Gorbatov et al. [161] showed that the addition of Co up to 10% results in gradual, almost linear, reduction of the APBE. The comparison of results is provided in Fig. 6(c). As shown, at 10% of Co, Gorbatov et al. showed that the APBE reduced by ~20 mJ/m^2 – a rate significantly higher than the results of the present study.

Effect of Mo: For the case of Mo, six different compositions ranging from 0.1 to 7 % have been considered. The effect of Mo addition to Ni_3Al on the APBE is shown in Fig. 5(d). An overall reducing effect similar to Cr and Co has been witnessed as a result of the Mo addition. The rate at which the Mo solutes reduce the APBE (~3 mJ/m^2 per percent mole fraction) is between that of Cr (~5 mJ/m^2 per percent mole fraction) and Co (~1.5 mJ/m^2 per percent mole fraction), *c.f.* Figs.5(b), 5(c), and 5(d). Temperature effects in the case of Mo are unique. Specifically, for compositions below 1%, $\Delta\gamma_{APB}$ stays constant up to 1000 K followed by a slight reduction at higher temperatures. For composition above 1%, an increase in temperature leads to an increase, a plateau, then a decrease in APBE. In other words, the reducing effect of temperature on APBE appears to be suppressed from room temperature (300 K) to intermediate (~800 K). Using DFT calculations, Crudden et al. have shown that the addition of Mo at 7% can reduce the APBE by ~12 mJ/m^2, which is in good agreement with this study, see Fig. 6(d) [163].

It is convenient to cast an understanding of the effect of individual elements on the APBE into an empirical relation that can be later used to predict the APBE of a multicomponent alloy.

Following Crudden et al. [163], the relative APBE is assumed to be linearly dependent on the mole fraction of the solutes, i.e.

$$\Delta\gamma_{APB} = \sum_{i=1}^{n} K_i x_i, \quad (7)$$

where K_i are the coefficients for the APBE change induced by each solute type (at mole fraction x_i in γ' phase). The coefficients K_i (i = 1, 2, 3, 4) obtained from the linear fit of the data presented in Fig. 5 are provided in Table 6. It is apparent that Ti has the strongest (positive) influence on APBE, while Co has the weakest (negative) influence.

4.5.3. Composition and temperature effects on APBE for multicomponent γ' phase

Having established a baseline on the effect of individual elements, the current section aims to elucidate the combined effect of multiple solutes on the APBE in the γ' phase. We note that prior alloy design practices have heavily relied upon the knowledge of the individual solute elements, similar to that generated from Section 4.2, the mutual interactions among the solute elements have been assumed negligible [163]. Indeed, the scope of most prior research is confined to the effect of individual solute elements [90,99,161]. This work takes Inconel 939 (wt. % composition given in Table 3), a Ni-base superalloy that is primarily γ' strengthened, as a model material system to investigate the effect of adjustment in solute mole fraction on the APBE. The composition of the γ' phase according to Thermo-Calc is also given in Table 2. Although the Inconel 939 contains 7 major alloying elements (whose mole fraction > 1%), there are only Al, Ti, Cr, Co, and Mo with mole fraction > 1% in the γ' phase. As elements may preferentially reside in either phases, increasing the overall fraction of an element does not necessarily lead to an increase of said element in the desired phase. In this work, only elements—other than Ni—in the γ' phase

with mole fraction above 1% will be considered for adjustment, including Al, Cr, Co, and Ti. Two adjustment strategies have been considered, i.e.

(1) Adjusting the mole fraction of one alloying element at the expense of Ni – dubbed "Sacrificial Ni",

(2) Adjusting the mole fraction of one alloying element while maintaining the ratio of all other elements – dubbed "Constant Ratio".

Strategy (1) is common among alloy design where the minor additives are introduced while the major base element appear as a balancing element. Strategy (2) becomes increasing important as additive manufacturing (AM) based alloy design approaches maturity [145]. With powder-based AM, composition of alloys can be adjusted by mixing additives into base powders. The composition of the resulting alloy would then have increased mole fractions of the additives while the fractions of all other elements would reduce at a constant ratio. The compositions considered in this work—using Inconel 939 as a base alloy—following these two strategies have been provided in Table 2, along with the number of atoms in each species in the atomistic models. For adjustment of each element, 5 different compositions are considered. To ensure the completeness of understanding, not only addition of elements, but also reduction of them, are considered. Using Thermo-Calc, the limits within which an element can be adjusted is determined, ensuring formation of no more than 5% of any new phases (in addition to γ and γ') and no less than 10% of γ' phase. The phase mole fractions of the γ and γ' phases corresponding to the compositional adjustment are given in Table 7.

A CE comprising 6 elements has been performed involving DFT calculation of the total energy of 498 periodic atomic clusters, resulting in ECIs with a cross-validation score of this CE 30 meV/atom. Based on this cluster expansion, the reference APBE of the pure Ni_3Al phase of

γ_{APB} = 268 mJ/m^2 was obtained (Table 4). Results presented subsequently in this section, shown in Figs. 7 and 8, are the change in the APBE ($\Delta\gamma_{APB}$) based on this reference value. Due to the combined presence of alloying elements, the relative APBE ($\Delta\gamma_{APB}$) of the base Inconel 939 is 120 ± 20 mJ/m^2 at the temperature range of 500 K ~ 1300 K.

Effect of adjustments in Al: An overall change in the fraction of Al, using both strategies, from ~2.5% to ~5.4% alters the concentration of Al inside γ' phase from ~8% to ~12% (Table 2). As shown in Figs. 7(a) and 8(a), both temperature and adjustment in Al fraction have moderate effect on the APBE of the γ' phase. An increase in temperature from 500 K to 1300 K reduces the $\Delta\gamma_{APB}$ by 20 ~ 30 mJ/m^2, while an increase from 8.0% to 12.0% of Al in γ' phase leads to a drop in $\Delta\gamma_{APB}$ from 120 ± 20 to 90 ± 10 mJ/m^2. This reducing effect of Al is expected as the increase in Al content in the γ' phase reduces the fractions of other solutes. It is also noted from Figs. 7(a) and 8(a) that the two composition adjustment strategies resulted in very similar results.

Effect of adjustments in Ti: In the case of Ti, ~3% increase in the overall composition of Ti following both strategies, starting from ~2%, results in the change of Ti concentration inside γ' phase from ~8% to ~13% (see Table 2). As shown in Figs. 7(b) and 8(b), an increase in temperature from 500 K to 1300 K slightly reduces the $\Delta\gamma_{APB}$ by 20 mJ/m^2. An increase in Ti composition drastically increases the APBE. In both strategies, with an increase of Ti fraction ranging from ~8.00% to ~13.00% in the γ' phase, $\Delta\gamma_{APB}$ increased from ~40 mJ/m^2 to ~120 mJ/m^2. This behavior agrees with the observation made in the ternary case (Section 4.2) where the addition of Ti from 1-15% increased the APBE from ~6 to ~140 (mJ/m^2). The adjustment of Ti fraction using the two composition adjustment strategies resulted in very similar results.

Effect of adjustments in Cr: Using either compositional adjustment strategies, the overall fraction of Cr can vary from below 5% to above 25% without the formation of new phases.

Variations of overall Cr fraction using both strategies resulted very similar, small variation in the composition in the γ' phase (Table 2), i.e. from ~1% to 1.6%. It should be noted, however, that the phase fractions are significantly different via the two compositional adjustment strategies (Table 7). For all compositions obtained from Constant Ratio, γ' phase fraction is almost constant and has a value of ~27%, while sacrificial Ni results in γ' phase fraction ranging from ~10% to ~30%. The changes in composition, result in a slight increase in APBE by 20 mJ/m^2 at all temperature ranges (Figs. 7(c) and 8(c)). The increase in APBE is almost linear throughout the range of compositions. This trend is opposite to what has been witnessed before in the case of ternary γ' phase. This is likely due to the fact that the actual variation of Cr in the γ' phase is exceedingly small compared to that of Ti + Co, and that these variations (increase in Ti and decrease in Co) favors the increase in APBE. Consistent with observations made in other elemental adjustments, increase in temperature from 500 to 1300 K results in a moderate reduction in APBE of 20 mJ/m^2. Although adjustment of Cr under both strategies changes the APBE in a similar way, the "sacrificial Ni" strategy lead to a greater variation in the APBE (compare Figs. 7(c) and 8(c)).

Effect of adjustments in Co: As shown in Table 2, without the formation of a new phase, adjustment of the overall fraction of Co from ~15% to ~36% can be achieved using Constant Ratio strategy, which results in the concentration of Co inside γ' phase changing from ~5% to 16%. On the other hand, a wider compositional range of overall and in-γ' fractions of Co spanning from ~5% to ~43% can be achieved via Sacrificial Ni strategy, which leads to the concentration change of Co inside γ' phase from ~1% ~30%. Distinct from all other atomic species, one should note that the addition of Co using either strategy reduces the phase fraction of γ' significantly (Table 7). As shown in Figs. 7(d) and 8(d), similar to the cases of other elements, increase in temperature reduces the APBE by ~20 mJ/m^2. Interestingly, APBE change due to adjustment in Cr has a nonmonotonic

trend. As the change in fractions of all other elements (including Cr, Ti, and Al as shown in Table 2) favors the reduction of APBE, the initial increase in the APBE with increasing Co is likely due to the synergistic effect of the coexisting solutes. This suggests that the mutual interaction among solutes might not be negligible.

To illustrate, we first compare the relative APBE predicted by Eq. 7 with those obtained from CE at 500 K for multicomponent γ' phases, as shown by the orange circles in Fig. 9. The K_i parameters used were obtained by fitting the data presented in Section 4.2 (Table 6). The root-mean-squared error (RMSE) of the prediction is ~20 mJ/m^2. To improve the accuracy of empirical prediction, Eq. 7 can be modified realizing that the multiple solute atoms in the Ni_3Al phase may have significant mutual interaction. These interactions can be represented by "cross-terms" of two or more mole fractions of solutes, such as $x_{Ti}x_{Cr}$, $x_{Ti}x_{Co}$, $x_{Co}x_{Cr}$, and $x_{Ti}x_{Cr}x_{Co}$. Eq. 7 can, therefore, be rewritten as

$$\Delta\gamma_{APB} = \sum_{i=1}^{n} K_i x_i + F_1 x_{Ti} x_{Cr} + F_2 x_{Ti} x_{Co} + F_3 x_{Cr} x_{Co} + H x_{Ti} x_{Cr} x_{Co}, \qquad (8)$$

where K_i stands for the coefficients in Eq. 7 shown in Table 6, F_i and H are the coefficients for the binary and ternary cross-terms. At each temperature, based on the existing K_i, a set of F_i, and H parameters can be obtained. With the added cross terms, the performance of the fit is substantially improved (blue diamonds in Fig. 9). The RMSE for the new fit using Eq. 8 is only 6 mJ/m^2. The parameters and RMSE of the fits for data at all temperatures are provided in Table 6. The same improvement in the performance of fits is evident in all temperatures.

Predictions made by Eq. 8 show good agreement with the literature. As was discussed before, this study focuses on the effect of alloying on the relative APBE ($\Delta\gamma_{APB}$). Experimental measurement based on TEM reported APBE values of 180 ~ 250 mJ/m^2 for stoichiometric and

near-stoichiometric Ni_3Al (see Table 4). Using these values as reference, APBE measurement by Baither et al. [152] leads to $\Delta\gamma_{APB}$ = -34~100 mJ/m^2 for Nimonic-105 alloy and $\Delta\gamma_{APB}$ = 8~170 mJ/m^2 for Nimonic-PE16 alloy. In this work, Eq. 8 predicts -25 mJ/m^2 for Nimonic-105 and 124 mJ/m^2 for Nimonic-PE16[1]. We notice that Eq. 8 slightly under predicts the $\Delta\gamma_{APB}$ (within the scatter band) for Nimonic-105 and is in perfect agreement with experiments for Nimonic-PE16.

4.6. Conclusions

In this work, utilizing the ATAT toolkit, density functional theory-based cluster expansion (CE) calculations were performed combined with Monte Carlo sampling to investigate the effect of composition and temperate on the antiphase boundary energy of the γ' phase. The effects of both individual solute elements in a ternary environment and the coexistence of multiple solute elements are systematically investigated. The following conclusions have been reached:

(1) In a ternary γ' phase, i.e. $Ni_{3-x}Al_{1-y}M_{x+y}$, the addition of Ti significantly increases the APBE, while addition of Cr, Co and Mo all reduces the APBE. Per percent addition in mole fraction, Ti, Cr, Co, and Mo induce the change of APBE by ~140, ~70, ~50, and ~25 mJ/m^2, respectively.

(2) The effect of temperature on the APBE depends on the composition. In most cases, temperature moderately decreases the APBE, by 20~40 mJ/m^2. Exceptions seem to be the additions of Ti or Mo into Ni_3Al – where the effect of temperature change from 300K to 1300K only results in a minor fluctuation in APBE of <5 mJ/m^2.

[1] We realize the existence of 3.2 % (at.) Fe in the γ' phase of Nimonic-PE16. However, the effect of Fe on the APBE was shown to be small [173]. The dilute presence of Fe is therefore ignored in the present work.

(3) The effect of individual solutes on the APBE energy obtained in an isolated, ternary condition (i.e. in $Ni_{3-x}Al_{1-y}M_{x+y}$) does not translate to a multi-solute environment. The mutual synergistic interactions among the solute are not negligible.

(4) Interaction between Cr and Co appears to be the strongest across all temperature ranges, while the interaction between Ti and Co is almost negligible. The binary Ti-Cr and ternary Ti-Cr-Co interactions are moderate.

(5) Empirical, master equations that predicts the APBE based on the composition of the γ' phases are obtained from fitting of the present calculations.

Tables

Table 4. 1 A comparison of elastic and lattice constants, of different atom types, between results of this study and existing literature. DFT – density functional theory; Exp. – experiment.

						This study		Literature	
Al		C_{11}	C_{12}	C_{44}		a		a	
	Exp.[209]	116.3	64.8	30.9		4.0377 Å		4.019 Å	
	Exp.[210]	114.3	61.92	31.62				Exp.[211]	
	Exp.[209]	107.3	60.8	2.83					
	DFT [212]	121	63	33.0					
	DFT [213]	105	54	26					
	DFT [214]	103	56	30					
	This study	123.31	54.45	39.83					
Ti		C_{11}	C_{12}	C_{13}	C_{33}	C_{44}	a	c/a	a	c/a
	Exp.[215]	176.1	86.9	68.3	190.5	50.8			2.95107 Å	1.587 Å
	Exp.[216]	160	90	66	181	46	2.939 Å	1.5800	Exp.[217]	Exp.[217]
	DFT [218]	171.6	85	78.6	187.5	39				
	DFT [219]	174.5	87	78	188	42				
	DFT [220]	194	69	80	175	41				
	This study	189.9	62.8	69.9	194.6	42.03				
Ni		C_{11}	C_{12}	C_{44}		a		a	
	Exp.[221]	253	158	122		3.5178 Å		3.508 Å Exp. [222]	
	Exp.[221]	252	152	123					
	Exp.[216]	250	150	120					
	MD [223]	240	140	140					
	DFT [224]	290	154	---					
	DFT [225]	287	155	150					
	This study	276.7	153.4	134.5					
Cr		C_{11}	C_{12}	C_{44}		a		a	
	Exp.[226]	391	90.53	102		2.8473 Å		2.498 Å Exp. [227]	
	Exp.[228]	339.8	58.6	99.0					
	DFT[228]	340	59	100					
	DFT [225]	508	170	127					
	This study	505	134	106					
Co		C_{11}	C_{12}	C_{13}	C_{33}	C_{44}	a	c/a	a	c/a
	Exp.[229]	307	165	103	358	75			2.497 Å	---
	Exp.[230]	295	159	111	335	71	2.4917 Å	1.6230	Exp. [227]	Exp. [227]
	Exp.[231]	306.3	165.1	101.9	357.4	75.3			2.51 Å	1.622
	DFT [225]	353	188	116	443	63			Exp. [232]	Exp. [232]
	DFT [233]	325	165	105	365	90				
	DFT [233]	295	135	85	340	95				
	This study	381.8	142.6	102.4	416	96.8				
Mo		C_{11}	C_{12}	C_{44}		a		a	
	Exp.[234]	450.02	172.92	125.03		3.1279 Å		3.147 Å [235]	
	Exp.[236]	464.79	158	108.94					
	Exp.[237]	463.0	161.1	103.8					
	DFT[238]	463	163	103					
	DFT[239]	459.7	161.1	103.8					
	DFT [240]	484.0	162.0	95.3					
	This study	408.9	173.3	76.2					

Table 4. 2 Compositions of γ' phase considered in this study in the multicomponent cases (Section 4.3). Numbers give the at. % fraction of each element. Numbers in parentheses are the numbers of atoms included in the atomistic structures. Bold numbers correspond to the case of Inconel 939.

	Constant Ratio					**Sacrificial Nickel**				
Al	2.56	3.80	4.19	4.60	5.60	2.48	3.60	4.19	4.60	5.25
Ni	68.28 (1503)	67.39 (1482)	**67.04 (1474)**	66.67 (1467)	65.87 (1447)	68.61 (1510)	67.64 (1487)	**67.04 (1474)**	66.67 (1466)	65.98 (1450)
Al	8.58 (189)	10.00 (220)	**10.52 (231)**	11.05 (243)	12.25 (269)	8.51 (187)	9.75 (214)	**10.52 (231)**	11.05 (243)	11.84 (260)
Ti	13.88 (306)	12.54 (276)	**12.03 (265)**	11.52 (253)	10.36 (228)	13.91 (306)	12.79 (281)	**12.03 (265)**	11.52 (253)	10.76 (236)
Cr	1.24 (27)	1.54 (34)	**1.64 (36)**	1.75 (38)	1.98 (43)	1.21 (27)	1.48 (33)	**1.64 (36)**	1.75 (38)	1.91 (42)
Co	6.14 (135)	6.74 (148)	**6.99 (154)**	7.25 (159)	7.89 (173)	5.88 (129)	6.57 (144)	**6.99 (154)**	7.25 (159)	7.83 (172)
Ti	2.00	4.00	4.38	5.00	5.50	1.80	3.60	4.38	4.80	5.26
Ni	68.03 (1505)	67.2 (1479)	**67.04 (1474)**	66.83 (1468)	66.64 (1465)	68.53 (1516)	67.04 (1486)	**67.04 (1474)**	66.80 (1468)	66.57 (1462)
Al	13.05 (289)	10.87 (239)	**10.52 (231)**	10.00 (220)	9.56 (212)	11.20 (291)	10.52 (247)	**10.52 (231)**	10.20 (231)	9.88 (217)
Ti	8.51 (188)	11.56 (254)	**12.03 (265)**	12.69 (279)	13.18 (289)	11.09 (183)	12.03 (244)	**12.03 (265)**	12.46 (265)	12.88 (283)
Cr	2.00 (44)	1.68 (37)	**1.64 (36)**	1.59 (35)	1.54 (34)	1.70 (44)	1.64 (37)	**1.64 (36)**	1.62 (36)	1.58 (35)
Co	6.08 (134)	6.86 (151)	**6.99 (154)**	7.20 (158)	7.42 (163)	6.61 (126)	6.99 (146)	**6.99 (154)**	7.2 (154)	7.45 (163)
Cr	9.00	18.00	24.35	25.00	26.47	5.90	9.00	24.35	25.00	25.94
Ni	66.54 (1457)	66.74 (1464)	**67.04 (1474)**	67.09 (1476)	67.31 (1480)	70.05 (1536)	69.46 (1522)	**67.04 (1474)**	66.94 (1472)	66.88 (1471)
Al	10.93 (239)	10.66 (234)	**10.52 (231)**	10.51 (231)	10.53 (232)	10.71 (235)	10.65 (234)	**10.52 (231)**	10.54 (231)	10.60 (233)
Ti	11.26 (247)	11.77 (258)	**12.03 (265)**	12.05 (265)	12.00 (264)	10.82 (237)	11.15 (244)	**12.03 (265)**	12.02 (265)	11.96 (263)
Cr	1.06 (23)	1.47 (32)	**1.64 (36)**	1.66 (36)	1.67 (37)	0.75 (16)	1.01 (22)	**1.64 (36)**	1.67 (36)	1.68 (37)
Co	8.88 (194)	7.81 (172)	**6.99 (154)**	6.89 (152)	6.67 (147)	6.21 (136)	6.29 (138)	**6.99 (154)**	7.03 (154)	7.08 (156)
Co	14.20	16.50	18.22	30.00	36.00	5.00	11.00	18.22	28.00	43.00
Ni	68.95 (1519)	67.85 (1493)	**67.04 (1474)**	61.24 (1339)	58.23 (1271)	72.98 (1619)	70.69 (1557)	**67.04 (1474)**	59.49 (1305)	42.03 (923)
Al	10.54 (232)	10.52 (231)	**10.52 (231)**	10.76 (235)	11.01 (240)	9.52 (211)	10.28 (227)	**10.52 (231)**	10.89 (239)	11.28 (247)
Ti	11.82 (260)	11.96 (263)	**12.03 (265)**	12.10 (265)	11.93 (260)	11.93 (265)	11.91 (262)	**12.03 (265)**	12.10 (266)	11.70 (257)
Cr	1.68 (37)	1.66 (37)	**1.64 (36)**	1.58 (35)	1.58 (34)	1.51 (33)	1.64 (36)	**1.64 (36)**	1.92 (42)	3.18 (70)
Co	5.09 (112)	6.16 (136)	**6.99 (154)**	13.08 (286)	16.25 (355)	1.45 (32)	3.54 (78)	**6.99 (154)**	14.03 (308)	30.18 (663)

Table 4. 3 Base composition in, wt%, of Inconel 939 [187].

C	Cr	Co	Mo	W	Ta	Nb	Al	Ti	Ni
0.15	22.4	19.0	<0.01	2.02	1.45	1.05	2.00	3.71	Bal.

Table 4. 4 Summary of the CE performed for the current study and a comparison of the obtained {111} APBE with literature.

CE (This study)	Cross validation score (meV/atom)	Number of clusters relaxed	APBE of pure Ni_3Al (mJ/m^2)
Ni-Al	0.007	95	320.737
Ni-Al-Ti-Co[1.]	0.028	60	208.749
Ni-Al-Ti-Cr	0.029	59	221.705
Ni-Al-Ti-Mo	0.032	132	252.858
Ni-Al-Ti-Cr-Co-Mo	0.030	498	268.734

	Method	Composition	APBE
Literature:	DFT [201]	Ni–25Al	223
	DFT [198]	Ni–25Al	240
	DFT [196]	Ni–25Al	270/210[2.]
	DFT [188]	Ni–25Al	220/172[2.]
	DFT [202]	Ni–25Al	306/188[2.]
	DFT [206]	Ni–25Al	152
	DFT [174]	Ni–25Al	315/181[2.]
	DFT [90]	Ni–25Al	344
	DFT [163]	Ni–25Al	310
	CE [90,99]	Ni–25Al	318
	CE [183]	Ni–25Al	300
	Exp. [241]	Ni–24.2Al	194 ± 22[3.]
	Exp. [203]	Ni–25Al	195 ± 13[3.]
	Exp. [204]	Ni–25Al	180 ± 30[4.]
	Exp. [241]	Ni–25.9Al	250 ± 29[3.]
	PST [242,243]	Ni–25Al	135[5.]
	PST [153]	Ni–25Al	161[5.]

1. This cluster expansion is employed to study both the effect of individual Titanium and Cobalt solutes.
2. The higher and lower values correspond to idealized and fully-relaxed conditions.
3. Corrected values using either Cockayne correction or Image simulations.
4. Uncorrected values.
5. Values determined from the precipitation strengthening theories (PST).

Table 4. 5 Composition ranges of the ternary γ' phases considered in this work. The underlined, bold faced elements are solutes added.

Ternary alloy	Solute Site Preference	Minimum solute fraction (%)	Maximum solute fraction (%)	Number of compositions
Ni-Al-**Ti**	Al	1.00	15.00	8
Ni-Al- **Cr**	Al	0.1	9.0	7
Ni-Al-**Co**	Ni	1.0	23.0	6
Ni-Al- **Mo**	Al	0.1	7.0	6

Table 4. 6 Fitted coefficients for Eqs. 7 and 8. The coefficients have the unit mJ/m^2. The root mean square errors (RMSE) evaluate the fit of Eqs. 7 and 8 (with the coefficients given in this table) for data shown in Figs. 7 and 8.

T (K)	K_1 (Ti)	K_2 (Cr)	K_3 (Co)	K_4 (Mo)	F_1 (Ti-Cr)	F_2 (Ti-Co)	F_3 (Cr-Co)	H (Ti-Cr-Co)	RMSE Eq. 7	RMSE Eq. 8
500	8.862	-4.497	-1.229	-2.574	0.8166	0.0916	-4.337	0.3211	19.79	6.00
700	8.196	-4.793	-1.423	-2.495	0.6286	0.0954	-4.440	0.3724	24.17	4.90
900	8.011	-5.256	-1.574	-2.512	0.5223	0.0628	-5.266	0.4626	23.66	6.04
1100	7.795	-6.184	-1.838	-2.726	0.6641	0.0634	-5.681	0.4975	26.83	7.32
1300	7.560	-7.962	-2.410	-3.247	0.8702	0.1109	-5.532	0.4792	34.45	7.78

Table 4. 7 Mole fractions of the γ and γ’ phases as a result of compositional adjustments.

Constant Ratio

Al	γ	γ’	Ti	γ	γ’	Cr	γ	γ’	Co	γ	γ’
2.56	77.79	15.67	2	85.60	12.92	9	70.98	27.30	14.2	62.04	31.39
3.8	72.36	26.15	4	72.79	25.75	18	69.87	28.56	16.5	68.11	29.33
4.19	70.68	27.86	4.38	70.68	27.86	24.35	70.68	27.86	18.22	70.68	27.86
4.6	68.83	29.60	5	65.26	31.25	25	70.37	27.72	30	81.62	17.12
5.6	59.40	34.16	5.5	59.55	33.53	26.47	65.85	27.70	36	87.96	10.88

Sacrificial Nickel

Al	γ	γ’	Ti	γ	γ’	Cr	γ	γ’	Co	γ	γ’
2.48	78.83	14.68	1.8	87.96	10.61	5.9	88.51	10.08	5	64.69	31.97
3.6	73.43	24.81	3.6	75.35	23.20	9	83.46	15.12	11	69.97	28.60
4.19	70.68	27.86	4.38	70.68	27.86	24.35	70.68	27.86	18.22	70.68	27.86
4.6	68.03	29.77	4.8	66.85	30.29	25	69.52	28.14	28	72.06	25.45
5.25	60.47	33.01	5.26	60.49	32.82	25.94	64.83	28.68	43	78.60	17.19

Figures

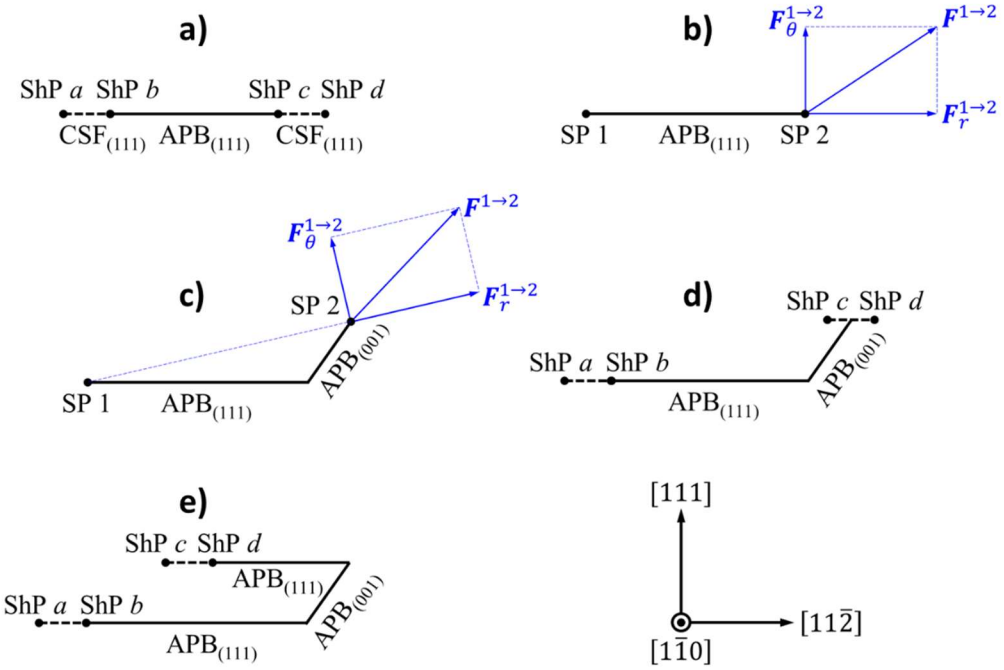

Figure 4. 1 A schematic illustration of a typical cross-slip mechanism in the γ' alloys and the resulting slip irreversibility when loading is reversed. APBs are represented by bold solid line segments, while the CSFs are represented by bold dashed line segments. The forces felt by SP 2 is represented by the thin blue arrows.

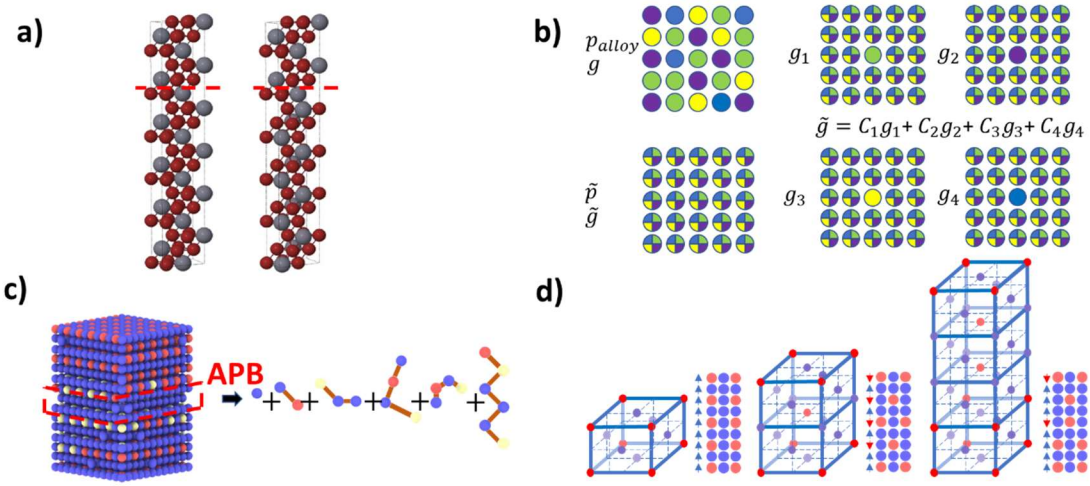

Figure 4. 2 Schematic illustrations of popular methods to study the effect of impurities on APB energy in γ'. (a) Direct DFT approach (image recreated with permission from Ref. [174]); (b) coherent potential approximation (CPA) method; (c) cluster expansion-based method; (d) one dimensional long period structure (1D-LPS) method.

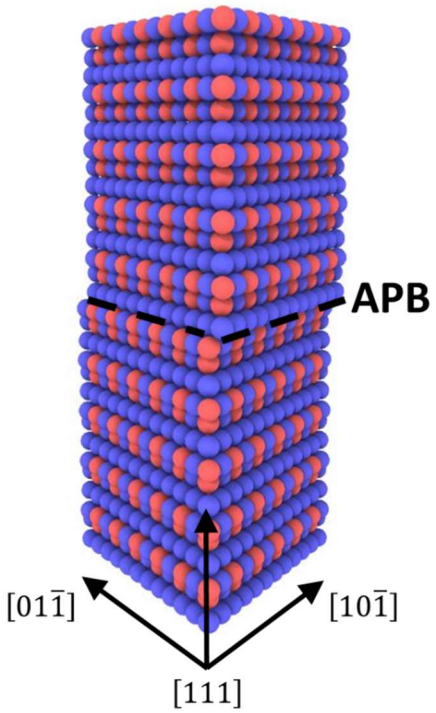

Figure 4. 3 A typical atomistic structure used to calculate APBE. The APB was created by shifting the top crystallite with respect to the lower crystallite by $a/2[1\bar{1}0]$.

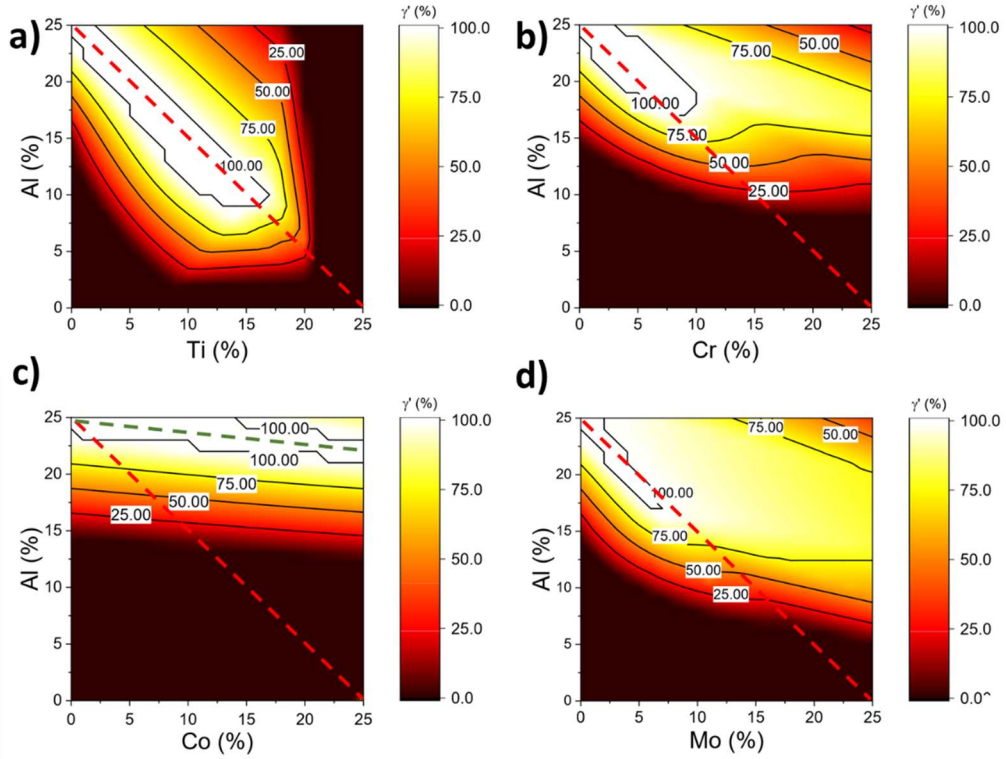

Figure 4. 4 Phase fractions of γ’ as a function of compositional adjustment in a ternary alloy Ni-AL-M. (a) M=Ti (b) M=Cr (c) M=Co (d) M=Mo. Elemental fractions are given in mole fractions.

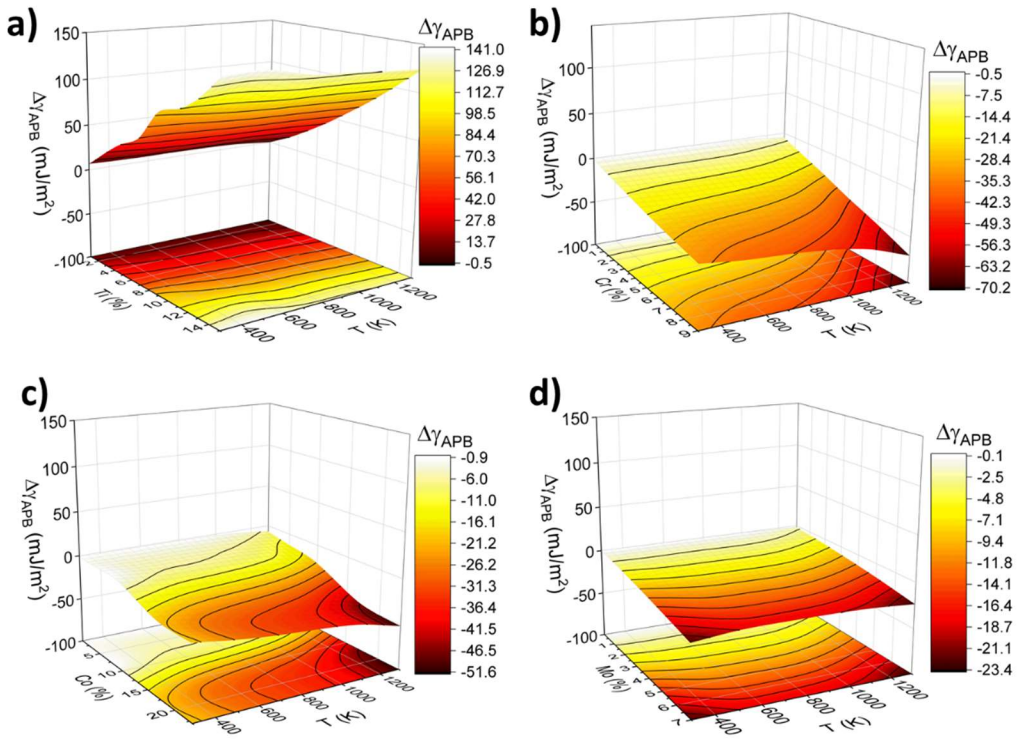

Figure 4. 5 Effect of Composition and Temperature change on the relative APB energy of ternary alloy. Single elements, including (a) Ti, (b) Cr, (c) Co, and (d) Mo are added to pure Ni3Al phase.

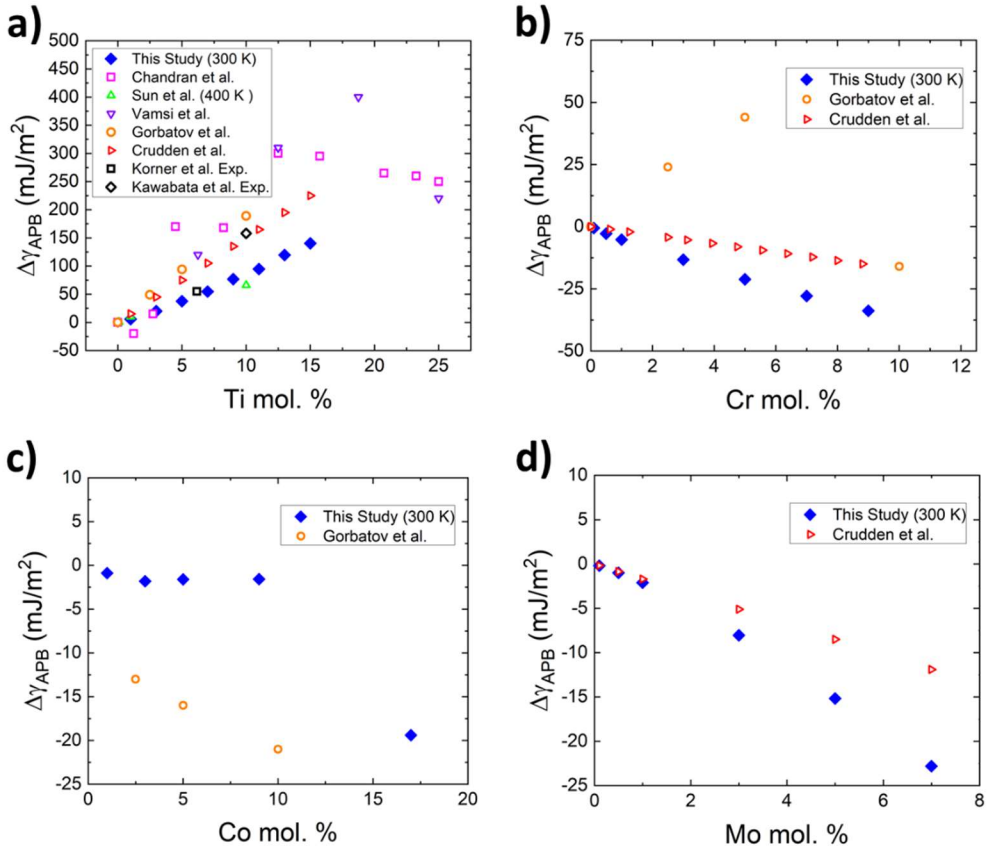

Figure 4. 6 Comparison of relative APB energy in ternary alloys as a result of compositional variation obtained in this study with literature. Data points of this study correspond to the temperature of 300K. Two black markers in (a) represents the results from experiments. The calculation of $\Delta\gamma_{APB}$ used absolute APB energy of 195 mJ/m^2 reported by Kruml [203] as reference.

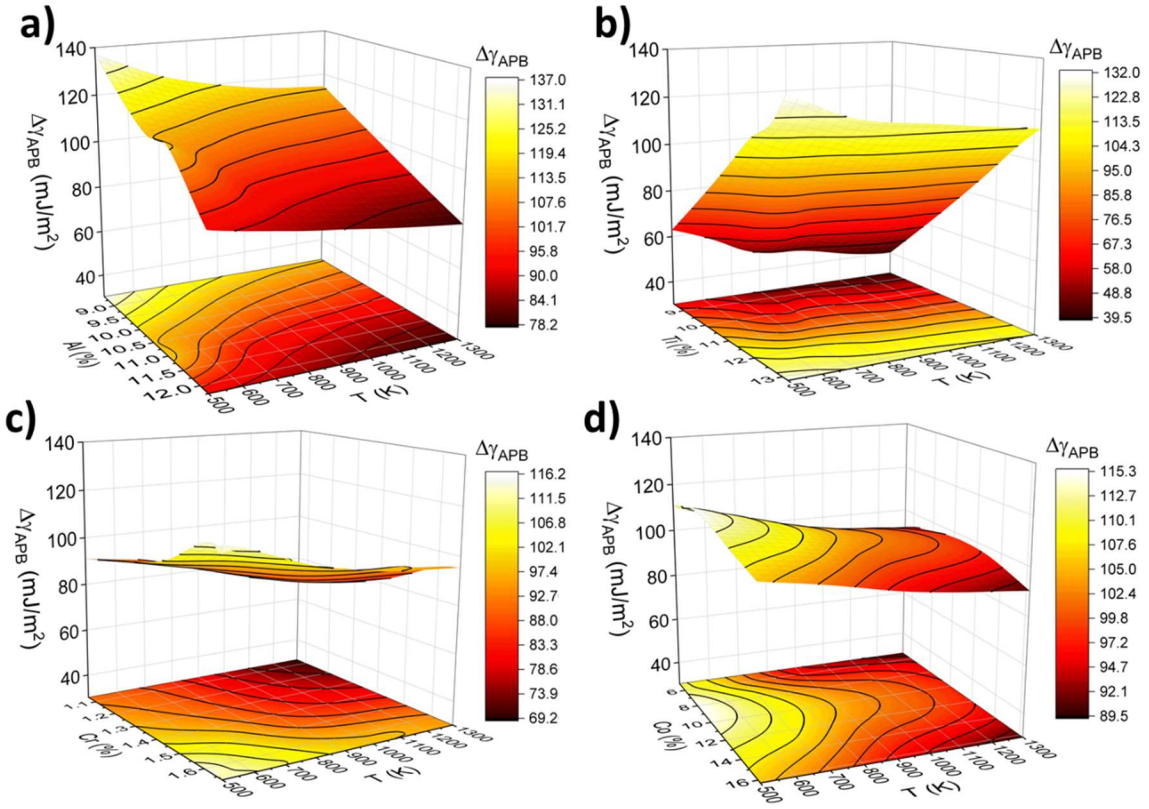

Figure 4. 7 Variation of relative APB energy of Inconel 939 by compositional modification, using "constant ratio" strategy. Figures (a), (b), (c), and (d) correspond to adjustments of Al, Ti, Cr, and Co elements. The compositions in the plots are the actual compositions in the γ' phase.

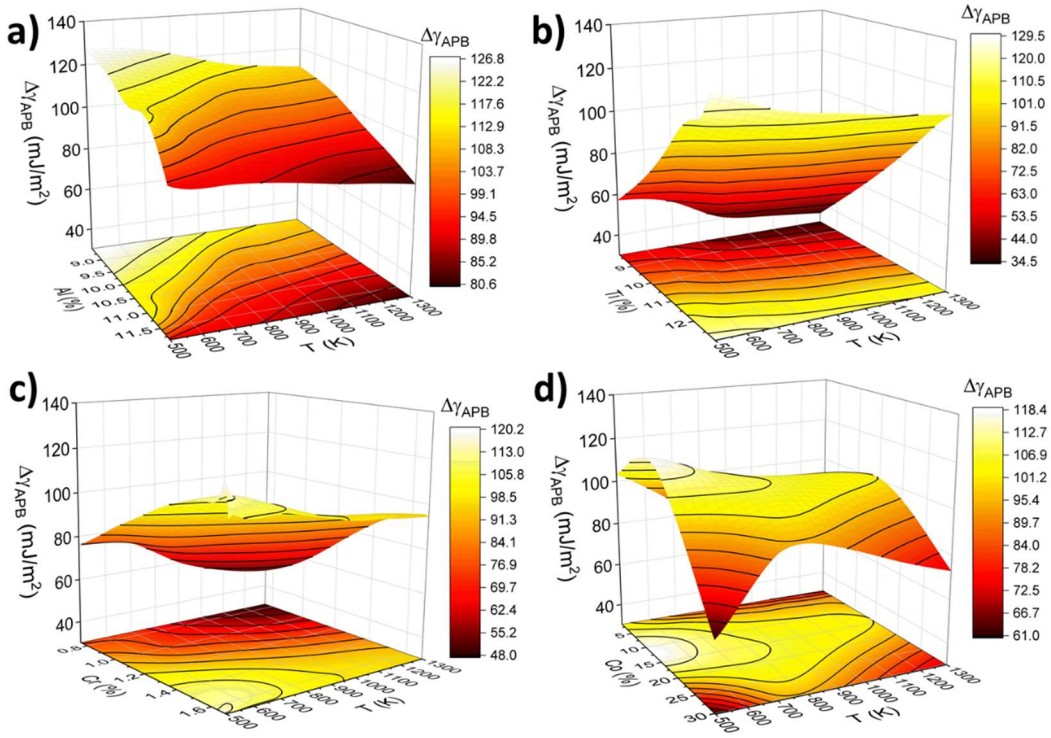

Figure 4. 8 Variation of relative APB energy of Inconel 939 by compositional modification, using "sacrificial Ni" strategy. Figures (a), (b), (c), and (d) correspond to adjustment of Al, Ti, Cr, and Co elements. The compositions in the plots are the actual compositions in the γ' phase.

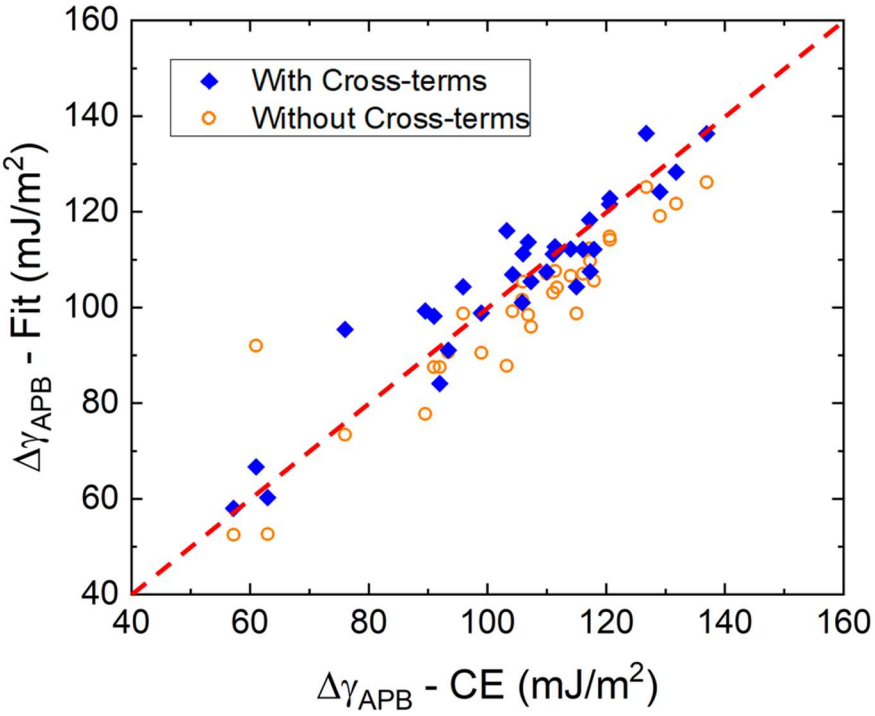

Figure 4. 9 Comparison of the predictive performance of Eq. 7 (without cross terms) and Eq. 8 (with cross terms).

CHAPTER 5 ENERGETIC, STRUCTURAL AND MECHANICAL PROPERTIES OF TERRACED INTERFACES

5.1. Abstract

Taking the well-understood Cu-Ni {111} semi-coherent interface as a prototype, we demonstrate an important, yet long-been-overlooked, size effect on the properties of terraced interfaces — i.e. the facet length scale effect. Interfacial facets are considered as super interface disconnections (SIDs). We then studied the SID's size effect on the energy, structure, and mechanical response of terraced interfaces by using atomistic simulations and defect theories. We found that the specific facet energy — therefore the specific energy of the terraced interface — exhibits a periodic change with the SID's size. The periodic change is associated with the quantized transitions in their dislocation structures. Correspondingly, the mechanical response of terraced interfaces also exhibits clear regime shifts, as reflected in changes in the nucleation and emission mechanisms for lattice dislocations.

Keywords: Semi-coherent interfaces; Disconnections; Misfit dislocations; Mechanical Response; Interface energy

5.2. Introduction

A solid-solid variant of the terraced surfaces — referred in this work exclusively as "terraced interfaces"— forms between similar or dissimilar crystals as grain boundaries or phase boundaries. Facets on these asymptotically flat interfaces may strongly influence their mechanical response for several reasons. First, the presence of the low-energy facets at an interface reduces the interface energy and increases mechanical and thermal stability. For instance, Cu-Nb interfaces with terraces, fabricated by the accumulative roll bonding (ARB) technique [244], possess great thermal stability and can persist in despite of severe plastic deformation [245,246]. In addition, the local stress state near facets at an interface is generally distinct from the applied stress state, e.g., a remote, pure normal or shear loading to the originally flat interface would be transformed to a local, combined normal/shear loading on the facets [247,248]. Such a change in stress state has been demonstrated to tailor segregation of rare earth elements along the twin boundaries [248–251]. Further, due to the elastic mismatch between the adjoining crystals, stress concentrations tend to be induced at the apices — or ridges and valleys — formed by neighboring facets. These stress concentrations may assist the emission of lattice or interfacial dislocations, which can be beneficial for interfaces that would otherwise be brittle, e.g. metal/ceramic interfaces [252].

The mechanical response of faceted interfaces may greatly depend on the structures and specific properties of these low energy facets. Coherent facets may possess strong resistance to the nucleation and emission of dislocations as well as slip transmission for dislocations. Semi-coherent facets, similar to semi-coherent interfaces, may facilitate the nucleation of lattice dislocations from the misfit dislocation networks (MDN) [253] in response to normal loading and may slide accompanied with the formation of interface dislocations loops at the MDN or by the

collective translation of the MDN [254,255]. It is worth noting that the concept of surface/interface facets may be multiscale, varying from the atomic-scale interfacial disconnections/steps to the macroscopic surface facets of single crystals visible to the naked eye. For terraced interfaces, the change in the facet size may alter the coherency and dislocation structure at interface, resulting in different mechanical responses.

Modeling efforts, in pursuit of predicting the morphology of the terraced interfaces/surfaces, mostly follow Herring's initial thermodynamics argument. According to Herring [256], the morphology of the terraced interfaces/surfaces is the result of minimization of interface free energy, which may depend on both orientation and curvature (facet edge energy). While this framework may be effective in predicting the energy and morphology of solid-liquid interfaces, and the like (such as solid-gas interfaces), where the specific energy of the low-energy facet is only dependent on its orientation [257], its direct application to solid-solid interface should be used with caution. It is evident that the total area of an asymptotically flat interface, when the orientations of facets have been prescribed, is independent of the absolute size of the facets. Yet the facet size has been shown to be quite constant at a given temperature [258]. The governing factors for the facets' characteristic dimensions has been attributed to the minimization of the excess energies associated with the facet junctions (edge energy) [259]. In addition to the minimization of the total edge energy, the key could also lie in the fact that the specific interface energy is a function of not only its orientation, but also a facet's size. To date, mathematical models capable of accurately predicting the morphology of the solid/solid interfaces have been constructed [260]. However, these mathematical models utilized a description of the specific interface energy that is only a function of adjoining crystals' orientation and the interface's habit

plane. Because of this, an intrinsic property of the interfacial facets, i.e. their size dependence, cannot be fully captured.

On a terraced interface, depending on the associated lattice mismatch, misorientation of closed-packed atomic planes, and their size, facets may contain characters of dislocations, steps, and disclinations [261–263]. In this work, facets are treated, in a general sense, as super interfacial disconnections (referred to as SIDs) [261,262]. The nomenclature "super" is used here to distinguish the facets from the disconnections in the conventional sense (whose height is on the order of one atomic spacing) [261,262]. A general interfacial disconnection, shown in Fig. 1, is characterized by a Burgers vector, $\boldsymbol{b}$, and a step vector, $\boldsymbol{l}$, which are defined as:

$$\boldsymbol{b} = \boldsymbol{l}_\alpha + \boldsymbol{l}_\beta \tag{1a}$$

$$\boldsymbol{l} = -\boldsymbol{l}_\beta \tag{1b}$$

where the right-hand, finish-start rule is obeyed [261,262]. Under this setup, a facet/SID is said to contain dislocation and step characters if $\boldsymbol{b}$ is parallel/antiparallel to $\boldsymbol{l}$. A facet/SID contains a disclination character if $\boldsymbol{b}$ is non-parallel to $\boldsymbol{l}$. Lastly, a facet/SID with a pure step character would require that $|\boldsymbol{b}| = 0$.

The energy of a given SID is related to all of its characters: the Burgers vector contributes to its overall coherency strain energy and the step vector contributes to its overall surface energy. To the first order of approximation, the total energy of a SID, per unit length in ξ direction, can be expressed as

$$\frac{E_{\text{disc.}}}{L} = \frac{E_b}{L} + \frac{E_l}{L} \tag{2a}$$

$$\frac{E_b}{L} = \frac{k\alpha\bar{\mu}|\boldsymbol{b}|^2}{4\pi} \ln\frac{R}{r} \tag{2b}$$

$$\frac{E_l}{L} = \gamma(\boldsymbol{l})|\boldsymbol{l}|. \quad (2c)$$

Here k is a factor accounting for the differences in the strain energy between a dislocation and a disconnection, α accounts for the character of a disconnection, i.e. $\alpha = 1$ for screw and $\alpha = 1/(1-\nu)$ for edge, $\bar{\mu}$ is an effective shear modulus at interface. Note that Eqns. (2b), with the form of the line energy of an edge dislocation, is merely an approximation as the core energy part of the disconnection obviously differ from that of a regular dislocation. In addition, isotropic assumption is used here, while crystals are anisotropic in general in reality. Due to the mismatch in elastic properties, the strain field of interfacial dislocations/disconnections differs from that of ones in bulk [46]. By using the parameter $\bar{\mu}$, the effect of the heterophase interfaces on the strain energy of these line defects can be approximated [264]. With the change in size $|\boldsymbol{l}|$, the energy of a disconnection, $\frac{E_{\text{disc.}}}{L}$, changes, as both the Burgers vector and the surface energy $\gamma(\boldsymbol{l})$ may vary. In addition, the specific facet energy per unit area, evaluated as $\gamma_{\text{facet}} = E_{\text{disc.}}/(L|\boldsymbol{l}|)$, may vary, not only as a function of the direction of the step vector ($\boldsymbol{l}/|\boldsymbol{l}|$), but also of its magnitude ($|\boldsymbol{l}|$). It follows that minimization of overall interfacial energy would inevitably involve the minimization of γ_{facet}. However, how this specific facet energy of a disconnection evolves as a function of its size $|\boldsymbol{l}|$ has not been clearly elucidated in the literature.

To shed some light on this complexity, this work focuses on a simplified case of facets/SIDs, i.e. ones with only dislocation + step characters. Atomistic simulations performed on faceted Cu-Ni (111) semi-coherent interfaces are utilized to investigate the structural, energetic, and mechanical characteristics of interfacial facets (or SIDs). Semi-coherent interfaces are considered here due to their ubiquitous nature in a wide range of materials [265], including precipitation hardened alloys [138,139,266–269], eutectic alloys [270,271] and nano-multilayered

composites [51,272–277]. The contribution of this work is twofold: (1) a mechanism, by which the facet energy, γ_{facet}, (hence the interface energy) varies as a function of SID's size, is elucidated; (2) the role of SID's size on the interfacial mechanical response, to both compression and shear is revealed and analyzed in detail. Although this work is performed on a particular material system, i.e. FCC Cu and FCC Ni, the findings are expected to be applicable to a broader range of semi-coherent interfaces between materials with same lattice structure. This rest of this article is organized as follows: Section 2 details the methodology we have adopted for the atomistic simulations and analyses of the results. In Section 3, we present the main findings of this work, which pertain to the structures (Section 3.1), energy characteristics (Section 3.2), and the mechanical responses (Section 3.3) of interfacial facets. In Section 4, we provide detailed discussion of our results, regarding the limitations of the present work, and the implications of our findings to related fields. Finally, in Section 5, we draw our conclusions.

5.3. Methodology

In this work, we use molecular statics (MS) and molecular dynamics (MD) performed using the parallel atomistic simulation program LAMMPS [43] to investigate the structure, energies, and mechanical responses of the faceted Cu-Ni (111) semi-coherent interfaces. The interactions among Cu and Ni atoms [278] are modeled by the embedded atom method (EAM) [45,279]. This particular set of potentials can reliably reproduce a broad range of materials properties of Cu, Ni and Cu-Ni compounds, including melting points, enthalpy of mixing, ground state lattice structures, point defect formation energies, etc. The authors are aware of the negative free energy (Gibbs) of mixing of the Cu-Ni system at finite temperatures, which dictates that a thermodynamic driving force exists for Cu to alloy with Ni. This arise from Cu-Ni system's slightly positive mixing enthalpy and the positive mixing entropy ($G = H - TS$). We stress that the

interfacial alloying effect is not among the foci of this study. Instead, the focus of this paper is on the diffusionless, displacive characteristics, such as structure of the MDNs, nucleation/emission of dislocations from interface, etc., that are shared by the entire class of the (111) FCC-FCC semi-coherent interfaces. The results of this paper is not expected to be strongly influenced by the Cu-Ni intermixing, as time scale for such a process is much longer as compared to the nanosecond time scale of MD.

For computational simplicity, an asymptotically flat, faceted interface is not modeled, as that would require a computational cell that is too large, due to the imposed periodic boundary conditions. Instead, Cu-Ni bi-crystals containing a pair of disconnections with opposite signs are modeled, as shown in Fig. 2. As shown, the same crystallographic orientation, x//$[11\bar{2}]$ z//$[1\bar{1}0]$ and y//[111], is obeyed by all atomistic models. The interface[2] plane is perpendicular to the y-direction. Each model has a dimension of 32.8 × 18.9 nm in the x-z plane. Under zero strains, this box would fit 74 and 76 periodic lengths of Cu and Ni in the x and z directions, respectively, which corresponds to 26.751 and 26.752 nm. Due to the applied boundary conditions, these dimensions yield strains in the Cu and Ni layers below 5×10^{-5}, which correspond to ~10 MPa of stress. Note that the smallest x-z dimension to satisfy this condition is 16.4 × 9.5 nm [253], the in-plane dimensions in the present study are enlarged by a factor of four to increase the probability of observing dislocation nucleation events. Periodic boundary conditions are applied in the x and z directions, while fixed boundary conditions are applied in y direction. As shown in Fig. 2, regions on top and bottom of the models, with thickness of 10 Å, are fixed, as denoted by the brown-colored atoms. Obeying the periodic boundary conditions, in each model, two disconnections are created on the interface, along the close packed $(11\bar{1})$ plane. To investigate

[2] Here, the "interface" refers to the regions of the interface excluding the disconnections.

the effect of the disconnection height (h)—or length of step vector ($|\boldsymbol{l}|$), a total of more than 24 atomistic models have been created, corresponding to h = 0 - 20 nm or $|\boldsymbol{l}|$ = 0 - 21.3 nm. To minimize boundary effects, a minimum distance of d = 10 nm between the interface and the fix boundaries is guaranteed in all models.

Following the methods used by prior works [253,255,280,281], the residual stresses of initial structures was iteratively relaxed. The resulting structures has a state of stress $\sigma_{yy}^{Cu}, \sigma_{yy}^{Ni} \approx 0$ and $\sigma_{xx}^{Cu}, \sigma_{zz}^{Cu}, \sigma_{xx}^{Ni}, \sigma_{zz}^{Ni} < 10$ MPa. This stress relaxation is necessary, as the calculation of interfacial energies could be significantly affected by the residual coherency strains [266]. Followed by relaxation, each structure is mechanically loaded under three stress-controlled shear and compression conditions. The applied shear stress is parallel to the interface and along x directions (σ_{xy}), the applied compression is perpendicular to the interface (σ_{yy}). The choice of these loading conditions was dictated by the following reasons: (1) the introduction of parallel disconnections has been shown to strongly strengthen an interface's shear resistance along the perpendicular direction [282], namely x direction in the present study; (2) typical loading conditions in the experiments, pillar compression [283–285] and nanoindentation [286,287], etc., typically involves compression and/or shear loading on the interfaces. Indeed, simulations of shear loading along z direction (σ_{yz}) of the terraced interfaces performed in this work revealed little strengthening effect (strengths about 200 MPa). The loadings were iterative and 50 MPa was applied at each loading step. At each loading step, the following boundary conditions are ensured:

(for shear) $\sigma_{xy}^{Cu} = \sigma_{xy}^{Ni}, \quad \frac{1}{2}\left(\sigma_{xx}^{Cu} + \sigma_{xx}^{Ni}\right) = 0$

$$\frac{1}{2}\left(\sigma_{zz}^{Cu} + \sigma_{zz}^{Ni}\right) = 0, \quad \sigma_{yy}^{Cu} = \sigma_{yy}^{Ni} = 0 \tag{3a}$$

(for compression) $\sigma_{yy}^{Cu} = \sigma_{yy}^{Ni}, \qquad \frac{1}{2}\left(\sigma_{xx}^{Cu} + \sigma_{xx}^{Ni}\right) = 0$

$$\frac{1}{2}\left(\sigma_{zz}^{Cu} + \sigma_{zz}^{Ni}\right) = 0, \tag{3a}$$

Detailed explanations on the application of the stress controlled shear loading has been given elsewhere [255,283] and will not be reiterated here. During loading the temperature is maintained at 5K.

The evaluation of γ_{facet} as a function of $|\boldsymbol{l}|$ is achieved by measuring the interface energy in two ways, namely the projected interface energy ($\gamma_{\text{Proj.}}$) and the specific interface energy ($\gamma_{\text{Spec.}}$), see Eqn. 4. Isolated measurement of γ_{facet} for a single facet is not feasible as various energy components of the atomistic system are highly coupled. However, the measurement of $\gamma_{\text{Spec.}}$ is expected to well correlate with γ_{facet}. The aforementioned qualities are evaluated according to the equations below:

$$\gamma_{Proj.} = \frac{1}{A_{Proj.}}\left(E_{Interface}(N_{Cu}, N_{Ni}) - N_{Cu}E_{Cu} - N_{Ni}E_{Ni}\right), \tag{4a}$$

$$\gamma_{Spec.} = \frac{1}{A_{total}}\left(E_{Interface}(N_{Cu}, N_{Ni}) - N_{Cu}E_{Cu} - N_{Ni}E_{Ni}\right), \tag{4b}$$

where N_{Cu} and N_{Ni} are the respective number of atoms for Cu and Ni in a bicrystal atomistic model, $E_{\text{Interface}}$ is the total energy of the bicrystal model, E_{Cu} and E_{Ni} are the respective per atom energies for Cu and Ni under bulk condition, $A_{Proj.}$ is the area of an interface projected to the x-z plane (calculated as the x-z cross-section area of the bicrystal model), A_{total} is the total area of an interface accounting for the area of the facets. The A_{total} total area for a terraced interface (with step height h) is calculated according to the total number atoms immediately adjacent to the interface $N_{int}^{h\neq 0}$. The area (A_{flat}) and the number of interfacial atoms ($N_{int}^{h=0}$) of the flat (111)

interface are used as references. The area of any terraced interface can then be calculated as $A_{total} = \frac{N_{int}^{h\neq 0}}{N_{int}^{h=0}} A_{flat}$.

5.4. Results

5.5.1. Structure of FCC (111) semi-coherent interfaces and disconnections

The disconnections on the Cu-Ni (111) semi-coherent interface exist on the $(11\bar{1})$ and $(\bar{1}\bar{1}1)$ planes of both crystals, assuming that the plane normal points from Ni to Cu. The step vector of the respective crystals, $\boldsymbol{l}_\alpha$ and $\boldsymbol{l}_\beta$, are antiparallel. This is schematically shown in Fig. 3a, using the Disconnection 1 as an example. In addition, due to the bulk lattice mismatch between Cu and Ni of around 2.7% the character of the disconnections on this type of interfaces is not always pure step. The corners of this disconnection are formed by {111} interfacial facets with a 70.5° angle. It is trivial to show that the opposing disconnection to the one shown in Fig. 3a has an opposite Burgers vector. The pair of disconnections, i.e. disconnections 1 and 2 in Fig. 2, therefore exists as a dipole. In addition, the Burgers vector of these disconnections varies as a function of the disconnection height *h*, or step vector length $|\boldsymbol{l}|$. Indeed, as shown in Fig. 3b, the $|\mathbf{b}|$ appears to be periodic function of *h*, whose period is ~77 Å. This behavior can be rationalized by observing that the spacing between the {111} planes in Cu and Ni is $d_{\{111\}}^{Cu}$ = 2.087 Å and $d_{\{111\}}^{Cu}$ = 2.032 Å, respectively, and that at $\mathcal{H}$ = 77.2 Å the Cu and Ni terraces on either side of the disconnection are almost of equal height—with a mismatch of only 0.004%. This suggests that the Burgers vector of a disconnection on the Cu-Ni (111) interface is 0 when h = n $\mathcal{H}$, where n is an integer, and increase piece-wise linearly with the disconnection height. When h is just below

n $\mathcal{H}$, the addition of one extra atomic plane creates misfit dislocations on the facet of the disconnections[3].

Depending on the height of the interfacial disconnections, the dislocation structure on the facet of disconnections may display distinct features. Figure 3 shows three typical structures of disconnections, corresponding to Cases I, II and III noted in Fig. 3b. Detailed disregistry analyses, examples of which shown in the Suppl. Mater. Section S2, have been performed, revealing the characteristics of the dislocations. As shown in the atomistic configurations, the misfit dislocations displayed a very noticeable spiral pattern at nodes. This phenomenon has been reported explained in detail by Shao et al. [253,280]. For Case I, the facet of the disconnection is coherent along the step vector $\boldsymbol{l}$ (recall Fig. 3a). In this case, if using the step vector as a search vector[4], the net Burgers vector content (from MDN, which is different from the **b** defined in Eqn. 1a) is 0 over the distance encompassed by the disconnection. Indeed, as shown in Fig. 4a, the facet of the disconnection only contains dislocations with line sense near-parallel to the γD direction with no intersection with the search vector. The net Burgers vector along the z direction over the entire dimension of the computational cell is $\mathbb{B}_z$ = 2(Bγ + γA) = 2BA = $\bar{a}[1\bar{1}0]$, where $\bar{a}$ is the lattice constant of a interfacial reference lattice, on which the Burgers vectors of interfacial dislocations are formally defined [263].

For Case II, the facet of the disconnection is semi-coherent along the step vector $\boldsymbol{l}$. Treating the positive z direction as the line sense of the disconnection, the net Burgers vector along the search vector, as shown in the Section S1 of the Suppl. Mater., varies depending on the position

[3] In passing, "facet of disconnections" will exclusively refer to facets on the $(\bar{1}\bar{1}1)$ and $(11\bar{1})$ planes; while "facet of the interface" will exclusive refer to facets on the (111) plane in this article.
[4] The concept of "search vector" was first proposed by Frank [427] and Bilby [428]. Later on, this has been widely used by a number of researchers in their follow up work [263,429,430].

of the search vector on the z axis. However, with the occurrence of a horizontal dislocation γD and inclined dislocations γA and Bγ, the average net Burgers vector is 1.5γD. When projected to the y direction, 1.5γD equals δD, which is identical in magnitude with the (111) planar spacing at the disconnection. At the step height of h = $\mathcal{H}$, the step vectors for both Cu and Ni are equal and opposite, i.e. $\boldsymbol{l}_{\alpha} = -\boldsymbol{l}_{\beta}$. From Fig. 3, it is apparent that the largest possible Burgers vector of the disconnection in Case I is 1.5γD (observe that the largest gap formed on the terrace between Cu and Ni is one (111) planar spacing). In this case, the zero Burgers vector of the disconnection can be regarded as the result of the cancelation due to the sudden onset of the net Burgers vector of the MDN along the step vector $\boldsymbol{l}$ on the facet of the disconnection. In Case II, the net Burgers vector along z direction has not been altered and is identical to Case I, i.e. $\mathbb{B}_z = 2(B\gamma + \gamma A) = 2BA$. Also similar to Case I, the maximum Burgers vector of the disconnection achievable for Case II is 1.5γD. Further increase in the disconnection height induces the onset of Case III.

For Case III, an additional horizontal dislocation γD appears on the facet of the disconnection. The net Burgers vector of the MDN along the step vector is invariantly 3γD on this facet, regardless of the location of the search vector on the z-axis. Similar to the prior case, the Burgers vector of this disconnection is zero at the onset of this regime, and grows to a maximum of 1.5γD with the increasing step vector (correspondingly, the increasing step height).

The illustrated disconnection in Fig. 4 exist on the (c) plane of the Thompson's Tetrahedron (TT) [47,288]—corresponding to the $(\bar{1}\bar{1}1)$ plane in Miller indices. The complex dislocation structure on the facet of the disconnection continues on to the (d) plane ((111) plane in Miller indices). The stacking faults of the connecting planes, shown as brown-colored regions in the bottom panels of Fig. 4, join by stair-rod dislocations with Burgers vector of γδ. These stair-rod dislocations exist between stacking faults at the corners of the disconnection, forming an acute

angle of 70.5°. Analyses so far has centered on the structure of one disconnection in the disconnection conjugate on the (111) interface plane whose facet's plane normal facing Cu side is along Cγ. Structure of the second disconnection (Fig. 5) in the disconnection pair, whose plane normal facing Cu side is along γC, are quite similar to the first one. A noticeable difference is that the stair-rod dislocations (with greek-greek type Burgers vectors) now exist between stacking faults forming an obtuse angle of 109.5°. Detailed structure of the stair-rod dislocation at location 1 in Fig. 5a, has been provided in Fig. 5b. This stair-rod dislocation has a Burgers vector of γδ/BA following the convention by Thompson [288]. All of stair-rod dislocations observed so far "turns" stacking faults from one slip plane to another. Another family of these turns (such as one at location 2 in Fig. 5a) is of the contracted type, as illustrated by Fig. 5c. The morphology of the intersection is dominated by the attraction/repulsion force between partial dislocations on the same and opposite sides across the obtuse intersection line, which has been discussed in detail by Hirth and Lothe [47].

5.5.2. Energy of FCC (111) semi-coherent interfaces with disconnections

Energy of disconnections are functions of both their step vector and Burgers vector. Therefore, the interface energy —per unit area— is expected to vary as a function of these parameters. In addition, since the Burgers vector of a disconnection has been shown, in the previous section, to be a function of the step vector, the interface energy of the faceted (111) interface may experience certain periodic features as the height of the disconnections is gradually increased. Figure 6a shows the variation in the projected interfacial energy, $\gamma_{Proj.}$, as a function of the disconnection height h. It is evident that this energy increases approximately linearly with increasing h. This indicates that the step component (Eqn. 2c) dominates the energy of a disconnection. Indeed, the interface energy of a flat, semi-coherent (111) Cu-Ni interface is around

470 mJ/m^2, the introduction of a pair of disconnections with facet area comparable to that of the facets of interface is expected to substantially increase the interface energy. It is also worth noting that near the boundaries between cases, drops of interface energy exist, as shown in the insets of Fig. 6a. This indicates the influence of disconnection's Burgers vector on interface energy, although small as compared to that of the step vector. A baseline reference, i.e. the interface energy of the flat Cu-Ni (111) interface (~ 475 mJ/m^2), is given in Fig. 6 as blue dashed lines. Note that this energy is close to, but lower than, the $\gamma_{Proj.}$ for h = 2 Å.

To isolate the effect of disconnections' Burgers vector, specific interface energies ($\gamma_{Spec.}$, Eqn. 4b) are calculated, which account for the area of the disconnections' facets in the total interfacial area. As shown in Fig. 6b, the specific interfacial energy fluctuates in the range of 470 mJ/m^2 ~ 490 mJ/m^2. The variation in $\gamma_{Spec.}$ shows qualitative correspondence with the nominal variation in Burgers vector as the height of disconnections gradually increases. Obvious drops of specific interface energy occur at the boundaries between Cases I, II and III, although it is interesting to note that within the domain of each case (Fig. 6b), the specific interface energy does not monotonically increase as the increase of the disconnection height within each case. Instead, small drops in specific interface energy exist before its eventual increase.

This phenomenon indicates that, even though the strain energy associated with a disconnection (first term on the right hand side of Eqn. 2a) may increase as the magnitude of its Burgers vector increases, the facet energy— $\gamma(\boldsymbol{l})$, a per unit area quantity—may decrease. Indeed, $\gamma(\boldsymbol{l})$ includes the contributions from both the core energies of the MDN and the energies of the coherent regions, both of which are influenced by the applied stress on the interface plane [266]. As was shown by Shao et al. [266], the flat interface energy may increase as much as 50 mJ/m^2, when a tensile stress of 8 GPa is applied normal to the interface. Indeed, a fully coherent Cu-Ni

interface, depending on its orientation, may incur a coherency stress of several GPa [289]. As the Burgers vector of the dipolar disconnections increases, stresses in the regions between the disconnections increases noticeably due to their coupling. This can be observed in Fig. 7(a-h), which shows the distribution of volumetric strain in both Cu and Ni on the x-y plane. Each letter designation of these sub-figures corresponds to a lettered data point in Fig. 6. It can also be readily shown that other components of strains behave in a similar manner. These varying strain fields as a function of the disconnection's Burgers vector modifies the energies of the {111} facets.

The impact of Burgers vector on the elastic strain energy of the disconnections can also be quantified. Figures 7(r-y) shows the distributions of average per atom excess potential energy on the x-y planes for models corresponding to the lettered data points in Fig. 6b (r-y in Fig. 7 correspond to points a-h in Fig. 6b). It is evident that the atoms on the interfacial facets exhibits potential energies that severely deviate from the respective cohesive energies of pure Cu and Ni under bulk conditions. This is due to the strong influence of the chemical interaction energy between Cu and Ni and the core energy of the MDN. To the first order of approximation, the strain energy of a bicrystal due to the disconnections can be quantified by integrating the per atom excess potential energy over the volume excluding interfacial regions. For convenience, the interface region is numerically defined as an ensemble of atoms near/at the interface plane that possess an excess potential energy of $\left|E_{Ex.}^{i}\right| > 0.0006$ eV, where *i* stands for the species of the atom. The total excess energy per bicrystal model divided by the length of the model in z direction would yield an energy per unit length, $\frac{E_{Tot.}}{L}$, which correlates with the strain energy per unit length of disconnection, $\frac{E_{disc.}}{L}$.

For convenience, the former quantity, $\frac{E_{Tot.}}{L}$, for each atomistic model has been normalized by the line energy of a screw type Shockley partial ($\frac{E_{SP}}{L}$) in a hypothetical FCC crystal and presented in Figs. 8a. The hypothetical crystal has a lattice constant and elastic moduli identical to the average between those of Cu and Ni, such that $\bar{a}$ = 3.57 Å and $\bar{\mu}$ = 62 GPa. The lower and upper bounds of integration have been chosen as r = 1 nm and R = 16 nm, the latter corresponds to the spacing of the disconnections in the present work. Lettered data points correspond to those identified in Fig. 6b. It is noted from Fig. 8a that the energy minima do not reside at zero level. This is likely due to the non-vanishing stress-field near a semi-coherent interface. The total defect strain energy per unit length, $\frac{E_{Tot.}}{L}$, can also be plotted against the nominal magnitude of disconnections' Burgers vector (Fig. 8b). Treating this non-vanishing energy as a constant ($\frac{E_0}{L}$), the $\frac{E_{Tot.}}{L}$ vs. $|\mathbf{b}|$ curves in Case I to III can be fitted to quadratic functions of the form

$$\frac{E_{Tot.}}{L} = \frac{E_0}{L} + 2km\bar{\mu}|\boldsymbol{b}|^2 + \mathcal{O}\left({E_{disc.}}^2\right) \quad (5)$$

where m, with a typical form of $\frac{\ln R/r}{4\pi}$ or $\frac{\ln R/r}{4\pi(1-\nu)}$, is a constant that accounts for the character and cylindrical integration boundaries of the disconnection, the second term is essentially identical to Eqn. 2b. $\mathcal{O}\left({E_{disc.}}^2\right)$ stands for the interaction energy of between the disconnections, which is neglected to the first order of approximation. The quadratic fits are also shown in Fig. 8b. The fit parameters, normalized by $\frac{E_{SP}}{L}$ have been provided in Table 1. The fit returns a factor $2km\bar{\mu}/\frac{E_{SP}}{L}$ ≈ 0.8, which leads to a $E_{disc.}/E_{SP}$ = 0.9 at $|\mathbf{b}|$ = 1.46 Å (magnitude of the Burgers vector of a Shockley partial in the aforementioned hypothetical crystal). This indicates that the k factor in Eqn. 2b and 5 has a near-identity value.

5.5.3. Mechanical response of FCC (111) semi-coherent interfaces with disconnections

Two different types of loading conditions, i.e. normal-to-interface compression ($-\sigma_{yy}$) and parallel-to-interface shear ($\sigma_{yx} > 0$ or $\sigma_{yx} < 0$), were applied to the bicrystal models to investigate the interfaces' response, in terms of both strength and unit deformation mechanisms. Under both loading conditions, the interfaces always first emit dislocations into the Cu layer. This is ascribed to the lower energy barrier associated with the nucleation/emission process, which is due to the lower elastic constants—therefore lower dislocation line energy—and the lower stacking fault energy in Cu. In addition, the dislocations almost always (aside from a few models with very small disconnection heights) emit from the edges of the disconnections. Depending on the loading condition, loading direction, and the dislocation structure of the disconnections, the mechanisms via which the dislocations nucleate and emit vary. In addition, correspondence between the disconnection's structure, Burgers vector and interfacial strength exist.

5.5.4. Dislocation nucleation/emission from interface under compression

Under compressive loading ($-\sigma_{yy}$), the interfaces containing Case I disconnections may nucleate/emit dislocations via two mechanisms depending on the disconnection height (h). For smaller disconnection heights, i.e. $h < 25$ Å, the dislocations nucleate from the condensed dislocation nodes on the horizontal portions of the interface. This mechanism is same as that at flat interface, which has been documented previously [290].

At $h > 25$ Å, another mechanism is activated (Fig. 9). The step-by-step process is shown in Figs. 9a-e, which is viewing the (c) plane along the vector $\mathbf{v}//C\gamma//[\bar{1}\bar{1}1]$. Detailed disregistry analyses have been performed (shown in the Suppl. Mater. Section S3) to characterize the dislocation structures during the process, which are shown in Figs. 9f-j, which correspond to the sequence shown in Figs. 9a-e. The blue lines with directions in this figure and the following

figures denote the Shockley partial dislocation lines; red segments are the stair-rod dislocations identified in Figs. 4 and 5; while blue segments denote the complex dislocation junctions formed at the edges of disconnections during the deformation processes. The compression along z-direction, has a resolved shear stress (RSS) along the slip systems (c)-γA and (c)-Bγ, with a Schmidt factor of 0.157. Under this RSS, dislocations γA and Bγ bow out and extend the width of the stacking faults (green arrows in Fig. 9h).

Continued bowing extends the dislocation half loops beyond the interface and into the Cu crystal. At the location of one stair-rod dislocation, a dislocation loop Dγ nucleates inside of an existing stacking fault region (Fig. 9g). Immediately after its nucleation, dislocation loop Dγ expands, which is followed by the extension of the stair-rod dislocation associated with the creation of two partials Bγ and γA (Fig. 9h). A six-fold dislocation node (red dot in Fig. 9i) has therefore been formed, which is identical to dislocation nodes on a generalized FCC (111) semicoherent interface, barring differences in the characters of the surrounding dislocations due to their directions. Nucleation of small dislocation loops near dislocation junctions and the their subsequent growth has been well documented [253,255], and were ascribed to the relieve of the concentrated core energies. Subsequently, the partials γA with opposite lines directions annihilate (green, double headed arrow in Fig. 9h), a more complex dislocation junction structure therefore forms (green line segment in Fig. 9i). The approaching loops of Dγ and γA inside Cu can therefore annihilate (Fig. 9i). As a result, a perfect dislocation DA, dissociated into partials γA and Dγ is emitted into the Cu layer. A new type of dislocation pattern, nearly identical to that of the Case II disconnection, is formed in the facet plane.

This operation emits a mixed dislocation (can be both DA or DB) with a strong edge character into Cu. Effectively, this creates an extra $(111)_{Cu}$ plane on the positive side of the (c)

plane, along –**v** direction as shown in Fig. 9. Concomitantly, an extra half $(111)_{Ni}$ plane is created on the Ni sided of the facet. Note that this is a strictly mass-conservative operation by dislocation's nucleation and glide, and no diffusion is involved. Continued compressive loading eventually leads to the emission of a dislocation, with opposite line sense to Dγ and γA shown in Fig. 9j, into Ni. Note that under this mechanism, only Disconnection 1 is active, as the operation of Disconnection 2 would first emit a dislocation to Ni, due to the crystal symmetry of FCC, which is energetically less favored.

Cases II and III facets respond differently to compressive loading as compared to Case I. A typical process is shown in Fig. 10. The step-by-step snapshots are provided in Fig. 10a-c, which show the atomic plane on which the facet of a disconnection exist. Of interest is the Disconnection 2, as the contained dislocations tend to migrate towards the Cu side due to the RSS under the applied compressive stress. Plan views in Fig. 10 are along the –**v** direction, which views the triangle ABD from inside of the TT, the ABD plane is therefore designated (–c). Dislocation structures here have also been characterized by disregistry analyses. As shown in Figs. 10e-f, the emission process involves the combination of dislocation nodes with stair-rod dislocations, dissociation of dislocations from stair rod dislocations, as well as annihilation between dislocation loops. The net result of such a process is exactly the opposite of the process identified in Fig. 9: it increases the coherency along the step vector direction.

5.5.5. Dislocation nucleation/emission from interface under shear loading

Depending on the shear loading direction, i.e. $\sigma_{yx} > 0$ or $\sigma_{yx} < 0$, the deformation mechanism exhibited by the interface varies. Similar to the interfaces' mechanical response to compression, under shear, dislocations emit into Cu from the edges of the disconnections. Therefore, under both shear directions, only the top-most facet of interface is active, as the

activation of the bottom facet of interface would emit dislocations into Ni, which is not energetically favored.

When $\sigma_{yx} > 0$, the MDN on the facet of the interface migrate towards the –x direction, which is also the eventual direction along which dislocations are emitted into Cu. The emitted dislocations are Shockley partials of edge type. The process is depicted in Fig. 11. Snapshots of the atomic plane on which the top facet of interface reside are shown in plan-view (Figs. 11a-c). The viewing direction is along –y. Dislocation structures, as characterized by disregistry analyses, have been shown in Figs. 11d-f. Details on the diregistry analyses are shown in the Suppl. Mater. Section 3. On the facet of interface, MDN with pure edge dislocations exist. The Burgers vectors of all the partials are either parallel to or have a significant component in the shear loading direction. Under this σ_{yx}, Cδ partials are driven along the –x direction. While the Bδ and δA partials are driven into each other in such a way that the area of the stacking faults is reduced. The net force felt by each partial dislocation is schematically marked in Fig. 11d using green arrows. Under these forces, the Cδ partial moves along Cδ direction and the dislocation nodes (red dots in Fig. 11d) moves and reacts with the stair-rod dislocations (short red line segments in Fig. 11d). The resulting dislocation junction then re-dissociate into a greek-greek/roman-roman type stair-rod and the partial Cδ (Fig. 11e). At a stress level that is sufficiently high, the partial Cδ fully emit into Cu, leaving a stacking fault behind (Fig. 11f). In principle, this emission process only needs to overcome an energy barrier set forth by the additional stacking fault energy, as well as the changes dislocation line energy due to changes in the elastic moduli from interface to Cu. The resolved shear stress required for this process is expected to be lower than the mechanisms depicted by Figs. 9 and 10, where significant dislocation bowing is also required.

When $\sigma_{yx} < 0$, the dislocation emission mechanism is identical to that of the disconnection 2 under compression, which is depicted in Fig. 10. The step-by-step process shown by the snap shots of the top interface plane is given in Fig. 12. The plan views (Fig. 12a-c) are along the viewing direction of –y. Corresponding dislocation structures have been characterized by disregistry analyses and have been presented in Fig. 12d-f. As seen, the main distinction of the current mechanism from the one active when $\sigma_{yx} > 0$ is the emission of a perfect dislocation, instead of a single Shockley partial. The emitted trailing partial dislocation, Cδ, feels a much stronger force (twice as strong) due to the applied stress compared with the leading partial, Bδ, since the former's Burgers vector is perfectly aligned with the loading direction. The emission of Bδ is therefore due to its resultant force from the applied shear stress as well as the interaction force from partial Cδ. Similar principles also apply for the mechanisms identified for the facets of disconnections under compression (Figs. 9 and 10). The critical stress for dislocation emission under this mechanism is also expected to be significantly higher than that for the case when $\sigma_{yx} > 0$, as the energy barrier of emitting one perfect dislocation is higher than that of only one partial.

5.5.6. Strengths of the faceted interfaces under compression and shear

Under compression, the distinct dislocation emission mechanism of Case I disconnection, suggests that the emission process is controlled by the initial bowing of partial dislocations that were initially parallel to the step vectors (schematically shown in Fig. 9f). Therefore, compressive strength[5] of the interfaces are inversely related to the magnitude of the step vector $|\boldsymbol{l}|$, and thus to the disconnection height h. Under isotropic assumptions, the critical compressive stress to bow these partial dislocations to radius $|\boldsymbol{l}|/2$, or $h/2\sin(70.5°)$ is

[5] Critical stress for the emission of the first dislocation(s).

$$\sigma_{comp} = \sigma_0 + \frac{m\bar{\mu}\bar{b}}{|l|} = \sigma_0 + \frac{n\bar{\mu}\bar{b}}{h} \quad (6)$$

where m and n are constants accounting for the line tension of the dislocations under various radii of curvature, Schmidt factor, relation between $|\boldsymbol{l}|/2$ and $h/2$, etc., $\bar{b}$ is the effective magnitude of Burgers vectors of interfacial partial dislocations, and σ_0 is a constant stress corresponding to the compressive strength of a hypothetical Case I disconnection with $h \to \infty$. As shown in Fig. 13, the compressive strength indeed obeys Eqn. 6 in Case I. A curve fit with σ_0 = 3.61 GPa, n =9.03, $\bar{\mu}$ = 62 GPa and $\bar{b}$ = 1.46 Å has been provided in Fig. 13 as the dash-dotted line. Under very small values of h, the required σ_{comp} is so high that another dislocation nucleation mechanism from dislocation nodes of the MDN is activated [290]. This mechanism, which corresponds to a compressive strength of ~10 GPa, deviates the measured compressive strength from the inverse power law (Fig. 13). Dislocation emission for Cases II and III do not require the initially confined bowing of partial dislocations as a function of disconnection height, which is reflected in Fig. 13 as the flat features within the Cases II and III.

On the other hand, characteristic strength levels seem to exist for each case. For Case I, at its minimum, the strength of the interface is ~5 GPa; for Case II, it is relatively constant ~3.8 GPa; for Case III, it is ~ 2.8 GPa. The compressive strength appears to drop significantly at the boundaries between cases. This behavior is ascribed to the different dislocation structures on the facets of the disconnections. As shown in Fig. 4, going from Case I to III, the total number of dislocations with line directions parallel/antiparallel to AB direction increases. Under applied compression, the RSS drives the networks of dislocations towards one edge of facets, as noted in Figs. 10, 11 and 12. Similar to a scenario of dislocations' pile-up at grain boundaries, dislocations on the facets also piles up at the edges of disconnections. The mechanical advantage provided by

the dislocation pile-ups essentially governs the strength of the interfaces for Cases II and III. It can further be inferred that with additional increase in the case number and additional dislocations added to the facets, compressive strength would further reduce.

Under shear loading, the strength of the interfaces is substantially smaller than that under compression. This, in part, is due to the striking difference in the maximum Schmidt factor between the two loading conditions, i.e. $S_{\text{Shear}} = 1.00$ vs. $S_{\text{Comp.}} = 0.33$. This can be verified by comparing the compressive strength for Case III, ~2.8 GPa, and the shear strength when $\sigma_{yx} < 0$, ~ 1 GPa. This comparison is meaningful as the dislocation structures on the facets of disconnections are identical to the ones on the facets of interface. The interfacial shear strengths under both loading directions rapidly increases as the Case I disconnection height increases. At the onset of Case II, substantial drops of shear strength (0.25 GPa for $\sigma_{yx} < 0$ and 0.37 GPa for $\sigma_{yx} > 0$) occur. After the initial drop, subsequent trends of variations in shear strengths are less discernable, if any. In addition, as predicted in Section 3.3.2, the overall shear strength of the interface under $\sigma_{yx} < 0$ is greater than under $\sigma_{yx} > 0$.

The initial increase, as a function of the disconnection height, in the interface shear strength demonstrated by Case I disconnections can be ascribed to the existence of the residual stresses as variation in the Burgers vectors in the disconnections (Fig. 7i-p shows the variation in the residual shear strains). These residual strains can be as high as 0.0075 near the facets of the disconnection, which, estimated by Cu's shear modulus of 48 GPa, correspond to a residual shear stress of $\sigma_{yx} = \pm 0.36$ GPa. The emission of dislocations would need to overcome this stress inhomogeneity, therefore, for Case I disconnections, the interfacial shear strength increases with the increase of disconnection height and Burgers vector (see the red hollow triangles and red filled squares in Fig. 13). At the boundary between Cases I and II, the stress inhomogeneity was removed (compare

Figs. 7k and l), this strengthening effect due to the build-up of Burgers vector in the disconnection was removed. Note that the stresses drop by 0.2~0.4 GPa. In addition, in Cases II and III, networks of MDNs form on the facets of disconnections, and, under the RSS due to the applied shear loading, are forced to the edges at which emissions of dislocations occur. In these cases, the interaction between the dislocations on the facets of disconnections and those on the facets of interface cannot be overlooked. In fact, as explained in the Suppl. Mater. Section S4 with help of Nabarro's interaction equations [47,48], the γD type of edge partials on the facet planes tend to facilitate the emission process. Under the influence of this dislocation-dislocation interaction, the strengthening effect due to the stress inhomogeneity breaks down and the strength variation after the initial drop becomes less significant with increasing disconnection height.

5.5. Discussion

This work is concerned with the interfacial facets. Using the concept of super disconnections, this work sheds light on structure, energy, and mechanical properties of interfacial facets. While generality was maintained throughout the analyses of our results, the applicability and limitations of our findings need to be formally discussed.

5.5.1. Relevance between modeled geometries with reality

First, it is apparent that the terraced interface considered in this work resemble a "step-terrace-step" configuration rather than the well-known "hill-and-valley" geometry (see Fig. 2). This model construct was specifically adopted so that the various effects of facet size can be captured without substantially changing the size of the simulation box. Indeed, this construct insures that the asymptotic normal of the interface is [111]. When the size of the $(\bar{1}\bar{1}1)$ and $(11\bar{1})$ facets are varied, the simulation box would only vary in the y dimension. In contrast, if the classical "hill-and-valley geometry" was adopted, the asymptotic interface normal would deviate

from [111]. Two complexities would result: (1) a periodic box with admissible strains—in x and z direction may be too large, (2) variation of facet size would result in dimensional change, not only in y direction (to eliminate boundary effects), but also in the x direction (if the step vectors fall within the x-y plane). While this work only considered the size effect on the inclined facets (Disconnections 1 and 2 shown in Fig. 2), a similar size effect on the "horizontal" facets of the interface also exists. In fact, one could easily show that the underlying mechanism for the size effect herein shares the same root as the one we have discussed in our original submission. Due to this very reason, we intentionally neglected this length scale effect. The choice of the x-dimension of our simulation cell ensures that the two "horizontal" facets have near-zero Burgers vectors, when treated as disconnections.

Second, the facets modeled in this work are of the special, {111} type. Other low-index facets, such as the {100} and {110} types have not been investigated in this work. A generalized interface between two FCC crystals may contain facets of the {100} {110} and {111} type. Also, terraced interfaces between two dissimilar crystals, such FCC-BCC, BCC-HCP, etc., have not been considered. Due to our choice of the facets, the step vectors on both adjoining surfaces are parallel/anti-parallel to the {112} direction. The resulting possible Burgers vectors of the disconnections, therefore, are also parallel/anti-parallel to the step vectors. This choice of special case of interfacial super disconnections simplified the analyses involved in this work. However, we expect that the principles that have been discovered in this work, i.e. the effects of size, coherency, dislocation structure, and Burgers vector on a facet, would be generally applicable to a broad range of facet types. In addition, this work puts forward a methodology on the analyses of more complex facets, which involved the disclination characters, i.e. with out-of-facet Burgers vectors.

5.5.2. Original understanding gained towards the structural, energetic and mechanical properties of terraced interfaces

This work demonstrates that the structures of the interfacial disconnections are composed of basic building blocks of a regular flat interface, namely MDN, coherent regions, and dislocation nodes. The edges of the disconnections comprise stair-rod dislocations of the acute and obtuse types, which connects the stacking faults on two adjoining facet planes. The coherent regions on two connecting facet planes join by the coherent step corners. Although these coherent corners are associated with excess energies, the formal treatment of which is beyond the scope of this work. Instead, this work sums this energy contribution with the interfaces' chemical energy, core energy and near-field coherency energy and explicitly evaluated the effect of the Burgers vector of disconnections on the energy-structure-property correlation. It was shown that these inherent energy components dominate the specific energy ($\gamma_{Spec.}$) of an interface, with relatively small influenced from the disconnection's Burgers vector. Nonetheless, it was also shown in this work that the Burgers vector contributes to the total energy of the disconnections in a manner similar to that of a dislocation. A clear quadratic relation between the excess interfacial strain energy and the Burgers vector of a disconnection can be seen.

Mechanisms by which dislocations are emitted from interfaces have also been carefully analyzed. These mechanisms were found to depend on not only the loading conditions, but also on the specific dislocation structure of the super disconnections. For instance, emission of dislocations from Case I disconnections under compression requires the lateral bowing of the partial interfacial dislocations and a subsequent nucleation of a dislocation loop with Burgers vector along the step vector of the disconnection. Emission of dislocations from Case II disconnections under compression requires the combination of dislocation nodes with stair-rod

dislocations, forming complex junctions, and the subsequent dissociation of dislocations from said junctions. Under compressive loading, the applied compressive state of stress is resolved into the facet planes as shear stress, which activates the motion of dislocations therein.

As the dislocation structure of the facets of disconnections can be similar to facets of the interface, commonalities also exist in the dislocation emission mechanism between the flat interfaces and the facets. Under shear loading, the specific emission mechanisms are dependent on the loading direction with respect to the disconnections. Two mechanisms can be active. The first mechanism is identical to the one active for Case II disconnections under compression. Both mechanisms involve the formation of junctions between dislocation nodes and stair-rod dislocations, and the subsequent dissociation of these junctions.

It is important to note that the mass-conserving dislocation operations to emit a dislocation are non-unique, although the aforementioned critical events, namely dislocation bowing, combination/dissociation between a dislocation node with stair-rod dislocations, are necessary. For instance, in the Supplemental Materials Section S5, we have provided several possible alternative mechanisms to the ones identified for dislocation emission from facets under compression (Fig. 9). It is apparent that these mechanisms can operate at a much smaller spatial period and is therefore permissible in a smaller simulation cell. Since these mechanisms correspond to a much smaller bowing radius for a given dislocation, the corresponding emission stress is likely to be higher, vice versa. Therefore, caution must be given to the obtained stress values as they may be very much dependent on the size of the simulation cell.

The obtained shear and compressive strengths of the faceted interface correspond to the first event of dislocations' emission, which were shown to strongly depend on the dislocation structure and Burgers vector of the disconnections. It was found that the compressive strength for

interfaces with Case I disconnections is inversely related to the height—therefore Burgers vector—of the disconnections. With each increase in the case number, which is associated in the increase in the net Burgers vector in the MDN on the facets, the compressive strength exhibits a clear reduction. Pile-up of MDN at the edge of facets was found to have contributed to such behavior. The shear strength of interfaces with Case I disconnections was shown to increase with increasing height, which has been ascribed to the increasingly heterogeneous stress distribution associated with the increasing Burgers vector. For Cases II and III disconnections, the emission of dislocations under shear loading are influenced strongly by the presence of parallel dislocations on the neighboring facets. Therefore, the variation in strength is less significant.

In this work, although we report the shear and compressive strengths of the faceted interfaces, the precise values should not be directly compared with experiments. Indeed, the emission of dislocations are thermally activated [47,291] and strongly dependent on strain rate and temperature. In this work, we make no attempt to predict the precise critical stress for the emission of dislocations under compression and shear. Instead, we emphasize the lateral comparison on the impact of dislocations, with their height, dislocation structure and Burgers vector as variables, on the associated strength of interfaces.

5.5.3. Technical implications of the present work

Due to the presence of MDNs, typical semi-coherent interfaces possess relatively low resistance to shear compared to the adjoining materials' theoretical shear strengths [255,283,292–296]. Typical shear strengths of interfaces are: around 0.5 GPa for Cu-Nb interfaces [255,292,293], 0.8 GPa if the Cu-Nb interfaces are Kr+ ion implanted [294], ~1.0 GPa for Mg-Nb interfaces [296], ~0.6 GPa for Cu-CrN interfaces [283]. The reduced shear strength increases the resistance to slip transmission across an interface by promoting core-spreading of an incoming

gliding dislocation [172,297,298], thereby increasing the strength of a material with interfaces engineered parallel or perpendicular to the loading direction [287,297,299]. However, such "weak interfaces" may reduce materials' overall strength if substantial resolve shear stress exists on the interface plane, which, in turn, may lead to strong mechanical anisotropy.

Terraced interfaces appear to improve an interface's overall resistance to shear, while not substantially raising the localized shear strength to maintain core-spreading of incoming dislocations. For instance, the ARB induced, mechanically stabilized Cu-Nb interfaces have been shown to contain the classic 'hill and valley' structure along a compact direction [254,265,300]. These interfaces have markedly higher peak shear strength (~1.8 GPa) as compared to their flat counter parts, when loaded perpendicular to the 'hills and valleys' [245]. Recent atomistic investigations on this matter suggest that, by engineering interfacial facets onto flat Cu-Nb interfaces, their shear resistance can be improved by 0.3~0.8 GPa [282]. These instances indicate that immense design space may exist for terraced semi-coherent interfaces with tailored shear characteristics by means of interfacial morphology control. Indeed, present findings suggest that, due to the variation of their Burgers vector, the preferred size of facets (at least those without a disclination character) on a terraced interface, might be quantized. In addition, the critical stress for dislocation emission from facets is strongly dependent on their size as well.

Besides the severe plastic deformation processes, such as ARB, routes for fabrication of materials with intentionally terraced interfaces may include thin film growth with/without surface roughening by ion bombardment. For instance, due to their lattice mismatch, growth of Ge thin film on a Si substrate has been shown to proceed via the Stranski-Krastanov growth mode, i.e. an initial, uniform growth for several atomic monolayers followed by growth of non-flat nano-hut clusters, then transitioning to large 3D islands [301]. Another example of similar nature is offered

by heteroepitaxial growth of AlN on Si(111) [302]. In this case, the large lattice mismatch led to growth of wurtzitic AlN in the Volmer-Weber island growth mode from the beginning, leading to a rough AlN top surface [303]. Subsequent growth of dissimilar materials on the rough surfaces then results in terraced interface. In addition to growth induced roughening, surface roughening by ion bombardment has long been known and studied, from ion induced pattern formation on amorphous surfaces [304] to ion induced roughening on surfaces of polycrystalline metal thin films [305]. Ion beam roughened surfaces offer growth templates on top of which new growth would adopt different surface morphologies [306], thereby offering an additional avenue for engineering interfaces with intentional roughness.

5.6. Conclusions

In this work, using atomistic simulations, the energetic, structural and mechanical characteristics of terraced Cu-Ni {111} semi-coherent interfaces have been systematically analyzed by treating the facets as interfacial super disconnections. It was found that the dislocation character of a facet periodically emerges and disappears as a function of its size, corresponding to the periodic changes in its specific energy. In addition, the dislocation structure on a facet also changes as its length increases, which is associated with the quantized changes in coherency along the step vectors. The mechanical response of a faceted interface has also been shown to greatly depend on the facet size, which is manifested by the dependence of dislocation emission mechanism on a facet's dislocation structure, and the dependence of dislocation emission stresses on both the facet's Burgers vector and dislocation structure.

Tables

Table 5. 1 Fit parameters for strain energies associated with terraces formed by a pair of disconnections, per unit length along z direction.

Fit parameters	$2k\alpha\bar{\mu}/\frac{E_{SP}}{L}$	$\frac{E_0}{L}/\frac{E_{SP}}{L}$
Case I	0.86	1.10
Case II	0.78	1.35
Case III	0.78	1.78

Figures

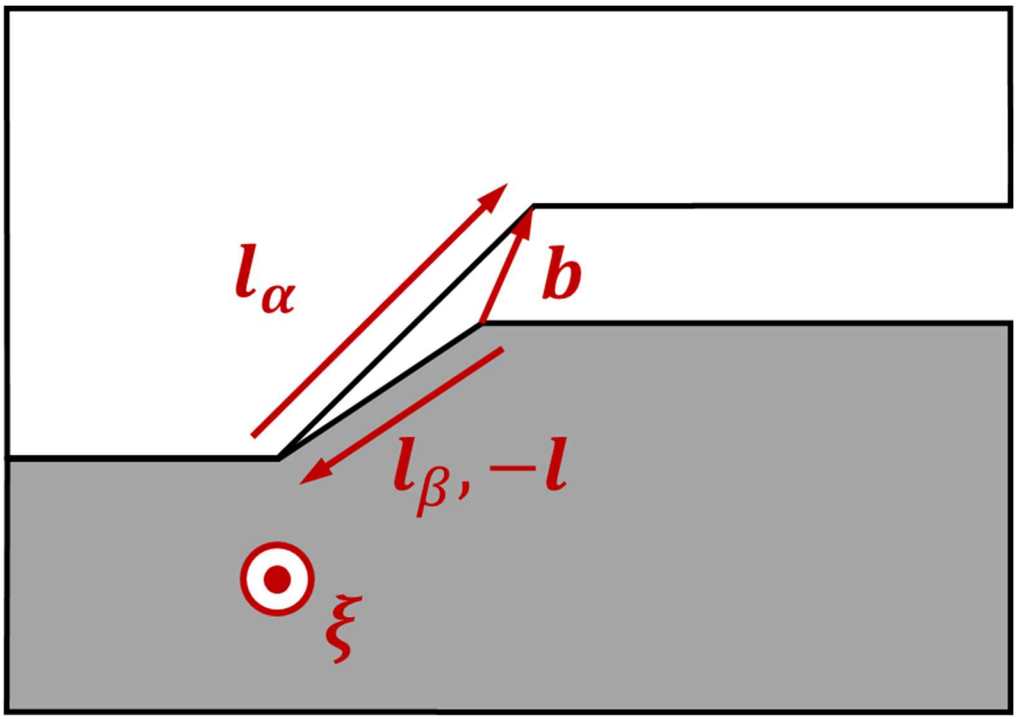

Figure 5. 1 A schematic illustration of an interfacial disconnection.

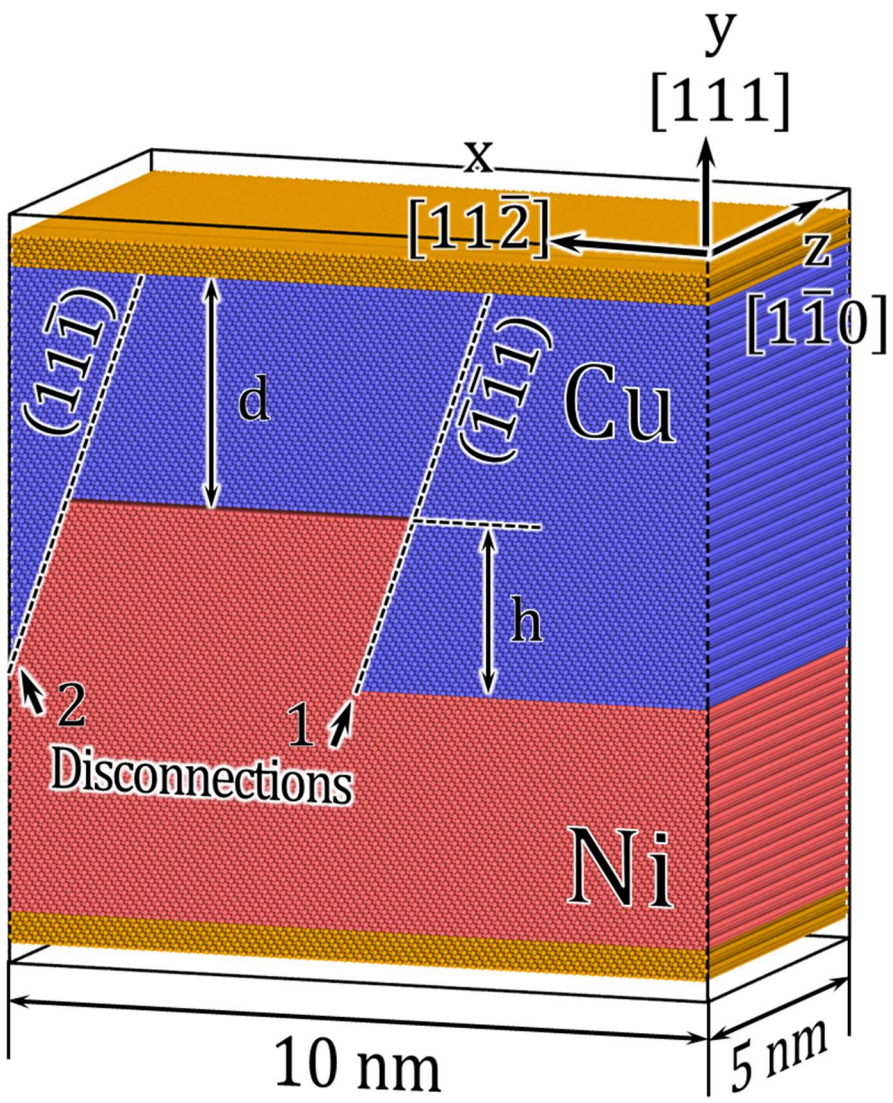

Figure 5. 2 Illustration of atomistic configurations of the interfacial models containing disconnections. Blue atoms are Cu, red atoms are Ni, while brown atoms are fixed during the MS/MD simulations.

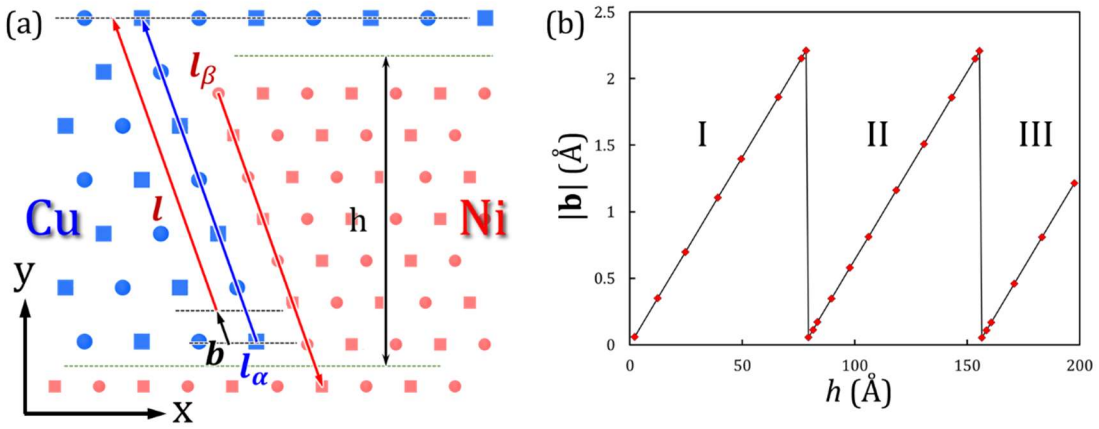

Figure 5. 3 Schematic illustration of the relation between $\boldsymbol{l}_\alpha$, $\boldsymbol{l}_\beta$, $\boldsymbol{l}$, $\boldsymbol{b}$ and h in the context of Disconnection 1 on a FCC (111) semi-coherent interface. Blue symbols denote Cu atoms, red symbols denote Ni atoms. Squares and circles denote the AB stacking of FCC in the <110> direction. Lattice mismatch between Cu and Ni has been exaggerated. Squares and circles denote A-B stacking on the (110) plane of an FCC crystal. (b) Relation between the nominal magnitude of the disconnection Burgers vector (|**b**|) and disconnection height (h).

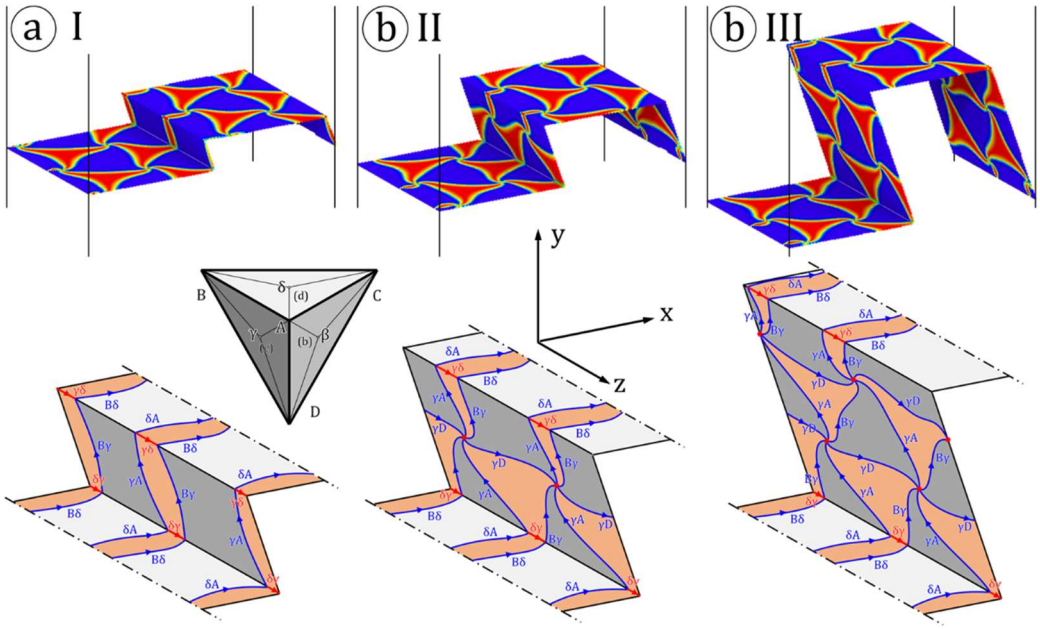

Figure 5. 4 Structures of the disconnections for Cases I, II and III noted in Fig. 3(b) have been shown in (a), (b) and (c), respectively. Top half of the figures shows the atoms on the interfaces colored by centro symmetry parameter (CSP), where red correspond to CSP = 6 and blue correspond to CSP = 0. Bottom half of the figures schematically shows the corresponding dislocations structures. Burgers vectors of the dislocations are given following the Thompson's convention, the Thompson's tetrahedron (TT) is also shown as an inset. The TT is oriented so that x//δC, y//Dδ and z//BA.

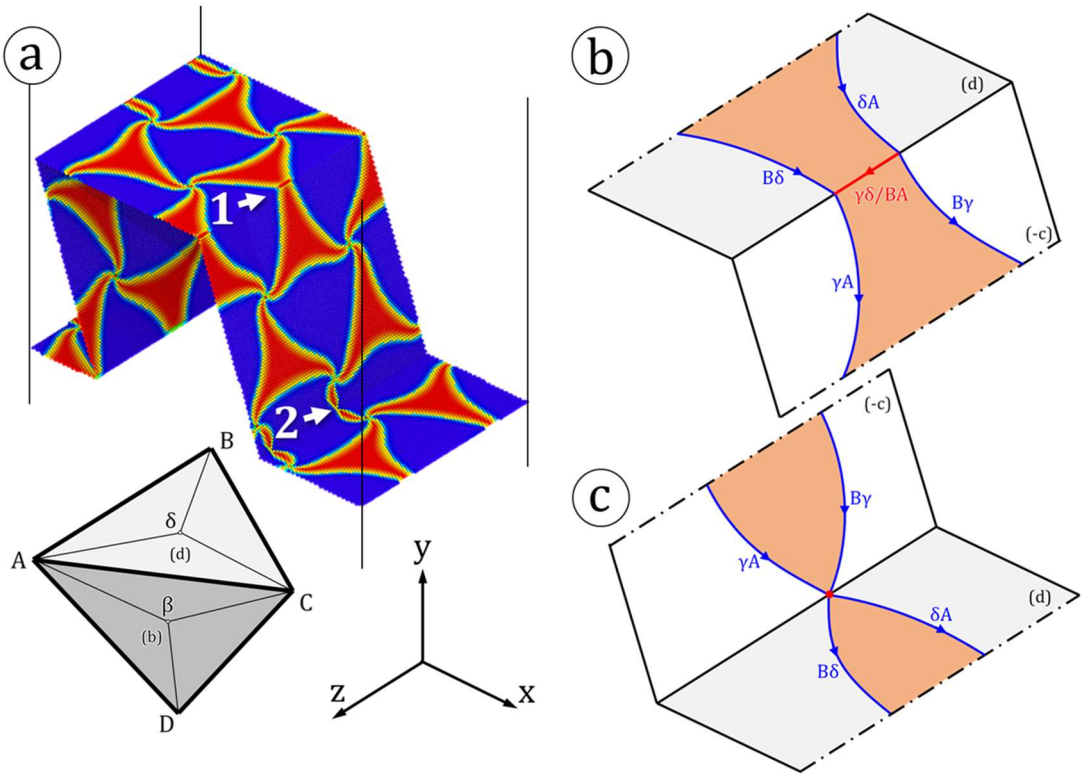

Figure 5. 5 Special types of dislocation junctions that "bend" dislocation and stacking faults from one plane to another, existing on the facet plane that forms an obtuse angle with the interface plane (a). This facet plane has been marked as (-c) plane to denote the viewing direction from inside of the TT (not visible). (b-c) show the detailed structures of these special-case junctions, marked by numbers 1 and 2, respectively.

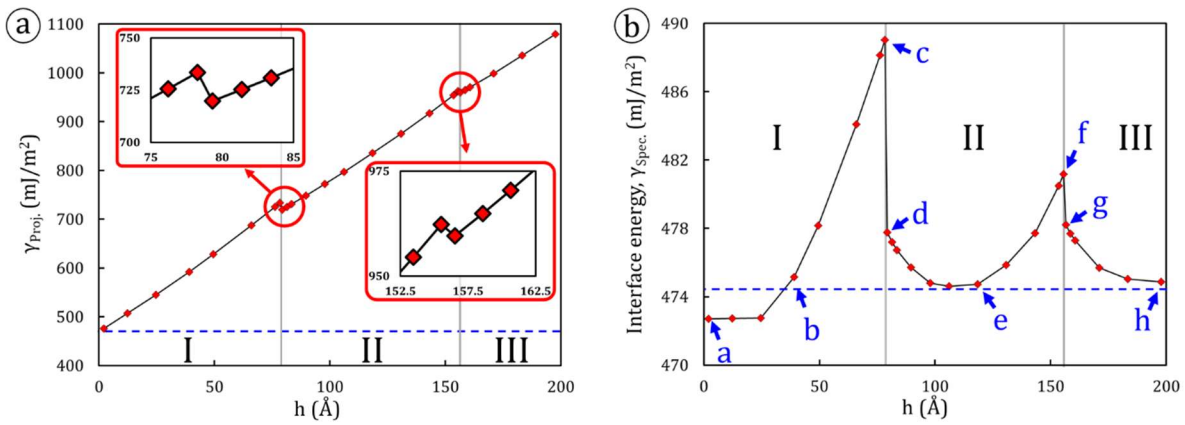

Figure 5. 6 Calculated interface energy, per unit area, based on two accounts: (a) excess energy of an interface divided by the projected interface area on the x-z plane, denoted as γProj., (b) excess energy of an interface divided by the total interface area, including the area of the facets, denoted as γSpec.. The blue horizontal dashed lines denote the case of the flat interface.

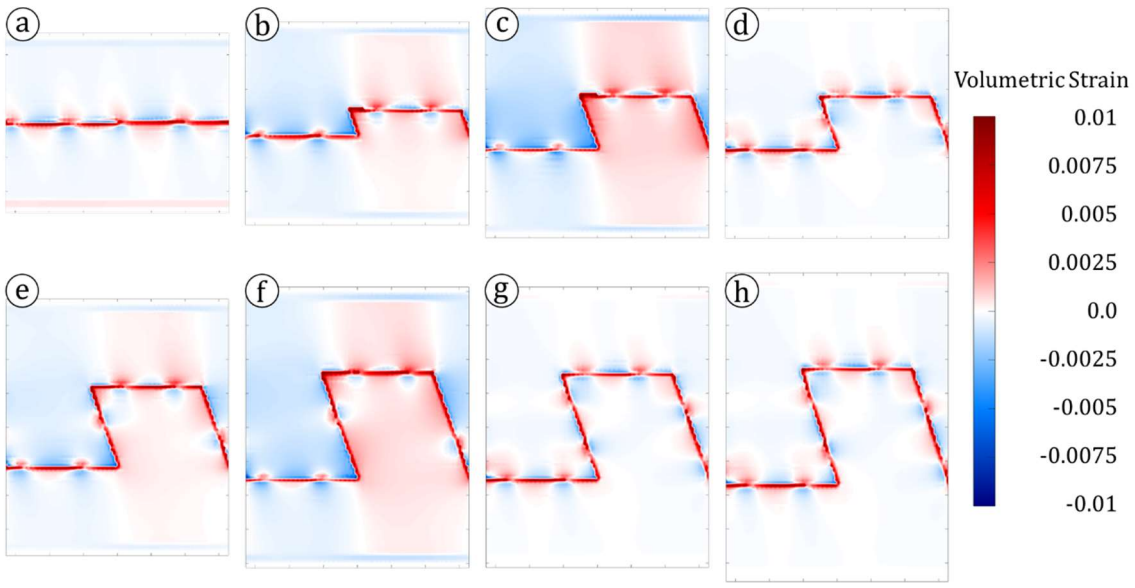

Figure 5. 7 (a-h) Distribution of volumetric strain in the bicrystal models in the x-y plane. Each data point represents the average value along the z direction. The subfigures, respectively, correspond to points *a* – *h* in Fig. 6b.

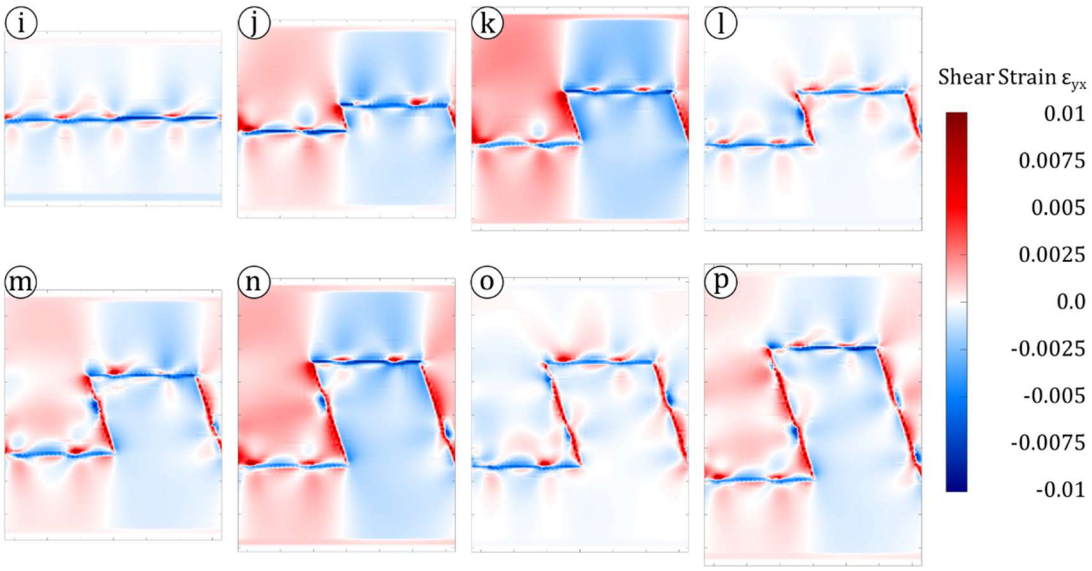

Figure 5. 8 (i-p) Distribution of shear strain in the bicrystal models in the x-y plane. Each data point represents the average value along the z direction. The subfigures, respectively, correspond to points a – h in Fig. 6b.

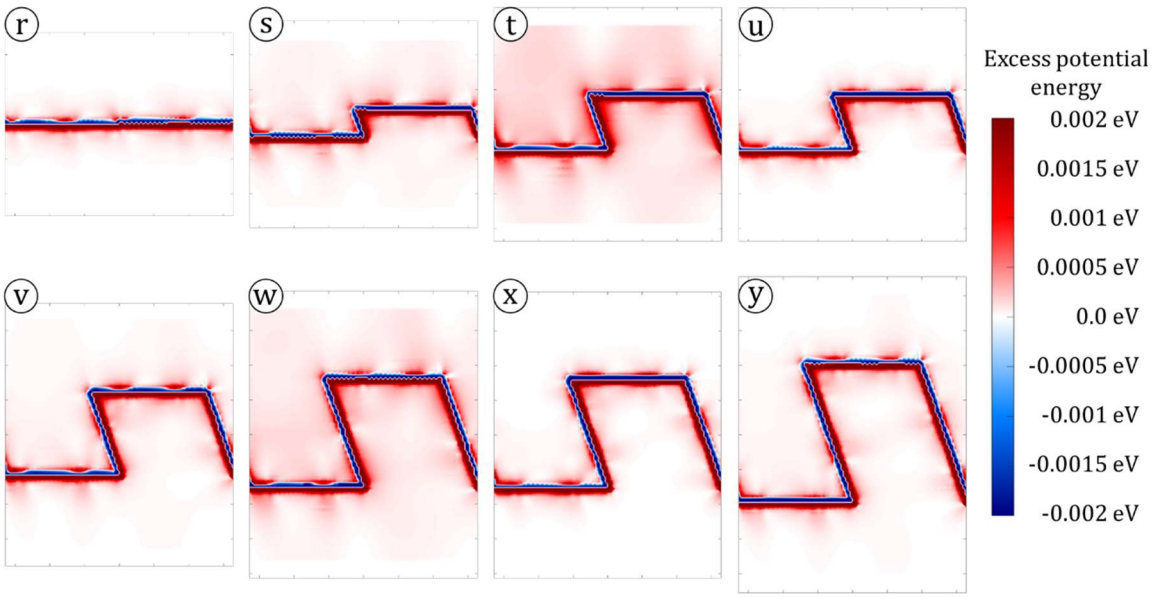

Figure 5. 9 (r-y) Distribution of per atom excess potential energy near interfaces, on the x-y plane, corresponding to the data points marked in Fig. 6b. Each data point corresponds to an average value along the z-direction. The subfigures, respectively, correspond to points *a* – *h* in Fig. 6b. The reference cohesive energies for Cu and Ni are 3.54 eV and 4.45 eV, respectively, according to Onat and Durukanoğlu [35].

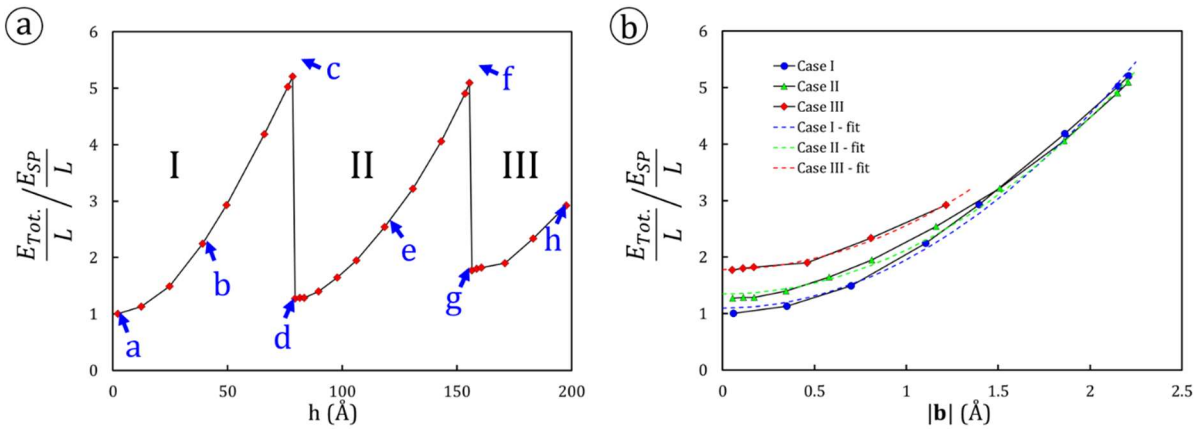

Figure 5. 10 Normalized total defect energy per unit length as a function of the disconnection height (a) and the magnitude of Burgers vector (b).

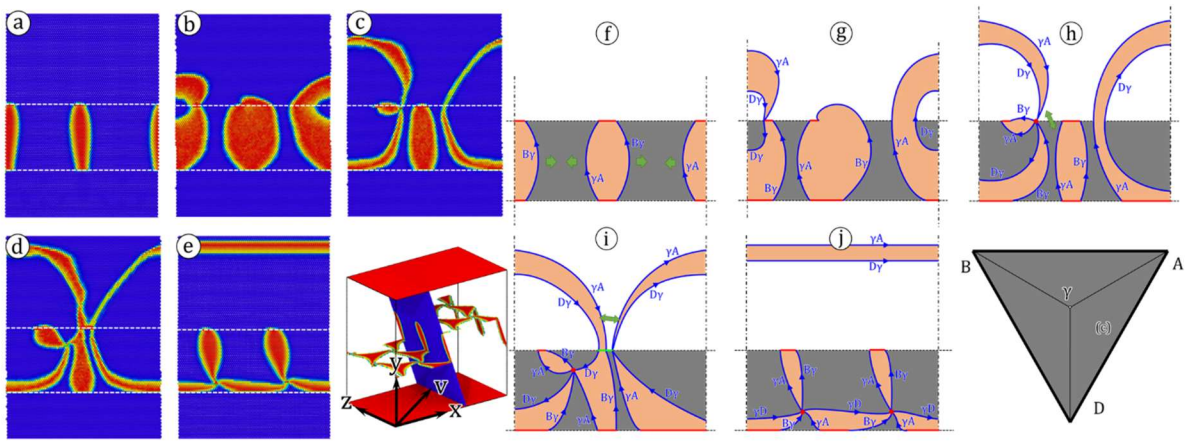

Figure 5. 11 Emission of lattice dislocation from the facets of a Case I disconnection under compressive loading. **(a-e):** Snapshots of atomic plane aligning with the facet at various stage of the emission process. The relative orientation of this plane with respect to the bilayer model is shown in the accompanying inset. Atoms are colored by the centro-symmetry parameter (CSP), with blue representing CSP = 0 and red representing CSP = 6. **(f-j):** Dislocation structure characterized by disregistry analyses. Orientation of all two-dimensional representations follows the (c) plane of the Thompson's tetrahedron shown on the bottom right. The dashed lines denote the location of disconnections' edges. The dash-dotted lines denotes the location of the periodic boundaries.

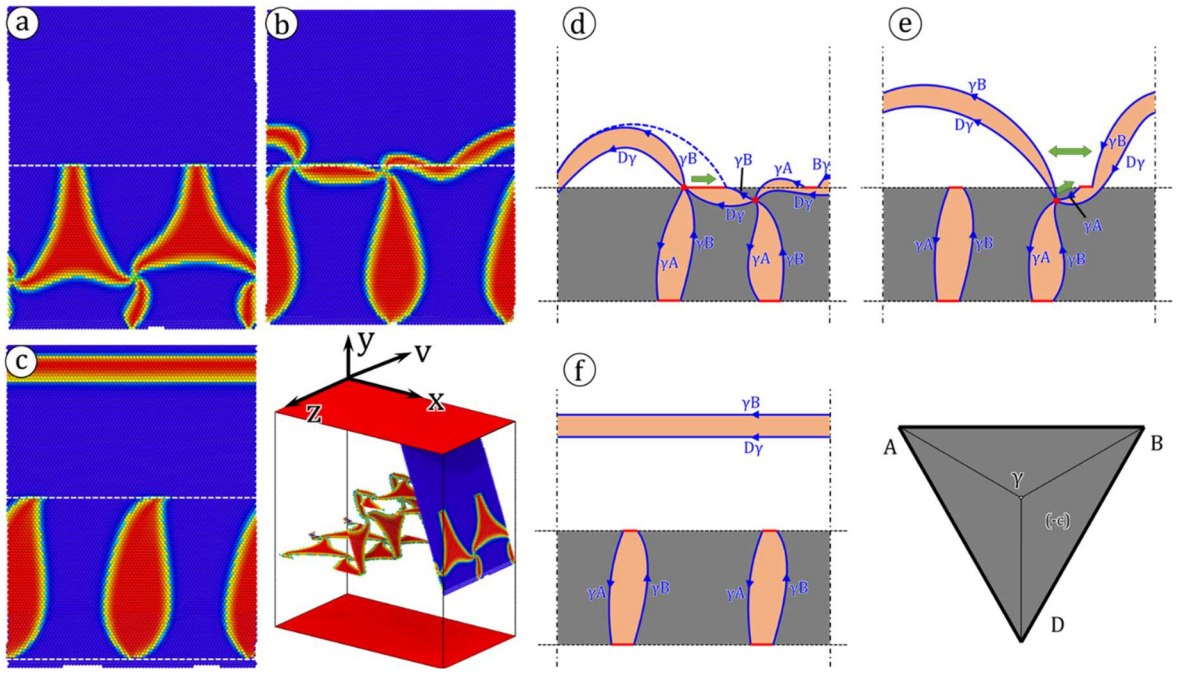

Figure 5. 12 Emission of lattice dislocation from the facets of a Case II disconnection under compressive loading. **(a-c):** Snapshots of atomic plane aligning with the facet at various stage of the emission process. The relative orientation of this plane with respect to the bilayer model is shown in the accompanying inset. Atoms are colored by the centro-symmetry parameter (CSP), with blue representing CSP = 0 and red representing CSP = 6. **(d-f):** Dislocation structure characterized by disregistry analyses. Orientation of all two-dimensional representations follows the (-c) plane of the Thompson's tetrahedron shown on the bottom right.

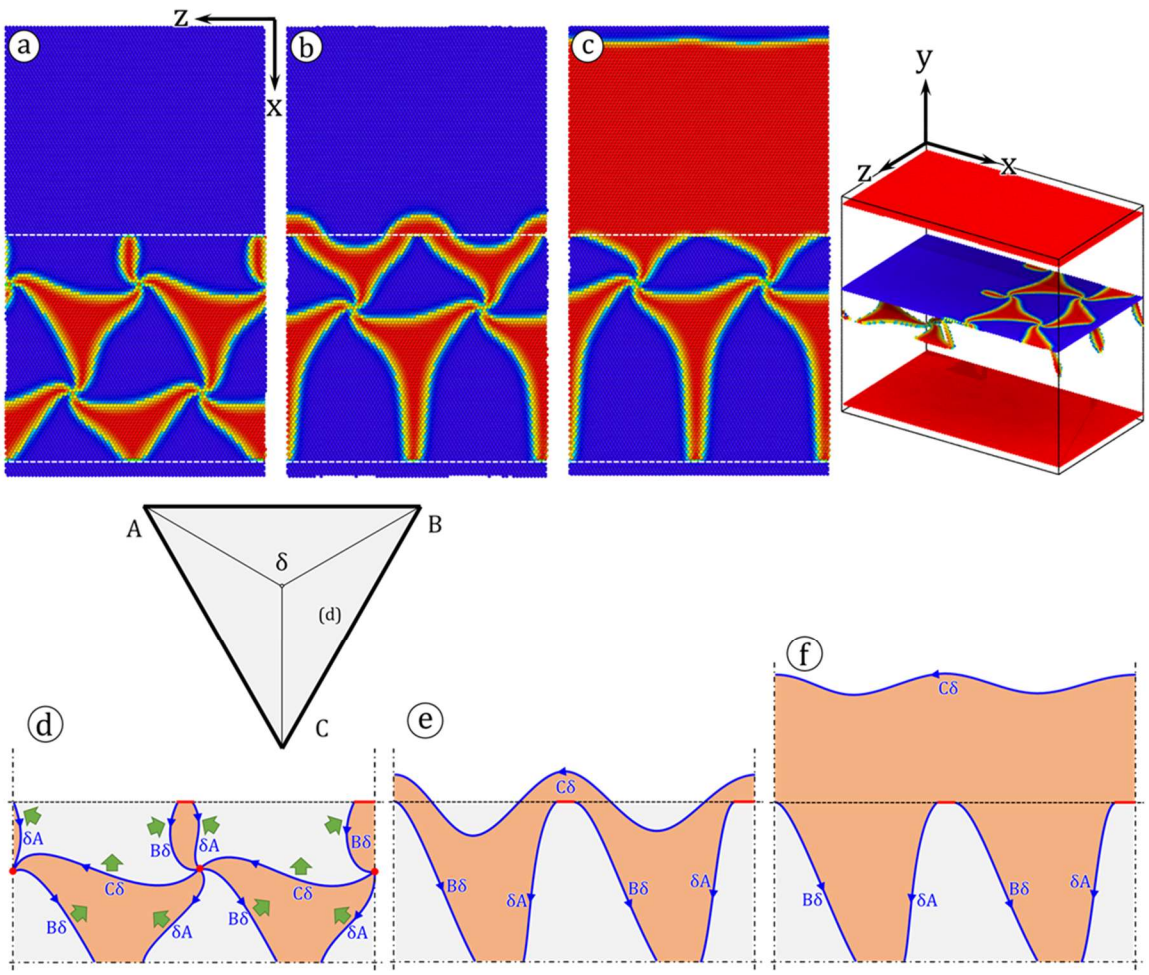

Figure 5. 13 Emission of lattice dislocation from the facet of a (111) interface under a shear stress $\sigma_{yx} > 0$. (a-c) show the snapshots of the atomic plane as indicated on the image on the top right. (d-f) show detailed dislocation structures characterized from disregistry analysis.

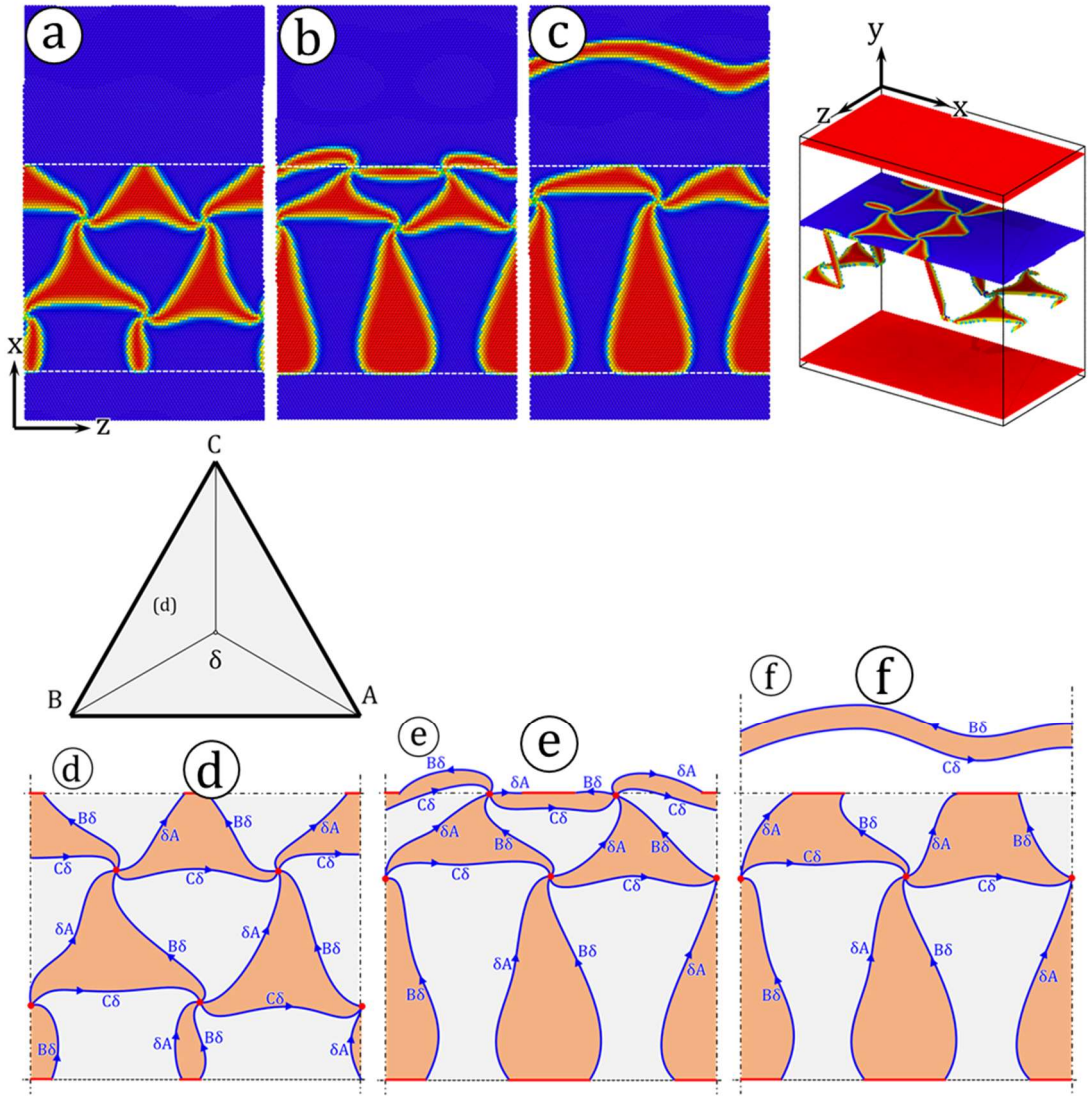

Figure 5. 14 Emission of lattice dislocation from the facets of a Case I disconnection under shear loading, where $\sigma_{yx} < 0$. The applied shear stress σ_{yx} is on the x-z plane and along the negative sense of the x axis. (a-c) show the snapshots of the atomic plane as indicated on the image on the right hand side. (d-f) show the dislocation structures characterized by disregistry analysis.

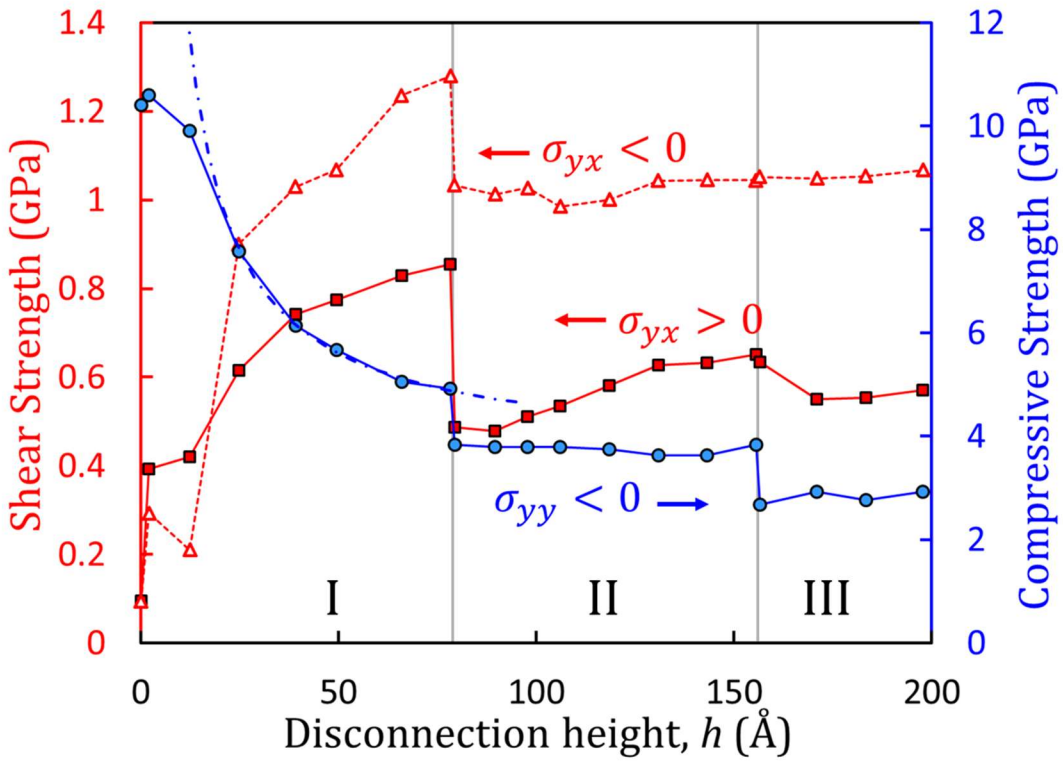

Figure 5. 15 Shear and compressive strengths of terraced interfaces as a function of the disconnection height, or facet size. These strengths are defined as the critical stress for the emission of the first lattice dislocation(s).

CHAPTER 6 MECHANICAL FAILURE OF CrN/Cu/CrN INTERFACIAL REGIONS UNDER TENSILE LOADING

6.1. Abstract

Quantitative assessment of the adhesion strength of ceramic hard coatings on substrates is a subject of great technological and scientific relevance, the achievement of which has proven difficult over the past two decades. Here we show that a micro-pillar tension testing protocol may serve as an effective method for this purpose, and demonstrate its effectiveness through a combination of micro tension testing and crystal plasticity finite element analyses (CPFEA). Tensile loading perpendicular to the interfaces, as well as accompanying CPFEA simulations, was conducted on CrN/Cu/CrN/Si micro-pillar tensile specimens fabricated from vapor phase deposited thin film sandwich structures. All tensile loading induced fracture were observed to occur within the Cu interlayer and near one Cu/CrN interface of the CrN/Cu/CrN sandwich structure. Observations, measurements, and discussions were made regarding the fracture surfaces, fracture stresses, and primary fracture mechanisms. Fracture surface examinations indicated ductile tensile fracture, induced by the formation of voids. It is shown that, due to the geometric constraint imposed by the ceramic layers in the current testing configuration, interlayer plasticity and the critical fracture stress display a strong dependence on the Cu interlayer thickness. It is postulated as a failure criterion that cooperation of deviatoric and hydrostatic stress components is needed to induce the nucleation and growth of voids. The relevance of the present work to the interfacial mechanical integrity of other metal/ceramic interfaces is discussed.

6.2. Introduction

Adhesives enjoy extensive industrial usage, including in the aerospace and automotive industries for metal-to-metal bonding [307]. For adhesive joints with macroscopic dimensions, protocols for testing the adhesive strength have been developed for both shear loading (e.g., see Ref. [308–310]) and tensile loading (e.g., see Ref. [311,312]).

In the past three decades, thin ceramic coatings with thicknesses of ~10 μm or below applied onto metallic substrates have become an important tool in the arsenal of surface engineering (e.g., see Ref. [313]). For example, coatings on machining tools lead to increased machining performance and tool life [314,315]; coatings on gears [316] and on bearings [317] lead to increased contact fatigue life. To promote adhesion of ceramic coatings to substrates, a metal interlayer is often deposited in between, forming a thin-ceramic-layer/metal-interlayer/substrate sandwich structure [8,10]. The interfacial strengths of such coating/interlayer/substrate sandwich structures far exceed the typical adhesive bond strength, usually below 100 MPa [307,318] . Existing macroscale testing protocols developed for adhesion of thin coatings to substrates make use of adhesives for test execution, e.g., in the stub-pull test (e.g., see Ref. [319]). Hence, they are typically unable to apply sufficiently high stresses to the ceramic-coating/metal-interlayer/substrate interfacial region to affect the desired interfacial mechanical failures for such strong interfaces.

At present, the laser spallation test offers an established, and arguably the best, experimental methodology for obtaining a quantitative measure of the tensile strengths of interfaces between thin films and substrates [320,321]. In the laser spallation test, an energetic laser beam is incident upon the substrate side of a substrate/thin-film assembly and sets up a compressive stress pulse in the substrate. The reflection of the compressive wave from the free

surface of the film generates tension at the substrate/film interface, and causes film spallation from the substrate when this interfacial tensile stress reaches a critical magnitude. While laser spallation tests have yielded quantitative measures of interfacial tensile strength [322], this testing methodology is associated with limitations due to specimen geometry (typically flat-wafer type specimens) and substrate absorption. Past laser spallation measurements on ceramic-layer/metal-adhesion-layer/substrate systems has also shown an apparent dependence of the interfacial strength on the metal interlayer thickness [16], the nature of such a dependence was not understood in detail.

The development of focused ion beam (FIB) micro/nano scale machining and in-situ instrumented micro/nano scale mechanical testing capabilities offers possibilities for new experimental approaches to obtaining quantitative data and direct observations regarding interfacial mechanical failures of coating/interlayer/substrate sandwich structures. In a previous paper [283], we described a new, in-situ, microscale mechanical testing protocol. By axially compressing micro-pillars made of ceramic/metal/substrate sandwich structures with the interfaces inclined at 45° with respect to the axial loading direction, shear failures were affected close to the metal/ceramic interface. Coupled with concurrent scanning electron microscopy (SEM) observations, and in combination with multiscale simulations, new insights into the nature of shear failure at metal/ceramic interfaces were gained.

In the present paper, we report on results of axial tensile loading, in situ an SEM, of micro-pillars fabricated from vapor deposited CrN/Cu/CrN/Si(001) thin film specimens, with the tension direction perpendicular to the interfaces. The combination of instrumented pillar tension testing, concurrent SEM observations, and additional post-test observations indicates that, under tensile loading, interfacial regions of CrN/Cu/CrN sandwich structures fail within the Cu interlayer close

to one Cu/CrN interface. There is clear evidence suggesting that the tensile loading produced plastic deformation within the Cu interlayer, and that the extent of this plastic deformation varied with the Cu interlayer thickness. Clear signs of dimpling were observed on the tensile fracture surfaces, which suggest that the nucleation, growth, and coalescence of voids are the responsible failure mechanisms. Correspondingly, the apparent tensile failure stress of the CrN/Cu/CrN interfacial region showed a significant dependence on the Cu interlayer thickness. In the laser spallation test, due of the nature of stress pulse propagation, the interfacial failure occurs under very high strain rate loading, $> 10^6$/sec [323]. To our knowledge, results shown in this paper offer the first example of quantitative testing on tensile failure of metal/ceramic interfacial regions in coating/substrate systems at low strain rates. To gain further mechanistic insights into the experimentally observed tensile fracture of CrN/Cu interfaces, grain-level crystal plasticity finite element analysis (CPFEA) simulations were performed to analyze the plastic deformation in the Cu interlayer. The experimentally observed size effects, i.e., the influence of the Cu interlayer thickness on plasticity within the interfacial region and on the tensile failure strength, were investigated in detail. Reviewing literature for the mechanisms governing ductile fracture, we further propose a physics-based failure criterion suitable to use in the CPFEA simulations. In the rest of this paper, section 2 describes the procedures for experimentation and simulations. Section 3 describes the results of experimentation and simulation, followed by a discussion. Section 4 gives a brief summary.

6.3. Experimentation and simulation procedures

6.3.1. Vapor phase deposition, structural characterization, micro-pillar fabrication, and instrumented pillar tension testing

Polycrystalline CrN and Cu layers were vapor deposited in an ultra-high-vacuum chamber with a base pressure < 3×10^{-9} Torr. Cleaned Si(001) substrates, 50.8 mm in diameter, were first subjected to an Ar (99.999%+) inductively coupled plasma (ICP) etch for ~5 min at –50 V bias. Two sputter guns were fitted with elemental Cr (99.95%) targets and one gun with elemental Cu (99.95%). Immediately following the ICP etch, a thin CrN buffer layer, ~55 nm in thickness, was first deposited, followed immediately by sequential deposition of a Cu interlayer and a CrN top layer. CrN deposition occurred in an Ar/N2 (99.999%+) mixture and Cu deposition occurred in pure Ar, both with ICP assist. All depositions occurred without intentional substrate heating, and resulted in a polycrystalline CrN buffer layer next to Si(001), followed by a polycrystalline Cu interlayer and a polycrystalline CrN top layer, ~6 μm in thickness. CrN/Cu/CrN/Si(001) specimens were made with varying Cu interlayer thicknesses, keeping thicknesses of the CrN buffer layer and top layer nominally the same. Additional details on vapor deposition procedures have been described previously [324,325].

Composition of CrN/Cu/CrN/Si(001) thin film specimens were characterized by X-ray photoelectron spectroscopy (XPS). A Kratos AXIS 165 system was used for the XPS measurements. Morphology and structure of CrN/Cu/CrN/Si(001) thin film specimens were characterized by combining X-ray diffraction (XRD), SEM, Ga^+ focused ion beam (FIB) sectioning, and transmission electron microscopy (TEM). A PANalytical Empyrean system with Cu Kα radiation was used for XRD measurements. Scanning imaging with electron- or ion-induced secondary electrons (SE/ISE) and Ga^+ FIB milling were carried out on an FEI Quanta3D Dual-Beam FEG instrument, which also housed an EDAX X-ray energy dispersive spectroscopy (EDS) system. A JEOL JEM2011 microscope operated at 200 kV was used for TEM examinations.

Cylindrical micro-pillars were fabricated from CrN/Cu/CrN/Si(001) thin film specimens by combining top-down annular and sideways scripted Ga^+ FIB milling [325,326]. The initial top-down annular FIB milling was applied perpendicular to the film surface, and yielded a CrN/Cu/CrN/Si sandwich pillar with the axial direction perpendicular to the interfaces and the bottom section wider than the top. This tapered pillar was subjected to a subsequent sideways scripted FIB milling, done in such way that the Ga^+ ion beam was incident from the side upon the bottom pillar portion only. Multiple FIB cuts were performed while the pillar rotated around its own axis, reducing the diameter of the pillar bottom portion and leaving the pillar top portion made of the CrN top layer untouched. This sideways scripted FIB milling yielded the final micro-pillar structure, with a "mushroom cap" top portion made of the CrN top layer only, connected to a taper-free "stem" which contained the CrN/Cu/CrN/Si interfaces. A schematic of the micro-pillar structure is shown in Fig. S1 of the Supplemental Materials. In all experiments, the diameters of the taper-free portion of the CrN/Cu/CrN/Si pillars, D, ranged from 2 to 4 μm. A custom diamond hook was fabricated from a commercial, 25 μm diameter, cylindrical diamond punch by FIB milling. The finished diamond hook had an overall external dimension less than 20 μm and an "inverse V" shaped slot at the top of the hook, with the "V-angle" matching that of the "mushroom cap" top portion of the micro-pillar. Tension load was applied when the diamond hook engaged the micro-pillar top portion and retracted along the pillar axial direction. From one CrN/Cu/CrN/Si thin film specimen, a number of such "mushroom shaped" micro-pillars with interfaces perpendicular to the pillar axes were fabricated such that repeated axial tension tests could be performed with the custom diamond hook.

In-situ axial tension test of CrN/Cu/CrN/Si(001) micro-pillars was conducted on a NanoMechanics Inc. NanoFlip® instrumented micro/nano mechanical testing device placed

within and coupled to the FEI Quanta3D FIB instrument. Tension testing began by utilizing the x-y displacement capabilities of the NanoFlip instrument to engage the custom diamond hook with the "mushroom cap" of the micro-pillar. Once engaged, application of a tensile load along the pillar axial direction was carried out under displacement control at a target displacement rate of 10 nm/sec. The total loading force, P, the total hook displacement, Δ, and a video of SE images of the micro-pillar under testing were simultaneously acquired. Post-test morphological observations were made after the tension testing resulted in fracture close to one CrN/Cu interface of the CrN/Cu/CrN sandwich structure.

6.3.2. The grain level crystal plasticity finite element analysis (CPFEA)

Grain level deformation of the micro-pillar tensile samples is simulated by CPFEA [327–329]. As shown in Figs. 1 and 2, the Cu grains within the Cu interlayer are largely columnar, with column radius of ~100 nm and column axes approximately perpendicular to the Cu/CrN interface. A strong <111> texture is exhibited by the Cu interlayer, with the <111> direction perpendicular to the interfaces. In the pillar specimens, the Cu interlayer can be treated as being sandwiched between two nominally rigid platens, i.e., the CrN top portion and the Si bottom portion. The Si bottom portion joins the Cu interlayer by a thin CrN buffer layer. For comparison, the elastic moduli of Cu, CrN and Si are listed in Table 1 [44,298,330,331]. In effect, the CrN platen is rigid relative to the Cu interlayer since the tensile elastic modulus (C_{11}) of CrN is about three times as high as that of Cu. Although the elastic moduli of Si is comparable to Cu, the fracture stress of this elastic-brittle material is substantially higher than Cu in the microscale [332]. Therefore, in effect, the Si bottom pillar portion can also be regarded as a rigid boundary of the Cu interlayer. As will be discussed in the forthcoming sections, the geometrical constraints exerted by the CrN top pillar portion of the micro-pillar tensile specimen appear to be more severe, reflecting a higher

rigidity for CrN as compared to Si. In this work, we only model the tensile deformation of disk-shaped Cu interlayers, with a fixed diameter of D = 3 μm and varying Cu interlayer thickness h = 0.20, 0.28, 0.55, 0.85, and 0.98 μm (Fig. 3(a)). The bottom surface of the Cu disks was kept completely rigid, while tensile displacements, corresponding to an engineering strain of e = 10 %, were applied to the top surface in the y direction while fixing the displacements in the x and z directions. The circumferential surface of the Cu disks was kept free.

Each Cu disk was modeled to be made up of an aggregate of 15 grains, with an average grain size $d \approx 0.77$ μm (Fig. 3(b)). In order to create the 3D geometry of the micro-pillar, we used Neper [333,334], a versatile tool in generation and meshing of polycrystalline grain structures. The columnar grains were created by Voronoi tessellation using randomly distributed centroids (seeds) across the basal plane. Unrealistic grain boundary geometries were avoided by applying regularization upon tessellation. Ten-node quadratic tetrahedral elements with four integration points were used for meshing, which enabled us to have piece-wise flat grain boundaries. A nominally uniform mesh size for all the elements across the entire structure was considered. Orientation distribution of the grains was also defined in the tessellation module of Neper. For all grains, the [111] orientation perfectly aligned with the y direction (Fig. 3(a)), while the orthogonal $[11\bar{2}]$and $[\bar{1}10]$ directions were randomly oriented in the x – z plane.

The number of grains modeled in this work is a compromise between computational accuracy and efficiency. If the actual grain size as found in the experiments were to be considered, a total of ~400 grains would have to be modeled. However, in order to explore the nucleation of voids, localized inhomogeneity such as concentration of stresses near/at interfaces would have to be captured. The resolution of such phenomena requires a refined mesh with respect to the size of the grains, which significantly increases the computational cost. In the current setup, a total of

35017, 47945, 91962, 140063 and 169871 elements were used for the cases of h = 0.2, 0.28, 0.55, 0.85, and 0.98 μm, respectively. The same element size was maintained across all cases. For the case of h = 0.98 μm, about 11,400 finite elements were used per grain on average, which agrees with the number recommended by Zhao et al [335]. Although the CPFEA used in the present study does not explicitly model pile-up of dislocations at, or the transmission of dislocations through, the grain boundaries, a Hall-Petch like behavior can be captured [336]. To this end, we also performed a study on the effect of grain size, where three interlayer models with identical thickness of h = 0.2 μm and varying numbers of Cu grains (the number of Cu grains = 4, 15, and 27, Supplemental Materials, Section S2) were considered. It was concluded that, under the strong geometrical constraints imposed by the loading surfaces, only negligible differences existed in the resulting stress-strain responses. Qualitatively, similar distributions in the stresses, including the von Mises stress and the hydrostatic stress, were observed in the cases with varying grain sizes.

The CPFEA simulations were performed by ABAQUS® with a user defined subroutine (UMAT) developed by Marin and coworkers [327,329,337,338]. Using this UMAT, the elasto-visco-plastic deformation behavior of metallic polycrystals can be simulated. Detailed derivation and numerical implementation of the model can be found in Ref. [329]. We provide a reiteration for only the essential bits of formulations in the Section S3 of Supplemental Materials. The visco-plastic behavior is described by the governing equation for the kinetics of the slip systems. As a well-acknowledged approximation, all slip systems are assumed to have the same slip kinetics, i.e.

$$\dot{\gamma}^{\alpha} = \dot{\gamma}_0 \left[\frac{|\tau^{\alpha}|}{\kappa_s^{\alpha}}\right]^{1/m} \mathrm{sign}(\tau^{\alpha}), \qquad (1)$$

where $\dot{\gamma}^{\alpha}$ is the shear strain rate of slip system α, $\dot{\gamma}_0$ is the characteristic (or reference) shear strain rate, κ_s^{α} is the current strength (or critical resolved shear stress, CRSS) of slip system α, while τ^{α} is the current RSS of slip system α. κ_s^{α} is given by its rate, i.e.,

$$\dot{\kappa}_s^{\alpha} = h_0 \left(\frac{\kappa_{s,S}^{\alpha} - \kappa_s^{\alpha}}{\kappa_{s,S}^{\alpha} - \kappa_{s,0}^{\alpha}} \right) \sum_{\alpha=1}^{12} |\dot{\gamma}^{\alpha}|, \qquad (2)$$

where $\kappa_{s,0}^{\alpha}$ and $\kappa_{s,S}^{\alpha}$ are the starting and saturation CRSS of slip system α, h_0 is the initial strain hardening rate, due to dislocation accumulations. The associated constants for slip kinetics are given in Table 2, which reproduces the experimental results from Lienert et al [339], as shown in Fig. S5 of the Supplemental Materials. Note, however, this corresponds to a macroscopic flow behavior of polycrystalline Cu with grain size of ~ 30 μm. Reductions of grain sizes may lead to substantially stiffer plastic responses. Ultimate strengths as high as 1 GPa, for instance, is not uncommon for nano-crystalline Cu [340]. However, the true plastic flow behavior of the Cu samples in this study is not well known. To this end, we also performed additional simulations using stronger flow strengths as inputs (Section S4 of the Supplemental Materials). As a result, although the new tensile simulations yielded undoubtedly stronger stress-strain responses, their deformation characteristics share striking similarities with the simulations performed using parameters from Ref. [339]. It is therefore expected that, although the overall simulated mechanical responses may show a strengthened or softened trend depending on the different flow rules used, the effect from the thickness of the Cu interlayer would persist. Analyses of the CPFEA results is centered mainly around the distribution of two quantities in the samples, the hydrostatic stress ($\sigma_{hyd.} = \frac{1}{3}\sigma_{ii}$) and the von Mises stress ($\sigma_{vM} = \left(\frac{3}{2}\sigma_{ij}^{dev}\sigma_{ij}^{dev}\right)^{1/2}$), where σ_{ij}^{dev} is the deviatoric stress ($\sigma_{ij}^{dev} = \sigma_{ij} - \frac{1}{3}(\sigma_{ii})\delta_{ij}$). The former gives rise to the driving force for void

growth but does not lead to plastic deformation, while the latter induces plastic deformation in the material.

6.4. Results and discussion

6.4.1. Results of experimentation

XPS spectra were collected from top surfaces of CrN films and Cu films, separately deposited, after a brief 4kV Ar^+ ion surface etch. The Cu XPS spectra showed various Cu core level transitions, and the CrN spectra showed transitions from Cr core level transitions and the N 1s transition. The N to Cr ratio determined by using factory supplied sensitivity factors is close to 1:1. Only background was observed at the location of the O 1s transition in both Cu and CrN spectra, indicating that sputter deposited Cu and CrN films had oxygen impurity level at or below the XPS detection limit of ~1 at.%.

Figure 1 shows typical morphologies of sputter deposited CrN/Cu/CrN/Si(001) thin film specimens. The ISE image of Fig. 1(a) shows a FIB cross section of one as-deposited CrN/Cu/CrN/Si(001) specimen. The uniform Cu interlayer, with thickness h ~ 720 nm, and the CrN top layer, ~6000 nm in thickness, are clearly visible in Fig. 1(a). The CrN buffer layer next to Si is too thin to be visible. The CrN top layer has a dense nano-columnar structure with no evidence of inter-columnar voids. The nanoscale roughness of the CrN top surface, shown in the SE image of Fig. 1(b), is consistent with the nano-columnar structure of the CrN top layer. Similar morphologies were observed from all CrN/Cu/CrN/Si(001) specimens.

Figure 1 also shows typical XRD data from as-deposited thin film specimens. Figure 1(c) shows a θ-2θ diffraction pattern from one CrN/Cu/CrN/Si(001) specimen, with a Cu interlayer thickness h of ~200 nm. The diffraction signal is dominated by the CrN top layer because of its

much higher thickness: all observed diffraction peaks are indexed to the B1 CrN structure, with a lattice constant a = 4.18 ± 0.01 Å, close to the CrN bulk lattice parameter of 4.16Å [341]. The CrN top layer is polycrystalline, with alignment of CrN <111> and CrN <200> along the Si [001] growth direction. Figure 1(d) shows a 2θ diffraction pattern from the same CrN/Cu/CrN/Si(001) specimen at a fixed glancing X-ray incidence angle ω = 2.5°. Diffraction peaks from the glancing incidence pattern are again indexed to the B1 CrN structure. The inset of Fig. 1(d) shows the $\sin^2\psi$ plot of the data shown in Fig. 1(d), in which the CrN lattice parameter a is plotted vs. $\sin^2\psi$ where ψ is the angle between the scattering vector $\vec{K}$ and the specimen surface normal, $\Psi = 2\theta/2 - \omega$. Assuming an equal biaxial stress σ_R within the CrN layer, the relationship between a and ψ is given by

$$a(\Psi) = \left(\frac{1+\upsilon}{E}\sigma_R\right) a_o sin^2\Psi + \left(1 - \frac{2\nu}{E}\sigma_R\right) a_o, \qquad (3)$$

where E, ν, and a_o are respectively the Young's modulus, Poisson's ratio, and stress-free lattice parameter of CrN [342]. A linear least squares fit to the data shown in the inset of Fig. 1(d) yielded a slope of -0.015 ± 0.015 Å and an intercept of 4.177 ± 0.006 Å. With the values of E and ν taken respectively as the CrN bulk values, 375GPa and 0.2 [38], the values of σ_R and a_o are obtained from the fitted slope and intercept as $\sigma_R = -1.1$ GPa and a_o = 4.17 Å. The so-obtained a_o value is consistent with the bulk CrN lattice parameter of 4.16 Å. This modest level of residual compressive stress is characteristic of all CrN films deposited under the present conditions, and is consistent with the observation that the CrN films are dense and without inter-columnar voids.

To assess the structure of the Cu interlayers deposited on top of the thin CrN buffer layer, separate Cu/CrN/Si(001) thin film specimens were deposited following the same deposition procedure for the CrN/Cu/CrN/Si(001), minus the CrN top layer. Figure 1(e) shows a 2θ

diffraction pattern from one Cu/CrN/Si(001) specimen, with a Cu layer thickness h of ~720 nm, at a fixed glancing X-ray incidence angle ω = 2.5°. The diffraction signal is dominated by the Cu layer: all diffraction peaks are indexed to the A1 Cu structure. From the $\sin^2\psi$ plot shown in the inset of Fig. 1(e), a similar analysis yielded a slope of 0.024 ± 0.005 Å and an intercept of 3.598 ± 0.002 Å. With the values of E and ν taken respectively as the Cu bulk values, 110GPa and 0.34 [343], the values of residual stress and stress-free lattice parameter are determined to be $\sigma_R = +0.4$ GPa and a_o = 3.61 Å. The so-obtained a_o value is consistent with the bulk Cu lattice parameter of 3.615 Å [39], and the Cu film is seen to possess a low level of residual tensile stress. Figure 1(f) shows a θ-2θ diffraction pattern from the same Cu/CrN/Si(001) specimen, which shows that the polycrystalline Cu film has its <111> and <200> directions aligned with the Si [001] growth direction. The structural characteristics shown in Figs. 1(e) and 1(f) are representative of all Cu films deposited onto the CrN buffer layer.

Results of TEM examination of as-deposited CrN/Cu/CrN/Si(001) specimens are shown in Fig. 2. Figure 2(a) shows a bright-field (BF) image of one portion of a typical CrN/Cu/CrN/Si(001) specimen. A uniform polycrystalline CrN buffer layer next to the Si substrate, ~55 nm in thickness, is clearly visible. The interface between the CrN buffer layer and the Cu interlayer is clean, without signs of secondary phases and interfacial voids. Figure 2(b) shows the dark-field (DF) image from the same area. The Cu interlayer consists of a random mixture of columnar and near-equiaxed Cu grains. Typical widths of Cu columns are ~60 nm, and below 100 nm. Additional observations showed that the Cu interlayer is uniform in thickness, and the interface between the Cu interlayer and the CrN top layer is similar to the Cu/CrN-buffer interface, without signs of interfacial voids.

A typical FIB fabricated CrN/Cu/CrN/Si(001) micro-pillar with a "mushroom cap" top portion is shown in the ISE image of Fig. 4(a). The thickness of the Cu interlayer of this specimen, h, is 850 nm. The different ISE contrasts exhibited by the Si substrate, the Cu interlayer, and the CrN top layer pillar portions make them readily distinguishable in the image. The CrN buffer layer next to Si is too thin to be discernable in this image. The pillar axis is perpendicular to the CrN/Cu/CrN/Si interfaces. The FIB milled, custom diamond hook is shown in the SE image of Fig. 4(b). The external extent of the hook is less than 25 μm. The top of the hook has an "inverse V" shaped opening, with the V-angle matching that of the "mushroom cap" top portion of the micro-pillar. The SE image shown in Fig. 4(b) shows the typical configuration of engagement between the diamond hook and the micro-pillar specimen shown in Fig. 4(a), prior to application of a tensile load along the pillar axial direction.

Figure 5(a) shows a collection of data obtained from in-situ tension testing of CrN/Cu/CrN/Si micro-pillars. The tensile stress, σ, calculated from the tensile load P through $\sigma = 4P/(\pi D^2)$ where D is the pillar diameter, is plotted vs. the total displacement Δ. Three $\sigma - \Delta$ curves were obtained from three separate pillars fabricated from one CrN/Cu/CrN/Si specimen, with a Cu interlayer thickness h of 980 nm. Qualitatively similar $\sigma - \Delta$ curves were observed from all three pillars: with an initial rise in σ with increasing Δ, followed by a plateau where Δ increases further at an approximately constant σ, and finished with a large and discontinuous hook displacement excursion when the pillar suffered a catastrophic fracture into two parts. Three more $\sigma - \Delta$ curves are shown in Fig. 5(a), obtained from three separate pillars fabricated from another CrN/Cu/CrN/Si specimen, with h = 550 nm. As h decreases from 980 nm to 550 nm, the extent of the plateau on the $\sigma - \Delta$ curve diminishes significantly while the tensile failure stress, σ_f, increases. Two additional $\sigma - \Delta$ curves are shown in Fig. 5(a), obtained from two separate pillars

fabricated from another CrN/Cu/CrN/Si specimen, with h = 200 nm. At h = 200 nm, σ_f increases further while the extent of the plateau on the $\sigma - \Delta$ curve becomes imperceptible. Figure 5(b) plots measured values of σ_f vs. h. Separate data points at the same h value denote experimental results on separate pillars, and illustrate the level of experimental scatter. As h decreases from 980 nm to 200 nm, the measured σ_f value exhibits a pronounced increase, by almost a factor of 2 and significantly above the data scatter.

Figure 6 shows the morphology of tensile fracture of CrN/Cu/CrN/Si pillars, with h = 980 nm. Figure 6(a) shows an SE image of one broken bottom pillar portion. The Si portion of the pillar remained intact, and connected to the Si substrate. No failure was observed at the Cu interlayer/CrN buffer layer interface and the CrN buffer layer/Si substrate interface, and the predominant fraction of the Cu interlayer remains connected to the bottom portion of the pillar, as confirmed by Cu K EDS mapping. Figure 6(b) shows an SE image of the broken top portion of the same pillar, attached to the opening of the diamond hook. It is clear that the CrN "mushroom cap" top pillar portion also remained intact, without signs of damage. Figure 6(c) shows a high-resolution SE image of the surface of the broken bottom pillar portion shown in Fig. 6(a). The Cu fracture surface shows clear signs of plastic deformation due to the process of tension induced fracture, exhibiting the "cup-and-cone" morphology with many spikes and ridges, albeit at the nano scale. Figures 6(d) and 6(e) show Cr K and Cu K EDS maps of the same broken top pillar portion. The uniform and strong intensity of Cr K radiation across the entire image in Fig. 6(d) confirms that the predominant makeup of the top pillar portion is CrN, including the fracture surface. In Fig. 6(e), perceptible Cu K radiation intensity is only observed near one edge of the fracture surface, readily identifiable in the corresponding SE image of Fig. 6(b). In particular, little Cu K radiation is observed across the majority of the fracture surface. The combined

observations made in Figs. 6(a), 6(b), 6(d), and 6(e) indicate that the tension induced fracture occurred within the Cu interlayer but close to the CrN top layer/Cu interlayer interface. Figure 6(c) further indicates that the process of tension induced fracture is associated with extensive plastic deformation of the Cu interlayer.

Figure 7 shows SE images illustrating the overall tensile fracture morphology of CrN/Cu/CrN/Si micro-pillars as h varies. As h decreases from 850 nm to 200 nm, Figs. 7(a), 7(b), 7(c), and 7(d) show that the final tensile fracture occurred close to the interface between the CrN top pillar portion and the Cu interlayer, leaving the predominant fraction of the Cu interlayer attached to the bottom pillar portion and the interface between the Cu interlayer and the CrN buffer layer intact. Additional EDS mapping again indicated that, at all h values, the tensile fracture occurred within the Cu interlayer, but close to the interface between the CrN top layer and the Cu interlayer. Figures 8(a), 8(b), 8(c), and 8(d) show respectively typical morphologies of Cu interlayer tensile fracture surfaces, at h values of 850 nm, 550 nm, 280 nm, and 200 nm. At h = 850 nm, pronounced nanoscale cup-and-cone-like structures were observed on the Cu interlayer fracture surface, similar to that shown in the h = 980 nm case in Fig. 6(c). This cup-and-cone type structure diminishes as h decreases to 550 nm and becomes much less perceptible at h values of 280 nm and 200 nm, except at the rims. Such observations of diminished plasticity of the Cu interlayer are consistent with the fact that little or no plateau was observed on the $\sigma - \Delta$ curves for the h = 280 nm and h = 200 nm cases.

6.4.2. Results of CPFEA simulations

6.4.2.1. Description of the elasto-plastic response of the Cu interlayers of varying thicknesses

The stress-strain responses of the Cu interlayers obtained from simulation, as a function of their thickness h, are shown in Fig. 9. It is of interest to note that, even though the true plastic flow rule of the material was taken to be identical in all cases, the apparent mechanical response becomes significantly stiffer with the reduction of h. This indicates a strong influence of the constraints exerted by the loading geometry. Indeed, with a smaller h, the rigid loading platens couple more strongly, which imposes a stronger hydrostatic tension. In this case, the applied tensile load gives rise to a uniaxial strain condition, which on one hand, substantially amplifies the strain response, while on the other hand, retards the onset of plasticity. This is consistent with the results shown in Fig. 10(a), which displays the distribution of the hydrostatic stress, σ_{hyd}, in the Cu interlayers at the engineering strain of e = 10%. Apparently, the localized hydrostatic stress is distinctly higher for h = 0.2 μm than that for h = 0.98 μm. When h = 0.2 μm and e = 10%, a hydrostatic stress value as high as 3 GPa is observed when the average tensile stress is only ~1.3 GPa. The results also reveal that the hydrostatic stress tends to concentrate near the center of the "interfaces", modeled as rigid boundaries in the current set of simulations. This is expected, since such locations are farthest from a free surface and "benefits" most from the rigid boundary conditions. As h increases, the hydrostatic stress component decays quickly. In fact, the hydrostatic stress on the "interfaces" for the case of h = 0.98 μm is virtually zero except for locations near the grain boundaries (faint reddish colors in Fig. 10(a)). This observation provides evidence, in part, to support the dependence of the apparent failure stress on h, as shown in Fig. 5(b). It should be pointed out that the actual extent of the geometrical constraint is dependent on the actual rigidity of the boundaries, or barring interfacial sliding, the rigidity of the ceramic neighboring the metal interlayer. For instance, based on the difference in elastic moduli of CrN and Si, the interface close to the Si side is subjected to considerably less constraint than that close

to the CrN side, contrary to the simulations in which perfect rigidity was assumed for both top and bottom surfaces. This is qualitatively consistent with the experimental observation that the eventual tensile fracture all occurred near the interface between the CrN top portion and the Cu interlayer portion of the pillar.

Additional observations from Fig. 10(b) provides an explanation for the morphology of the failure surfaces shown in Figs. 5 and 6, where pull-up lips are evident indicating ductile fracture near the perimeter of the Cu interlayers. As shown by Fig. 10(b), locations with pronounced von Mises stress, σ_{vM}, exist on the outer ring of the interlayers near the "interfaces", which may serve as the initiation point of the slip-induced ductile failure. Opposite to the trend shown in Fig. 10(a), the von Mises stress reduces to near-zero values at the center of the interfaces for all thicknesses. This, again, is expected, since slip should be least preferred where the hydrostatic stress is at a maximum.

It is interesting to note, at e = 10%, although both the overall hydrostatic stress and the von Mises stress components increase with reducing h, the increase in the former surpasses the latter by more than a factor of three. This lead to important questions: 1) under what conditions do the specimens fail? 2) which stress component(s) should be used to construct a failure criterion? Apparently, due to the different rates at which the stress components evolve with h, different failure criteria may lead to distinctly different tensile failure stresses. In the next section, we attempt to provide a physics-based answer to these questions.

6.4.2.2. An empirical failure criterion for void dominated fracture

Apparent from Figs. 6, 7, 8 and the accompanying discussions, the tensile failure of the specimen is due to the nucleation, growth, and coalescence of nanoscale voids, whose driving force

is provided by the presence of hydrostatic stresses. However, homogeneous nucleation of voids, e.g., through condensation of vacancies, is extremely difficult under room temperature conditions. Void nucleation has to rely on a heterogeneous mechanism with pre-existing nuclei [344–346]. According to Bringa et al [347], grain boundaries, especially triple junctions, contain localized free volume and can serve as favorable sites for void nucleation. Without grain boundaries, dislocation intersections can also provide free volume and serve as nucleation sites for voids [348]. In the present work, the tips of dislocation pile-ups, either at grain boundaries or at the metal/ceramic interfaces, are ideal sources for such nucleation. In addition, according to relevant density functional theory (DFT) calculations [283,349], the regions near the metal/nitride interfaces may be mechanically weaker than in bulk metal, making the interface a preferred location for void nucleation. It was also shown by Bringa et al. [347] that, to accommodate fracture, the growth of voids cannot solely rely on the diffusion of vacancies, instead it requires plasticity. In addition, from the standpoint of theoretical mechanics, the existence of remotely applied deviatoric stress component has been shown to noticeably reduce the hydrostatic stress limit for cavitation instability of elastic-plastic solids [350,351]. It is therefore reasonable to argue that, although the hydrostatic tension is the driving force for the nucleation of voids, plastic deformation serves as an important facilitator in the process. It is expected that void induced fracture requires the "cooperation" between the hydrostatic stress and the von Mises stress components. Absent of either stress component, successful nucleation and growth of void cannot be achieved.

The nucleation rate of voids can be written, according to the classical nucleation theory [47,352,353], as

$$J = N_0 \upsilon_D \exp\left(-\frac{Q^* - \sigma V}{kT}\right) = N_0 \upsilon_D \exp\left[-\frac{(\sigma^* - \sigma)V}{kT}\right], \quad (4)$$

where J is the global void nucleation rate per unit volume, N_0 is the number of void nucleation sites per unit volume, υ_D is an attempt frequency and is taken to be the Debye frequency of Cu, 1.27×10^{13} /s [354], Q^* is the activation energy, σ^* is the athermal critical nucleation stress, σ is the current local stress, V is the activation volume, and k is the Boltzmann's constant. The activation volume can be estimated as $V \approx b^3$, where b is the magnitude of the Burgers vector ($b \approx$ 2.6 Å for Cu). Based on the discussion above, we propose an empirical relation for this local stress, in the form of a cooperative stress, i.e.,

$$\sigma = \left(\sigma_{\text{hyd.}}{}^{l} \sigma_{\text{vM}}{}^{n}\right)^{1/2}, \tag{5}$$

where $l + n = 2$. Parameters l and n address the relative importance of the hydrostatic stress component over the von Mises stress component, and can be obtained by fitting the modeling output to the experimental data. The empirical relation expressed in Eq. (5) incorporates the effect of the deviatoric stress component and differs from conventional stress criteria used for relating interfacial cavitation phenomena in metal matrix composites (MMC), which relies on a critical local hydrostatic stress only [355,356] or a local normal stress perpendicular to interfaces [356–358]. The adaptation of Eq. (5) in the analysis of our CPFEA results, as well as its prediction as compared to the conventional criteria, is discussed in the following text.

Hauschildt et al [359] reported that, driven by electromigration, the activation energy (Q^*) for void nucleation in Cu is ~1 eV. This energy, which is associated with the thermodynamic process of creating internal free volume, is dependent only on the intrinsic bond characteristics of a given material and should be independent of the specific mechanisms through which voids are nucleated (i.e., eletromigration, mechanical deformation, etc.). Under the present tensile loading conditions, massive nucleation, growth, and coalescence of voids, i.e., the eventual tensile fracture,

happen within the temporal resolution of SEM observation (~ 1s). The normalized nucleation rate, J/N_0, is therefore ~0.5/s if a moderate assumption that 50% of the nucleation sources have been activated into voids within the observation window of a second. Assuming a temperature $T = 300$ K, this means that the local stress should exceed ~1.8 GPa in order for the nucleation rate to be observable. When the local stress approaches this value, the nucleation rate increases rapidly [360]. However, nucleation of one void would drastically release the strain energy of its surrounding, reduce the local stress below this value again, and prevent further void nucleation at this locality. We call this the threshold cooperative stress for fracture (σ_{th}). According to Eq. (5), to induce fracture, the threshold cooperative stress criterion has to be satisfied. This stress level is comparable to the failure stress reported in Fig. 5(b). However, this value is higher than the typical stress observed in the present set of CPFEA simulations, due to the input plastic flow rule (shown in Fig. S5 in the Supplemental Materials). Therefore, to analyze the present CPFEA results, a reduced threshold stress value was used, which corresponds to the failure of ~37% of elements on the metal/ceramic interfaces.

According to the presently proposed failure criterion, expressed in Eq. (5), and three sets of parameters of l and n, i.e. $l = 0.5$, $n = 1.5$; $l = n = 1.0$; and $l = 1.5$, $n = 0.5$, the tensile failure stress (σ_f) values were then obtained for different h values from the CPFEA results, shown in Fig. 11. The corresponding threshold stresses are 318 MPa, 306 MPa, 311 MPa, respectively, for $l = 0.5$, $n = 1.5$; $l = n = 1.0$; and $l = 1.5$, $n = 0.5$. Depending on the choice of l and n, different (decreasing or increasing) trends are obtained for the $\sigma_f - h$ relationship. When $l = 0.5$, $n = 1.5$ or $l = n = 1.0$, trends similar to that shown in Fig. 5(b) are observed, i.e., increasing σ_f with decreasing h. This indicates that, although the hydrostatic stress component becomes overwhelmingly large for the thinner interlayers, the failure is more decisively dependent on the von Mises stress

component. This also agrees with the prior observations that plastic deformation is a necessary condition for void nucleation [347,348]. To further illustrate the appropriateness of Eq. (5), conclusion reached based on the conventional critical stress criterion based on the hydrostatic stress component only, which corresponds to a choice of $l = 2$ and $n = 0$, was also tested. This led to relatively flat $\sigma_f - h$ behavior with a slight increase in σ_f with increasing h, opposite to the observed trend as displayed in Fig. 5(b). As shown in Figs. 9 and 11, such an increasing trend is already visible when $l = 1.5$ and $n = 0.5$. On the other hand, a choice of the von Mises stress component alone as a failure criterion is unphysical, as it does not provide a driving force for void growth.

The failure points are also indicated in Fig. 9 by the black hollow markers, on the respective stress-strain curves. The mismatch in the absolute levels of the failure stress, i.e. ~500 MPa in the CPFEA simulations vs ~1.5 GPa in the experiments, can be ascribed to the relatively soft flow rule utilized as the input to the UMAT. Utilization of significantly stronger flow rules would elevate the threshold stress to a level comparable to 1.8 GPa, which, in turn, would increase the failure stresses similar to what was reported in Fig. 5. Nonetheless, the change in the absolute flow strength of Cu would simply scale the data points in Fig. 11, but not impact the general trends of variation shown in Fig. 11. For comparison, the data point from Fig. 5(b) have been incorporated into Fig. 11 (black squares) as the second vertical axis. As both vertical axes originate from zero, such an overlay gives a direct comparison between the trends of $\sigma_f - h$ measured from experiments and from CPFEA. It appears that the prediction based on Eq. (5) with $l = 0.5$ and $n = 1.5$ produces a reasonable agreement with the experimental results.

However, the CPFEA simulations appear to predict a stronger increase in σ_f with decreasing h at small h values. This may arise from the fact that the current failure criterion did not consider

the finite cohesive strength of the CrN/Cu interface. If such an additional criterion is put in place, an asymptote would exist (e.g., the horizontal dashed line at ~550 MPa in Fig. 11 denotes such a behavior), limiting the failure stress. However, the exact value of such cohesive strengths is presently unknown, and would require further investigations combining DFT simulations and experimental efforts.

The snapshot of the hydrostatic as well as the von Mises stress components of the Cu interlayers at the moment of failures, captured by adopting the failure criterion expressed in Eq. (5) with $l = 0.5$ and $n = 1.5$, is provided in Fig. 12. It is apparent that, the thinner Cu interlayers (e.g., $h = 0.20$ μm and $h = 0.28$ μm) that failed at relatively small strains (see Fig. 9) have very high hydrostatic stresses on the interfaces, while the respective von Mises stresses are relatively low. Conversely, the thicker Cu interlayers (e.g. $h = 0.98$ μm) that failed at much larger strains (see Fig. 9) have substantially higher von Mises stress as compared to the thinner interlayers, while the hydrostatic stresses at interfaces are relatively low. In effect, the overall ductility achieved by the thinner Cu interlayers is substantially less than that achieved by the thicker interlayers. This observation is consistent with the observed h dependence of plasticity, shown in Fig. 5(a). In addition, the increase in the von Mises stress component with increasing h at failure is also consistent with the observations provided in Figs. 7 and 8, i.e. more pronounced dimpling at larger Cu interlayer thicknesses.

6.5. Discussion

It is interesting to comment on the difference between the strain rate affected in the present micro-pillar tensile testing and that typically present in the laser spallation testing. At the present displacement rate of 10 nm/s, assuming perfect rigidity of the CrN and Si pillar portions, the strain rate for the present tests ranges from ~$5\text{x}10^{-2}$/s to ~$1\text{x}10^{-2}$/s as the Cu interlayer thickness varies

between ~200 nm to ~1000 nm. The strain rate is thus 8 orders of magnitude lower than that affected by the laser spallation test. The difference in failure mode for the metal/ceramic interfacial region resulting from such a difference in the strain rate has not been explored in detail, and awaits future studies.

Granted, the current CPFEA simulations ignore several complications present within the current set of experiments. The actual <111> fiber texture of the Cu interlayers is not a complete one, as evidenced by the presence of the Cu (200) reflection in Fig. 1(f), while a complete one was assumed in the CPFEA. Whether a more realistic representation of the texture within the Cu interlayer may improve the correspondence between the measured dependence of σ_f on h and that generated from CPFEA simulations remains to be clarified in the future. The actual configuration of the CrN/Cu/CrN/Si micro-pillars is not strictly cylindrical with one identical diameter throughout the pillar length, due to the differential Ga^+ ion milling rate between CrN, Cu, and Si, as evidenced by the image shown in Fig. 4(a). A small differential in the pillar diameter at the CrN/Cu junction may serve to accentuate stresses at the perimeter of the CrN/Cu interface, which was not considered in the CPFEA performed. Nonetheless, it is our belief that the present CPFEA captures the main physics of the micro-pillar tension test, and reaches the correct conclusion that the variation in the distribution of the hydrostatic and von Mises stress components within the tested volume and their cooperation is what leads to the observed dependence of the tensile failure stress on the Cu interlayer thickness.

It is intriguing to consider the implications of Eq. (5), in particular that low temperature tensile fracture near the metal/ceramic interface would not happen absent a significant degree of plastic deformation within the metal layer close to the interface. Considering the low flow stress and extensive ductility of Cu, it is interesting to contemplate whether using a stronger metal

interlayer with a much higher flow stress would serve to effectively retard the void nucleation and growth process, to the point that the experimentally measured eventual tensile failure stress can approach the ideal tensile strength of the metal/ceramic interface. In addition, given the trend of "thinner is stronger" observed in this paper, the geometric constraints are expected to be increased with the reduction of the interlayer thickness, which suppresses the plastic deformation. When the interlayer thickness is reduced to the nm level, the suppression of plasticity is expected to be maximized. A natural question to ask is "at what thickness of the metal interlayers does the micro tension test reflect the true cohesive strength of the metal/ceramic interface"? Exploration in these direction is also left for future work.

6.6. Summary

We have utilized an in-situ micro-pillar tensile testing protocol to assess the critical tensile fracture stress of ceramic/metal/ceramic interfacial regions, applicable to a wide variety of thin ceramic coating/substrate systems. We demonstrated the effectiveness of this microscale testing protocol using CrN/Cu/CrN micro-pillars as the model system. The tensile failure stress was measured as a function of the Cu interlayer thickness, and showed a significant thickness dependence. Morphological and compositional characterizations indicate that the tensile fracture involves plastic deformation of the Cu interlayer, as evidenced by a pronounced dimpled morphology of the fracture surfaces. The extent of the plasticity associated with the fracture, again, depends on the interlayer thickness. Crystal plasticity finite element analyses on the Cu interlayers subjected to similar loading conditions are performed in an attempt to understand and explain these experimental observations. We showed that the plastic response of the Cu interlayers is strongly affected by the geometrical constraints exerted by the much more rigid loading surfaces straddling the interlayer on both sides. As the layer thickness decreases, a significant hydrostatic stress

component is generated within the layer, which substantially increases its stiffness. Meanwhile, the von Mises stress component within the layer is reduced, which limits the amount of resulting plasticity. An empirical failure criterion, which imposes a critical value on a weighted geometric mean between the hydrostatic and von Mises stress components, has been proposed. Using this criterion, the trend of measured tensile failure stress as a function of the interlayer thickness—observed in the present micro-tension experiments—is captured.

Tables

Table 6. 1 Elastic moduli of Cu, CrN, and Si according to data collected from literature [44,298,330,331].

Material	C_{11} (GPa)	C_{12} (GPa)	C_{44} (GPa)
Cu	179.3	123.2	81.0
CrN	546.0	184.0	20.0
Si	171.5	67.1	81.1

Table 6. 2 Constants governing the flow kinetics of single crystal Cu.

h_0	$k_{s,0}^{\alpha}$	$k_{s,S}^{\alpha}$	m	$\dot{\gamma}_0$
250 MPa	19 MPa	130 MPa	0.02	1.0

Figures

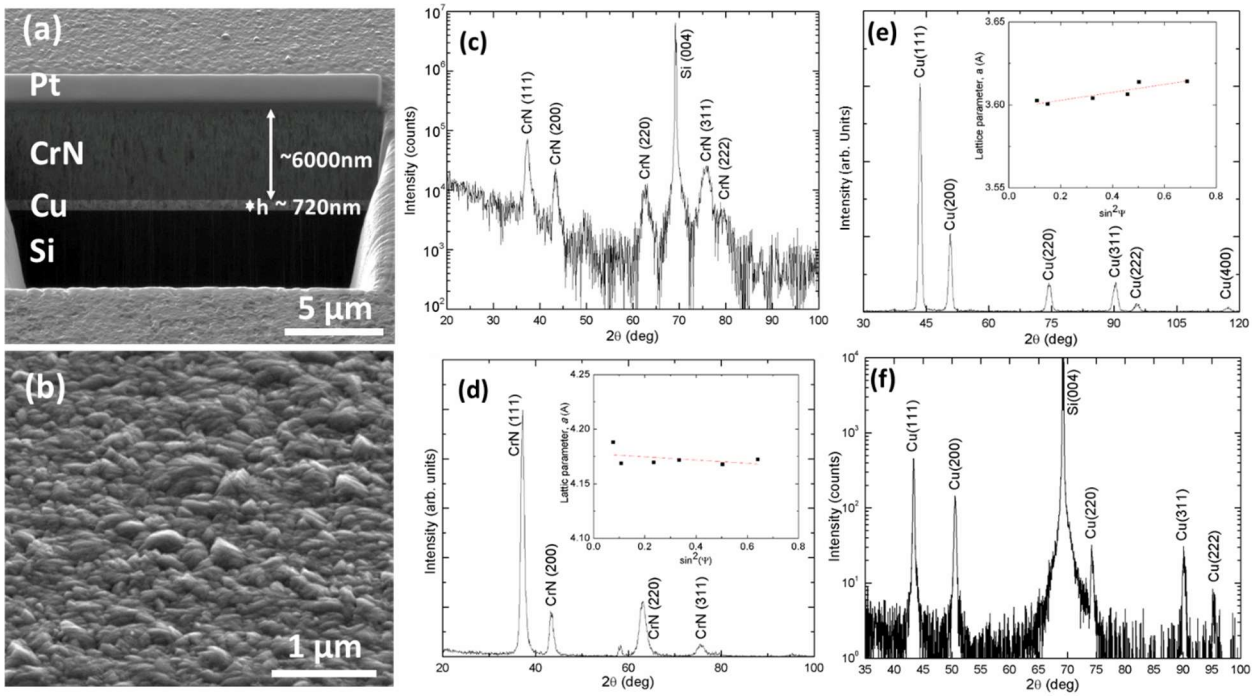

Figure 6. 1 Morphology and structure of as-deposited thin film specimens: (a) an ISE image of a FIB cross section of one CrN/Cu/CrN/Si(001) specimen, with a Cu interlayer thickness ~ 720 nm and a CrN top layer thickness of ~ 6000 nm; (b) an SE image of the top CrN surface of the same specimen; (c) a θ-2θ XRD scan from one CrN/Cu/CrN/Si(001) specimen; (d) a 2θ XRD scan from the same specimen shown in (c) at a fixed incidence angle ω = 2.5°. The inset is the associated $\sin^2\psi$ plot; (e) a 2θ XRD scan from a Cu/CrN/Si(001) specimen at ω = 2.5°, with the $\sin^2\psi$ plot shown in the inset; (f) a θ-2θ XRD scan from the same specimen shown in (e). Image has been adapted with permission from [361].

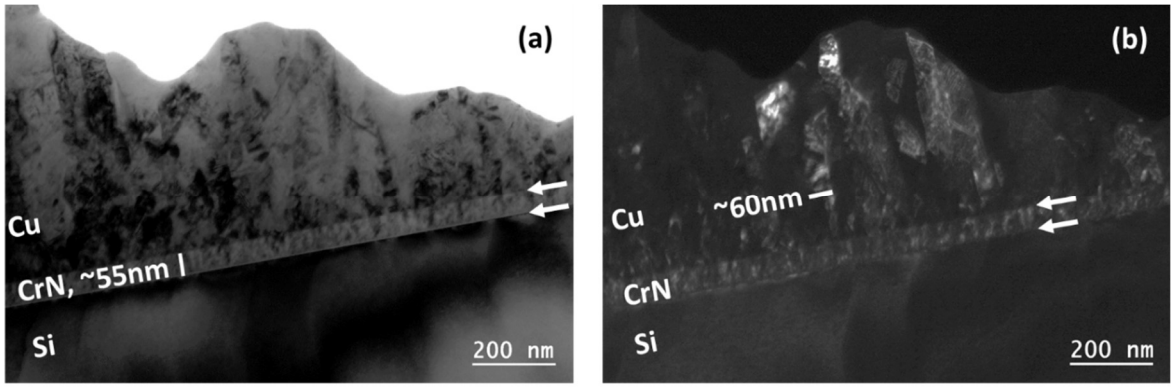

Figure 6. 2 TEM examination of a typical as-deposited CrN/Cu/CrN/Si(001) film: (a) a BF image showing the CrN buffer layer and the Cu interlayer. The bar and the arrows mark the ~55nm thick CrN buffer layer and the CrN/Si and Cu/CrN interfaces; (b) a DF image showing a random mixture of columnar and near-equiaxed Cu grains. The bar accentuates the typical width of Cu nano columns, and the arrows mark the CrN/Si and Cu/CrN interfaces. Image has been adapted with permission from [361].

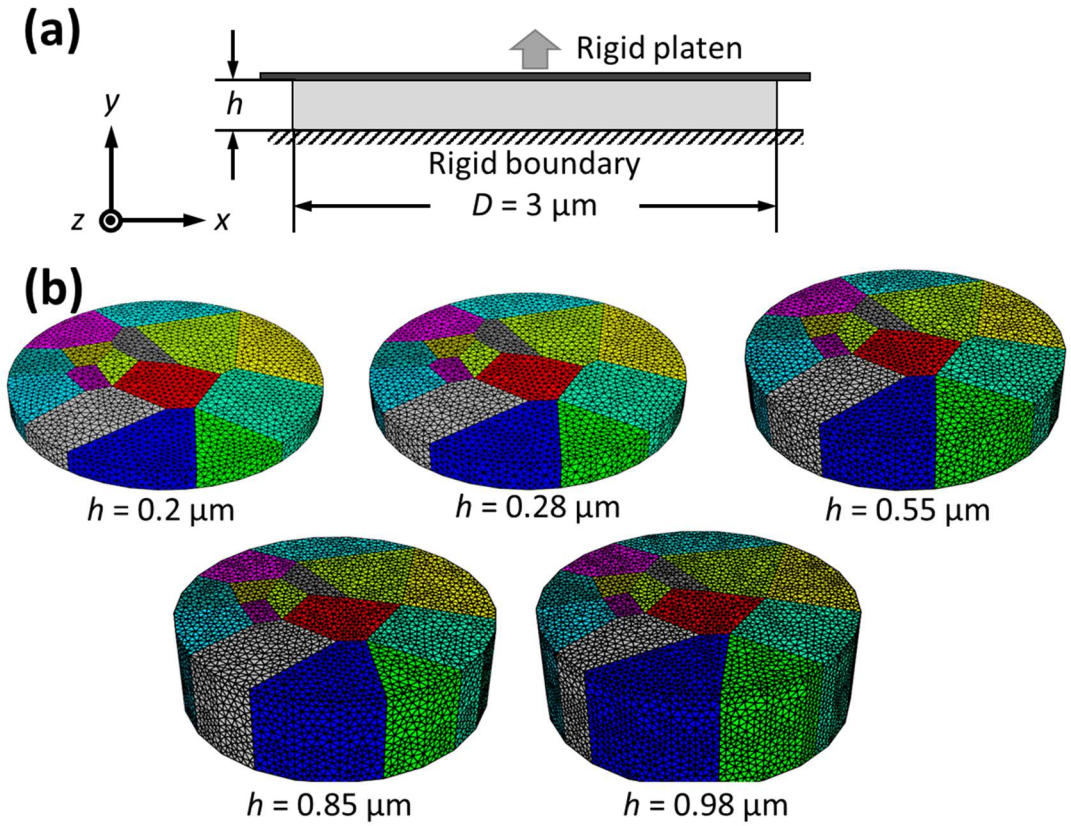

Figure 6. 3 Geometry (a) and grain morphologies (b) of the crystal-plasticity finite element models.

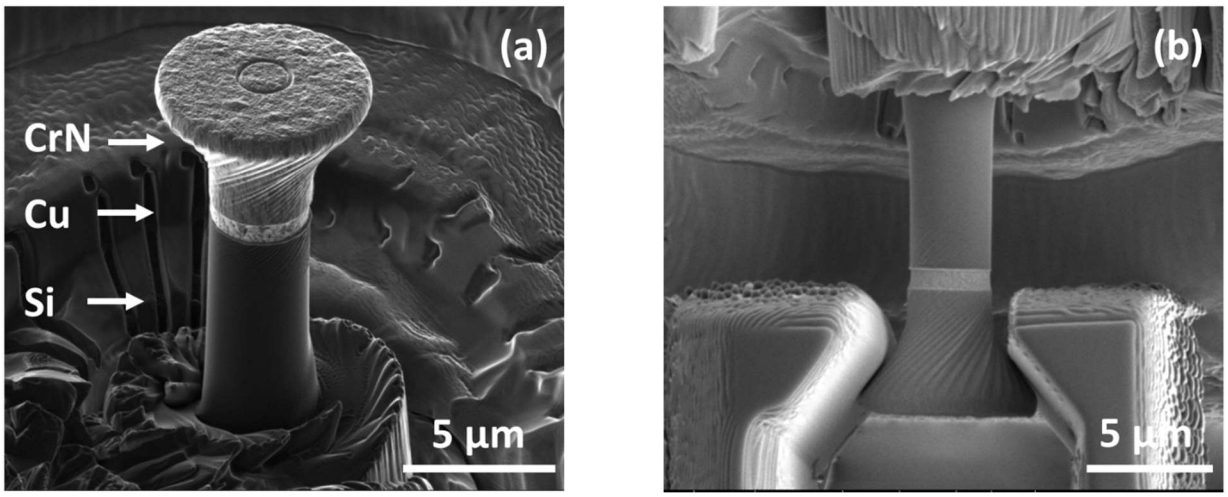

Figure 6. 4 Micro-pillar tension testing setup: (a) an ISE image of a typical CrN/Cu/CrN/Si(001) "mushroom shaped" pillar fabricated by combining top-down annular and sideways scripted Ga^{+} FIB milling; (b) an SE image of the same pillar engaged with the "inverse V" shaped diamond hook prior to actual tension loading. Image has been adapted with permission from [361].

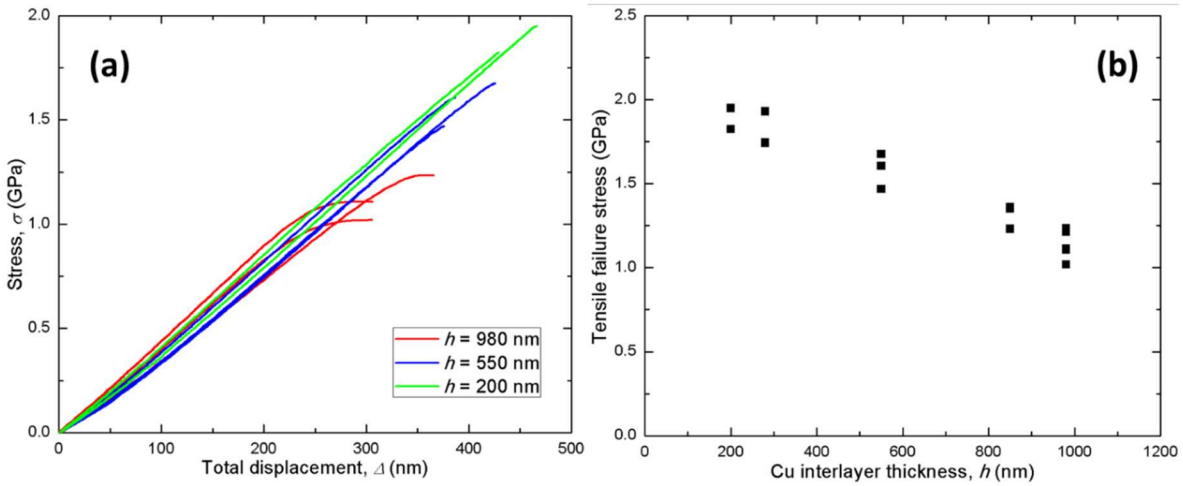

Figure 6. 5 Micro-pillar tension testing results: (a) stress-total displacement curves obtained from CrN/Cu/CrN/Si(001) pillars with Cu interlayer thickness *h* of 980 nm, 550 nm, and 200 nm; (b) tensile failure stress plotted vs. *h*. Image has been adapted with permission from [361].

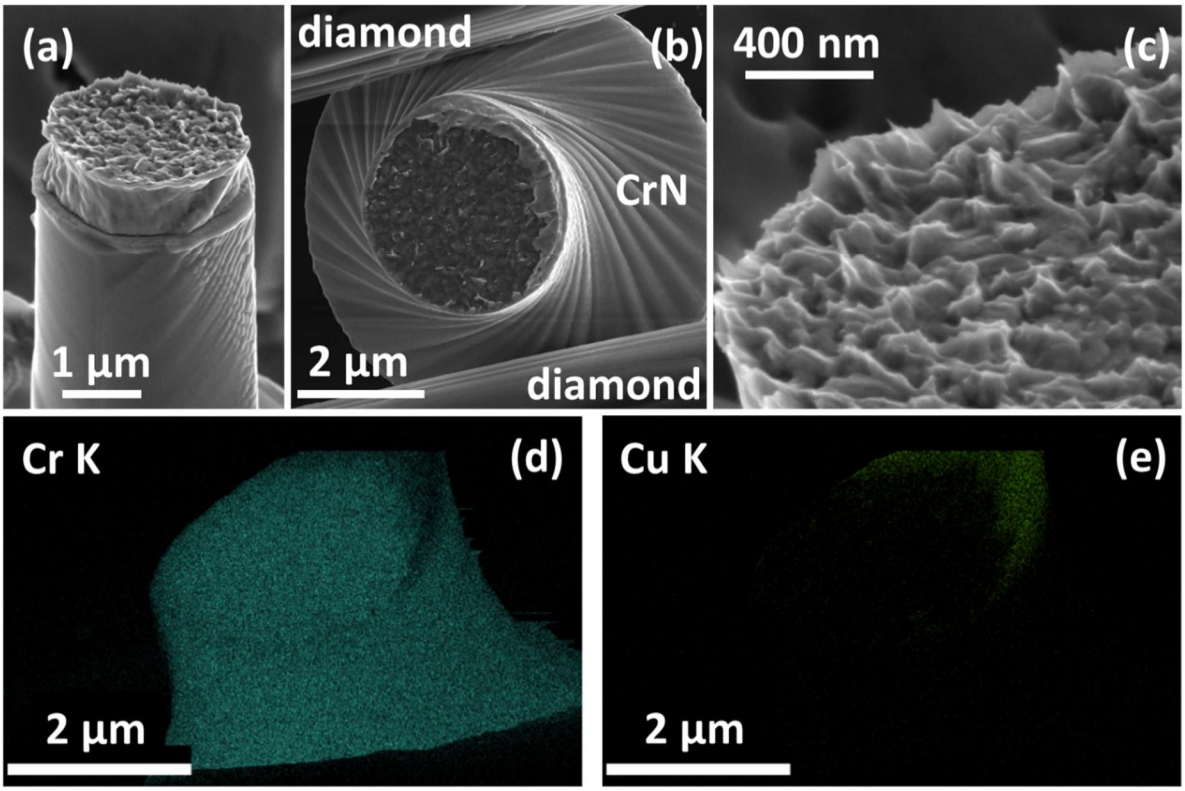

Figure 6. 6 Morphology of tensile failure of CrN/Cu/CrN/Si(001) micro-pillars with h = 980 nm: (a) an SE image of the broken bottom pillar portion connected to the Si substrate; (b) an SE image of the broken top portion of the same pillar; (c) a high-resolution SE image of the surface of the broken bottom pillar portion; (d) the Cr K EDS map of the broken top pillar portion; (e) the Cu K EDS map of the same broken top pillar portion. Image has been adapted with permission from [361].

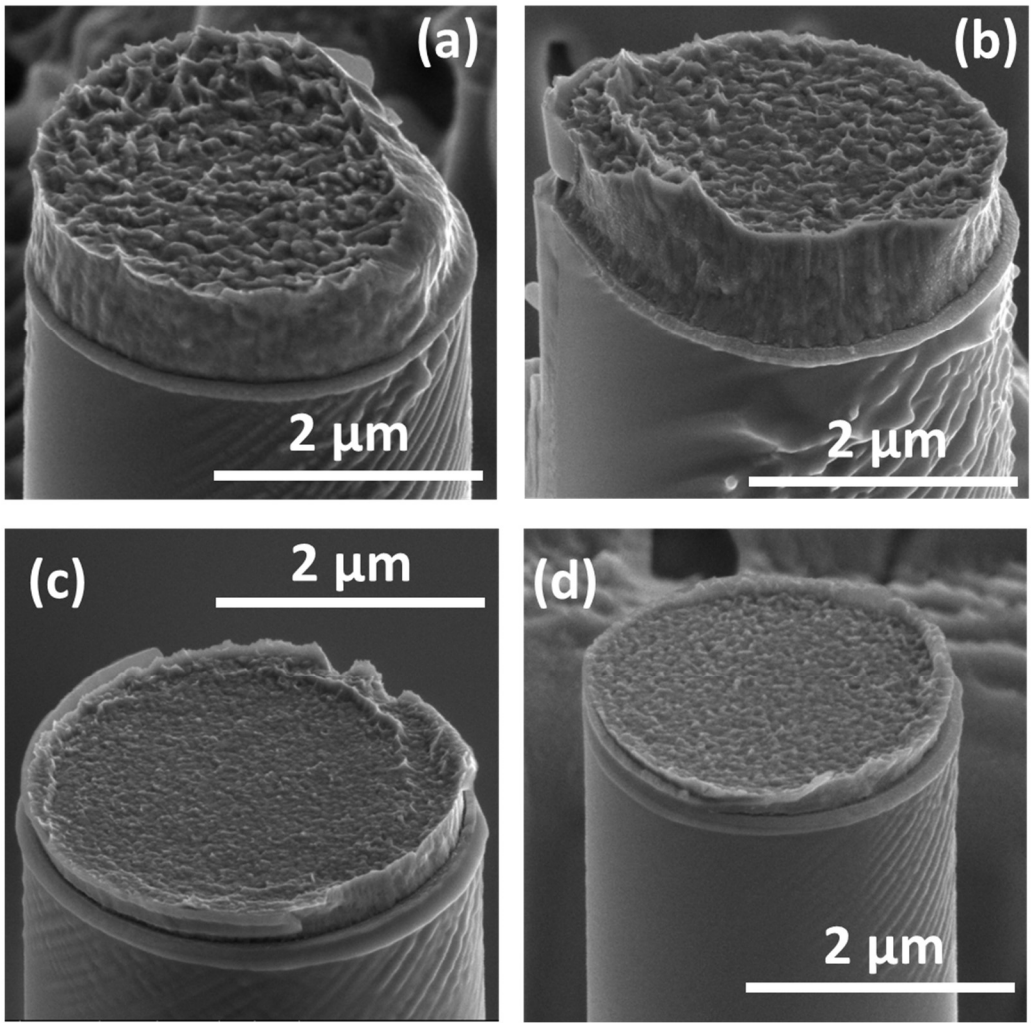

Figure 6. 7 Tensile failure of CrN/Cu/CrN/Si micro-pillar specimens: SE images of pillars at *h* values of (a) 850 nm; (b) 550 nm; (c) 280 nm; (d) 200 nm. Image has been adapted with permission from [361].

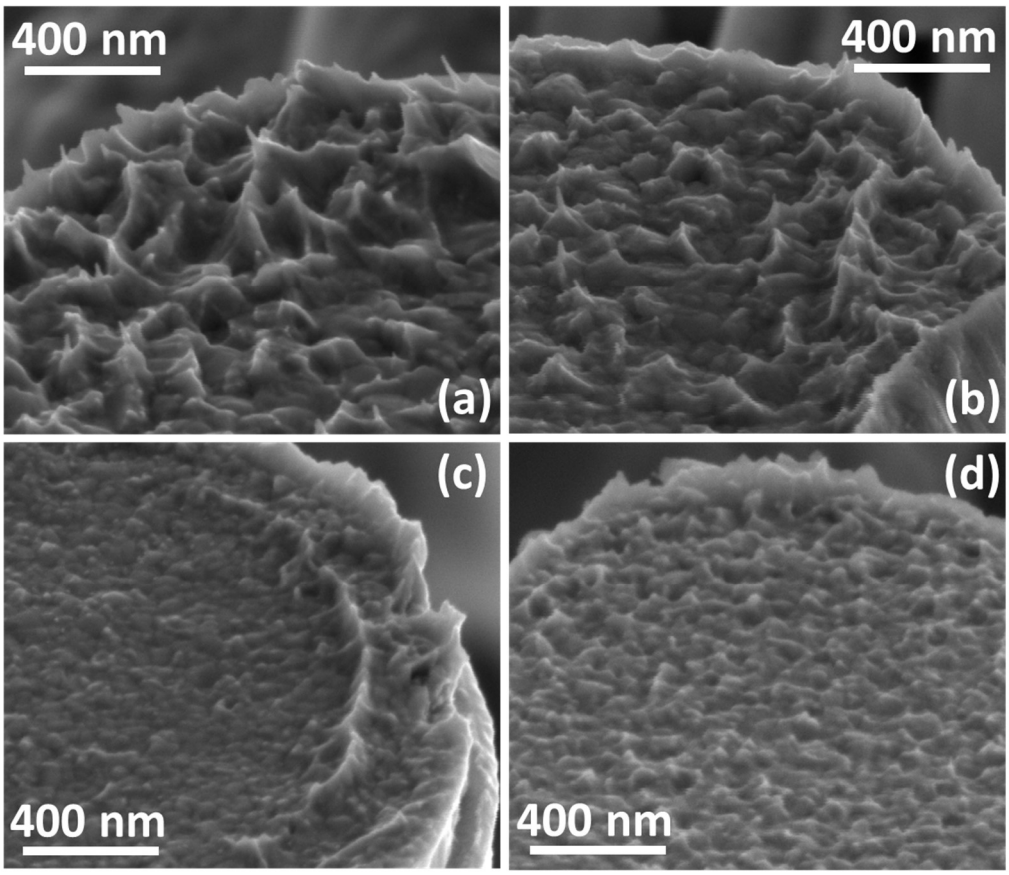

Figure 6. 8 Morphologies of Cu interlayer tensile failure surfaces: high-resolution SE images at *h* values of (a) 850 nm; (b) 550 nm; (c) 280 nm; (d) 200 nm. Image has been adapted with permission from [361].

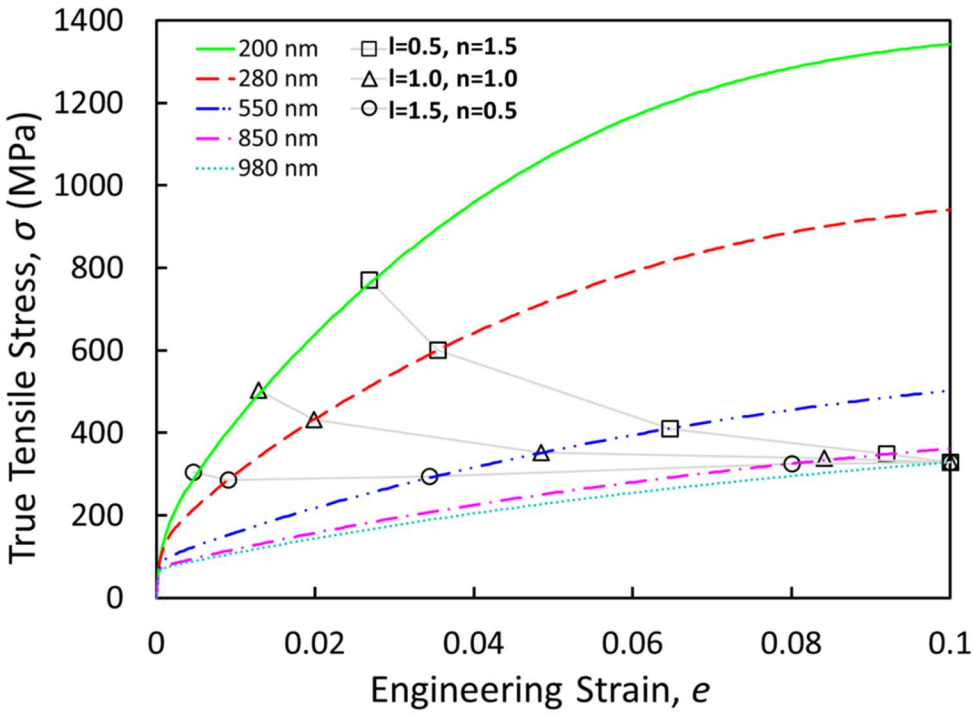

Figure 6. 9 CPFEA output of the stress-strain responses of Cu interlayers of different thicknesses.

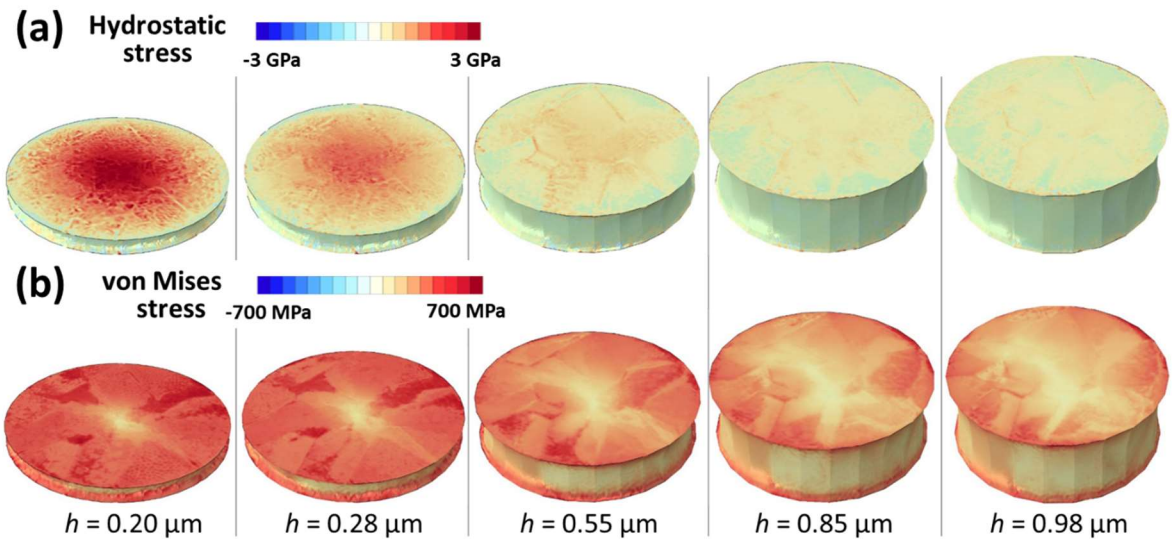

Figure 6. 10 Distribution of hydrostatic (a) and von Mises (b) stress components in the Cu interlayer at an engineering strain of e = 10 %.

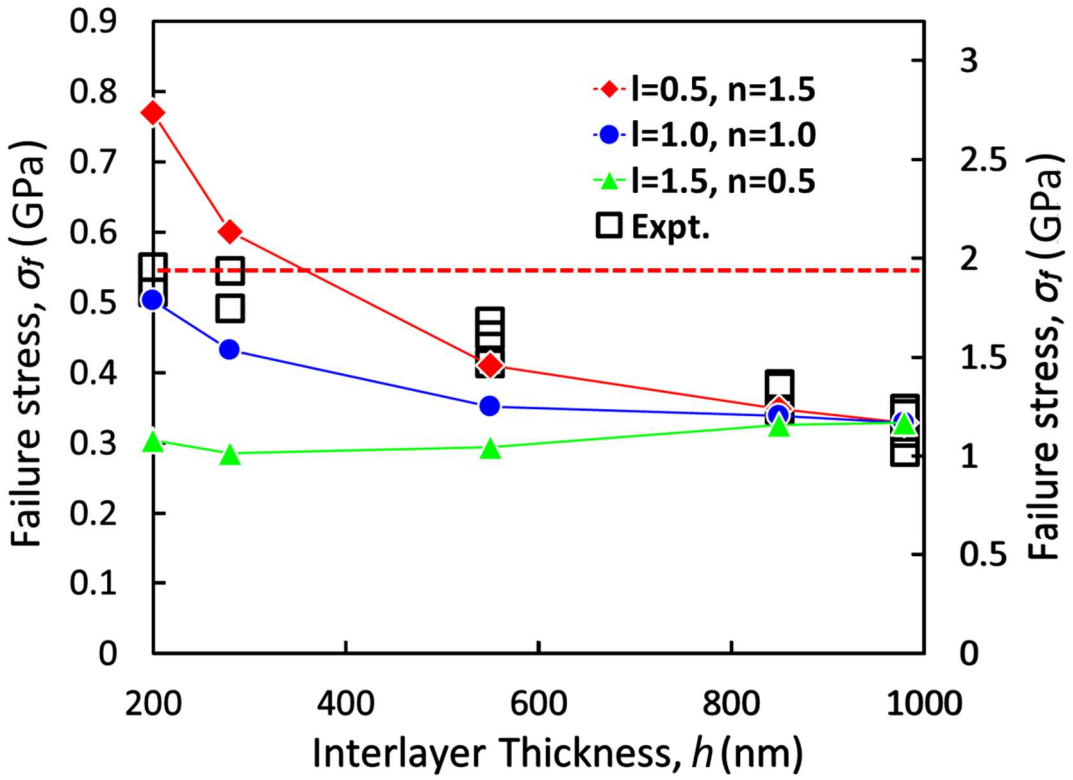

Figure 6. 11 Failure stresses, according to the presently proposed failure criterion, as a function of the Cu interlayer thickness.

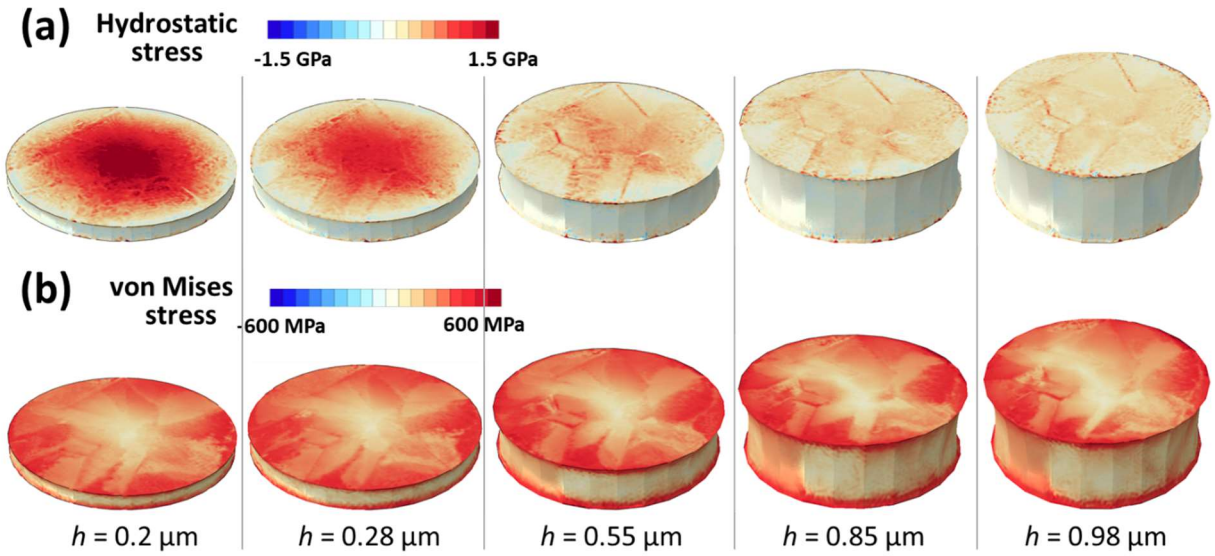

Figure 6. 12 Distribution of hydrostatic (a) and von Mises (b) stress components in the Cu interlayer at the onset of tensile failure.

CHAPTER 7 INVESTIGATING THE INTERACTION BETWEEN PERSISTENT SLIP BANDS AND SURFACE HARD COATINGS VIA CRYSTAL PLASTICITY SIMULATIONS

7.23. Abstract

Fatigue cracks often initiate from the surface extrusion/intrusions formed due to the operation of persistent slip bands (PSBs). Suppression of these surface topographical features by hard surface coatings can significantly extend fatigue lives under lower stress amplitudes (i.e., high cycle fatigue), while cracks initiate early in the coating or in the coating–substrate interface under higher stress amplitudes (i.e., low cycle fatigue), deteriorating the fatigue performance. However, both beneficial and detrimental effects of the coatings appear to be affected by the coating–substrate material combination and coating thickness. A quantitative understanding of the role of these factors in the fatigue performance of materials is still lacking. In this study, crystal plasticity simulations were employed to elucidate the dependence of the coating's effects on two factors—i.e., the coating thickness and loading amplitudes. The results revealed that the thicker coatings more effectively suppress the operation of the PSBs, but generate higher tensile and shear stresses, normal and parallel to the interfaces, respectively, promoting interfacial delamination. The tensile stresses parallel to the interface within the coating, which favors coating fracture, are not sensitive to the coating thickness.

Keywords: crystal plasticity simulations; persistent slip band; surface hard coating; fatigue crack initiation

7.24. Introduction

Fatigue cracks for many metals often initiate from surface markings (i.e., intrusions and extrusions) formed due to cyclic slip localization [2,362]. This localized slip activity is associated with permanent changes in the microstructure of the material developed during the cyclic loading, and the slip markings can re-emerge at the same locations upon reapplication of the load even after surface polishing [6]. Due to their persistent nature, these surface markings are commonly referred to as persistent slip markings (PSMs), and the localized deformation volume is referred to as persistent slip bands (PSBs). Cyclic plastic deformation in the PSBs is typically accommodated by the motion of dislocations on the primary slip system [8,9,363].

For FCC materials, these dislocations have the same Burgers vectors and form very organized bundles known as veins (see Figure 1a). When these bundles collapse along the primary slip direction, PSBs are formed [364]. A typical dislocation microstructure (i.e., the ladder structure) of the PSBs constitutes regularly spaced dislocation walls separating dislocation channels, in which screw "runner" dislocation propagates in a to-and-fro manner. The width of the dislocation channels within PSBs are on the order of 1 μm and is significantly larger than that of the one between dislocation veins. The cyclic plastic deformation therefore localizes at the PSBs [363].

PSBs typically form within a specific range of resolved plastic shear strain amplitude of $\Delta\gamma_{pl}/2 \approx 0.0001\sim0.01$, within which the volume fraction of the PSBs linearly varies from 0% to 100%. The precise values of this range are also material-dependent. This behavior for single-crystal Cu is shown by the cyclic stress–strain curve obtained by Mughrabi [10] (see Figure 1b). Accordingly, the plastic strain amplitude within the PSB is constant at around 1% [365]. In addition, the width of the PSBs is slightly material-dependent but generally invariant with respect to the loading

amplitude. As a result, the change in loading amplitude only alters the PSB density—i.e., the higher the loading amplitude is, the higher the PSB density becomes [10].

In polycrystalline metals, the location of the PSBs may shift from the surface to subsurface under very low stress or strain amplitudes (i.e., in the very high cycle fatigue regime) owing to the absence of global plasticity and the dominance of the subsurface, localized plastic deformations due to the elastic incompatibility among grains or between grains and defects [366]. Thus, the corresponding PSB–grain boundary interaction may lead to subsurface fatigue crack initiation [21]. Nevertheless, the PSM-induced surface crack initiation is still the governing mechanism in the low cycle fatigue (LCF) and high cycles fatigue (HCF) regimes encountered in many engineering applications [16,367,368]. Therefore, any surface treatments that act to suppress or interfere with the formation and/or operation of the PSBs may delay the initiation of fatigue cracks and substantially extend fatigue life. Well-known methods in this regard include intermittent surface repolishing, shot/sand surface peening, and surface hard coatings [6,12,369–372].

Surface repolishing aims to completely remove the PSMs—together with any other roughness created due to cyclic loading—at appropriate intervals mid-service, eliminating any stress concentrations (even crack embryos). Fatigue life had been shown to be extended almost indefinitely using this method, as long as sufficient serviceable material remained [12]. However, this method, due to its subtractive nature, is not suitable for part surfaces that require tight tolerances. Shot/sand peening, on the other hand, is performed prior to service and induces plastic deformation on the surface layer driven by the impact of shot or sand particles, which leaves a compressive residual stress and a refined microstructure on the surface [369,371]. However, this method results in a relatively rough surface finish and is not suitable for mating surfaces. Lastly,

surface hard coatings can circumvent some disadvantages of the other methods because they are generally very thin (a few hundred nm to a μm) and create a smooth surface [372].

There are extensive works focused on examining the effect of various types of coatings—including metallic mono-/multi-layers, ceramic, metallic glass, diamond-like carbon—on the fatigue resistance of metallic specimens [370,373–379]. It has been generally observed that the coatings can improve the HCF performance of the test specimens, while they are often detrimental to the LCF performance. In the LCF regime, higher loading amplitudes tend to induce fracture within the coatings and/or lead to delamination at the coating–substrate interfaces. The precise effect of coatings on the fatigue resistance of a material greatly depends on several factors, including the coating–substrate material combination, mechanical properties and thickness of the coating, and the binding and shear strengths of the coating–substrate interface, etc. [370,372,380]. However, due to the time-intensive nature of the fatigue data generation, systemic evaluations of the influence of the aforementioned factors are still lacking.

Using crystal plasticity (CP) simulations, we aim to elucidate the effect of the coating thickness and the applied cyclic plastic strain amplitude on several characteristics of PSB–coating interaction that tend to influence the fatigue performance of coated materials. These characteristics include (1) the suppressive effects of coatings on the operation of PSBs, (2) the normal stress developed in the coating layer along the loading direction, (3) the interfacial normal stress developed perpendicular to the interface, and (4) the interfacial shear stress developed parallel to the interface. The first characteristic retards, while the rest accelerate, the initiation of fatigue cracks in the substrate. This work by no means attempts to perform direct CP simulations of fatigue failure of coated metallic materials. Instead, it focuses on the interaction between the coating and the PSBs under different loading amplitudes and aspires to generate an understanding that may

benefit the geometrical design and material selection of the coatings. Indeed, cyclic damage (in the forms of dislocations and vacancy) accumulates during each cycle via cyclic plasticity and, upon reaching a critical level, leads to the initiation of fatigue cracks [35,381]. The surface coatings' suppression of the plastic deformation per cycle is therefore indicative of the coatings' beneficial effects on a part's overall fatigue resistance. As such, instead of simulating the accumulation of cyclic damage over the entire fatigue life, this work only considers the loading portion of a single cyclic loading period after the PSBs has formed.

7.25. Computational Methods

CP simulations were performed using the Düsseldorf advanced material simulation kit (DAMASK) developed by the Max-Planck-Institut für Eisenforschung [382]. Spectral solver based on fast Fourier transform (FFT) implemented in the Portable, Extensible Toolkit for Scientific Computation (PETSc) was utilized to solve for the displacement field [383,384]. The simulation model is composed of substrates made of a single crystalline austenitic stainless steel (SS) 316 and physical vapor-deposited (PVD) thin Cr coatings. Prior literature has indicated that the common PVD Cr coatings are nanocrystalline and exhibit isotropic mechanical behavior [372].

7.25.1. Model Setup

Figure 2 illustrates the geometries of the simulation model. To investigate the characteristics of the interaction between PSBs and surface coatings, only the tensile loading portion of one fatigue cycle is applied. The intended boundary conditions (BCs) on the lateral coating surfaces are free—i.e., the surface tractions are zero. A rate-controlled uniaxial tension was applied by enforcing only the zz component of the deformation gradient rate tensor ($\dot{F}_{zz}$), while ensuring that $\sigma_{xx} = 0$ and $\sigma_{yy} = 0$. Since this work employed the spectral solver implemented in PETSc, which imposed a full periodic BC on the computational cells [382], the presence of free surfaces was mimicked by adding two soft ~1-μm thick buffers layers on both sides of the sample (see Figure

2a), which is similar to the approach by [363,385,386]. A strong contrast in elastic moduli and strengths existed between the buffer layers and the samples (the elastic constants were at least one order of magnitude lower and the strengths were at least three orders of magnitudes lower for the buffer layer). The effective BCs are therefore free, periodic, and periodic in the x-, y-, and z-directions, respectively.

To conserve computational resources, the y-dimension of the simulation cells was minimized and kept constant at ~0.2 μm. Thus, the models were thin slab-shaped. The width of the substrate along the x-direction was also kept constant at ~34 μm. The PSBs were modeled to be 45° off the loading axis (z) and to have a constant thickness of t_{PSB} = 1 μm in accordance with direct experimental observations in the open literature. Indeed, for metallic materials such as Cu, Ni, and SS 316, the thickness of the PSBs was ~1 μm [16,387]. Constrained by the periodic BC, the height of the models along the z-direction was dictated by the thickness (t_{PSB}) of and spacing (d_{PSB}) between the PSBs—i.e., $h = \sqrt{2}\,(t_{PSB} + d_{PSB})$. The spacing d_{PSB} varied between 1 and 8 μm, which corresponds to a PSB volume fraction of 50%~11%, and an overall shear plastic strain range of approximately $\Delta\gamma_{pl}$ = 0.01~0.002 assuming a 0.01 plastic strain amplitude in the PSBs. Three different coating thicknesses (t_{coat}), namely 0.5, 1.0, and 2.0 μm, were considered here. These parameters of the models are listed in Table 1.

Both isotropic and anisotropic plastic flow rules have been utilized in the models. The buffer layers and the coatings were treated by isotropic plasticity. This assumption is sound since the buffer layers only have marginal resistance to deformation and the nanocrystalline Cr coatings exhibit isotropic mechanical behavior. Correspondingly, the plastic flow rule is written as [382]

$$\dot{\gamma}_p = \dot{\gamma}_0 \left(\frac{\sqrt{3J_2}}{M\xi} \right)^n, \tag{1}$$

where $\dot{\gamma}_p$ is the plastic shear strain rate, $\dot{\gamma}_0$ is a reference strain rate, n is the stress exponent, J_2 is the second invariant of the deviatoric stress tensor, and M is the Taylor factor. The ξ term in the denominator is the resistance to plastic flow. The rate of ξ is given as

$$\dot{\xi} = \dot{\gamma}_p h_0 \left| 1 - \frac{\xi}{\xi_\infty} \right|^a \operatorname{sgn}\left(1 - \frac{\xi}{\xi_\infty}\right), \tag{2}$$

where $\dot{\gamma}_p$ is the plastic shear strain rate, h_0 is the strain hardening coefficient, ξ_∞ is the saturation resistance to plastic flow, and a is a material-dependent exponent.

Anisotropic plasticity was used for the substrate (including both the matrix and the PSBs) and a phenomenological hardening law was used. The flow rule is written as

$$\dot{\gamma}_p^\alpha = \dot{\gamma}_0^\alpha \left| \frac{\tau^\alpha}{\xi^\alpha} \right|^n \operatorname{sgn}(\tau^\alpha), \tag{3}$$

where τ^α is the resolved shear stress on the slip system α, ξ^α is the slip resistance on the slip system, $\dot{\gamma}_0^\alpha$ is the reference strain rate, and n is the stress exponent. Since only the loading portion of a cyclic loading period was modeled, the back-stress term—which is necessary to capture the kinematic hardening effect in cyclic loading—is not included in the present study. The rate form of the resistance ξ^α is given as

$$\dot{\xi}^\alpha = {h_0}^{s-s} \sum_{\alpha'=1}^{N_s} \left| \dot{\gamma}^{\alpha'} \right| \left| 1 - \frac{\xi^{\alpha'}}{\xi_\infty^{\alpha'}} \right|^a \operatorname{sgn}\left(1 - \frac{\xi^{\alpha'}}{\xi_\infty^{\alpha'}}\right) h^{\alpha\alpha'}, \tag{4}$$

where $\dot{\gamma}^{\alpha'}$ is shear strain rate on the slip system α', ξ_∞ is the resistance saturation value, $h^{\alpha\alpha'}$ is the slip hardening matrix (including both self- and latent hardening), and a is a material-dependent exponent.

The elastic and plastic flow constants used for the SS 316, PSB, coatings, and buffer layers are summarized in Table 2 and Table 3. The stress–strain behaviors produced by the elastic and plastic constants are shown in Figure 3. The elastic constants of both the Cr coating and the SS 316 substrate (including both the PSBs and the matrix) were obtained from the open literature [1,226,388]. To obtain the plastic flow constants of SS 316, the stress–strain response of a "virtual single crystal"—which was an average of many tensile tests (>50) on single crystals of randomized orientations under the isostrain assumption—was fitted to an experimental curve [389–391]. This technique, also referred to as the "material point" simulation, is a standardized practice to establish flow constants for crystal plasticity simulations [339,382,392].

PSBs within the substrate were modeled as different materials with identical elastic constants and crystallographic orientations but lower shear resistances (~100 MPa in the PSBs compared to ~300 MPa in the matrix) on the primary slip system. As discussed in the introduction, due to the wider dislocation channels within the PSB compared to the matrix, the PSBs have substantially lower critical resolved shear stress (CRSS). The applied overall strains are therefore localized within the PSBs. For pure Cu, Ni, and Ag, the respective CRSSs are ~30, 50, and 20 MPa [393]. As for SS316, the CRSS of PSBs is not known to the authors' best knowledge and must be assumed. Considering the solid solution strengthening effect in SS316, the highest known CRSSs among the three aforementioned elemental metals, i.e., 50 MPa of Ni, was used. Assuming a Schmid factor of 0.5 (which applies for the current model geometries), the corresponding tensile yield strength is 100 MPa. As will be shown in Section 3, this choice of the CRSS appears to be sufficient to capture the strain localization within the PSBs. The slip activity on the secondary systems was completely suppressed by applying much higher critical resolved shear stresses (~40

GPa). The plastic flow constants of the coating and the buffer layer were calibrated so that they reproduce yield strengths of 750 and ~0 MPa, respectively.

Note that the crystallographic orientation of the substrate must be defined carefully, so that the primary slip system in the PSB experiences maximum shear stress under the tensile loading applied (see Figure 2b). In other words, the primary slip direction and slip plane should both be 45° off the loading axis. A cubic grid with the characteristic size ~0.09 × ~0.09 × ~0.09 μm has been chosen for all the models, leading to 2 Fourier points (FPs) along the y-direction, 400 to 440 (FP) along the x-direction, and 30 to 135 (FP) along the z-direction. The one-FP per voxel configuration is comparable to the one-integration point, C3D8R finite element type (according to ABAQUS), which was emulated in the model setup by DAMASK [394].

7.25.2. Post-Processing

The results were visualized using the open-source software package Paraview [395]. In all of the visualizations, the buffer layers have been removed to avoid any confusion. All the results visualized correspond to a specific point in the loading history, i.e., when the average shear strain in the primary slip system in the PSBs equals ~1%. Therefore, PSB volume fractions of 50%~11% correspond to overall shear plastic strain ranges of approximately $\Delta\gamma_{pl}$ = 1%~0.2%. Due to the presence of the coatings, the shear strain on the active slip system within the PSBs may vary depending on the distance to the coating–substrate interface. To assess the suppressive effect of coatings on the operations of PSBs, the plastic strain within the PSBs were plotted as a function of the x-coordinate. For this purpose, the PSBs were sliced into discrete bins of equal thickness along the x-direction. Average shear strain on the primary slip system was then obtained for each bin.

7.26. Results and Discussion

The results of the simulations were analyzed with respect to four characteristics of the coating–PSB interaction—i.e., (1) the suppressive effects of coatings on the operation of PSBs, (2) the normal stress developed in the coating layer along the loading direction, (3) the interfacial normal stress developed perpendicular to the interface, and (4) the interfacial shear stress developed parallel to the interface. For instance, typical results, including the distributions of shear strain, as well as shear and normal stresses of three selected simulations, are shown in Figure 4 for three cases: (a) t_{coat} = 0.5 μm, d_{PSB} = 1 μm, and $\Delta\gamma_{pl}$ = 0.01, (b) t_{coat} = 0.5 μm, d_{PSB} = 8 μm, and $\Delta\gamma_{pl}$ = 0.002, and (c) t_{coat} = 2 μm, d_{PSB} = 1 μm, and $\Delta\gamma_{pl}$ = 0.01, respectively. Note that the d_{PSB} and $\Delta\gamma_{pl}$ parameters are coupled, as discussed in the previous section. Apparently, all these characteristics appear to be influenced by both the coating thickness and overall loading amplitude (reflected in the density of PSBs). In what follows, we analyze and discuss these influences from the four aforementioned aspects.

7.26.1. Suppressive Effects of the Coating on the Operation of PSBs (Distribution of Plastic Shear Strain in the PSBs)

Comparing the first column of Figure 4a, 4c, it is apparent that the thicker coating (t_{coat} = 2 μm) inhibited the slip activities ($\gamma_{primary}$) within the PSB, especially at locations near the coating–substrate interfaces. As expected, this suppression effect was attenuated with the increase in the strain amplitude applied (compare Figure 4a, 4b, which represented higher and lower applied strain amplitudes, respectively). To quantitatively compare the suppressive effect of the coatings, the plastic shear strain on the primary slip system within the PSBs are plotted in Figure 5 as a function of the distance from the coating–substrate interface along the x-direction. The plots were generated using the binning analysis, described in Section 2.2. Each panel of the figure corresponds to a different PSB spacing (d_{PSB}) and, accordingly, a different applied plastic strain range ($\Delta\gamma_{pl}$). The

plots were obtained at the point of loading history which corresponds to an average of ~1% plastic shear strain over the entire PSBs.

The qualitative observations made in Figure 4 are echoed in Figure 5. Coatings with increasing thickness had stronger suppression effects on the operation of PSBs. This is reflected by the consistently lower shear strain magnitudes in PSBs that interacted with thicker coatings. Comparing Figure 5a–5d), the suppression effects were attenuated significantly with the increasing applied strain amplitude. This is concomitant with the increasing plastic shear strain in the PSBs near the coating–substrate interfaces as the loading amplitude increases. For instance, at a lower applied strain range (such as at 0.002 for the case of d_{PSB} = 8 μm as shown in Figure 5d), the coatings had a profound effect suppressing the plastic shear strains near the coating–substrate interface. With a coating thickness of 0.5 μm, the shear strain within the distance of 0.5 μm from the interface was lower than the prescribed 1% magnitude. With a coating thickness of 2 μm, this distance extended beyond 2 μm. However, at a higher applied plastic shear strain range of 0.01, this distance reduced to 0.13 μm for the thinner coating and ~1.3 μm for the thicker coating, shown in Figure 5a. The attenuation at higher strain amplitudes (smaller d_{PSB}) can be ascribed to the close coupling of neighboring PSB–substrate interactions, which induced larger elastic deflections within the coatings. As will be demonstrated in the later sections, this coupling also influences the stresses at/near the coating–substrate interfaces.

7.26.2. Fracture Tendency within the Coatings (Distribution of σzz in the Coatings)

Hard coatings, especially ceramic ones, may fracture from pre-existing flaws due to tensile stresses parallel to the coating layer. As shown in the third column of Figure 4a, 4b, the tensile stress (σ_{zz}) in the coating appear to rise at the locations where PSBs intersect with the coating for specimens at a small coating thickness of t_{coat} = 0.5 μm. In addition, due to the load transfer from the substrates to the coatings, σ_{zz} is discontinuous across the interface. Due to the superposition of

the neighboring PSB–coating interactions, the maximum σ_{zz} may be higher at a smaller PSB spacing (higher applied strain ranges). As an example, the profiles of σ_{zz} in the coating near the interface along the z-direction (i.e., values on the dashed lines shown in Figure 4) are plotted in Figure 6 for the 0.5-μm thick coating.

The observations made from Figure 4 are confirmed in the σ_{zz} profiles shown in Figure 6, noting the values of the stress within the blue shades (locations on the interfaces where PSBs intersect with the coatings). At higher applied strain amplitudes (such as the 0.01 plastic strain range reflected by d_{PSB} = 1 μm, Figure 6a), both the overall and the peak values of the σ_{zz} are higher compared to lower applied strain amplitudes, indicating a higher tendency to develop tensile fracture, as expected. Figure 7a shows the variation of the peak σ_{zz} values as a function of d_{PSB} (reflecting the applied strain amplitude $\Delta\gamma_{pl}$), demonstrating a similar decreasing trend of the peak σ_{zz} with increasing d_{PSB} for all t_{coat} values.

Comparing the third column of Figure 4c with that of the Figure 4a, 4b, it is interesting to note that when the thickness of the coating is large, the distribution of the σ_{zz} within the coating is less influenced by the presence of the PSBs. For instance, Figure 8 shows the profiles of σ_{zz} in the coating along the z-direction at both the surface and the interface. In both coating thicknesses shown, the profiles of σ_{zz} in the coatings at the interface were nearly identical (see the thick and the thin dashed lines). However, for the case of a thin coating (t_{coat} = 0.5 μm), significant variations in the stress can be observed on the surface (thin solid line). However, when the coating is thick (t_{coat} = 2 μm), σ_{zz} is approximately invariant at the surface (thick solid line). The combined observations made in the third column of Figure 4 and in Figure 8 imply that a coating's sensitivity to the presence of a potential surface flaw in the coating is different for different coating thicknesses. For instance, a thinner coating only experiences higher tensile stresses near the PSBs,

a flaw at other locations may still be relatively safe and may not lead to early onset of fracture. On the other hand, the tensile stress on the surface of thicker coatings is uniform which makes thick coatings more susceptible to tensile fracture from surface flaws.

To further investigate the variation of σ_{zz} at different locations within the coating, its standard deviation (SD) along the z-direction for all model geometries was calculated. Figure 9 shows the SD of σ_{zz} at interface and the coating surface with respect to the ratio of d_{PSB} to the coating thickness t_{coat} (i.e., $\lambda = d_{PSB}/t_{coat}$). It is evident that, as the ratio λ increases (i.e., thickness of the coating decreases with respect to the PSB spacing), the variation of σ_{zz} along the z-direction at the coating surface significantly increases. On the other hand, the variation of σ_{zz} at the interface is always quite significant and is not affected by λ. This agrees with the observations made earlier in Figure 8.

7.26.3. Delamination Tendency at the Coating–Substrate Interface

The tendency for coating–substrate delamination was assessed by evaluating the interfacial stresses σ_{xx} and τ_{xz}, which were perpendicular and parallel to the interfaces, respectively. As shown in Figure 4, due to the model setup of a perfectly bonded interface, both σ_{xx} and τ_{xz} stress components were continuous across the interface. Similar to the behavior of σ_{zz}, σ_{xx} appeared to slightly increase when the loading amplitude increased (i.e., when d_{PSB} decreased). Interestingly, the magnitude of τ_{xz} showed an opposite trend—it appeared to decrease when the loading amplitude increased (i.e., when d_{PSB} decreased). This can be seen by comparing Figure 4a, 4b in the second and the fourth columns. The opposite trends observed here may be ascribed to the "symmetries" in the σ_{xx} and τ_{xz} values on both sides of the location where the PSBs intersect with the coating.

In Figure 6, the profiles of σ_{xx} and τ_{xz} at the interface along the z-direction (i.e., values on the dashed lines shown in Figure 4) are plotted for the 0.5-μm coating thickness. At the PSB spacing

of 8 μm, the interfacial stresses induced by an individual PSB is clear (see Figure 6d). The sign of the τ_{xz} component is opposite at the locations left and right of the intersection between the PSB and coating (see the red and blue arrows marking the $\pm\tau_{xz}$). On the other hand, the sign of the σ_{xx} is the same on the left and right of this intersection—i.e., both values are positive (see the red arrows marking the $+\sigma_{xx}$ in Figure 6d). As a result, when the density of the PSB increases, the superposition of the stress fields from neighboring PSB–coating interactions increases the maximum magnitude of σ_{xx} and reduces the maximum magnitude of the τ_{xz}. The variation of the maximum σ_{xx} and τ_{xz} stresses are discernable from Figure 6 by comparing the four panels. In addition, the magnitude of both stress components also increased with increasing coating thickness (compare Figure 4a, 4c in the second and fourth columns). The σ_{xx} and τ_{xz} appeared to somewhat signify the "suppressive" action of the coatings—as a function of the thickness—on the operations of the PSBs (compare Figure 4 and Figure 5). In other words, the suppressive effects tend to be stronger when the values of these stresses increase.

For a clearer comparison, the peak values of these stresses for all the simulations have been obtained and plotted in Figure 7b, 7c. The substantial increases in the peak σ_{xx} and τ_{xz} values due to the increase in the coating thickness are also evident. The combined action of the two stresses may be responsible for the delamination of the coating–substrate interface. This is in line with the critical plane approach put forth by Fatemi and Socie [396], which stated that the planes with large plastic shear strain and large normal stress tend to initiate fatigue cracks.

Figure 5 has shown that the suppression imposed by the coating on the operation of the PSBs is more effective at larger coating thicknesses. Nevertheless, excessively thick coatings are associated with the risk of early crack initiation due to coating tensile fracture (with pre-existing surface flaws) and coating–substrate delamination (due to the combined action of both tensile and

shear stresses at the interface). Therefore, thicker coatings are only preferred if a coating with higher fracture toughness as well as an ideal coating–substrate adhesion can be achieved. Otherwise, thicker coatings may be detrimental to the fatigue performance of the coated parts.

On the other hand, while the applied plastic shear strain range is expected to monotonically affect the tendency of tensile fracture in the coating (i.e., higher amplitude leads to easier fracture), its effect on coating–substrate delamination may be more complex. Since the increase in the applied strain range decreases τ_{xz} but increases σ_{xx}, there may exist an intermediate plastic shear strain amplitude that favors delamination the most, assuming that the interfacial delamination is driven by the combined action of normal and shear stresses.

7.27. Conclusions

Crystal plasticity-based simulations were used to investigate the suppressive effects of coatings on the operation of surface PSBs. The impact of both coating thickness and the applied strain amplitude (reflected by a variable density of PSBs) on the suppressive effects were evaluated. Four characteristics of the PSB–coating interactions—including (1) the suppressive effects of coatings on the operation of PSBs, (2) the normal stress developed in the coating layer along the loading direction, (3) the interfacial normal stress developed perpendicular to the interface, and (4) the interfacial shear stress developed parallel to the interface—were investigated.

The following conclusions can be drawn from this research:

(1) Assuming a perfect coating–substrate adhesion and the absence of coating fracture, thicker coatings offered better suppression against the plastic shear deformation of the PSBs.

(2) The suppression effects of the coatings were attenuated at higher applied plastic shear strains (higher PSB densities).

(3) The distribution of the normal stress parallel to the loading direction in thinner coatings was highly heterogeneous and was strongly affected by the PSBs. However, the distribution of this stress was much more uniform for thicker coatings.

(4) The interfacial shear stress parallel to the loading direction and the interfacial normal stress perpendicular to the interface increased significantly with increasing coating thickness, which can potentially result in delamination.

(5) The peak values of the stresses mentioned in Conclusions (3) and (4) varied differently with increasing applied strains due to the superposition of the stress fields caused by the neighboring PSB–coating interactions.

In general, although thicker coatings may be beneficial to the fatigue performance of the coated parts, excessive coating thickness can lead to early crack initiation due to coating tensile fracture and coating–substrate delamination. The beneficial effect of the coatings on fatigue performance therefore is limited by the fracture toughness of the coating, and the adhesion strength of the coating–substrate interfaces. Therefore, the enhancement in the fatigue performance of a coating–substrate system hinges upon the careful selection of the correct coating–substrate material combination as well as the appropriate coating thickness.

Author Contributions: Conceptualization, S.S., J.W., and N.S.; methodology, S.S.; validation, M.S.D. and S.S.; formal analysis, M.S.D., S.S., J.W., and N.S.; investigation, M.S.D., S.S., J.W., and N.S.; resources, S.S., N.S., and J.W.; data curation, M.S.D. and S.S.; writing—original draft preparation, S.S.; writing—review and editing, M.S.D., S.S., J.W., and N.S.; visualization, M.S.D. and S.S.; supervision, S.S. and N.S.; project administration, S.S., J.W., and N.S.; funding acquisition, S.S., J.W., and N.S. All authors have read and agreed to the published version of the manuscript.

Tables

Table 7. 1 Design of simulations performed in the current study. The meaning of t_{PSB} and d_{PSB} are shown in Figure 2b.

t_{PSB} (μm)	**d_{PSB} (μm)**			
0.5	1	2	4	8
1	1	2	4	8
2	1	2	4	8

Table 7. 2 Anisotropic elastic and plastic material constants used for SS316 substrate (including PSB).

Material	C_{11} **(GPa)**	C_{12} **(GPa)**	C_{44} **(GPa)**	$\dot{\gamma_0}$ **(1/sec)**	n	ξ_0 **(MPa)**	ξ_∞ **(MPa)**	a	h_0 **(MPa)**
SS 316 matrix	207.0	133.0	117.0	0.001	20.0	115.0	430.0	2.25	50.0
PSB primary	207.0	133.0	117.0	0.001	50.0	40.0 [1]	400.0[1]	2.25	50.0

[1] These values are for the primary slip system in the PSB. The slip activities in the secondary slip systems were suppressed by using much higher slip resistances (at least 1000 times higher).

Table 7. 3 Isotropic elastic and plastic material constants used for the buffer layers and coatings.

Material	C_{11} **(GPa)**	C_{12} **(GPa)**	$\dot{\gamma_0}$ **(1/sec)**	M	n	ξ_0 **(MPa)**	ξ_∞ **(MPa)**	a	h_0 **(MPa)**
Buffer	20.0	10.0	0.1	3	5	3.0	6.3	2.5	7.5
Coating	279.0	115.0	0.001	30	20	20.0 [1]	100.0 [1]	2.5	18.0

[1] Although the ξ_0 and ξ_∞ appear to be quite low, when combined with the M and n, they produced a true yield strength of 750 MPa and a strength of 2.5 GPa at 0.5 strain (see Figure 3).

Figures

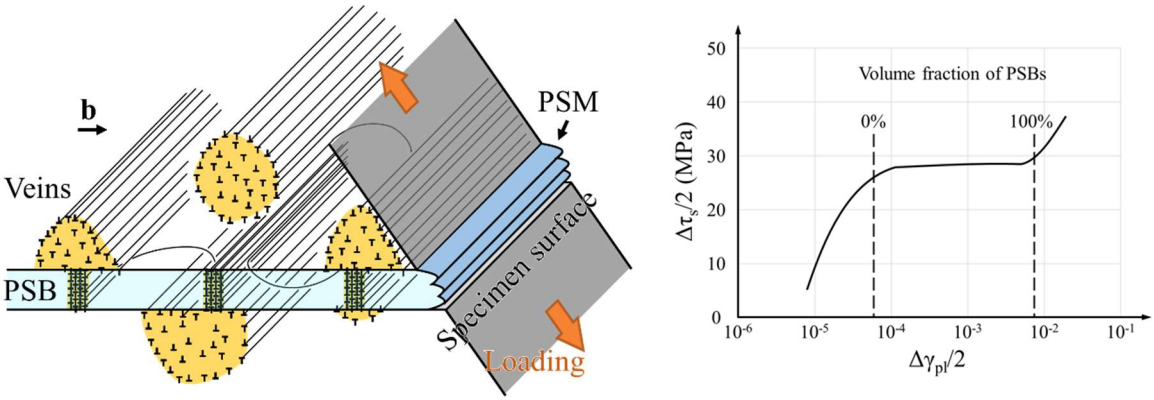

(**a**) (**b**)

Figure 7. 1 (a) A schematic illustration of a persistent slip band (PSB), vein structure, specimen surface, and the surface persistent slip marking (PSM). (b) The cyclic stress–strain curve of single-crystal Cu [8].

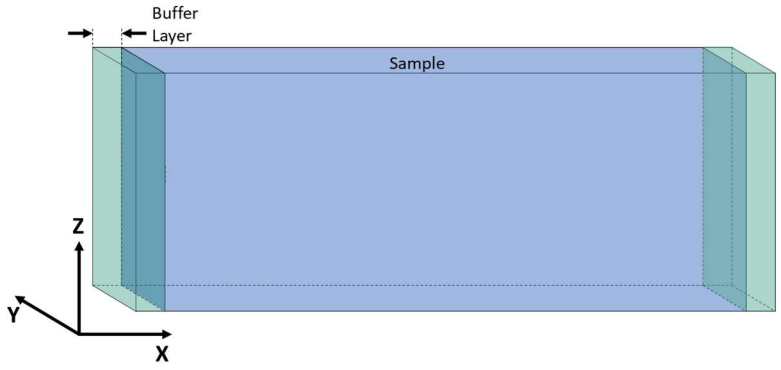

(**a**)

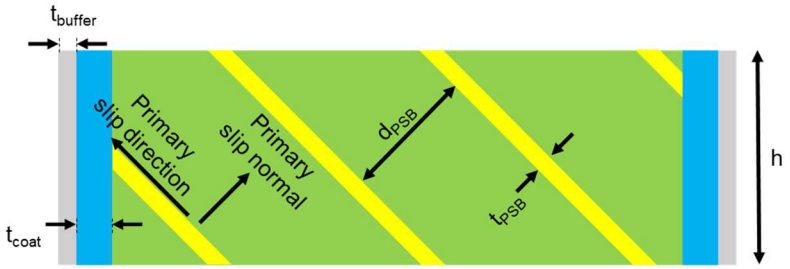

(**b**)

Figure 7. 2 Schematic representation of model geometries: **(a)** a three-dimensional view of the overall geometry of the models omitting the details of the sample, and **(b)** the front view of the simulation cells highlighting the interior geometry and dimensions of the sample.

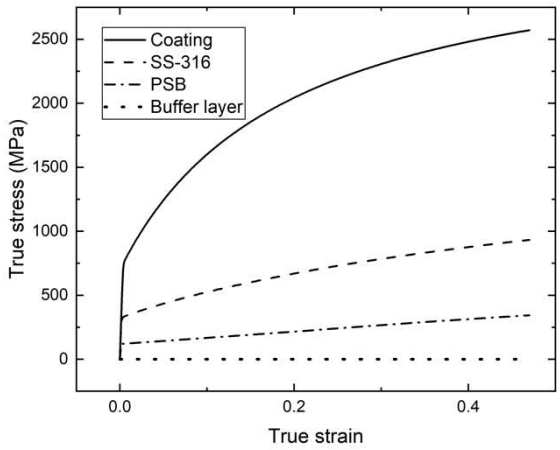

Figure 7. 3 The stress–strain responses of the four material types considered in this study.

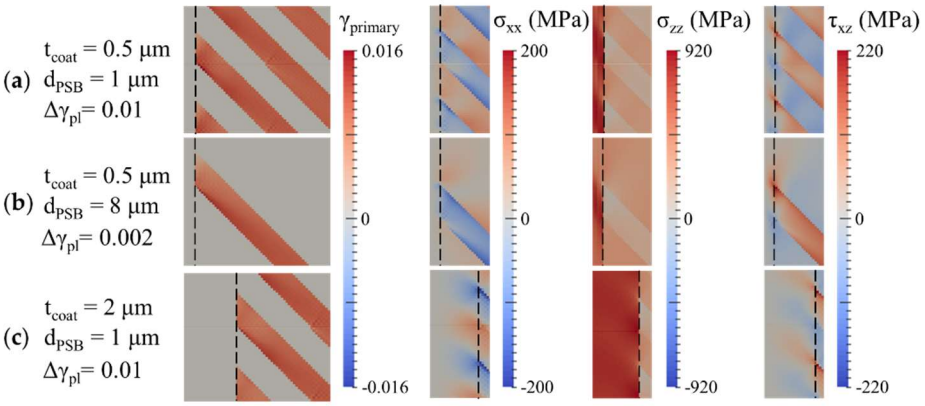

Figure 7. 4 Contour plots of shear strains within the PSBs, as well as normal and shear stresses near the coating–substrate interfaces (marked using the black dashed lines) for four cases of simulations: (a) t_{coat} = 0.5 µm, d_{PSB} = 1 µm, and $\Delta\gamma_{pl}$ = 0.01, (b) t_{coat} = 0.5 µm, d_{PSB} = 8 µm, and $\Delta\gamma_{pl}$ = 0.002, and (c) t_{coat} = 2 µm, d_{PSB} = 1 µm, and $\Delta\gamma_{pl}$ = 0.01.

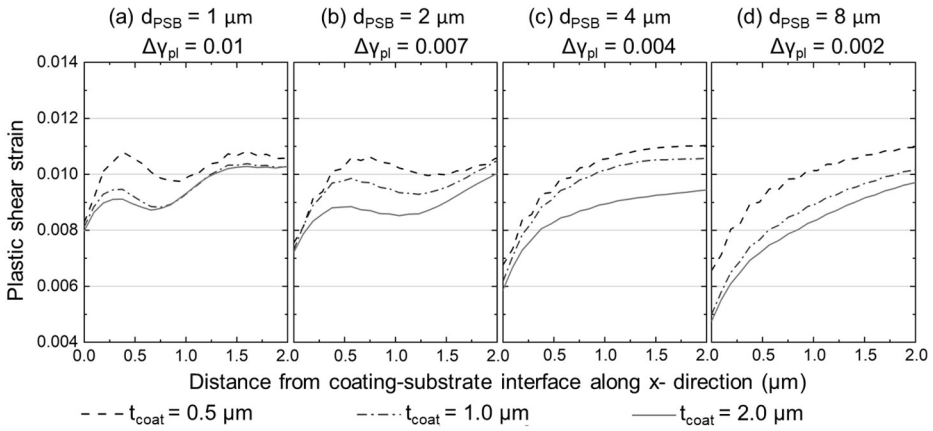

Figure 7. 5 Distribution of shear strain along x on the primary slip system within the PSBs for various PSB spacings and equivalent applied plastic strain ranges: (**a**) d_{PSB} = 1 μm and $\Delta\gamma_{pl}$ = 0.01, (**b**) d_{PSB} = 2 μm and $\Delta\gamma_{pl}$ = 0.007, **(c)** d_{PSB} = 4 μm and $\Delta\gamma_{pl}$ = 0.004, and (**d**) d_{PSB} = 8 μm and $\Delta\gamma_{pl}$ = 0.002.

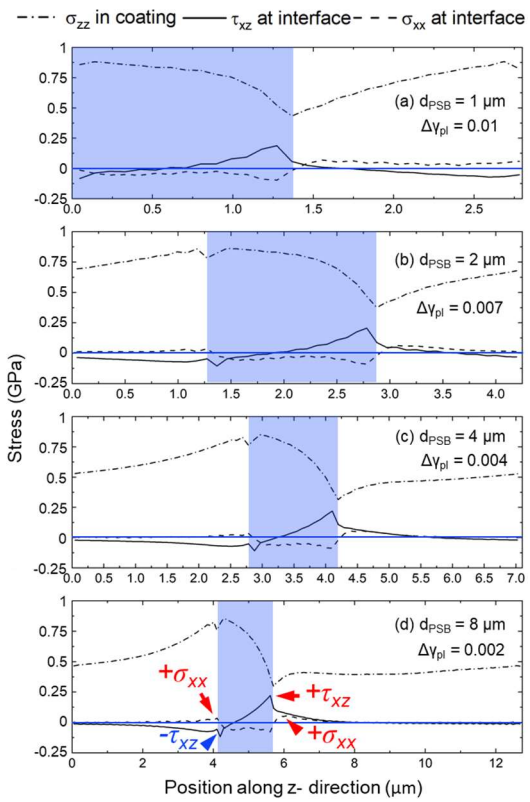

Figure 7. 6 Stress profiles, including the σ_{zz} in the coating near the interface, σ_{xx} at the interface, and τ_{xz} at the interface, of the computational cells with 0.5-μm coating thickness. The blue shades indicate the locations where the PSBs intersect with the coatings. Note that the horizontal axes are not of the same scale, which led to their different appearance in thickness. The four panels respectively show data for (a) d_{PSB} = 1 μm and $\Delta\gamma_{pl}$ = 0.01, (b) d_{PSB} = 2 μm and $\Delta\gamma_{pl}$ = 0.007, (c) d_{PSB} = 4 μm and $\Delta\gamma_{pl}$ = 0.004, and (d) d_{PSB} = 8 μm and $\Delta\gamma_{pl}$ = 0.002.

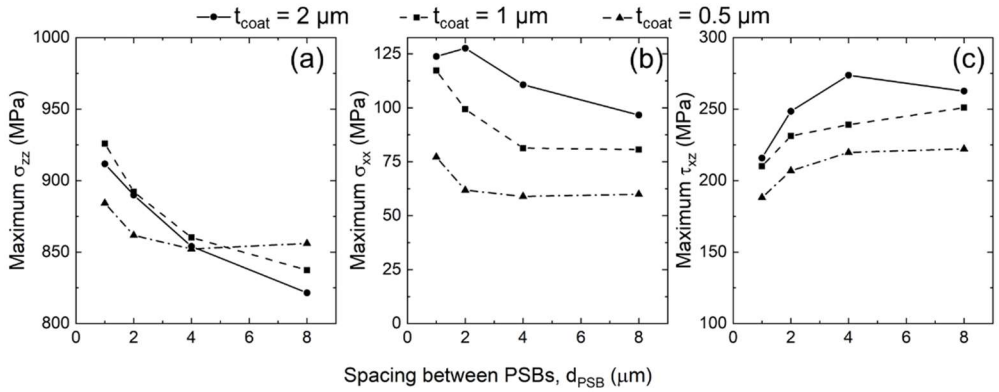

Figure 7. 7 The maximum stresses, including **(a)** σ_{zz} in the coating at the interface, as well as **(b)** σ_{xx} and **(c)** τ_{xz} at the interface, as functions of the increasing PSB spacing, d_{PSB}. Note that the applied plastic shear strain range is inversely related to d_{PSB}—i.e., d_{PSB} = 1 μm corresponds to $\Delta\gamma_{pl}$ = 0.01, d_{PSB} = 2 μm corresponds to $\Delta\gamma_{pl}$ = 0.007, d_{PSB} = 4 μm corresponds to $\Delta\gamma_{pl}$ = 0.004, and d_{PSB} = 8 μm corresponds to $\Delta\gamma_{pl}$ = 0.002.

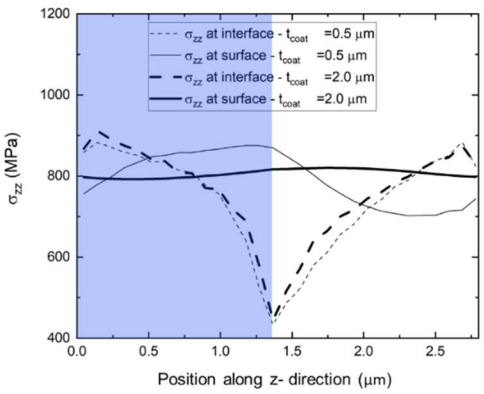

Figure 7. 8 The profiles of σ_{zz} along the z-direction on both sides of the coating for two simulations: (1) t_{coat} = 0.5 μm, d_{PSB} = 1 μm and (2) t_{coat} = 2 μm, d_{PSB} = 1 μm. The corresponding stress and strain contours of these two simulations have been shown in Figure 4a, 4c. The blue shade indicates the location where the PSBs intersect with the coating.

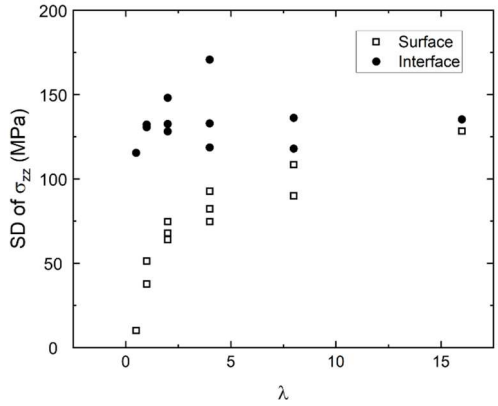

Figure 7. 9 The standard deviation (SD) of σ_{zz} at two locations—i.e., at the coating–substrate interface and coating surface, versus the ratio $\lambda = d_{PSB}/t_{coat}$.

CHAPTER 8 SYNERGISTIC EFFECT OF MICROSTRUCTURE AND DEFECTS ON THE INITIATION OF FATIGUE CRACKS IN ADDITIVELY MANUFACTURED INCONEL 718

8.1. Abstract

The role of microstructure and volumetric defects on the initiation of fatigue cracks in additively manufactured (AM) Inconel 718 (IN-718) are investigated in this study. A new crystal plasticity hardening model with a physics-based, location-dependent, behavior is proposed here. Heterogeneous evolution of the material resulting in strain localization and the formation of slip bands under cyclic loading are illustrated. It is shown that strain is more likely to localize in regions within larger grains with a higher resolved shear stress. A criterion correlating the life to the nucleation of cracks at various locations in the material to the characteristic features of the microstructure is presented. Life to the initiation of fatigue crack due to PSB operation at grain interior and grain boundary are calculated. Earlier crack initiation at grain interior in the material with larger grain size have been shown.

8.2. Introduction

Additive manufacturing (AM), such as laser beam powder bed fusion (LB-PBF), fabricates parts in a layer-by-layer fashion and offers significant benefits over conventional manufacturing such as near net shaping and consolidating assemblies into monolithic parts [397,398]. It therefore has strong potential to be adopted for fabrication of hard-to-machine alloys such as Ti alloys and Ni-base superalloys, whose applications typically involves complex geometries, to reduce machining cost [399–401]. However, additively manufactured (AMed) parts typically contain large population of volumetric defects which act as stress risers and can be detrimental to the

mechanical properties especially fatigue. Fatigue fracture of many AMed metallic materials in the mid and high cycle fatigue (MCF and HCF) regimes often is dominated by the volumetric defects, such as lack-of-fusions, gas entrapped pores, and keyholes, which can accelerate the initiation of fatigue cracks, introduce uncertainty to and deteriorate the fatigue performance [402,403]. In general, an inverse correlation between defect size and fatigue resistance exists for most AM materials [404,405].

Inconel 718 (IN-718) is perhaps the most popular Ni-base superalloy for various AM technologies owing to its excellent weldability [406]. Interestingly, this material does not appear to be as sensitive to the presence of defects as other alloys, e.g., Ti-6Al-4V, 17-4 precipitation hardening stainless steel, and Al alloys. In fact, in the machined surface condition, volumetric defects are not always responsible for the initiation of the main fatigue crack for AMed IN-718. For LB-PBF IN-718, Wan et al. [407] reported that the process induced gas-entrapped pores always served as the initiation sites for the main fatigue cracks in the MCF and HCF regimes, however Yang et al. [408] observed in HCF and very high cycle fatigue (VHCF) regimes that crack initiation can be either from volumetric defects or from crystallographic facets, despite that the critical defects from both works were mostly spherical and were ~20 μm in diameter. Recently, Muhammad et al. reported that, irrespective of the test frequency of 5 Hz or 20 kHz, fatigue crack initiation almost exclusively from crystallographic facets in HCF and VHCF regimes, even though the maximum defect diameter was ~40 μm [409]. These observations from the literature suggested that the defect- and facet- driven fatigue crack initiation mechanisms in the LB-PBF IN-718 may be competing. However, the factor governing this competition is not solely defect size and is presently not well known.

The crystallographic facets serving as the initiation sites suggests the initiation of fatigue cracks may be ascribed to persistent slip bands (PSBs) which form along slip planes [410]. Under cyclic loading, the operation of PSBs can not only form intrusions/extrusions at free surfaces and internal microstructural discontinuities, such as grain boundaries (GBs) or secondary phases, but also generate vacancies within the bands due to the climb/annihilation of edge dislocations. The former creates the driving force for crack formation, while the latter provides a pathway of "damaged material" for short crack growth – hence the planar feature of the crack initiation sites. The extent (or height) of the intrusions/extrusions formed, therefore the driving force for crack formation, is directly proportional to the size (in-plane dimension) of the PSBs. In addition, longer free slip distances (mean free path or MFP) between adjacent microstructural discontinuities favors the formation of the PSBs. Therefore, fatigue crack initiation via PSBs is easier with larger MFP, vice versa. The competition between the defect- and the PSB- driven crack initiation mechanisms can be hypothesized to be governed by the relative size of the defects and MFP.

This hypothesis appears to be consistent with the observations reported in the literature. In fact, Yang et al. showed that on the fracture surfaces where both initiation mechanisms were evident, the size of the facets were quite comparable with that of the volumetric defects – around 20 μm [408]. In contrast, the facet size reported by Muhammad et al. was well above 100 μm, which was significantly larger than the diameter of the largest defects observed via X-ray CT (~40 μm). In this case, the crack initiation via PSB was perhaps easier. This was further confirmed by their observations that the diagonally built specimens exhibited larger facets at crack initiation sites and better fatigue resistance compared to vertically built specimens. On the other hand, the IN-718 microstructure reported by Wan et al., where no PSB governed crack initiation was

observed, contained closely spaced of δ phase, which limited the MFP and inhibited the formation of PSBs [407].

In this work, the synergistic effect of microstructure and defects on the initiation of cracks under cyclic loading in AMed IN-718 has been investigated. A new crystal plasticity hardening model that takes into account the effect of MFP on the evolution of the critical resolved shear stress is proposed. The saturation stresses of different slip systems are also distinguished based on their location within the grain. Formation of slip bands within a grain where the strain is most likely to localize is then studied. The changes in crack initiation sites for cases where a volumetric defect exists in the representative volume element are compared to cases with no defect. Parameters affecting the morphology and density of slip bands are also discussed here. In what follows, section 2 highlights the physical aspect of the deformation process affecting the slip localization under cyclic loading, section 3 describes the crystal plasticity framework used here, results of the simulations are provided in section 4, and discussions are presented in section 5.

8.3. Physical aspects of the problem

From the Onset of loading up to the point that crack initiates in the material, heterogeneous evolution of the microstructure as a result of inelastic deformation can be regarded as damage accumulation that eventually leads to the nucleation of fatigue cracks. A clear understanding of the physics of such evolution lays down the foundation for a model that successfully predicts the crack initiation behavior under cyclic loading. As the material undergoes cyclic loading, the overall dislocation density increases. However, dislocations tend to agglomerate, in certain regions of the grain, in the form of bundles made from edge dislocation dipoles and multipoles. This results in the hardening of material response. In this configuration, deformations would be carried out by the screw dislocations spanning over neighboring bundles. Further cyclic deformation, causes

annihilation of dipoles within the bundles resulting in the formation of narrow channels where the majority of the slip activity is confined (see Fig. 1.a) [8,9,28,41,411].

In precipitate hardened alloys, the to-and-fro motion of dislocations within the channels, when they glide through the precipitate, will result in relative translation of the two halves of the precipitate. As illustrated schematically in Fig. 1.b, repetitive and irreversible shearing of precipitates, especially for alloys with relatively small precipitates, leads to the mechanical dissolution of the precipitates in the matrix. This will further soften the material by removing the obstacles that impede the dislocation motion and assist the glide of dislocations within the slip bands. The softening accompanied by the formation of slip bands and precipitate dissolution, along with the hardening led by the lack of mobile dislocations in the material, provide the necessary conditions for strain localization.

The mean free path (MFP), defined as the distance of a dislocation to its closest obstacle, has a strong effect on the yield strength of a slip system. Multiple factors, such as grain size and shape, precipitate distributions, and sub-grain structures, would alter the MFP and material points will have different MFP value. Therefore, a gradient in critical resolved shear stress exist in the material. As the result, one could expect that deformations would generally occur on the larger grains where the MFPs are larger. For the same reason, there are regions within the larger grains where dislocations can glide more easily. Thus, strain is more likely to be localized within those regions.

Homogeneous strain distribution shown by a uniform dislocation structure within fine grain material indicates that there is no preference for where the plastic deformation will happen. In contrast, the heterogeneous dislocation structure and formation of slip bands in the larger grains are confirmations of the MFP effects on PSB formation. Experimental observations highlighting

the role of MFP in the formation of slip bands are reported in the literature. PSBs are found more frequently among large grains [412]. This was attributed to relatively less constraint on deformation within a grain imposed by the grain boundary and higher dislocation density in fine grains [14]. Zhang et al have shown that multiple slip systems are active in fine grains and dislocation configuration is random compared to the formation of cells and walls in large grains. This suggests that a preferred slip condition, i.e., existence of a system with the advantage of easy glide over other systems, by a specific combination of grain orientation and morphology, could assist the formation of slip bands.

Nucleation of microstructurally small cracks within the material has been associated with the slip bands. Although, not all PSBs are active in a cycle of loading, two orders of magnitude higher strains are measured in PSBs as compared to the Matrix [413,414]. Non-uniform slip activities are observed within an individual PSB [415], but the magnitude of such variations is small. As a result of a large gradient in shear strain, PSB-matrix interfaces are identified as a candidate site for crack initiation [367,413]. Instances of sub-surface crack initiations from faceted regions, that could be associated with the PSBs, were also identified to more likely happen in the material with large grains [415]. Intrusions and extrusions formed at the cross section of PSBs with free surfaces and grain boundaries (GB) are among the main candidates for crack initiation. Magnitude of the extrusions are correlated to the grain size and PSB's characteristics [20]. Intrinsic material parameters such as extended fault energies in either disordered matrix or ordered precipitates will alter the structure and morphology of the slip bands, affecting the extent of extrusion and intrusions as well. Wider PSBs are found in material with wavy slip, whereas the low fault energies results in planar slip and lower PSB width [413].

Investigating the role of microstructure on the nucleation and growth of fatigue cracks, at least up to the length of a few grains, requires a comprehensive consideration of microstructural details. Classical approaches such as experimental observations, analytical investigation, and numerical simulations if used in harmony, complex problems could be tackled more efficiently. With the advancement of computational capability and more reliable constitutive modeling, numerical models that are capable of explicitly considering slip systems are employed to investigate the life of parts under cyclic loading. Total fatigue life is decomposed into several regimes in which distinct mechanisms take over. Multiple mean value parameters as so called "fatigue indicator parameters" at different length scales are proposed to represent the driving force for the nucleation and growth of fatigue cracks. These models have been successfully implemented to estimate the fatigue life of materials [416,417]. Due to the complexities embedded in the crack nucleation processes, a semi-empirical relation considering a coefficient describing the irreversibility of dislocation motion, a scalar representing the reference length scale, and a fatigue indicator parameter that quantifies the driving force for crack nucleation are used to calculate the life to the nucleation of fatigue crack.

On the other hand, energy-based models of nucleation and growth of fatigue cracks are widely used [418,419]. In a more detailed model by Sangid et al., the change in the energy of an operating PSB was calculated in a multiscale modeling scheme. The continuum scale effect of the external stress field, specific dislocation configuration within PSB, the work hardening term due to irreversible dislocation motion within PSB, along with the atomistic contributions from dislocation interaction with precipitate and grain boundaries of different characters, are considered in this model. Eventually, the failure criterion resulting in the initiation of fatigue crack is defined as the point where the PSB energy stabilizes and reaches its minimum value [381,420]. A

successful prediction of the fatigue crack initiation trend was achieved using this model. However, the working PSB is the starting point of this model.

The missing part of the puzzle that would be of great importance in understanding the role of microstructure and volumetric defects on the nucleation of fatigue crack is a model that considers the crystallographic information and predicts the heterogeneous evolution of the microstructure from the starting point of loading until the moment that crack initiates. Material models that are available can be adjusted such that they can capture either softening or hardening induced by deformation. However, the prescribed evolution of the microstructure suggests that, depending on the location, both softening and hardening can happen at the same time in different points of the material. Thus, a model that offers such a capability is the key to a physics based material model that predicts the effect of microstructural features on the life to the initiation of fatigue cracks.

In this paper, the synergistic effect of microstructure and defects on the initiation of cracks under cyclic loading in AMed IN-718 has been investigated. A new crystal plasticity hardening model that takes into account the effect of MFP on the evolution of the critical resolved shear stress is proposed. The saturation stresses of different slip systems are also distinguished based on their location within the grain. Formation of slip bands within a grain where the strain is most likely to localize is then studied. The changes in crack initiation sites for cases where a volumetric defect exists in the representative volume element are compared to cases with no defect. Parameters affecting the morphology and density of slip bands are also discussed here.

8.4. Methodology

Numerical simulations have been performed to investigate the fatigue crack initiation behavior of the additively manufactured IN-718. Theoretical framework utilized in the crystal

plasticity simulation are described in this section. Different material models used for IN-718 and pore regions are explained. The procedure adapted to obtain the material parameters is listed. Geometrical details related to the representative volume element and grid system are presented. Various grain morphology and crystallographic orientations assigned to the material are provided in details. Lastly the numerical scheme applied in this study is briefly mentioned.

8.4.1. Theoretical framework

Within the kinematic framework of crystal plasticity, total deformation is multiplicatively decomposed into elastic and plastic components:

$$\boldsymbol{F} = \boldsymbol{F}^e \boldsymbol{F}^p, \tag{1}$$

where $\boldsymbol{F}$ denotes the total deformation gradient and superscripts e and p are used to indicate the elastic and plastic components, respectively. The gradient of the velocity field, $\boldsymbol{L}$, in the current configuration is defined as:

$$\boldsymbol{L} = \dot{\boldsymbol{F}}\boldsymbol{F}^{-1}.$$

(2)Velocity gradient, in turn, can be decomposed additively into elastic and plastic parts:

$$\boldsymbol{L} = \boldsymbol{L}^e + \boldsymbol{F}^e \boldsymbol{L}^p \boldsymbol{F}^{e-1}, \tag{3}$$

where $\boldsymbol{L}^e$ and $\boldsymbol{L}^p$ are the elastic and plastic part of the velocity gradient, respectively. However, one should note that, since plastic velocity gradient, $\boldsymbol{L}^p$, is defined with respect to the intermediate configuration as, $\dot{\boldsymbol{F}}^p \boldsymbol{F}^{p-1}$, it should be pushed forward to the current configuration (i.e., the $\boldsymbol{F}^e(\ldots)\boldsymbol{F}^{e-1}$ operation), while there is no need for such transformation in the case of elastic component.

Here, two different material models i.e. phenomenological crystal plasticity and isotropic plasticity were adapted for different regions within the representative volume element. The crystal plasticity model is used for IN-718 and the Isotropic plasticity model is assigned to the regions representing the volumetric defects. In the following text, first, the crystal plasticity model is described followed by an abstract description of the isotropic model.

In the framework of crystal plasticity, the plastic velocity gradient is formulated based on the summation of tensors defined for each slip system, α, and the corresponding shear rate, $\dot{\gamma}_\alpha$:

$$\boldsymbol{L}^p = \sum_{\alpha=1}^{N_s} \dot{\gamma}_\alpha \, (\boldsymbol{s}_\alpha \otimes \boldsymbol{m}_\alpha), \tag{4}$$

where $\boldsymbol{s}_\alpha$ and $\boldsymbol{m}_\alpha$ are the unit vectors parallel to the slip direction and normal to the slip plane, respectively. The shear rate, $\dot{\gamma}_\alpha$, given by the following flow rule, was used for IN-718:

$$\dot{\gamma}_\alpha = \dot{\gamma}_0 \left| \frac{\tau_\alpha - \chi_\alpha}{\xi_\alpha} \right|^{1/m} sgn(\tau_\alpha - \chi_\alpha), \tag{5}$$

where $\dot{\gamma}_0$, is the reference rate of the shear deformation. τ_α is the resolved shear stress, χ_α is the back stress, and ξ_α is the critical resolved shear stress on slip system α and m is the strain rate sensitivity. As it can be seen, the driving force for the shear on crystallographic plane is the resolved shear stress. Given the resolved shear stress on all slip systems, the shear rate can be defined according to the constitutive model. Evolution of the slip resistance and back stress are defined through separate models.

Following the observation of a yield anomaly as a result of prior plastic deformation, the so-called Bauschinger effect, numerous attempts have been made to provide a mathematical framework that can capture the movements and changes to the size of yield locus in the stress space. The changes to the size of yield surface was addressed by introducing a micro-stress that

resist/assist the yielding of material under different loading condition (i.e., tension and compression). Thus, the evolution of that internal micro-stress affects the material response under cyclic loading. In a model proposed by Armstrong and Frederick (AF), the evolution of such micro-stress was correlated to the rate of plastic strain by:

$$\dot{\chi}_\alpha = u\dot{\gamma}_\alpha - r\chi_\alpha|\dot{\gamma}_\alpha|, \tag{6}$$

where u is the hardening coefficient and r is the dynamic recovery parameter. AF model is incorporated in the crystal plasticity framework used in this study to account for the evolution of back stress. The evolution of critical resolved shear stress in a slip system has been attributed to the shear strain in all active slip systems by:

$$\dot{\xi}_\alpha = \sum_{\alpha'=1}^{N_s} h_{\alpha\alpha'}|\dot{\gamma}_{\alpha'}|\left|1 - \frac{\xi_{\alpha'}}{\xi_{\alpha'}^{\infty}}\right|^a sgn\left(1 - \frac{\xi_{\alpha'}}{\xi_{\alpha'}^{\infty}}\right), \tag{7}$$

where $h_{\alpha\alpha'}$ is the hardening matrix that empirically considers the self and latent interaction among slip systems (α and α' are designations for slip systems). ξ_α^∞ is the saturation value of the slip resistant on system α. Superscript ∞, when used, denotes the saturation value of a physical property. Incorporating the existing hardening models, it seems challenging to explain the localized softening in the material, in contrast to the matrix that hardens as the cyclic deformation continues. To capture such physical observations, a hardening model has been proposed that takes into account a location dependent MFP parameter. This model allows for a contrasting evolution of slip resistance that is seen at the location where PSBs are being formed. At every material point, the MFP parameter is defined as the square root of the area of the slip planes surrounded by the grain boundary, designated by η_α. Based on the defined parameter, the initial slip resistance is expressed as:

$$\xi_\alpha = \xi_\alpha^0 + {C_{HP}}\Big/{\sqrt{\eta_\alpha}}, \tag{8}$$

where C_{HP} is the Hall-Petch parameter and ξ_α^0 is the reference slip resistant on system α. Hall-Petch parameter allows for material points with similar behavior, i.e., overall softening or hardening, to have different saturation stress values, which is a physically sound assumption. The evolution of the slip resistant on all slip systems can be calculated based on the formula:

$$\dot{\xi}_\alpha = h_0^{s-s} \sum_{\alpha'=1}^{N_s} h_{\alpha\alpha'} |\dot{\gamma}_\alpha| \left| 1 - \frac{\xi_{\alpha'}}{\xi_{\alpha'}^\infty + {C_{HP}}\Big/{\sqrt{\eta_\alpha}}} \right|^a sgn\left(1 - \frac{\xi_{\alpha'}}{\xi_{\alpha'}^\infty + {C_{HP}}\Big/{\sqrt{\eta_\alpha}}} \right) sgn(\eta_\alpha - \lambda), \tag{9}$$

where λ is the MFP threshold parameter, h_0^{s-s} is the hardening coefficient. Strain localization and formation of PSBs are also related to other intrinsic material parameters such as stacking fault energy and anti-phase boundary energy. These energetic parameters may result in different dislocation configurations that affects the PSB distribution. Effect of such parameters are lumped into the coefficient λ.

The isotropic elasto-plastic material model as it has been formulated within Düsseldorf Advanced Material Simulation Kit (DAMASK) is used for the pore. The plastic velocity gradient used in this model is given by:

$$\boldsymbol{L}_p = \frac{\dot{\gamma}_p}{M} \frac{\boldsymbol{M}_p^{dev}}{\left\| \boldsymbol{M}_p^{dev} \right\|_F} \tag{10}$$

where $\dot{\gamma}_p$ is the rate of plastic shear strain, $\boldsymbol{M}_p^{dev}$ is the deviatoric Mandel stress tensor and $\left\|\boldsymbol{M}_p^{dev}\right\|_F$ is the Frobenius norm of the deviatoric Mandel stress. The rate of shear in the material is defined by:

$$\dot{\gamma}_p = \dot{\gamma}_0 \left(\frac{\sqrt{3J_2}}{M\omega}\right)^n, \tag{11}$$

where J_2 is the second invariant of the Mandel stress tensor, $\boldsymbol{M}_p$. M is the Taylor factor, and n is the stress exponent. ω denotes the scalar resistance to plastic flow. The evolution of the resistance parameter ω is defined by:

$$\dot{\omega} = \dot{\gamma} h_0 \left|1 - \frac{\omega}{\omega^{\infty}}\right|^a sgn\left(1 - \frac{\omega}{\omega^{\infty}}\right), \tag{12}$$

where h_0 is the initial hardening parameter, ω^{∞} the saturation resistance, and a is the strain rate sensitivity exponent.

8.4.2. Model calibration

To obtain the material parameters for the crystal plasticity model (Eqs. 6-12), multiple virtual single crystal simulations were performed to match the obtained materials response under both tensile and cyclic loadings to experimentally measured curves. For these simulations, elastic constants identical to what have been used in the literature for IN-718 were used [421,422] and are shown in Table 1. This procedure, as detailed elsewhere, performs uniaxial tensile and fully reversed cyclic loadings 50 times on single crystals with random orientations [22,361,391,423]. Under the eigen-strain Taylor assumption, the average stress-strain curves from the simulations, which were assumed to represent the polycrystalline response, were then fitted to the experimental ones. For tensile simulations, a strain of 0.01 was applied. For cyclic loading, several strain amplitudes of 0.006, 0.008, and 0.01 were applied for 250 cycles. The obtained materials plastic

flow parameters are listed in Table 1. The tensile stress-strain curves and cyclic hysteresis loops for all strain amplitudes are presented in Fig.2. The stress-strain responses of the monotonic loading are provided for comparison.

8.4.3. Geometrical representation of the polycrystalline aggregate

To solve the system of partial differential equations resulting from the equilibrium equations, a fast Fourier transform (FFT)-based method, also referred to as the spectral method, implemented in the DAMASK has been used [382]. The spectral method implicitly assumes periodic boundary conditions on all boundary surfaces. Representative volume element (RVE) of the material discretized by a 33×33×32 grid system along X, Y, and Z directions were used to model aggregates of grains. Cubic RVE with a side length of 115 μm is modeled here. Polycrystalline aggregate containing 24 grains is generated by Voronoi tessellation of 24 randomly placed seeds. This way, a uniform grain size distribution is obtained. The microstructure was then modified to model a polycrystalline aggregates containing a large grain in the middle, which were surrounded by smaller grains. This type of geometry on one hand replicates the presence of both very large and very small grains in the LB-PBF microstructure, on the other hand, the large grain contained sufficient elements which permitted analysis of strain localization. Using this model, effect of microstructure on the strain localization behavior of IN-718 was investigated for vertically and diagonally built specimens under constant strain amplitude of 0.012 for 250 cycles. The cutaway views of the modelled geometries are provided in Fig. 3. Build orientation effect is also taken into account by the rotation of the load frame. For vertically built specimens, the loading direction was parallel to the Z direction while the load frame was rotated by -45° about the Y axis for diagonal specimens.

Different textures, as shown in Fig. 4. a-c, are assigned to the large grain, while orientations in the rest of the grain were kept constant. In order to design a comprehensive simulation matrix that truly takes into account the effect of texture, the variation of Schmid factor as a result of crystal rotation about the Z axis, shown in figure 4. d-f, is considered. For this purpose, three different crystallographic directions i.e. [100], [101], and [111] are selected and fixed to be parallel to the Z axis. Second, from an arbitrary initial point, the crystal was rotated counter clock wise for 360˚ about the Z axis and the variation in Schmid factor is calculated for all slip systems. The maximum value of the Schmid factor among all slip systems at each angle is plotted in Fig. 4. d-f. One should note that, due to periodicity only the Schmid values for the first 180˚ rotation are plotted. As indicated by red square marker few points with maximum/minimum value of the Schmid factor are chosen and the corresponding orientation is assigned to the grain of interest in the RVE. For vertically built specimens no variation in the Schmid factors are observed when rotated. Furthermore, due to the geometrical symmetry of the grain, no variation in the area of slip planes are expected. Thus, the only criteria for selection of the texture for vertically built specimen was the crystallographic direction parallel to loading direction.

In the case of [100] texture, the maximum Schmid factor, i.e. 0.5, will never be achieved in the current configuration. Therefore, the orientation corresponding to the maximum Schmid value (0.43) on (111) $[0\bar{1}1]$ system obtained at 17° is considered in the simulation. Considering the envelope of the Schmid curves for all slip systems, the orientations corresponding to the maximum and minimum of the Schmid factors, i.e. 35 and 90, are assigned to the microstructure with [101] texture. For the case of [111] texture, the maximum Schmid factor in one of the inclined planes, i.e. $(\bar{1}1\bar{1})$ at 168°, is assigned to the large grain. Similar texture and build orientations are considered for the columnar grain as well.

To further investigate the synergistic effect of microstructure and defects on fatigue crack initiation, multiple cases of the representative volume element containing a pore with a size varying from one to the other have been considered. To isolate the parameters affecting the material response and study the effect of pore size, only the diagonally built RVE with [111] texture is used here. Location of the pore remains constant for all cases. Three different pore diameters ranging between 3.5 to 17.5 μm are considered. Schematic representation of the RVE including pore is provided in Fig. 3.b. Similar to what has been used in the literature as the so-called buffer layer to model free surfaces, the preferred choice of material to use for the pores would be a significantly more compliant material both in elastic and plastic regimes. Maiti et al. have suggested two orders of magnitude lower elastic constants for the buffer layer to model free surface and void [424]. With that being said, due to convergence issues arising in the cyclic loading, a material with a similar elastic constant to what has been used for the In-718 and significantly lower yield strength has been applied to the pore region. The material parameters are listed in Table 2.

8.5. Results

8.5.1. Strain localization under cyclic loading

Heterogeneous microstructural evolution introduced by the proposed slip strength evolution law (Eq. 9) could capture strain localization in the material essential to simulate the formation and operation of PSBs. To visualize the strain localization behavior, the largest grain within the RVE has been sliced into sections parallel to the {111} slip planes as shown in Fig. 5. The absolute value of the shear strain for all slip systems that reside on the same crystallographic plane, will be averaged over all material points in each slice. This averaged strain value versus the section number is plotted in Fig. 5 a-b.

Two instances of strain localization at different regions of the grain are shown in Fig. 5. The gradual strain localization at the grain interior for the diagonally built specimen in the grain with [111] texture is shown in Fig. 5.a. Strain localization at the grain interior does not happen for all cases. For instance, localization at grain boundary has occurred for the vertically built material with [100] texture (Fig. 5.b). In both cases, at later stages in life, the contrast in slip activity between the regions where the strain is localized and those with limited slip activity has increased. The contour plots of the equivalent strain for the same two cases with [111] and [100] texture are provided in Fig 5. e and f, respectively. As it can be noticed, grain interior localization has occurred over the sections with larger MFP, located in the middle of the grain, as opposed to the regions close to the grain boundary.

8.5.2. Effect of pore on the cyclic response

Fully elastic simulation of the microstructure containing a pore undergoing monotonic loading is done to ensure the material parameters used for the pore region will not alter the mechanical response as compared to its elastically compliant counterpart. Two different sets of material parameters as listed in Table 2 are assigned to the pore region. As shown in Fig. 6, the stress solution of the material on a path, identified with a dashed arrow passing through the pore, has been plotted for both cases, i.e., pore with similar elastic constant to the matrix (solid line) and elastically more compliant material used for the pore (dashed line). The relative difference in the stress solution versus location has also been plotted on the same graph. A maximum of ~ 6 percent difference in the stress response was noticed across the two cases. Considering the higher equivalent Mises stress obtained when the identical elastic constants are used, the results of the current set of simulations would be more conservative compared to the ideal case.

Next, the slip band formation and strain localization in a grain that holds a pore are investigated. Three different pore diameters, i.e., 3.5, 10.5, and 17.5 μm are modeled. The result for the case with no pores is also included as a reference. For this purpose, the diagonally built grain with [111] texture is chosen. For comparison, the contours of equivalent strains on sections made to the grain are provided in Fig. 7. In order to provide more detail on shear strain distribution over the (111) plane, the grain has been sliced into 28 sections with equal thicknesses. This way, each slice will have a thickness equal to one voxel. In the contour plots, the material points with average strain values higher than 2 percent are shown in black. Regions with a higher fraction of areas that have surpassed the strain limit are highlighted as slip bands. The strain distribution for the case in which no volumetric defects exist in the grain is provided in the first row. In other cases, the location of the pore is emphasized with a dashed line drawn around sections containing the pore. Looking at the highlighted regions in the first three rows, the regions over which the strain has localized are more or less constant, while the localization has occurred over a narrower region of the largest pore.

8.6. Discussion

Slip bands are usually characterized by regions with significantly higher density of mobile dislocations, whose motion carries out plastic deformation. Since the only active mechanism that accommodates the deformation in the current crystal plasticity framework is the dislocation glide, regions with higher shear strain are equivalent to the slip bands. Thus, to find the location of slip bands, regions with higher shear strain must be identified. Using the predefined sections based on slip planes (similar to those defined in Fig. 5), shear strain is called localized and PSB is said to have formed if the shear strain on more than half of the area of that section exceeds 0.02. Using the described criterion, at each point in the loading history, one could decide whether the slip bands

are formed in the grain interior or at grain boundary. Figure 8.a and c show the fraction of area of the grain section that has a shear strain above 2 percent for two separate instances of grain interior and grain boundary localization.

According to experimental observations, the initiation of fatigue cracks in metallic materials has been correlated to the abrupt change in strain values at the PSB-matrix interface rather than high strain regions in the PSB interior. However, at locations such as grain boundaries, high stain values can result in the initiation of fatigue cracks due to the strain incompatibilities between two neighboring grains. Therefore, strain localization on sections adjacent to the grain boundary would result in crack initiation. Meanwhile, initiation of fatigue crack at the PSB-matrix interface would require a certain contrast in the strain localization among neighboring sections. The difference in areas over which strain has surpassed the 2 percent criterion between neighboring sections is shown in Fig. 8.b. As it can be noticed, the PSB-matrix interfaces are distinguishable through spikes in shear strain contrast. These regions are the main candidates for crack initiation. As a criterion, the crack would initiate on either side of the slip band where the difference in area reaches 25 percent. Considering the criteria defined for strain localization and crack initiation, the results of all the simulation cases are summarized in Table 8. For all cases, the location of strain localization as well as life to crack initiation are listed.

To further analyze the results and elucidate the conditions that have resulted in the localization at the grain interior versus grain boundary, a localization parameter is defined here. Simplifying the conditions that affect the slip activity, among all, resolved shear stress and MFP are considered in defining the localization parameter. However, one should note that the short/long range stresses resulting from various chemical species/precipitates that exist in the matrix will also

affect the motion of dislocations. For all the cases, the localization parameter is defined using the formula:

$$\delta = \theta^{0.25} \times \beta^2 \quad (13)$$

where δ is the localization parameter, θ is the averaged Schmid factor of all three slip systems that exist on a slip plane, and β is the area of the section where the localization has occurred. The normalized localization parameter for all the cases are plotted in Fig. 9. In this figure, each data point represents one of the simulations. Data points corresponding to different localization regions are bundled in Fig. 9. Significantly higher localization parameters are obtained for cases where the localization happens in the grain interior.

Based on the results obtained here, the higher resolved shear stress and larger MFP would lead to crack initiation from the grain interior. On the contrary, the competing mechanism for crack initiation at the grain boundary would activate in the case of lower resolved shear stress and smaller MFP. For instance, when the grain has the {111} texture, the highest plane area and a relatively high Schmid factor will coexist on the (111) plane and crack initiation criteria at the grain interior will be met at ~30 cycles. Similarly, a quick initiation of fatigue crack from the grain boundary has been observed at cycle ~40 when the low Schmid factor and small MFP are combined, i.e. {101} texture on $(\bar{1}\bar{1}1)$. Among all, the longer life to fatigue crack initiation was observed for the intermediate localization parameters.

For all cases, the normalized localization parameters versus life to initiation of crack are plotted in Fig. 10. Since the driving force for the stain localization at the grain interior counters the grain boundary localization, the inverse of the defined parameter versus life is plotted for cases

that crack initiates from the grain boundary (see Fig. 10.b). Thus, longer life as a result of a reduction in the localization parameter is observed when the localization happens in the grain interior. Considering the definition of the localization parameter, early crack initiation can be expected on slip planes with a larger MFP. Therefore, larger grain size will result in higher localization parameters and, consequently, shorter fatigue life is expected.

Strain localization simultaneously happens in many grains throughout the material. The location at which the localization happens, whether it be grain interior or grain boundary, will depend on the size of the grain and its orientation. Similarly, cracks may nucleate at multiple grains where the strain is localized and grow as the cyclic loading continues. A macroscopic crack will form when a few of these micro-cracks from neighboring grains are joined. Early growth of the microstructurally small cracks in each individual grain is energetically favored when the fracture surfaces are low-energy planes such as closed pack planes. Thus, initiation and growth of microstructurally small cracks at PSB-matrix interfaces are expected. The formation of facets on the fracture surface, close to the region where the crack initiated, with areas that are close to the average grain size, are indications of such a fracture mechanism. However, the persistence of such facets at various loading amplitudes suggests that no change in the failure mechanism has occurred. One should note that the final stage of fracture will appear as a plane perpendicular to the loading direction.

Fatigue crack initiation is also affected by the existence of pores in the microstructure. The strain localization profile as well as the contrast in localization are presented in Fig. 11. A schematic representation of the pore with the actual size and location is provided in the right column. In the case that no pores exist in the material, a crack would initiate at section 20 where the contrast in shear strain has met the criterion. An increase in the pore size would not change the

crack initiation site until the pore diameter equals ~17.5 μm. When the pore becomes large enough, the crack initiation will shift towards the pore. This behavior is clearly depicted in Fig 11.

8.7. Conclusions

In this work, proposing a new crystal plasticity hardening model, initiation of fatigue cracks of the IN-718 manufactured using AM technique are investigated. The effects of texture, built direction, and presence of pores are studied in detail. Following are the conclusions made in this study.

1. Strain localization under cyclic loading is strongly affected by the grain size and it can occur in the either grain interior or grain boundary.
2. As the cyclic loading continues the plastic shear deformation accumulates in regions within the grain and eventually results in the formation of crack.
3. Strain is most likely to localize inside the grain when the slip plane is large and grain is oriented such that it experiences a high resolved shear stress. Cracks would initiate at the PSB-matrix interface due to abrupt changes in strain.
4. A localization parameter can be defined that correlates the crack initiation site with texture and grain size. Larger MFP along with higher resolved shear stress would result in crack initiation from the grain interior while cracks initiate from the grain boundary in smaller grains. The number of cycles to crack initiation will increase by the reduction of localization parameter.
5. The existence of pores does not affect the strain localization behavior and life to the initiation of cracks unless they occupies a significant portion of the grain. Larger pores would shorten the fatigue life and reduce the width of the PSB, making it appear as a narrower region in the grain.

Tables

Table 8. 1 Parameters used in the phenomenological crystal plasticity material model for IN-718

C_{11}	C_{12}	C_{44}	$\dot{\gamma}_0$	m	u	r	$\dot{\chi}_0$	ξ_α^0	ξ_α^∞	a	h_0^{s-s}	C_{HP}	λ
GPa					MPa		MPa$\cdot S^{-1}$	MPa				MPa	μm
259.6	179.0	109.6	0.007	0.13	39.0	0.4	10.0	300.0	100.0	1.0	100.0	0.4	40.0

Table 8. 2 Parameters used in the isotropic plasticity material model for the pore region. a) The parameters used in the simulations. b) Parameters used to eliminate the Poisson's ratio and minimize the bulk modulus.

	C_{11}	C_{12}	C_{44}	$\dot{\gamma}_0$	M	n	a	ξ_α^0	ξ_α^∞	h_0^{s-s}
	GPa					MPa		MPa		
a)	259.6	179.0	109.6	0.01	20.0	4.0	2.5	0.02	0.5	0.075
b)	25.0	0.0	0.0	0.01	20.0	4.0	2.5	0.02	0.5	0.075

Table 8. 3 Location and life to crack initiation for different grain morphology obtained from simulation

Mean free path threshold	Texture & Build Orientation						
	[100]		[101]			[111]	
	V	D	V	D	D	V	D
40	GB/195	GI/175	GB/84	GB/171	GB/116	GB/183	GI/37
60	GI/229	GI/170	GB/82	GB /130	GB/135	GI/130	GI/43

V: vertically built specimen, D: Diagonally built specimen, GB: Grain boundary, GI: grain Interior

Figures

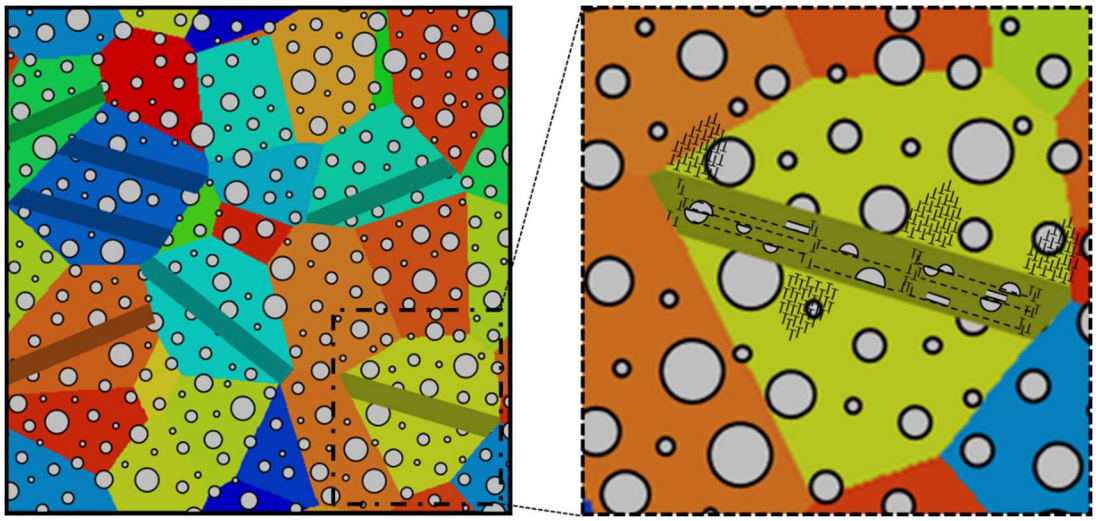

Figure 8. 1 Microstructural evolution as a result of softening accompanied by a) formation of PSBs b) mechanical dissolution of precipitates within the PSB due to localized shear deformation.

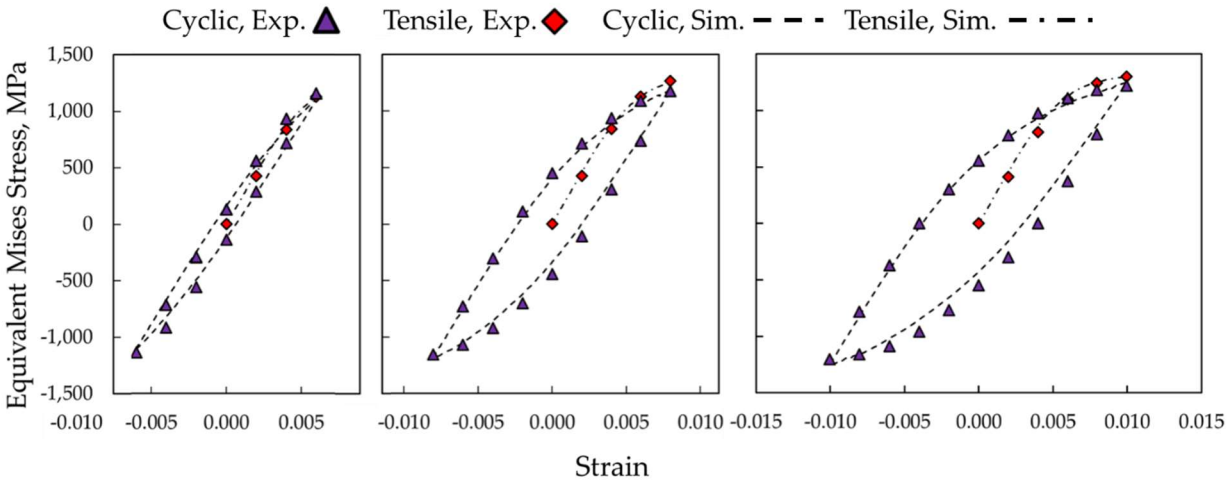

Figure 8. 2 Elasto-plastic response of a polycrystalline aggregate obtained from simulations, fitted to the monotonic and cyclic response from experiment [13] at different strain amplitudes: a) 0.006, b) 0.008, and c) 0.01. Insets are the fit to the monotonic material response.

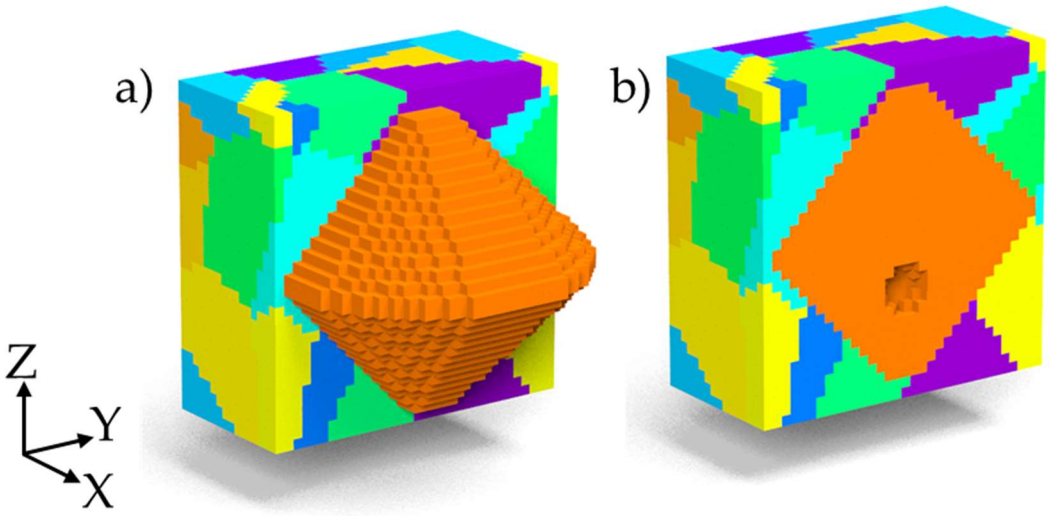

Figure 8. 3 Representative volume elements containing a polycrystalline aggregate of 24 grains used to simulate: a) pristine and b) defective grain structure.

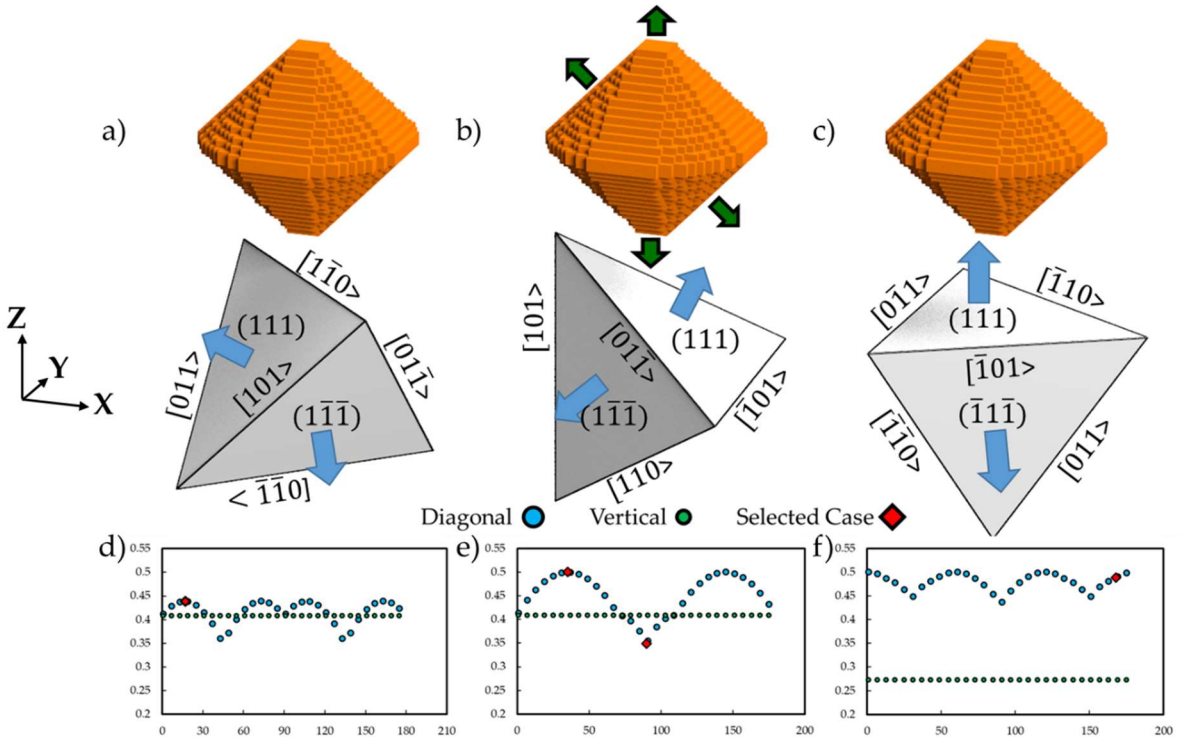

Figure 8. 4 Textures assigned to the microstructure used in the simulations. a) [100], b) [101], c) [111] represented by Thompson tetrahedron (blue arrows on the facets are showing the normal to slip planes).Variation of the Schmid factor as the result of rotation about the z axis for vertical and diagonally built specimens for d) [100], e) [101], and f) [111] textures. Loading directions are shown by arrows on the grain geometry.

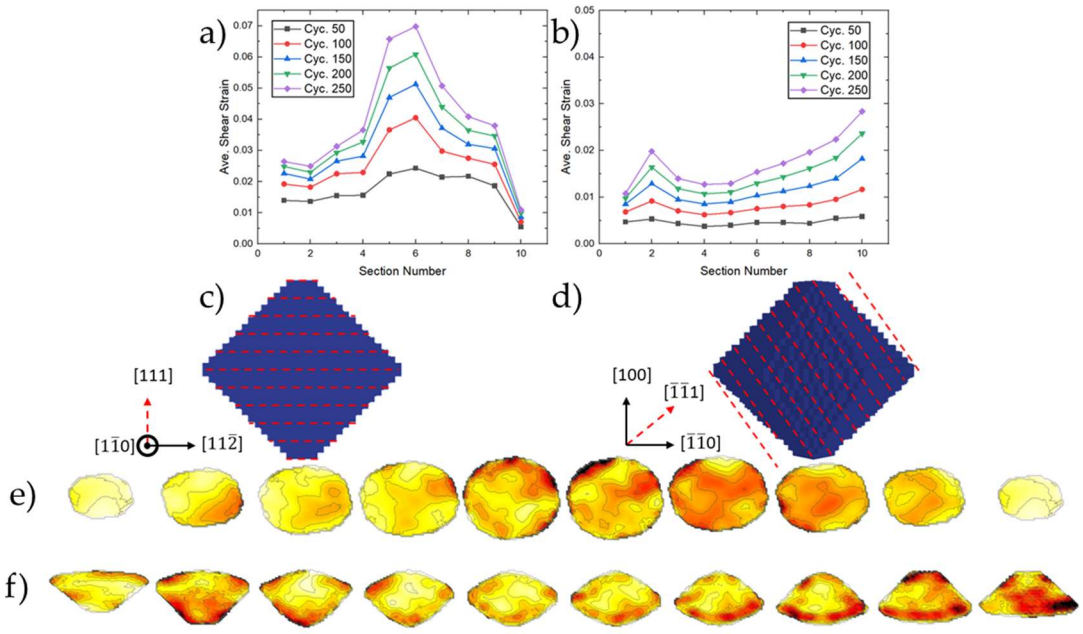

Figure 8. 5 Strain distribution across the grain for sections made parallel to the slip planes. The average of the absolute strain values per-section for a) diagonally built specimen with [111] texture, b) vertically built specimen with [100] texture. The sectioning lines parallel to the slip planes on the grains with c) [111], d) [100] texture. Contour plots for the strain distribution of the sections belonging to grains with e) [111], f) [100] texture.

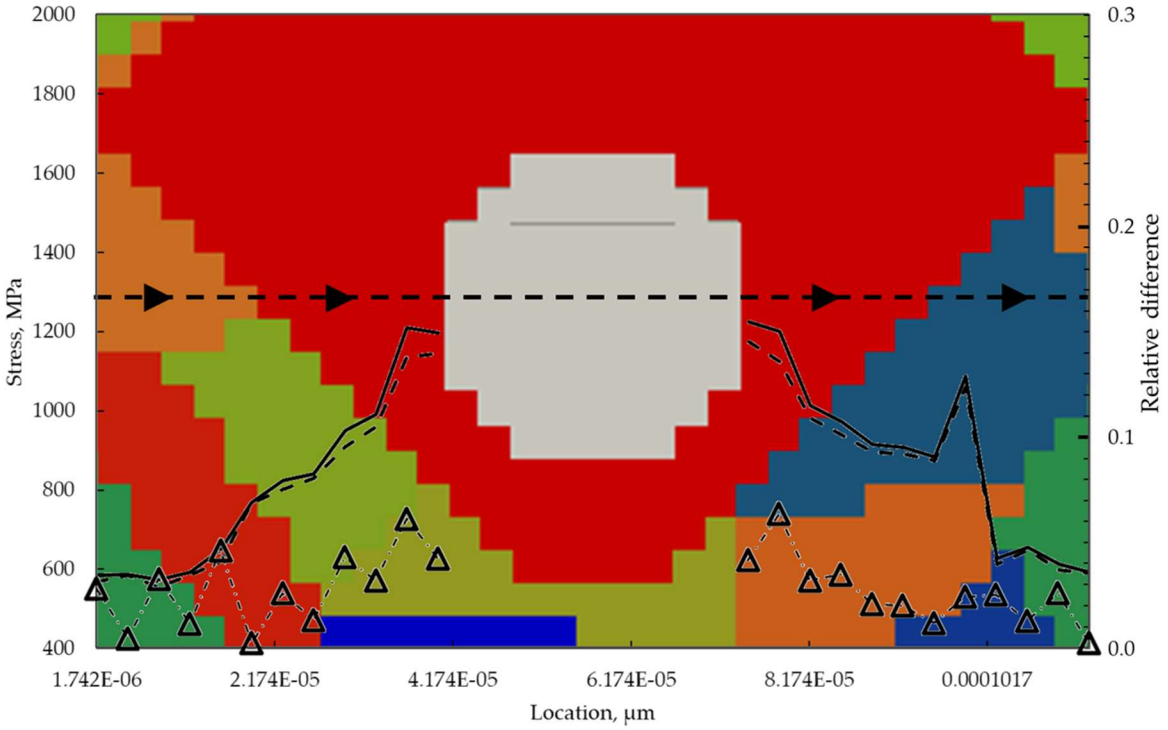

Figure 8. 6 Stress solution of elastically deformed polycrystal including a pore. Left axis: Equivalent Mises stress shown on the dashed arrow passing through the pore with parameters listed on the first row of Table 2 (solid line) and second row (dashed line). Right axis: Difference in the stress values obtained from different material parameters (triangle marker with dashed dotted line)

.

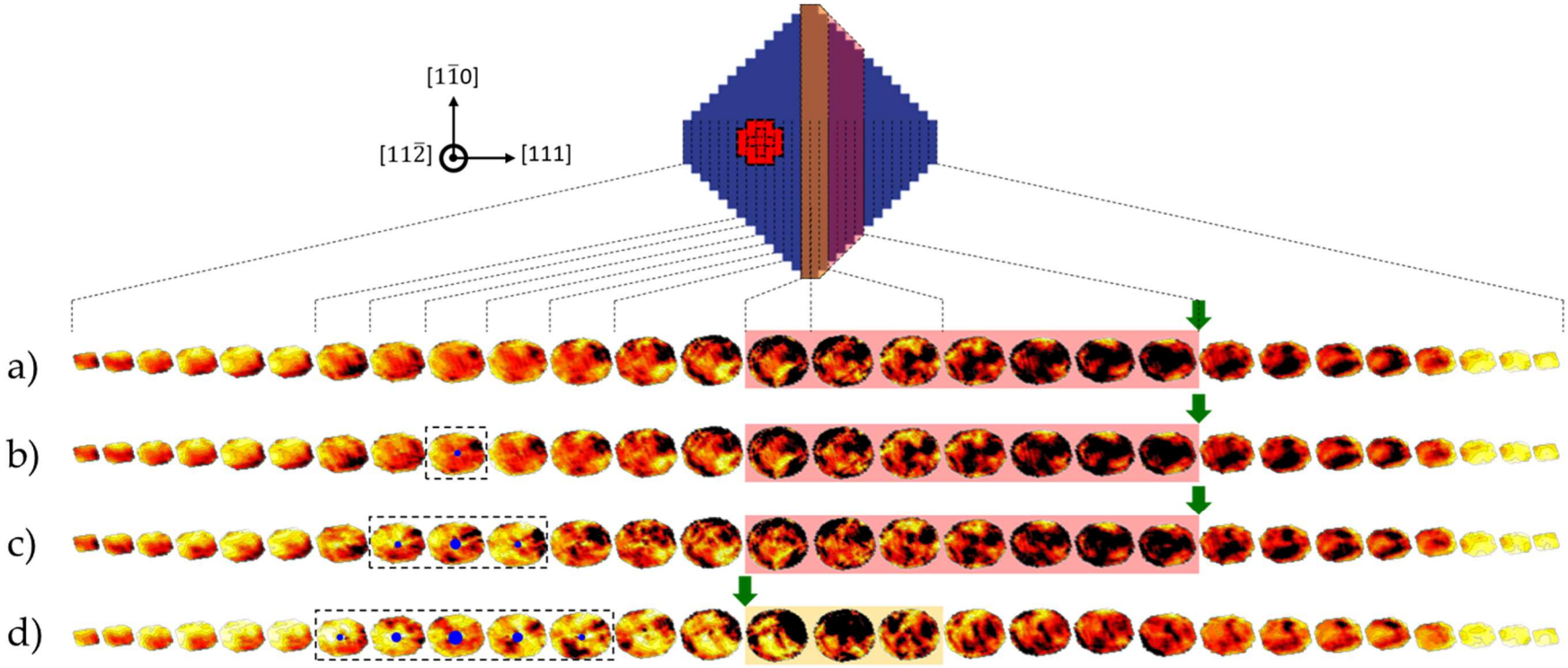

Figure 8. 7 Strain distribution of a grain containing a pore with varying size: a) no pore, b) 3.5 µm, c) 10.5 µm, d) 17.5 µm. Selected locations of the slices are emphasized with dashed lines such as sections that are containing part of the pore and slip band-matrix interface.

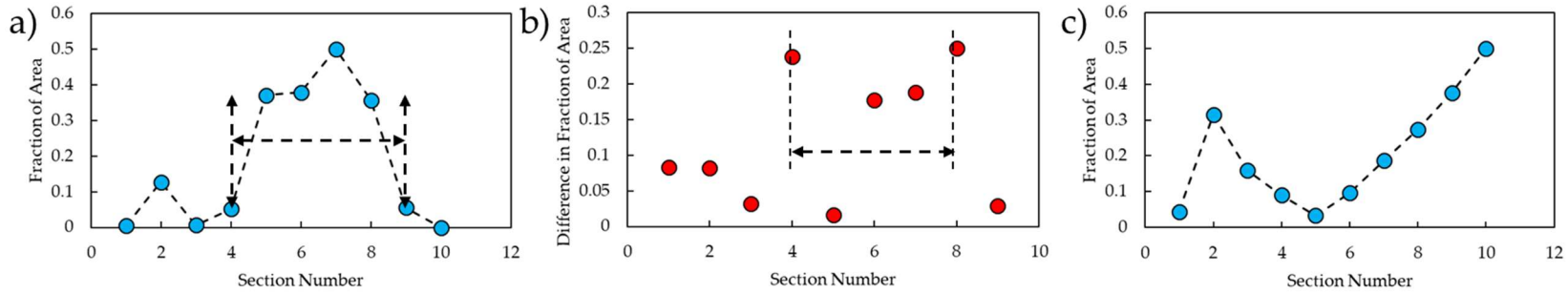

Figure 8. 8 Strain localization and formation of slip bands. a) Strain localization at grain interior in a diagonally built sample with [111] texture. b) Slip contrast between neighboring sections identifying the crack initiation site in a diagonally built sample with [111] texture. c) Strain localization at grain boundary in a vertically built sample with [100] texture. Slip bands are highlighted with dashed lines.

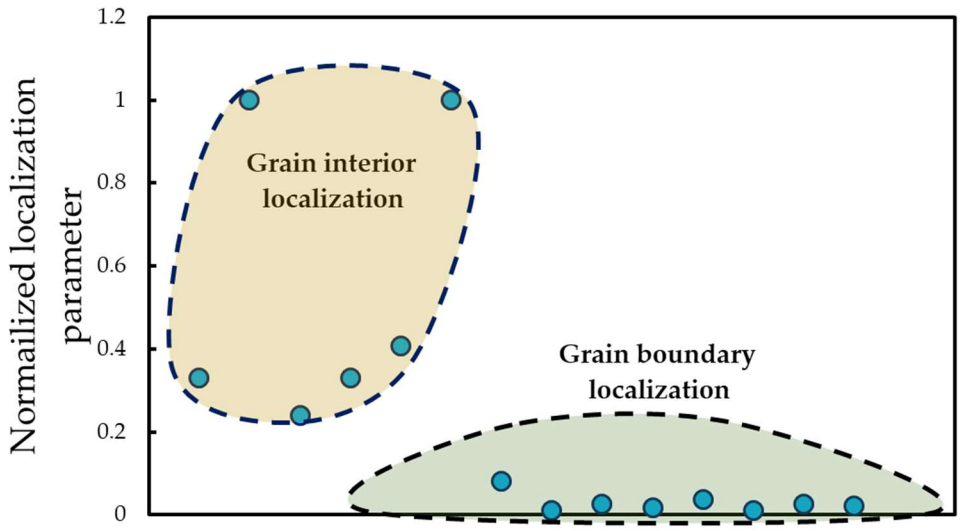

Figure 8. 9 Distribution of the normalized localization parameter among all cases that experience localization at grain interior versus grain boundary.

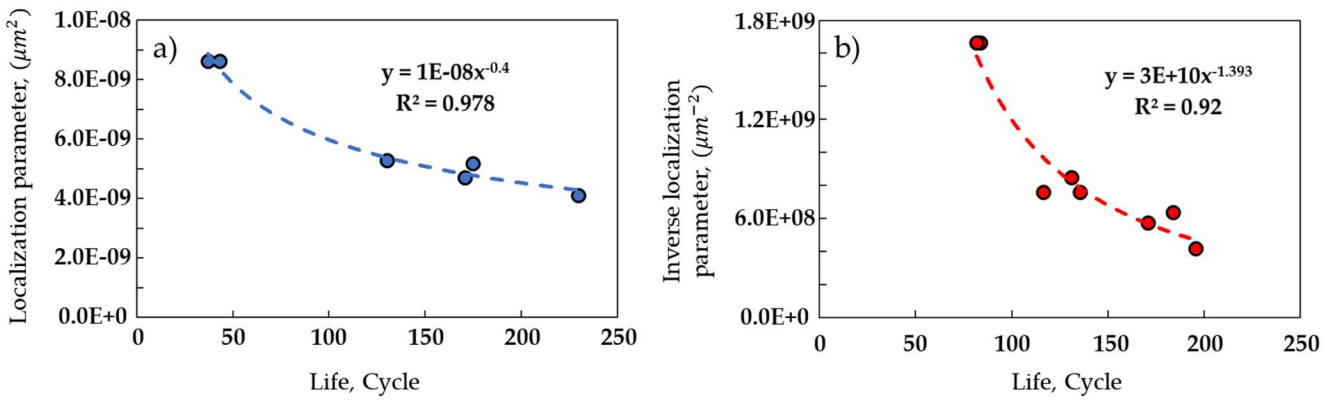

Figure 8. 10 Correlation between localization parameter and life to the crack initiation at a) grain interior and b) grain boundary.

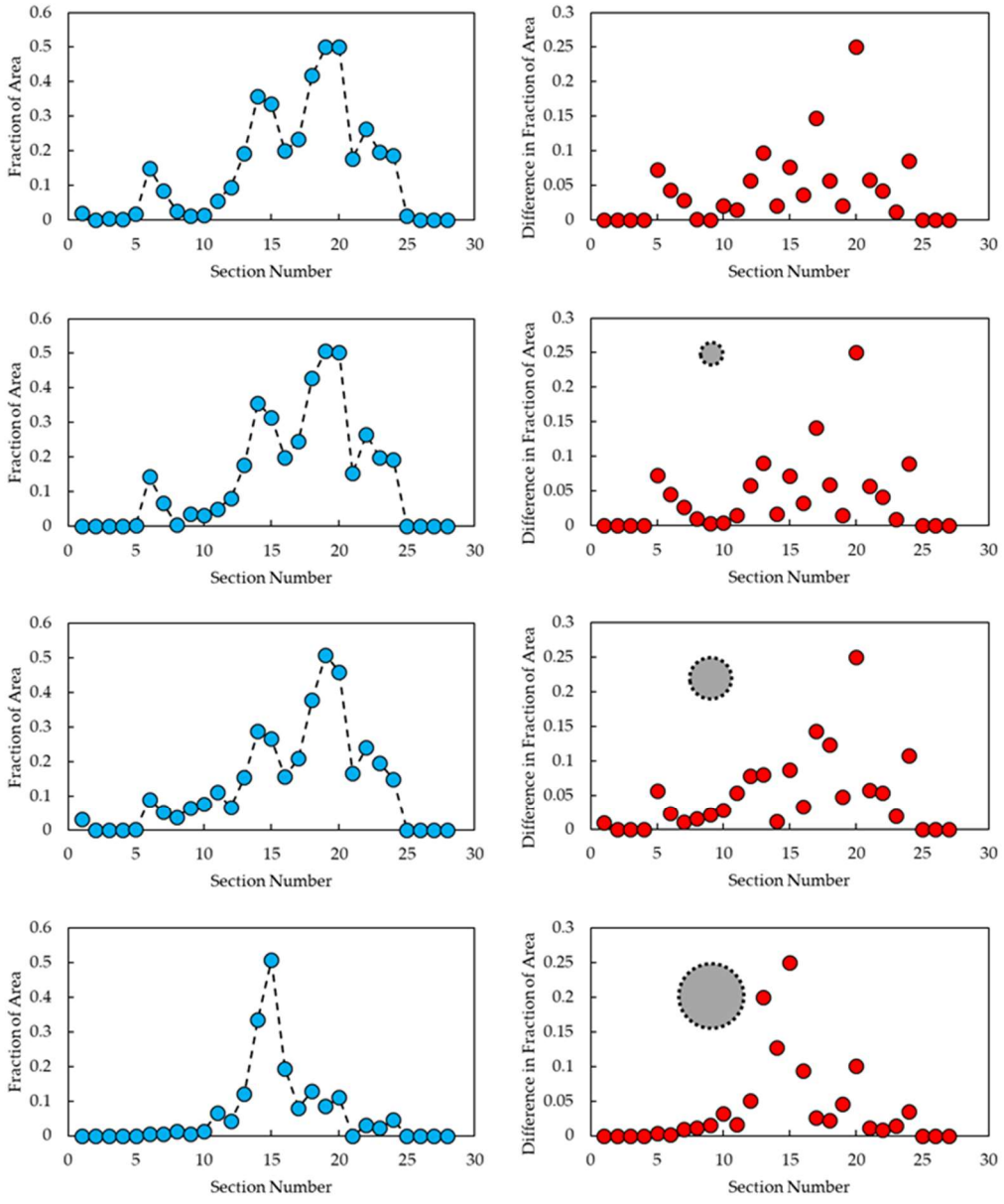

Figure 8. 5 Strain localization and crack initiation site affected by the presence of pore with varying size: a) no pore, b) 3.5 μm, c) 10.5 μm, d) 17.5 μm pore diameter.

CHAPTER 9 CONCLUSIONS

A comprehensive numerical multiscale modeling aimed towards providing a better understanding of the fatigue of additively manufactured Ni superalloys and related phenomena are provided in this dissertation. Physics-based simulations at various length scales are performed to provide insight into mechanisms that govern the fatigue of metallic materials. The findings at lower length scales can be used as the input for physically informed simulations at higher length scales. This way, a more clear understanding of the deformation mechanisms at different stages of the specimen's life can be achieved. In additively manufactured materials, a great deal of attention must be paid to their specific microstructural features, such as grain morphology and size, sub-grain microstructures, elemental segregation, and secondary phase formation. Physics-based material modeling that captures realistic material behavior is a strong tool for different industrial applications that require good mechanical performance under extreme conditions. Conclusions drawn from each individual study are summarized in this section.

Molecular dynamics simulations is used to elucidate the dependence of the operating stress of persistent slip bands on the wall dislocation density and the channel width. To investigate the parameters that affect the stress required to glide a dislocation within the channel, different channel widths and dislocation dipole spacing are considered. Adopting the existing framework of confined layer slip in nanoscale metallic multilayers, a mathematical model describing the rate-and temperature- dependent operating stress of persistent slip bands is proposed [146].

A new procedure utilizing the axial Ising model along with density functional theory calculation and cluster expansion is proposed to calculate the stacking fault energy of Binary nickel

alloys. Using this method, considering large super cells, the interaction of neighboring defects due to periodicity is minimized. A more realistic effect of chemical disorder in theoretical calculation of stacking fault energy (SFE) is made possible. The configurational temperature effect is taken into account by the application of the metropolis Monte Carlo algorithm [425].

Other than SFE, extended fault energies, in ordered phases, within the nickel superalloys such as antiphase boundary energy (APBE) are affecting the fatigue properties of the material. Using the cluster expansion method, the configuration dependent energy of the APB is calculated. The mean value of the APBE is obtained using the Monte Carlo sampling technique. Using this procedure, the effect of temperature as well as chemical disorder effects in multicomponent alloys on the APBE are studied [1].

Mechanical characteristics and the energy of a Cu-Ni {111} semi-coherent interface are studied using molecular dynamics. The periodic nature of the dislocation character of a facet that periodically emerges and disappears as a function of its size, corresponding to the periodic changes in its specific energy, is elucidated. The changes in the dislocation structure of a facet as a result of a change in the interface length are illustrated. This change is associated with the quantized changes in coherency along the step vectors. The mechanical response of a faceted interface has also been investigated. The response was shown to greatly depend on the facet size, which is manifested by the dependence of dislocation emission mechanism on a facet's dislocation structure, and the dependence of dislocation emission stresses on both the facet's Burgers vector and dislocation structure [426].

Tensile fracture stress of ceramic/metal/ceramic interfacial regions, applicable to a wide variety of thin ceramic coating/substrate systems, is assessed using an in-situ micro-pillar tensile testing protocol. The effectiveness of this microscale testing protocol using CrN/Cu/CrN micro-

pillars as the model system has been demonstrated. The thickness dependence of the tensile failure stress was shown and measured as a function of the Cu interlayer thickness. As evidenced by a pronounced dimpled morphology, it was shown that tensile fracture involves plastic deformation of the Cu interlayer. In an attempt to understand and explain these experimental observations, crystal plasticity finite element analyses on the Cu interlayers subjected to similar loading conditions are performed. Geometrical constraints exerted by the much more rigid loading surfaces straddling the interlayer on both sides strongly affect the plastic response of the Cu interlayers. A significant hydrostatic stress component is generated within the layer as the layer thickness decreases, which substantially increases its stiffness. The Von Mises stress component within the layer is reduced, limiting the amount of resulting plasticity. An empirical failure criterion, using a weighted geometric mean between the hydrostatic and von Mises stress components, has been proposed. The trend of measured tensile failure stress as a function of the interlayer thickness is captured using this criterion [361].

The suppressive effects of coatings on the operation of surface PSBs are investigated using crystal plasticity-based simulations. The effects of coating thickness and strain amplitude were evaluated. The suppressive effects of coatings on the operation of PSBs were studied. Normal stresses parallel to the loading direction in the coating layer were calculated for different thicknesses. Normal and shear stress components at the interface of the coating and substrate are also studied in detail. It was observed that the PSB operating can be attenuated by an increase in coating thickness, but increased normal and shear stresses at the PSB-substrate interface can potentially result in delamination [22].

A new hardening model is proposed that captures the heterogeneous evolution of the microstructure from the onset of loading until a crack initiates in the material. A physics-based

criterion is proposed that enables us to calculate the life of the initiation of fatigue crack at different locations in the material. Crystal plasticity simulations are performed to investigate the effect of grain size and morphology, along with volumetric defects, on the strain localization and formation of fatigue cracks. It was observed that strain is more likely to localize in planes with larger mean free paths. The Schmid factor, as a parameter that affects the resolved shear stress, affects the life of the initiation of crack. Unless the pore is significantly large compared to the grain, it will not affect the strain localization and crack initiation behavior in the material.

Considering the capabilities of the crystal plasticity method, many complex issues related to the fatigue of additively manufactured Ni superalloys can be studied in the future. Crystal plasticity simulations can be utilized to investigate the mechanical response of the material under more complex loading patterns such as multiaxial or variable amplitude loadings. Furthermore, different geometries and locations of the volumetric defects and their effects on the initiation of fatigue cracks can be investigated. Carbides and topologically closed pack phases can be explicitly modeled within the framework of crystal plasticity. Deboning or brittle fracture of these phases under cyclic loading and its effect on fatigue crack formation can be investigated. Crystal plasticity models can be applied to investigate the part-level behavior of AM metals using the proper homogenization scheme. This way, combined with the advanced experimental testing and characterization techniques, a more accurate design and failure analysis can be performed on the additive manufactured alloys.

CHAPTER 10 REFERENCES

[1] M. Dodaran, A.H. Ettefagh, S.M. Guo, M.M. Khonsari, W.J. Meng, N. Shamsaei, S. Shao, Effect of alloying elements on the γ' antiphase boundary energy in Ni-base superalloys, Intermetallics. 117 (2020). doi:10.1016/j.intermet.2019.106670.

[2] R.I. Stephens, A. Fatemi, R.R. Stephens, H.O. Fuchs, Metal Fatigue in Engineering, 2nd ed., John Wiley & Sons, 2000.

[3] S.-T. Tu, X.-C. Zhang, Fatigue Crack Initiation Mechanisms, in: Ref. Modul. Mater. Sci. Mater. Eng., Elsevier, 2016. doi:10.1016/B978-0-12-803581-8.02852-6.

[4] J.A. Ewing, J.C.W. Humfrey, The fracture of metals under repeated alternations of stress, Proc. R. Soc. London. 71 (1903) 79–79. doi:10.1098/rspl.1902.0065.

[5] H. Mughrabi, Microstructural mechanisms of cyclic deformation, fatigue crack initiation and early crack growth, Philos. Trans. R. Soc. A Math. Phys. Eng. Sci. 373 (2015) 20140132. doi:10.1098/rsta.2014.0132.

[6] N. Thompson, N. Wadsworth, N. Louat, Xi. The origin of fatigue fracture in copper, Philos. Mag. 1 (1956) 113–126. doi:10.1080/14786435608238086.

[7] J.. Hancock, J.. Grosskreutz, Mechanisms of fatigue hardening in copper single crystals, Acta Metall. 17 (1969) 77–97. doi:10.1016/0001-6160(69)90130-8.

[8] D. Kuhlmann-Wilsdorf, Theory of plastic deformation: - properties of low energy dislocation structures, Mater. Sci. Eng. A. 113 (1989) 1–41. doi:10.1016/0921-5093(89)90290-6.

[9] D. Kuhlmann-Wilsdorf, C. Laird, Dislocation behavior in fatigue, Mater. Sci. Eng. 27 (1977) 137–156. doi:10.1016/0025-5416(77)90166-5.

[10] H. Mughrabi, The cyclic hardening and saturation behaviour of copper single crystals, Mater. Sci. Eng. 33 (1978) 207–223. doi:10.1016/0025-5416(78)90174-X.

[11] H. Mughrabi, Dislocation wall and cell structures and long-range internal stresses in deformed metal crystals, Acta Metall. 31 (1983) 1367–1379. doi:10.1016/0001-6160(83)90007-X.

[12] Z.S. Basinski, R. Pascual, S.J. Basinski, Low amplitude fatigue of copper single crystals—I. The role of the surface in fatigue failure, Acta Metall. 31 (1983) 591–602. doi:10.1016/0001-6160(83)90049-4.

[13] Z.S. Basinski, S.J. Basinski, Fundamental aspects of low amplitude cyclic deformation in face-centred cubic crystals, Prog. Mater. Sci. 36 (1992) 89–148. doi:10.1016/0079-6425(92)90006-S.

[14] R. Keller, W. Zielinski, W.W. Gerberich, On the onset of low-energy dislocation substructures in fatigue: Grain size effects, Mater. Sci. Eng. A. 113 (1989) 267–280. doi:10.1016/0921-5093(89)90315-8.

[15] U. Essmann, H. Mughrabi, Annihilation of dislocations during tensile and cyclic

deformation and limits of dislocation densities, Philos. Mag. A. 40 (1979) 731–756. doi:10.1080/01418617908234871.

[16] H. Mughrabi, Cyclic Slip Irreversibilities and the Evolution of Fatigue Damage, Metall. Mater. Trans. A. 40 (2009) 1257–1279. doi:10.1007/s11661-009-9839-8.

[17] C. Buque, J. Bretschneider, A. Schwab, C. Holste, Effect of grain size and deformation temperature on the dislocation structure in cyclically deformed polycrystalline nickel, Mater. Sci. Eng. A. 319–321 (2001) 631–636. doi:10.1016/S0921-5093(00)02012-8.

[18] J. Polák, Electrical resistivity of cyclically deformed copper, Czechoslov. J. Phys. 19 (1969) 315–322. doi:10.1007/BF01712868.

[19] J.G. Antonopoulos, L.M. Brown, A.T. Winter, Vacancy dipoles in fatigued copper, Philos. Mag. A J. Theor. Exp. Appl. Phys. 34 (1976) 549–563. doi:10.1080/14786437608223793.

[20] U. Essmann, U. Gösele, H. Mughrabi, A model of extrusions and intrusions in fatigued metals I. Point-defect production and the growth of extrusions, Philos. Mag. A. 44 (1981) 405–426. doi:10.1080/01418618108239541.

[21] H. Mughrabi, R. Wang, K. Differt, U. Essmann, Fatigue Crack Initiation by Cyclic Slip Irreversibilities in High-Cycle Fatigue, in: Fatigue Mech. Adv. Quant. Meas. Phys. Damage, ASTM International, 100 Barr Harbor Drive, PO Box C700, West Conshohocken, PA 19428-2959, n.d.: pp. 5-5–41. doi:10.1520/STP30551S.

[22] M.S. Dodaran, J. Wang, N. Shamsaei, S. Shao, Investigating the Interaction between Persistent Slip Bands and Surface Hard Coatings via Crystal Plasticity Simulations, Crystals. 10 (2020) 1012. doi:10.3390/cryst10111012.

[23] G.E. Dieter, Mechanical Metallurgy, 3rd ed., McGraw-Hill, Boston, MA, 1986.

[24] M.A. Meyers, K.K. Chawla, Mechanical Behavior of Materials. 2007, 2007.

[25] V. Kazymyrovych, J. Bergström, C. Burman, The Significance of Crack Initiation Stage in Very High Cycle Fatigue of Steels, Steel Res. Int. 81 (2010) 308–314. doi:10.1002/srin.200900139.

[26] H. Mughrabi, Microstructural mechanisms of cyclic deformation, fatigue crack initiation and early crack growth, Philos. Trans. R. Soc. A Math. Phys. Eng. Sci. 373 (2015) 20140132. doi:10.1098/rsta.2014.0132.

[27] H. Mughrabi, Microscopic Mechanisms of Metal Fatigue, in: Strength Met. Alloy., Elsevier, 1979: pp. 1615–1638. doi:10.1016/B978-1-4832-8412-5.50248-4.

[28] P. Neumann, Dislocation dynamics in fatigue, Phys. Scr. (1987). doi:10.1088/0031-8949/1987/T19B/035.

[29] C. Laird, P. Charsley, H. Mughrabi, Low energy dislocation structures produced by cyclic deformation, Mater. Sci. Eng. 81 (1986) 433–450. doi:10.1016/0025-5416(86)90281-8.

[30] L. Kubin, M. Sauzay, Persistent slip bands: The bowing and passing model revisited, Acta Mater. 132 (2017) 517–524. doi:10.1016/j.actamat.2017.04.064.

[31] L. Kubin, M. Sauzay, Persistent slip bands: Similitude and its consequences, Acta Mater. 104 (2016) 295–302. doi:10.1016/j.actamat.2015.11.010.

[32] P. Charsley, Dislocation arrangements in polycrystalline copper alloys fatigued to saturation, Mater. Sci. Eng. 47 (1981) 181–185. doi:10.1016/0025-5416(81)90044-6.

[33] J.W. Pegues, S. Shao, N. Shamsaei, J.A. Schneider, R.D. Moser, Cyclic strain rate effect on martensitic transformation and fatigue behaviour of an austenitic stainless steel, Fatigue Fract. Eng. Mater. Struct. 40 (2017). doi:10.1111/ffe.12627.

[34] G. Baudry, A. Pineau, Influence of strain-induced martensitic transformation on the low-cycle fatigue behavior of a stainless steel, Mater. Sci. Eng. 28 (1977) 229–242. doi:10.1016/0025-5416(77)90176-8.

[35] M.D. Sangid, The physics of fatigue crack initiation, Int. J. Fatigue. 57 (2013) 58–72. doi:10.1016/j.ijfatigue.2012.10.009.

[36] M.D. Bryant, M.M. Khonsari, F.F. Ling, On the thermodynamics of degradation, Proc. R. Soc. A Math. Phys. Eng. Sci. 464 (2008) 2001–2014. doi:10.1098/rspa.2007.0371.

[37] M.M. Khonsari, M. Amiri, Introduction to Thermodynamics of Mechanical Fatigue, CRC Press, Florida, USA, 2013.

[38] M. Naderi, M. Amiri, M.M. Khonsari, On the thermodynamic entropy of fatigue fracture, Proc. R. Soc. A Math. Phys. Eng. Sci. 466 (2010) 423–438. doi:10.1098/rspa.2009.0348.

[39] M. Liakat, M.M. Khonsari, On the anelasticity and fatigue fracture entropy in high-cycle metal fatigue, Mater. Des. 82 (2015) 18–27. doi:10.1016/j.matdes.2015.04.034.

[40] S. Shao, M.M. Khonsari, J. Wang, N. Shamsaei, N. Li, Frequency dependent deformation reversibility during cyclic loading, Mater. Res. Lett. 6 (2018) 390–397.

[41] L.M. Brown, Dislocation bowing and passing in persistent slip bands, Philos. Mag. 86 (2006) 4055–4068. doi:10.1080/14786430500501689.

[42] S. Plimpton, LAMMPS Molecular Dynamics Simulator, (2019). https://lammps.sandia.gov/.

[43] S. Plimpton, Fast Parallel Algorithms for Short-Range Molecular Dynamics, J. Comput. Phys. 117 (1995) 1–19. doi:10.1006/jcph.1995.1039.

[44] Y. Mishin, M. Mehl, D. Papaconstantopoulos, a. Voter, J. Kress, Structural stability and lattice defects in copper: Ab initio, tight-binding, and embedded-atom calculations, Phys. Rev. B. 63 (2001) 224106. doi:10.1103/PhysRevB.63.224106.

[45] M.S. Daw, M.I. Baskes, Embedded-atom method: Derivation and application to impurities, surfaces, and other defects in metals, Phys. Rev. B. 29 (1984) 6443–6453. doi:10.1103/PhysRevB.29.6443.

[46] D.M. Barnett, J. Lothe, An image force theorem for dislocations in anisotropic bicrystals, J. Phys. F Met. Phys. 4 (1974) 1618–1635. doi:10.1088/0305-4608/4/10/010.

[47] J.P. Hirth, J. Lothe, Theory of Dislocations, 2nd ed., Krieger Publishing Company,

Malabar, FL, 1982.

[48] F.R.N. Nabarro, Mathematical theory of stationary dislocations, Adv. Phys. 1 (1952) 269–394. doi:10.1080/00018735200101211.

[49] G.I. Taylor, The Mechanism of Plastic Deformation of Crystals. Part I. Theoretical, Proc. R. Soc. A Math. Phys. Eng. Sci. 145 (1934) 362–387. doi:10.1098/rspa.1934.0106.

[50] E. Oren, E. Yahel, G. Makov, Dislocation kinematics: a molecular dynamics study in Cu, Model. Simul. Mater. Sci. Eng. 25 (2017) 25002. doi:10.1088/1361-651X/aa52a7.

[51] A. Misra, J.P. Hirth, R.G. Hoagland, Length-scale-dependent deformation mechanisms in incoherent metallic multilayered composites, Acta Mater. 53 (2005) 4817–4824. doi:10.1016/j.actamat.2005.06.025.

[52] R.C. Cammarata, K. Sieradzki, F. Spaepen, Simple model for interface stresses with application to misfit dislocation generation in epitaxial thin films, J. Appl. Phys. 87 (2000) 1227–1234. doi:10.1063/1.372001.

[53] T. Zhu, J. Li, A. Samanta, A. Leach, K. Gall, Temperature and Strain-Rate Dependence of Surface Dislocation Nucleation, Phys. Rev. Lett. 100 (2008) 25502. doi:10.1103/PhysRevLett.100.025502.

[54] C. Bathias, Fatigue Limit in Metals, John Wiley & Sons, Inc., Hoboken, 2014.

[55] N. Abdolrahim, H.M. Zbib, D.F. Bahr, Multiscale modeling and simulation of deformation in nanoscale metallic multilayer systems, Int. J. Plast. 52 (2014) 33–50. doi:10.1016/j.ijplas.2013.04.002.

[56] J.D. Honeycutt, H.C. Andersen, Molecular dynamics study of melting and freezing of small Lennard-Jones clusters, J. Phys. Chem. 91 (1987) 4950–4963. doi:10.1021/j100303a014.

[57] D. P. Mourer, E. S. Huron, K. R. Bain, E. E. Montero, P. L. Reynolds, J. J. Schirra, SUPERALLOY OPTIMIZED FOR HIGH TEMPERATURE PERFORMANCE IN HIGH-PRESSURETURBINE DISKS, (2003) 9.

[58] P. Caron, T. Khan, Evolution of Ni-based superalloys for single crystal gas turbine blade applications, Aerosp. Sci. Technol. 3 (1999) 513–523. doi:10.1016/S1270-9638(99)00108-X.

[59] N.K. Arakere, G. Swanson, Effect of Crystal Orientation on Fatigue Failure of Single Crystal Nickel Base Turbine Blade Superalloys, J. Eng. Gas Turbines Power. 124 (2002) 161–176. doi:10.1115/1.1413767.

[60] S.J. Patel, J.J. De Barbadillo, B.A. Baker, R.D. Gollihue, Nickel base superalloys for next generation coal fired AUSC power plants, in: Procedia Eng., Elsevier Ltd, 2013: pp. 246–252. doi:10.1016/j.proeng.2013.03.250.

[61] H. Zhang, C. Li, Q. Guo, Z. Ma, H. Li, Y. Liu, Improving creep resistance of nickel-based superalloy Inconel 718 by tailoring gamma double prime variants, Scr. Mater. 164 (2019) 66–70. doi:10.1016/j.scriptamat.2019.01.041.

[62] J.M. Oblak, D.F. Paulonis, D.S. Duvaal, Coherency Strengthening in Ni Base Alloys Hardened by D022 γ" Precipitates, Metall. Trans. 5 (1974) 143–153.

[63] Y.-Y. Lin, F. Schleifer, M. Fleck, U. Glatzel, On the interaction between γ″ precipitates and dislocation microstructures in Nb containing single crystal nickel-base alloys, Mater. Charact. 165 (2020) 110389. doi:10.1016/j.matchar.2020.110389.

[64] M.J. Donachie, S.J. Donachie, Superalloys: A Technical Guide, 2nd ed., ASM International, Materials Park, OH, 2002. doi:10.1361.

[65] T.M. Pollock, A.S. Argon, Creep resistance of CMSX-3 nickel base superalloy single crystals, Acta Metall. Mater. 40 (1992) 1–30. doi:10.1016/0956-7151(92)90195-K.

[66] F. Pettinari, J. Douin, G. Saada, P. Caron, A. Coujou, N. Clément, Stacking fault energy in short-range ordered γ-phases of Ni-based superalloys, Mater. Sci. Eng. A. 325 (2002) 511–519. doi:10.1016/S0921-5093(01)01765-8.

[67] M. Benyoucef, B. Décamps, A. Coujou, N. Clément, Stacking-fault energy at room temperature of the γ matrix of the MC2 Ni-based superalloy, Philos. Mag. A. 71 (1995) 907–923. doi:10.1080/01418619508236228.

[68] D.M. Esterling, A.R. McGurn, I.M. Boswarva, R.J. Arsenault, Stacking fault widths, energies and dislocation core structures, Mater. Sci. Eng. 68 (1984) 97–106. doi:10.1016/0025-5416(84)90247-7.

[69] C.B. Carter, S.M. Holmes, The stacking-fault energy of nickel, Philos. Mag. A J. Theor. Exp. Appl. Phys. 35 (1977) 1161–1172. doi:10.1080/14786437708232942.

[70] D.J.H. Cockayne, V. Vitek, Effect of Core Structure on the Determination of the Stacking-Fault Energy in Close-Packed Metals, Phys. Status Solidi. 65 (1974) 751–764. doi:10.1002/pssb.2220650236.

[71] Y. Yuan, Y.F. Gu, C.Y. Cui, T. Osada, T. Tetsui, T. Yokokawa, H. Harada, Creep mechanisms of U720Li disc superalloy at intermediate temperature, Mater. Sci. Eng. A. 528 (2011) 5106–5111. doi:10.1016/j.msea.2011.03.034.

[72] W.W. Milligan, S.D. Antolovich, The mechanisms and temperature dependence of superlattice stacking fault formation in the single-crystal superalloy PWA 1480, Metall. Trans. A. 22 (1991) 2309–2318. doi:10.1007/BF02664997.

[73] D.C. Ludwigson, Modified stress-strain relation for FCC metals and alloys, Metall. Trans. 2 (1971) 2825–2828. doi:10.1007/BF02813258.

[74] T. Rasmussen, K.W. Jacobsen, T. Leffers, O.B. Pedersen, S.G. Srinivasan, H. Jónsson, Atomistic Determination of Cross-Slip Pathway and Energetics, Phys. Rev. Lett. 79 (1997) 3676–3679. doi:10.1103/PhysRevLett.79.3676.

[75] T. Rasmussen, K.W. Jacobsen, T. Leffers, O.B. Pedersen, Simulations of the atomic structure, energetics, and cross slip of screw dislocations in copper, Phys. Rev. B. 56 (1997) 2977–2990. doi:10.1103/PhysRevB.56.2977.

[76] J. Bonneville, B. Escaig, Cross-slipping process and the stress-orientation dependence in

pure copper, Acta Metall. 27 (1979) 1477–1486. doi:10.1016/0001-6160(79)90170-6.

[77] J. Bonneville, B. Escaig, J.L. Martin, A study of cross-slip activation parameters in pure copper, Acta Metall. 36 (1988) 1989–2002. doi:10.1016/0001-6160(88)90301-X.

[78] A.S. Argon, W.C. Moffatt, Climb of extended edge dislocations, Acta Metall. 29 (1981) 293–299. doi:10.1016/0001-6160(81)90156-5.

[79] C.K.L. Davies, P.W. Davies, B. Wilshire, The effect of variations in stacking-fault energy on the creep of nickel-cobalt alloys, Philos. Mag. 12 (1965) 827–839. doi:10.1080/14786436508218920.

[80] C.R. Barrett, O.D. Sherby, INFLUENCE OF STACKING FAULT ENERGY ON HIGH TEMPERATURE CREEP OF PURE METALS, Trans. Metall. Soc. AIME. (1965).

[81] A.K. Mukherjee, J.E. Bird, J.E. Dorn, E. Org, EXPERIMENTAL CORRELATIONS FOR HIGH-TEMPERATURE CREEP, 1968. https://escholarship.org/uc/item/31p4z5v2 (accessed December 27, 2019).

[82] G. Thomas, The effect of short-range order on stacking fault energy and dislocation arrangements in f.c.c. solid solutions, Acta Metall. 11 (1963) 1369–1371. doi:10.1016/0001-6160(63)90035-X.

[83] S. Crampin, K. Hampel, D.D. Vvedensky, J.M. MacLaren, The calculation of stacking fault energies in close-packed metals, J. Mater. Res. 5 (2011) 2107–2119. doi:10.1557/JMR.1990.2107.

[84] M. Chandran, S.K. Sondhi, First-principle calculation of stacking fault energies in Ni and Ni-Co alloy, J. Appl. Phys. 109 (2011) 103525. doi:10.1063/1.3585786.

[85] T.L. Achmad, W. Fu, H. Chen, C. Zhang, Z.-G. Yang, Computational thermodynamic and first-principles calculation of stacking fault energy on ternary Co-based alloys, Comput. Mater. Sci. 143 (2018) 112–117. doi:10.1016/j.commatsci.2017.11.004.

[86] X. Nie, Renhui Wang, Yiying Ye, Yumei Zhou, Dingsheng Wang, Calculations of stacking fault energy for fcc metals and their alloys based on an improved embedded-atom method, Solid State Commun. 96 (1995) 729–734. doi:10.1016/0038-1098(95)00506-4.

[87] Y. Qi, R.K. Mishra, Ab initio study of the effect of solute atoms on the stacking fault energy in aluminum, Phys. Rev. B. 75 (2007) 224105. doi:10.1103/PhysRevB.75.224105.

[88] P.J.H. Denteneer, W. van Haeringen, Stacking-fault energies in semiconductors from first-principles calculations, J. Phys. C Solid State Phys. 20 (1987) L883--L887. doi:10.1088/0022-3719/20/32/001.

[89] L. Vitos, J.-O. Nilsson, B. Johansson, Alloying effects on the stacking fault energy in austenitic stainless steels from first-principles theory, Acta Mater. 54 (2006) 3821–3826. doi:10.1016/j.actamat.2006.04.013.

[90] R. Sun, C. Woodward, A. van de Walle, First-principles study on N3Al (111) antiphase boundary with Ti and Hf impurities, Phys. Rev. B. 95 (2017) 214121. doi:10.1103/PhysRevB.95.214121.

[91] E. Ising, Beitrag zur Theorie des Ferromagnetismus, Zeitschrift Für Phys. 31 (1925) 253–258. doi:10.1007/BF02980577.

[92] L. Onsager, Crystal Statistics. I. A Two-Dimensional Model with an Order-Disorder Transition, Phys. Rev. 65 (1944) 117–149. doi:10.1103/PhysRev.65.117.

[93] L. Vitos, P.A. Korzhavyi, J.-O. Nilsson, B. Johansson, Stacking fault energy and magnetism in austenitic stainless steels, Phys. Scr. 77 (2008) 065703. doi:10.1088/0031-8949/77/06/065703.

[94] S. Lu, Q.-M. Hu, B. Johansson, L. Vitos, Stacking fault energies of Mn, Co and Nb alloyed austenitic stainless steels, Acta Mater. 59 (2011) 5728–5734. doi:10.1016/j.actamat.2011.05.049.

[95] J.M. Sanchez, F. Ducastelle, D. Gratias, Generalized cluster description of multicomponent systems, Phys. A Stat. Mech. Its Appl. 128 (1984) 334–350. doi:10.1016/0378-4371(84)90096-7.

[96] A. van de Walle, M. Asta, G. Ceder, The alloy theoretic automated toolkit: A user guide, Calphad. 26 (2002) 539–553. doi:10.1016/S0364-5916(02)80006-2.

[97] P. Giannozzi, S. Baroni, N. Bonini, M. Calandra, R. Car, C. Cavazzoni, D. Ceresoli, G.L. Chiarotti, M. Cococcioni, I. Dabo, A. Dal Corso, S. de Gironcoli, S. Fabris, G. Fratesi, R. Gebauer, U. Gerstmann, C. Gougoussis, A. Kokalj, M. Lazzeri, L. Martin-Samos, N. Marzari, F. Mauri, R. Mazzarello, S. Paolini, A. Pasquarello, L. Paulatto, C. Sbraccia, S. Scandolo, G. Sclauzero, A.P. Seitsonen, A. Smogunov, P. Umari, R.M. Wentzcovitch, QUANTUM ESPRESSO: a modular and open-source software project for quantum simulations of materials, J. Phys. Condens. Matter. 21 (2009) 395502. doi:10.1088/0953-8984/21/39/395502.

[98] A. van de Walle, M.D. Asta, A. Walle, G. Ceder, Automating First-principles Phase Diagram Calculations, J. Phase Equilibria. 23 (2002) 348–359. doi:10.1361/105497102770331596.

[99] R. Sun, A. van de Walle, Automating impurity-enhanced antiphase boundary energy calculations from ab initio Monte Carlo, Calphad. 53 (2016) 20–24. doi:10.1016/j.calphad.2016.02.005.

[100] A. van de Walle, M. Asta, Self-driven lattice-model Monte Carlo simulations of alloy thermodynamic properties and phase diagrams, Model. Simul. Mater. Sci. Eng. 10 (2002) 521–538. doi:10.1088/0965-0393/10/5/304.

[101] X. Zhang, B. Grabowski, F. Körmann, A. V. Ruban, Y. Gong, R.C. Reed, T. Hickel, J. Neugebauer, Temperature dependence of the stacking-fault Gibbs energy for Al, Cu, and Ni, Phys. Rev. B. 98 (2018) 224106. doi:10.1103/PhysRevB.98.224106.

[102] G. Prandini, A. Marrazzo, I.E. Castelli, N. Mounet, N. Marzari, Precision and efficiency in solid-state pseudopotential calculations, Npj Comput. Mater. 4 (2018) 72. doi:10.1038/s41524-018-0127-2.

[103] J.P. Perdew, K. Burke, M. Ernzerhof, Generalized Gradient Approximation Made Simple, Phys. Rev. Lett. 77 (1996) 3865–3868. doi:10.1103/PhysRevLett.77.3865.

[104] F.D. Murnaghan, The Compressibility of Media under Extreme Pressures, Proc. Natl. Acad. Sci. 30 (1944) 244–247. doi:10.1073/pnas.30.9.244.

[105] R.E. Smallman, P.S. Dobson, Stacking Fault Energy Measurement from Diffusion, Metall. Trans. 1 (1970) 2383–2389. doi:https://doi.org/10.1007/BF03038367.

[106] H.-L. Chen, E. Doernberg, P. Svoboda, R. Schmid-Fetzer, Thermodynamics of the Al3Ni phase and revision of the Al–Ni system, Thermochim. Acta. 512 (2011) 189–195. doi:10.1016/j.tca.2010.10.005.

[107] H.P. Karnthaler, E.T. Mühlbacher, C. Rentenberger, The influence of the fault energies on the anomalous mechanical behaviour of Ni3Al alloys, Acta Mater. 44 (1996) 547–560. doi:10.1016/1359-6454(95)00191-3.

[108] MASSALSKI, T. B., Binary Alloy Phase Diagrams, ASM Int. 3 (1992) 2874. http://ci.nii.ac.jp/naid/10003259757/en/ (accessed May 26, 2020).

[109] K. Hagihara, T. Nakano, Y. Umakoshi, Plastic deformation behaviour in Ni3Ti single crystals with D024 structure, Acta Mater. 51 (2003) 2623–2637. doi:10.1016/S1359-6454(03)00060-0.

[110] P. Nash, The Cr−Ni (Chromium-Nickel) system, Bull. Alloy Phase Diagrams. 7 (1986) 466–476. doi:10.1007/BF02867812.

[111] G. Venkataraman, Y.W. Chung, Y. Nakasone, T. Mura, Free energy formulation of fatigue crack initiation along persistent slip bands: calculation of SN curves and crack depths, Acta Metall. Mater. 38 (1990) 31–40. doi:10.1016/0956-7151(90)90132-Z.

[112] Z. Du, D. Lü, Thermodynamic modeling of the Co–Ni–Y system, Intermetallics. 13 (2005) 586–595. doi:10.1016/j.intermet.2004.09.013.

[113] B.E.P. Beeston, L.K. France, No Title, J. Inst. Met. 96 (1968) 2454.

[114] L. Deléhouzée, A. Deruyttere, The stacking fault density in solid solutions based on copper, silver, nickel, aluminium and lead, Acta Metall. 15 (1967) 727–734. doi:10.1016/0001-6160(67)90353-7.

[115] E.H. Köster, A.R. Thölén, A. Howie, Stacking fault energies of Ni–Co–Cr alloys, Philos. Mag. 10 (1964) 1093–1095. doi:10.1080/14786436408225417.

[116] S.L. Shang, C.L. Zacherl, H.Z. Fang, Y. Wang, Y. Du, Z.K. Liu, Effects of alloying element and temperature on the stacking fault energies of dilute Ni-base superalloys, J. Phys. Condens. Matter. 24 (2012) 505403. doi:10.1088/0953-8984/24/50/505403.

[117] S.L. Shang, C.L. Zacherl, H.Z. Fang, Y. Wang, Y. Du, Z.K. Liu, Effects of alloying element and temperature on the stacking fault energies of dilute Ni-base superalloys, J. Phys. Condens. Matter. 24 (2012) 505403. doi:10.1088/0953-8984/24/50/505403.

[118] C. Li, S. Dang, P. Han, X. He, X. Long, Effect of Cr on the generalized stacking fault energy of impure doped Ni (111) surface: a first-principles study, Eur. Phys. J. B. 93 (2020) 156. doi:10.1140/epjb/e2020-10013-x.

[119] P.J. Craievich, J.M. Sanchez, Vibrational free energy in the Ni-Cr system, Comput. Mater.

Sci. 8 (1997) 92–99. doi:10.1016/S0927-0256(97)00021-9.

[120] I.L. Dillamore, R.E. Smallman, The stacking-fault energy of F.C.C. metals, Philos. Mag. 12 (1965) 191–193. doi:10.1080/14786436508224959.

[121] R.E. Schramm, R.P. Reed, Stacking fault energies of fcc fe-Ni alloys by x-ray diffraction line profile analysis, Metall. Trans. A. 7 (1976) 359–363. doi:10.1007/BF02642831.

[122] L.E. Murr, Interfacial phenomena in metals and alloys, Addison-Wesley Publishing Company, Reading, MA, 1975.

[123] M.J. Mills, P. Stadelmann, A study of the structure of Lomer and 60° dislocations in aluminium using high-resolution transmission electron microscopy, Philos. Mag. A. 60 (1989) 355–384. doi:10.1080/01418618908213867.

[124] Y. Mishin, Atomistic modeling of the $\gamma{\$}and $\gamma{\$}′-phases of the Ni–Al system, Acta Mater. 52 (2004) 1451–1467. doi:10.1016/j.actamat.2003.11.026.

[125] B. Hammer, K.W. Jacobsen, V. Milman, M.C. Payne, Stacking fault energies in aluminium, J. Phys. Condens. Matter. 4 (1992) 10453–10460. doi:10.1088/0953-8984/4/50/033.

[126] R.E. Voskoboinikov, Effective γ-surfaces in {111} plane in FCC Ni and L12 Ni3Al intermetallic compound, Phys. Met. Metallogr. 114 (2013) 545–552. doi:10.1134/S0031918X13070132.

[127] R.H. Rautioaho, An Interatomic Pair Potential for Aluminium Calculation of Stacking Fault Energy, Phys. Status Solidi. 112 (1982) 83–89. doi:10.1002/pssb.2221120108.

[128] Y. Mishin, D. Farkas, M.J. Mehl, D.A. Papaconstantopoulos, Interatomic potentials for monoatomic metals from experimental data and ab initio calculations, Phys. Rev. B. 59 (1999) 3393–3407. doi:10.1103/PhysRevB.59.3393.

[129] C. Woodward, D.R. Trinkle, L.G. Hector, D.L. Olmsted, Prediction of Dislocation Cores in Aluminum from Density Functional Theory, Phys. Rev. Lett. 100 (2008) 045507. doi:10.1103/PhysRevLett.100.045507.

[130] D.J. Siegel, Generalized stacking fault energies, ductilities, and twinnabilities of Ni and selected Ni alloys, Appl. Phys. Lett. 87 (2005) 121901. doi:10.1063/1.2051793.

[131] S. Kibey, J.B. Liu, D.D. Johnson, H. Sehitoglu, Predicting twinning stress in fcc metals: Linking twin-energy pathways to twin nucleation, Acta Mater. 55 (2007) 6843–6851. doi:10.1016/j.actamat.2007.08.042.

[132] S. Zhao, G.M. Stocks, Y. Zhang, Stacking fault energies of face-centered cubic concentrated solid solution alloys, Acta Mater. 134 (2017) 334–345. doi:10.1016/j.actamat.2017.05.001.

[133] G. Lu, N. Kioussis, V. V Bulatov, E. Kaxiras, Generalized-stacking-fault energy surface and dislocation properties of aluminum, Phys. Rev. B. 62 (2000) 3099–3108. doi:10.1103/PhysRevB.62.3099.

[134] J.A. Zimmerman, H. Gao, F.F. Abraham, Generalized stacking fault energies for

embedded atom FCC metals, Model. Simul. Mater. Sci. Eng. 8 (2000) 103–115. doi:10.1088/0965-0393/8/2/302.

[135] N. Bernstein, E. Tadmor, Tight-binding calculations of stacking energies and twinnability in fcc metals, Phys. Rev. B. 69 (2004) 094116. doi:10.1103/PhysRevB.69.094116.

[136] R. Meyer, L.J. Lewis, Stacking-fault energies for Ag , Cu , and Ni from empirical tight-binding potentials, (2002) 1–5.

[137] S.D. Antolovich, R. Bowman, The effect of microstructure on the fatigue crack growth resistance of nickel base superalloys, TMS-AIME, Warrendale, 1986.

[138] R.D. Field, T.M. Pollock, W.H. Murphy, The Development of $\gamma{\$}/$\gamma{\$}' Interfacial Dislocation Networks During Creep in Ni-Base Superalloys, in: Superalloys 1992 (Seventh Int. Symp., TMS, 1992: pp. 557–566. doi:10.7449/1992/Superalloys_1992_557_566.

[139] H. Long, H. Wei, Y. Liu, S. Mao, J. Zhang, S. Xiang, Y. Chen, W. Gui, Q. Li, Z. Zhang, X. Han, Effect of lattice misfit on the evolution of the dislocation structure in Ni-based single crystal superalloys during thermal exposure, Acta Mater. 120 (2016) 95–107. doi:10.1016/j.actamat.2016.08.035.

[140] J.M. Oblak, D.S. Duvall, D.F. Paulonis, An estimate of the strengthening arising from coherent, tetragonally-distorted particles, Mater. Sci. Eng. 13 (1974) 51–56. doi:10.1016/0025-5416(74)90020-2.

[141] M. Sundararaman, P. Mukhopadhyay, S. Banerjee, Precipitation of the δ-Ni3Nb phase in two nickel base superalloys, Metall. Trans. A. 19 (1988) 453–465. doi:10.1007/BF02649259.

[142] P.M. Mignanelli, N.G. Jones, E.J. Pickering, O.M.D.M. Messé, C.M.F. Rae, M.C. Hardy, H.J. Stone, Gamma-gamma prime-gamma double prime dual-superlattice superalloys, Scr. Mater. 136 (2017) 136–140. doi:10.1016/j.scriptamat.2017.04.029.

[143] C. Slama, M. Abdellaoui, Structural characterization of the aged Inconel 718, J. Alloys Compd. 306 (2000) 277–284. doi:10.1016/S0925-8388(00)00789-1.

[144] N. Baluc, R. Schäublin, Weak beam transmission electron microscopy imaging of superdislocations in ordered Ni 3 Al, Philos. Mag. A. 74 (1996) 113–136. doi:10.1080/01418619608239693.

[145] S. Shao, M.M. Khonsari, S. Guo, W.J. Meng, N. Li, Overview: Additive Manufacturing Enabled Accelerated Design of Ni-based alloys for Improved Fatigue Life, Addit. Manuf. (n.d.).

[146] M. Dodaran, M.M. Khonsari, S. Shao, Critical operating stress of persistent slip bands in Cu, Comput. Mater. Sci. 165 (2019). doi:10.1016/j.commatsci.2019.04.036.

[147] A.J. Ardell, Precipitation hardening, Metall. Trans. A. 16 (1985) 2131–2165. doi:10.1007/BF02670416.

[148] A. Ardell, Disorder strengthening of ordered L12 alloys by face centered cubic (A1)

precipitates, Intermetallics. 88 (2017) 81–90. doi:10.1016/j.intermet.2017.05.010.

[149] R.W. Kozar, A. Suzuki, W.W. Milligan, J.J. Schirra, M.F. Savage, T.M. Pollock, Strengthening Mechanisms in Polycrystalline Multimodal Nickel-Base Superalloys, Metall. Mater. Trans. A. 40 (2009) 1588–1603. doi:10.1007/s11661-009-9858-5.

[150] A.J. Ardell, Chapter 12: Intermetallics as Precipitates and Dispersoids in High-Strength Alloys, John Wiley & Sons, Ltd., New York, 1994.

[151] B. Reppich, Some new aspects concerning particle hardening mechanisms in $γ$' precipitating Ni-base alloys—I. Theoretical concept, Acta Metall. 30 (1982) 87–94.

[152] D. Baither, C. Rentenberger, H.P. Karnthaler, E. Nembach, Three alternative experimental methods to determine the antiphase-boundary energies of the $γ$' precipitates in superalloys, Philos. Mag. 82 (2002) 1795–1805.

[153] A. Ardell, C. Huang, Antiphase boundary energies and the transition from shearing to looping in alloys strengthened by ordered precipitates, Philos. Mag. Lett. 58 (1988) 189–197.

[154] E. Nembach, G. Neite, Precipitation hardening of superalloys by ordered γ′-particles, Prog. Mater. Sci. 29 (1985) 177–319. doi:10.1016/0079-6425(85)90001-5.

[155] G. Molenat, D. Caillard, Dislocation mechanisms in Ni 3 Al at room temperature. In situ straining experiments in TEM, Philos. Mag. A. 64 (1991) 1291–1317. doi:10.1080/01418619108225350.

[156] M.H. Yoo, On the theory of anomalous yield behavior of Ni3Al — Effect of elastic anisotropy, Scr. Metall. 20 (1986) 915–920. doi:10.1016/0036-9748(86)90466-7.

[157] M.H. Yoo, Stability of superdislocations and shear faults in L12 ordered alloys, Acta Metall. 35 (1987) 1559–1569. doi:10.1016/0001-6160(87)90102-7.

[158] S.D. Antolovich, Microstructural aspects of fatigue in Ni-base superalloys, Philos. Trans. R. Soc. A Math. Phys. Eng. Sci. 373 (2015) 20140128. doi:10.1098/rsta.2014.0128.

[159] B. Lawless, S.D. Antolovich, C. Bathias, B. Boursier, The effect of microstructure on the fatigue crack propagation and overload behavior of Waspaloy at room temperature, in: J.M. Wells, J.D. Landes (Eds.), Fract. Interact. Microstruct. Mech. Mech., The Metallurgical Society, Warrendale, 1984: pp. 285–301.

[160] D.E. Laughlin, K. Hono, eds., Physical Metallurgy, 5th ed., Elsevier, 2015. doi:10.1016/C2010-0-65716-6.

[161] O.I. Gorbatov, I.L. Lomaev, Y.N. Gornostyrev, A. V Ruban, D. Furrer, V. Venkatesh, D.L. Novikov, S.F. Burlatsky, effect of composition on antiphase boundary energy in Ni3Al bsaed alloys ab initio calculations, Phys. Rev. B. 93 (2016) 224106. doi:10.1103/PhysRevB.93.224106.

[162] R. Sun, C. Woodward, A. van de Walle, First-principles study on <math> <mrow> <msub> <mi>Ni</mi> <mn>3</mn> </msub> <mi>Al</mi> </mrow> <mo> </mo> <mrow> <mo>(</mo> <mn>111</mn> <mo>)</mo> </mrow> </math> antiphase

boundary with Ti and Hf impurities, Phys. Rev. B. 95 (2017) 214121. doi:10.1103/PhysRevB.95.214121.

[163] D.J. Crudden, A. Mottura, N. Warnken, B. Raeisinia, R.C. Reed, Modelling of the influence of alloy composition on flow stress in high-strength nickel-based superalloys, Acta Mater. 75 (2014) 356–370. doi:10.1016/j.actamat.2014.04.075.

[164] D. Caillard, N. Clément, A. Couret, P. Lours, A. Coujou, {111} Glide in Ni 3 Al at room temperature. In situ observations under weak-beam conditions, Philos. Mag. Lett. 58 (1988) 263–269. doi:10.1080/09500838808214763.

[165] Y. Mishin, Atomistic modeling of the $γ$ and $γ$′-phases of the Ni–Al system, Acta Mater. 52 (2004) 1451–1467. doi:10.1016/j.actamat.2003.11.026.

[166] B. Jelinek, S. Groh, M.F. Horstemeyer, J. Houze, S.G. Kim, G.J. Wagner, a. Moitra, M.I. Baskes, Modified embedded atom method potential for Al, Si, Mg, Cu, and Fe alloys, Phys. Rev. B. 85 (2012) 245102. doi:10.1103/PhysRevB.85.245102.

[167] sepideh kavousi, B. Novak, M.I. Baskes, M. Asle Zaeem, D. Moldovan, MEAM potential for high temperature crystal-melt properties of Ti-Ni alloys and its application to phase field simulation of solidification, Model. Simul. Mater. Sci. Eng. (2019). doi:10.1088/1361-651X/ab580c.

[168] Y. Koizumi, S. Ogata, Y. Minamino, N. Tsuji, Energies of conservative and non-conservative antiphase boundaries in Ti 3 Al: a first principles study, Philos. Mag. 86 (2006) 1243–1259. doi:10.1080/14786430500380126.

[169] W. Xu, A.P. Horsfield, D. Wearing, P.D. Lee, First-principles calculation of Mg/MgO interfacial free energies, J. Alloys Compd. 650 (2015) 228–238. doi:10.1016/j.jallcom.2015.07.289.

[170] T. Uesugi, K. Higashi, First-Principles Calculation of Grain Boundary Excess Volume and Free Volume in Nanocrystalline and Ultrafine-Grained Aluminum, Mater. Trans. 54 (2013) 1597–1604. doi:10.2320/matertrans.L-M2013816.

[171] R. Namakian, G.Z. Voyiadjis, An atomic displacive model for {10-12}<-1011> twinning in hexagonal close packed metals with the emphasis on the role of partial stacking faults in formation of {10-12} twins, Acta Mater. 150 (2018) 381–393. doi:10.1016/j.actamat.2018.03.028.

[172] J. Wang, R.G. Hoagland, J.P. Hirth, a. Misra, Atomistic modeling of the interaction of glide dislocations with “weak” interfaces, Acta Mater. 56 (2008) 5685–5693. doi:10.1016/j.actamat.2008.07.041.

[173] K. Kumar, R. Sankarasubramanian, U. V Waghmare, Tuning planar fault energies of Ni3Al with substitutional alloying: First-principles description for guiding rational alloy design, Scr. Mater. 142 (2018) 74–78. doi:10.1016/j.scriptamat.2017.08.021.

[174] M. Chandran, S.K. Sondhi, First-principle calculation of APB energy in Ni-based binary and ternary alloys, Model. Simul. Mater. Sci. Eng. 19 (2011) 25008. doi:10.1088/0965-0393/19/2/025008.

[175] S.K. Makineni, M. Lenz, S. Neumeier, E. Spiecker, D. Raabe, B. Gault, Elemental segregation to antiphase boundaries in a crept CoNi-based single crystal superalloy, Scr. Mater. 157 (2018) 62–66. doi:10.1016/j.scriptamat.2018.07.042.

[176] L. Vitos, Computational Quantum Mechanics for Materials Engineers, Springer London, London, 2007. doi:10.1007/978-1-84628-951-4.

[177] Z.W. Lu, S.-H. Wei, A. Zunger, S. Frota-Pessoa, L.G. Ferreira, First-principles statistical mechanics of structural stability of intermetallic compounds, Phys. Rev. B. 44 (1991) 512–544. doi:10.1103/PhysRevB.44.512.

[178] A. Van De Walle, M. Asta, First-principles investigation of perfect and diffuse antiphase boundaries in HCP-based Ti-Al alloys, Metall. Mater. Trans. A. 33 (2002) 735–741. doi:10.1007/s11661-002-1002-8.

[179] M. Rahaman, V.I. Razumovskiy, B. Johansson, A. V Ruban, Temperature dependence of stacking-fault and anti-phase boundary energies in Al Sc from ab initio calculations, Philos. Mag. 93 (2013) 3423–3441. doi:10.1080/14786435.2013.810817.

[180] C. Amador, J.J. Hoyt, B.C. Chakoumakos, D. de Fontaine, Theoretical and Experimental Study of Relaxations in Al3Ti and Al3Zr Ordered Phases, Phys. Rev. Lett. 74 (1995) 4955–4958. doi:10.1103/PhysRevLett.74.4955.

[181] A.T. Paxton, H.M. Polatoglou, Origin of the Modulated Phase in Copper-Gold Alloys, Phys. Rev. Lett. 78 (1997) 270–273. doi:10.1103/PhysRevLett.78.270.

[182] C. Colinet, A. Pasturel, Structural stability of one-dimensional long-period structures in the TiAl3 compound, J. Phys. Condens. Matter. 14 (2002) 311. doi:10.1088/0953-8984/14/26/311.

[183] M. Sluiter, Y. Hashi, Y. Kawazoe, The effect of segregation and partial order on the thermodynamics of (111) antiphase boundaries in Ni3Al, Comput. Mater. Sci. 14 (1999) 283–290. doi:10.1016/S0927-0256(98)00120-7.

[184] R.E. Smallman, Bishop R. J., Modern Physical Metallurgy and Materials Engineering, Elsevier, 1999. doi:10.1016/B978-0-7506-4564-5.X5000-9.

[185] U. Scheuer, B. Lengeler, Lattice distortion of solute atoms in metals studied by x-ray-absorption fine structure, Phys. Rev. B. 44 (1991) 9883–9894. doi:10.1103/PhysRevB.44.9883.

[186] J.-O. Andersson, T. Helander, L. Höglund, P. Shi, B. Sundman, Thermo-Calc & DICTRA, computational tools for materials science, Calphad. 26 (2002) 273–312. doi:10.1016/S0364-5916(02)00037-8.

[187] G. Sjoberg, D. Imamovic, J. Gabel, O. Cabellero, J.W. Brooks, J.-P. Ferte, A. Lugan, Evaluation of the IN 939 Alloy for Large Aircraft Engine Structures, in: Superalloys 2004 - Tenth Int. Symp., TMS, 2004: pp. 441–450. doi:10.7449/2004/Superalloys_2004_441_450.

[188] G. Schoeck, S. Kohlhammer, M. Fahnle, Planar dissociations and recombination energy of [110] superdislocations in Ni 3 Al: Generalized Peierls model in combination with ab

initio electron theory, Philos. Mag. Lett. 79 (1999) 849–857. doi:10.1080/095008399176544.

[189] S.Y. Yuan, Z.H. Jiang, J.Z. Liu, Y. Tang, Y. Zhang, Nano-twinning in a γ′ precipitate strengthened Ni-based superalloy, Mater. Res. Lett. 6 (2018) 683–688. doi:10.1080/21663831.2018.1538021.

[190] M.H.F. Sluiter, Y. Kawazoe, Site preference of ternary additions in Ni3Al, Phys. Rev. B. 51 (1995) 4062–4073. doi:10.1103/PhysRevB.51.4062.

[191] S. Ochial, Y. Oya, T. Suzuki, Alloying behaviour of Ni3Al, Ni3Ga, Ni3Si and Ni3Ge, Acta Metall. 32 (1984) 289–298. doi:10.1016/0001-6160(84)90057-9.

[192] E.S. Machlin, J. Shao, Quaternary gamma-prime (Ll2) pseudobinary properties as revealed by the ionicity modified pair potential model, Scr. Metall. 11 (1977) 859–862. doi:10.1016/0036-9748(77)90338-6.

[193] C. Wolverton, D. de Fontaine, Site substitution of ternary additions to Ni3Al (γ') from electronic-structure calculations, Phys. Rev. B. 49 (1994) 12351–12354. doi:10.1103/PhysRevB.49.12351.

[194] W.T. Loomis, J.W. Freeman, D.L. Sponseller, The influence of molybdenum on the γ/'phase in experimental nickel-base superalloys, Metall. Mater. Trans. B. 3 (1972) 989–1000. doi:10.1007/BF02647677.

[195] D. Blavette, A. Bostel, Phase composition and long range order in $γ$′ phase of a nickel base single crystal superalloy CMSX2: An atom probe study, Acta Metall. 32 (1984) 811–816. doi:10.1016/0001-6160(84)90154-8.

[196] O.N. Mryasov, Y.N. Gornostyrev, M. van Schilfgaarde, A.J. Freeman, Superdislocation core structure in L12 Ni3Al, Ni3Ge and Fe3Ge: Peierls–Nabarro analysis starting from ab-initio GSF energetics calculations, Acta Mater. 50 (2002) 4545–4554. doi:10.1016/S1359-6454(02)00282-3.

[197] Y. Mishin, Atomistic modeling of the γ and γ′-phases of the Ni–Al system, Acta Mater. 52 (2004) 1451–1467. doi:10.1016/j.actamat.2003.11.026.

[198] N.M. Rosengaard, H.L. Skriver, Ab initio study of antiphase boundaries and stacking faults in L 1 2 and DO 22 compounds, Phys. Rev. B. 50 (1994) 4848–4858. doi:10.1103/PhysRevB.50.4848.

[199] V.R. Manga, J.E. Saal, Y. Wang, V.H. Crespi, Z.-K. Liu, Magnetic perturbation and associated energies of the antiphase boundaries in ordered Ni3Al, J. Appl. Phys. 108 (2010) 103509. doi:10.1063/1.3513988.

[200] X.-X. Yu, C.-Y. Wang, Effect of alloying element on dislocation cross-slip in γ′-Ni 3 Al: a first-principles study, Philos. Mag. 92 (2012) 4028–4039. doi:10.1080/14786435.2012.700419.

[201] J. Wang, H. Sehitoglu, Dislocation slip and twinning in Ni-based L12 type alloys, Intermetallics. 52 (2014) 20–31. doi:10.1016/j.intermet.2014.03.009.

[202] A.T. Paxton, Y.Q. Sun, The role of planar fault energy in the yield anomaly in L12 intermetallics, Philos. Mag. A. 78 (1998) 85–104. doi:10.1080/014186198253697.

[203] T. Kruml, From dislocation cores to strength and work-hardening: a study of binary Ni3Al, Acta Mater. 50 (2002) 5091–5101. doi:10.1016/S1359-6454(02)00364-6.

[204] P. Veyssiere, J. Douin, P. Beauchamp, On the presence of super lattice intrinsic stacking faults in plastically deformed Ni 3 Al, Philos. Mag. A. 51 (1985) 469–483. doi:10.1080/01418618508237567.

[205] D. Raynor, J.M. Silcock, Strengthening Mechanisms in γ′ Precipitating Alloys, Met. Sci. J. 4 (1970) 121–130. doi:10.1179/msc.1970.4.1.121.

[206] K. V Vamsi, S. Karthikeyan, Effect of Off-Stoichiometry and Ternary Additions on Planar Fault Energies in Ni 3 Al, in: Superalloys 2012, John Wiley & Sons, Inc., Hoboken, 2012: pp. 521–530. doi:10.1002/9781118516430.ch57.

[207] T. Kawabata, D. Shindo, K. Hiraga, High-Resolution TEM Observations of Superdislocations in Ni3(Al, Ti), Mater. Trans. JIM. 33 (1992) 565–570. doi:10.2320/matertrans1989.33.565.

[208] A. Korner, Weak-beam study of superlattice dislocations moving on cube planes in Ni 3 (Al, Ti) deformed at room temperature, Philos. Mag. A. 58 (1988) 507–522. doi:10.1080/01418618808210427.

[209] J. Vallin, M. Mongy, K. Salama, O. Beckman, Elastic Constants of Aluminum, J. Appl. Phys. 35 (1964) 1825–1826. doi:10.1063/1.1713749.

[210] G.N. Kamm, G.A. Alers, Low-Temperature Elastic Moduli of Aluminum, J. Appl. Phys. 35 (1964) 327–330. doi:10.1063/1.1713309.

[211] V.N. Staroverov, G.E. Scuseria, J. Tao, J.P. Perdew, Tests of a ladder of density functionals for bulk solids and surfaces, Phys. Rev. B. 69 (2004) 75102. doi:10.1103/PhysRevB.69.075102.

[212] J.H. Westbrook, R.L. Fleischer, eds., Intermetallic Compounds - Principles and Practice, John Wiley & Sons, Ltd, Chichester, 2002. doi:10.1002/0470845856.

[213] Y. Le Page, P. Saxe, Symmetry-general least-squares extraction of elastic data for strained materials from ab initio calculations of stress, Phys. Rev. B. 65 (2002) 104104. doi:10.1103/PhysRevB.65.104104.

[214] G.J. Ackland, X. Huang, K.M. Rabe, First-principles thermodynamics of transition metals: W, NiAl, and PdTi, Phys. Rev. B. 68 (2003) 214104. doi:10.1103/PhysRevB.68.214104.

[215] E.S. Fisher, C.J. Renken, Single-Crystal Elastic Moduli and the hcp ->bcc Transformation in Ti, Zr, and Hf, Phys. Rev. 135 (1964) A482--A494. doi:10.1103/PhysRev.135.A482.

[216] P. Paufler, Landolt-Börnstein, New Series, K. H. Hellwege (ed.), Group III: Crystal and Solid State Physics, Vol. 12: Magnetic and Other Properties of Oxides and Related Compounds, Part c: Hexagonal Ferrites. Special Lanthanide and Actinide Compounds. Springer-Verlag, Cryst. Res. Technol. 18 (1983) 1546. doi:10.1002/crat.2170181220.

[217] R.M. Wood, The Lattice Constants of High Purity Alpha Titanium, Proc. Phys. Soc. 80 (1962) 783–786. doi:10.1088/0370-1328/80/3/323.

[218] C. Bercegeay, S. Bernard, First-principles equations of state and elastic properties of seven metals, Phys. Rev. B. 72 (2005) 214101. doi:10.1103/PhysRevB.72.214101.

[219] U. Argaman, E. Eidelstein, O. Levy, G. Makov, Thermodynamic properties of titanium from ab initio calculations, Mater. Res. Express. 2 (2015) 16505. doi:10.1088/2053-1591/2/1/016505.

[220] A.T. Raji, S. Scandolo, R. Mazzarello, S. Nsengiyumva, M. Härting, D.T. Britton, Ab initio pseudopotential study of vacancies and self-interstitials in hcp titanium, Philos. Mag. 89 (2009) 1629–1645. doi:10.1080/14786430903019032.

[221] J.R. Neighbours, F.W. Bratten, C.S. Smith, The Elastic Constants of Nickel, J. Appl. Phys. 23 (1952) 389–393. doi:10.1063/1.1702218.

[222] C. Kittel, Introduction to Solid State Physics, 2010. doi:10.1007/978-3-540-93804-0.

[223] T. Çain, B.M. Pettitt, Elastic constants of nickel: Variations with respect to temperature and pressure, Phys. Rev. B. 39 (1989) 12484–12491. doi:10.1103/PhysRevB.39.12484.

[224] K. Kociskova, P. Ballo, Atomic calculation of elastic constants for fcc metals: ab-initio and semiempirical approach, Kovoe Mater. 45 (2207) 81–84.

[225] H.H. Wang, G.Y. Guo, Gradient-corrected density functional calculation of structural and magnetic properties of BCC, FCC and HCP Cr, J. Magn. Magn. Mater. 209 (2000) 98–99. doi:10.1016/S0304-8853(99)00654-X.

[226] D.I. Bolef, J. de Klerk, Anomalies in the Elastic Constants and Thermal Expansion of Chromium Single Crystals, Phys. Rev. 129 (1963) 1063–1067. doi:10.1103/PhysRev.129.1063.

[227] P. Janthon, S. (Andy) Luo, S.M. Kozlov, F. Viñes, J. Limtrakul, D.G. Truhlar, F. Illas, Bulk Properties of Transition Metals: A Challenge for the Design of Universal Density Functionals, J. Chem. Theory Comput. 10 (2014) 3832–3839. doi:10.1021/ct500532v.

[228] A. Sumer, J.F. Smith, A Comparison of the Elastic Constants of Chromium as Determined from Diffuse X-Ray and Ultrasonic Techniques, J. Appl. Phys. 34 (1963) 2691–2694. doi:10.1063/1.1729792.

[229] G.R. Harp, R.F.C. Farrow, D. Weller, T.A. Rabedeau, R.F. Marks, Unusual stability of fcc Co(110)/Cu(110), Phys. Rev. B. 48 (1993) 17538–17544. doi:10.1103/PhysRevB.48.17538.

[230] R. f. . Hearmon, The elastic constants of anisotropic materials—II, Adv. Phys. (1956) 323–382.

[231] A.R. Wazzan, A. Bristoti, L.B. Robinson, A. Ahmedieh, Temperature dependence of the single-crystal elastic constants of Co-rich Co–Fe alloys, J. Appl. Phys. 44 (1973) 2018–2024. doi:10.1063/1.1662508.

[232] Appendix E: Parameter Tables of Crystals, in: Crystallogr. Surf. Struct., Wiley-VCH

Verlag GmbH & Co. KGaA, Weinheim, 2011: pp. 265–266. doi:10.1002/9783527633296.app5.

[233] G. Steinle-Neumann, L. Stixrude, R.E. Cohen, First-principles elastic constants for the hcp transition metals Fe, Co, and Re at high pressure, Phys. Rev. B. 60 (1999) 791–799. doi:10.1103/PhysRevB.60.791.

[234] F.H. Featherston, J.R. Neighbours, Elastic Constants of Tantalum, Tungsten, and Molybdenum, Phys. Rev. 130 (1963) 1324–1333. doi:10.1103/PhysRev.130.1324.

[235] V. Milman, B. Winkler, J.A. White, C.J. Pickard, M.C. Payne, E. V Akhmatskaya, R.H. Nobes, Electronic structure, properties, and phase stability of inorganic crystals: A pseudopotential plane-wave study, Int. J. Quantum Chem. 77 (2000) 895–910. doi:10.1002/(SICI)1097-461X(2000)77:5<895::AID-QUA10>3.0.CO;2-C.

[236] K.W. Katahara, M.H. Manghnani, E.S. Fisher, Pressure derivatives of the elastic moduli of BCC Ti-V-Cr, Nb-Mo and Ta-W alloys, J. Phys. F Met. Phys. 9 (1979) 773–790. doi:10.1088/0305-4608/9/5/006.

[237] S. Allard, Metals, Thermal and Mechanical Data, Pergamon, 1969.

[238] L. Koči, Y. Ma, A.R. Oganov, P. Souvatzis, R. Ahuja, Elasticity of the superconducting metals V, Nb, Ta, Mo, and W at high pressure, Phys. Rev. B. 77 (2008) 214101. doi:10.1103/PhysRevB.77.214101.

[239] H. Ikehata, N. Nagasako, T. Furuta, A. Fukumoto, K. Miwa, T. Saito, First-principles calculations for development of low elastic modulus Ti alloys, Phys. Rev. B. 70 (2004) 174113. doi:10.1103/PhysRevB.70.174113.

[240] Z. Liu, J. Shang, First principles calculations of electronic properties and mechanical properties of bcc molybdenum and niobium, Rare Met. 30 (2011) 354–358. doi:10.1007/s12598-011-0302-9.

[241] D.M. Dimiduk, A.W. Thompson, J.C. Williams, The compositional dependence of antiphase-boundary energies and the mechanism of anomalous flow in Ni 3 Al alloys, Philos. Mag. A. 67 (1993) 675–698. doi:10.1080/01418619308207184.

[242] A. Ardell, Order hardening: comparison between revised theory and experiment, Met. Sci. J. 14 (1980) 221–224.

[243] M. Grohlich, P. Haasen, G. Frommeyer, Precipitation hardening of NiAl by large volume fractions of $γ$′, Scr. Metall. 16 (1982) 367–370.

[244] J.S. Carpenter, S.C. Vogel, J.E. Ledonne, D.L. Hammon, I.J. Beyerlein, N.A. Mara, Bulk texture evolution of Cu-Nb nanolamellar composites during accumulative roll bonding, Acta Mater. 60 (2012) 1576–1586. doi:10.1016/j.actamat.2011.11.045.

[245] J. Wang, K. Kang, R.F. Zhang, S.J. Zheng, I.J. Beyerlein, N.A. Mara, Structure and Property of Interfaces in ARB Cu/Nb Laminated Composites, JOM. 64 (2012) 1208–1217. doi:10.1007/s11837-012-0429-7.

[246] S. Zheng, I.J. Beyerlein, J.S. Carpenter, K. Kang, J. Wang, W. Han, N.A. Mara, High-

strength and thermally stable bulk nanolayered composites due to twin-induced interfaces, Nat. Commun. 4 (2013). doi:10.1038/ncomms2651.

[247] J. Wang, L. Liu, C.N. Tomé, S.X. Mao, S.K. Gong, Twinning and De-twinning via Glide and Climb of Twinning Dislocations along Serrated Coherent Twin Boundaries in Hexagonal-close-packed Metals, Mater. Res. Lett. 1 (2013) 81–88. doi:10.1080/21663831.2013.779601.

[248] A. Kumar, J. Wang, C.N. Tomé, First-principles study of energy and atomic solubility of twinning-associated boundaries in hexagonal metals, Acta Mater. 85 (2015) 144–154. doi:10.1016/j.actamat.2014.11.015.

[249] J.F. Nie, Y.M. Zhu, J.Z. Liu, X.Y. Fang, Periodic Segregation of Solute Atoms in Fully Coherent Twin Boundaries, Science (80-.). 340 (2013) 957–960. doi:10.1126/science.1229369.

[250] C.H. Liebscher, A. Stoffers, M. Alam, L. Lymperakis, O. Cojocaru-Mirédin, B. Gault, J. Neugebauer, G. Dehm, C. Scheu, D. Raabe, Strain-Induced Asymmetric Line Segregation at Faceted Si Grain Boundaries, Phys. Rev. Lett. 121 (2018) 15702. doi:10.1103/PhysRevLett.121.015702.

[251] N.J. Peter, T. Frolov, M.J. Duarte, R. Hadian, C. Ophus, C. Kirchlechner, C.H. Liebscher, G. Dehm, Segregation-Induced Nanofaceting Transition at an Asymmetric Tilt Grain Boundary in Copper, Phys. Rev. Lett. 121 (2018) 255502. doi:10.1103/PhysRevLett.121.255502.

[252] N.A. Mara, N. Li, A. Misra, J. Wang, Interface-Driven Plasticity in Metal–Ceramic Nanolayered Composites: Direct Validation of Multiscale Deformation Modeling via In Situ Indentation in TEM, JOM. 68 (2016) 143–150. doi:10.1007/s11837-015-1542-1.

[253] S. Shao, J. Wang, A. Misra, R.G. Hoagland, Spiral patterns of dislocations at nodes in (111) semi-coherent FCC interfaces, Sci. Rep. 3 (2013). doi:10.1038/srep02448.

[254] J. Wang, C. Zhou, I.J.I.J. Beyerlein, S. Shao, Modeling interface-dominated mechanical behavior of nanolayered crystalline composites, JOM. 66 (2014) 102–113. doi:10.1007/s11837-013-0808-8.

[255] J. Wang, R.G. Hoagland, J.P. Hirth, A. Misra, Atomistic simulations of the shear strength and sliding mechanisms of copper–niobium interfaces, Acta Mater. 56 (2008) 3109–3119. doi:10.1016/j.actamat.2008.03.003.

[256] C. Herring, Some Theorems on the Free Energies of Crystal Surfaces, Phys. Rev. 82 (1951) 87–93. doi:10.1103/PhysRev.82.87.

[257] S.J. Watson, Emergent parabolic scaling of nano-faceting crystal growth, Proc. R. Soc. A Math. Phys. Eng. Sci. 471 (2014) 20140560. doi:10.1098/rspa.2014.0560.

[258] T.E. Hsieh, R.W. Balluffi, Observations of roughening/de-faceting phase transitions in grain boundaries, Acta Metall. 37 (1989) 2133–2139. doi:10.1016/0001-6160(89)90138-7.

[259] J.C. Hamilton, D.J. Siegel, I. Daruka, F. Léonard, Why Do Grain Boundaries Exhibit Finite Facet Lengths?, Phys. Rev. Lett. (2003). doi:10.1103/PhysRevLett.90.246102.

[260] B. Runnels, I.J. Beyerlein, S. Conti, M. Ortiz, A relaxation method for the energy and morphology of grain boundaries and interfaces, J. Mech. Phys. Solids. 94 (2016) 388–408. doi:10.1016/j.jmps.2015.11.007.

[261] J.P. Hirth, Dislocations, steps and disconnections at interfaces, J. Phys. Chem. Solids. 55 (1994) 985–989. doi:10.1016/0022-3697(94)90118-X.

[262] J.P. Hirth, R. Pond, Steps, dislocations and disconnections as interface defects relating to structure and phase transformations, Acta Mater. 44 (1996) 4749–4763.

[263] J.P. Hirth, R.C. Pond, R.G. Hoagland, X.-Y. Liu, J. Wang, Interface defects, reference spaces and the Frank–Bilby equation, Prog. Mater. Sci. 58 (2013) 749–823. doi:10.1016/j.pmatsci.2012.10.002.

[264] Z. Suo, Singularities, Interfaces and Cracks in Dissimilar Anisotropic Media, Proc. R. Soc. A Math. Phys. Eng. Sci. 427 (1990) 331–358. doi:10.1098/rspa.1990.0016.

[265] J. Wang, Q. Zhou, S. Shao, A. Misra, Strength and plasticity of nanolaminated materials, Mater. Res. Lett. 5 (2017). doi:10.1080/21663831.2016.1225321.

[266] S. Shao, F. Akasheh, J. Wang, Y. Liu, Alternative misfit dislocations pattern in semi-coherent FCC {100} interfaces, Acta Mater. 144 (2018) 177–186. doi:10.1016/j.actamat.2017.10.052.

[267] H. Gabrisch, D. Mukherji, R.P. Wahi, Deformation-induced dislocation networks at the $\gamma{\$}-$\gamma{\$}′ interfaces in the single-crystal superalloy SC16: A mechanism-based analysis, Philos. Mag. A. 74 (1996) 229–249. doi:10.1080/01418619608239699.

[268] C. Carry, J. Strudel, Apparent and effective creep parameters in single crystals of a nickel base superalloy-II. Secondary creep, Acta Metall. 26 (1978) 859–870. doi:10.1016/0001-6160(78)90035-4.

[269] A.K. Singh, N. Louat, K. Sadananda, Dislocation network formation and coherency loss around gamma- prime precipitates in a nickel- base superalloy, Metall. Trans. A. 19 (1988) 2965–2973. doi:10.1007/BF02647723.

[270] S. Zheng, S. Shao, J. Zhang, Y. Wang, M.J. Demkowicz, I.J. Beyerlein, N.A. Mara, Adhesion of voids to bimetal interfaces with non-uniform energies, Sci. Rep. 5 (2015). doi:10.1038/srep15428.

[271] S.J. Zheng, J. Wang, J.S. Carpenter, W.M. Mook, P.O. Dickerson, N.A. Mara, I.J. Beyerlein, Plastic instability mechanisms in bimetallic nanolayered composites, Acta Mater. 79 (2014) 282–291. doi:10.1016/j.actamat.2014.07.017.

[272] J. Wang, A. Misra, An overview of interface-dominated deformation mechanisms in metallic multilayers, Curr. Opin. Solid State Mater. Sci. 15 (2011) 20–28. doi:10.1016/j.cossms.2010.09.002.

[273] R.F. Zhang, J. Wang, I.J. Beyerlein, a. Misra, T.C. Germann, Atomic-scale study of nucleation of dislocations from fcc–bcc interfaces, Acta Mater. 60 (2012) 2855–2865. doi:10.1016/j.actamat.2012.01.050.

[274] N.A. Mara, D. Bhattacharyya, P. Dickerson, J.K. Baldwin, R.G. Hoagland, A. Misra, Metallic nanolayered composites exhibit ultra-high strength and ductility, (2008) 8–9.

[275] N.A. Mara, D. Bhattacharyya, R.G. Hoagland, A. Misra, Tensile behavior of 40 nm Cu/Nb nanoscale multilayers, Scr. Mater. 58 (2008) 874–877. doi:10.1016/j.scriptamat.2008.01.005.

[276] A. Misra, R.G. Hoagland, H. Kung, Thermal stability of self-supported nanolayered Cu/Nb films, Philos. Mag. 84 (2004) 1021–1028. doi:10.1080/14786430310001659480.

[277] A. Misra, X. Zhang, D. Hammon, R.G. Hoagland, Work hardening in rolled nanolayered metallic composites, Acta Mater. 53 (2005) 221–226. doi:10.1016/j.actamat.2004.09.018.

[278] B. Onat, S. Durukanoğlu, An optimized interatomic potential for Cu-Ni alloys with the embedded-atom method, J. Phys. Condens. Matter. (2014). doi:10.1088/0953-8984/26/3/035404.

[279] M. Daw, M. Baskes, Semiempirical, Quantum Mechanical Calculation of Hydrogen Embrittlement in Metals, Phys. Rev. Lett. 50 (1983) 1285–1288. doi:10.1103/PhysRevLett.50.1285.

[280] S. Shao, J. Wang, A. Misra, Energy minimization mechanisms of semi-coherent interfaces, J. Appl. Phys. 116 (2014) 23508. doi:10.1063/1.4889927.

[281] J. Wang, O. Anderoglu, J.P. Hirth, A. Misra, X. Zhang, Dislocation structures of $\Sigma{\$}3 {112} twin boundaries in face centered cubic metals, Appl. Phys. Lett. 95 (2009) 21908. doi:10.1063/1.3176979.

[282] R.F. Zhang, I.J. Beyerlein, S.J. Zheng, S.H. Zhang, A. Stukowski, T.C. Germann, Manipulating dislocation nucleation and shear resistance of bimetal interfaces by atomic steps, Acta Mater. 113 (2016) 194–205. doi:10.1016/j.actamat.2016.05.015.

[283] X. Zhang, B. Zhang, Y. Mu, S. Shao, C.D. Wick, B.R. Ramachandran, W.J. Meng, Mechanical failure of metal/ceramic interfacial regions under shear loading, Acta Mater. 138 (2017) 224–236. doi:10.1016/j.actamat.2017.07.053.

[284] D. Bhattacharyya, N.A.A. Mara, P. Dickerson, R.G.G. Hoagland, A. Misra, Compressive flow behavior of Al–TiN multilayers at nanometer scale layer thickness, Acta Mater. 59 (2011) 3804–3816. doi:10.1016/j.actamat.2011.02.036.

[285] N. Li, H. Wang, A. Misra, J. Wang, In situ nanoindentation study of plastic co-deformation in Al-TiN nanocomposites., Sci. Rep. 4 (2014) 6633. doi:10.1038/srep06633.

[286] H.C. Barshilia, K.S. Rajam, Characterization of Cu/Ni multilayer coatings by nanoindentation and atomic force microscopy, Surf. Coatings Technol. 155 (2002) 195–202. doi:10.1016/S0257-8972(02)00008-7.

[287] S. Shao, H.M. Zbib, I.N. Mastorakos, D.F. Bahr, Deformation mechanisms, size effects, and strain hardening in nanoscale metallic multilayers under nanoindentation, J. Appl. Phys. 112 (2012). doi:10.1063/1.4748149.

[288] N. Thompson, Dislocation nodes in face-centred cubic lattices, Proc. Phys. Soc. Sect. B.

(1953). doi:10.1088/0370-1301/66/6/304.

[289] S.N.S.N. Medyanik, S. Shao, Strengthening effects of coherent interfaces in nanoscale metallic bilayers, Comput. Mater. Sci. 45 (2009) 1129–1133. doi:10.1016/j.commatsci.2009.01.013.

[290] S. Shao, J. Wang, I.J. Beyerlein, A. Misra, Glide dislocation nucleation from dislocation nodes at semi-coherent {111} Cu–Ni interfaces, Acta Mater. 98 (2015) 206–220. doi:10.1016/j.actamat.2015.07.044.

[291] S. Shao, A. Misra, H. Huang, J. Wang, Micro-scale modeling of interface-dominated mechanical behavior, J. Mater. Sci. (2017). doi:10.1007/s10853-017-1662-9.

[292] N.A. Mara, D. Bhattacharyya, J.P. Hirth, P. Dickerson, A. Misra, Mechanism for shear banding in nanolayered composites, Appl. Phys. Lett. 97 (2010) 21909. doi:10.1063/1.3458000.

[293] N. Li, N.A. Mara, J. Wang, P. Dickerson, J.Y. Huang, A. Misra, Ex situ and in situ measurements of the shear strength of interfaces in metallic multilayers, Scr. Mater. 67 (2012) 479–482. doi:10.1016/j.scriptamat.2012.06.008.

[294] S. Mao, S. Özerinç, W.P. King, R.S. Averback, S.J. Dillon, Effect of irradiation damage on the shear strength of Cu–Nb interfaces, Scr. Mater. 90–91 (2014) 29–32. doi:10.1016/j.scriptamat.2014.07.009.

[295] R.W. Hertzberg, R.P. Vinci, J.L. Hertzberg, Deformation and Fracture Mechanics of Engineering Materials, 5th ed., Wiley, Hoboken, NJ, 2012.

[296] S.K. Yadav, S. Shao, Y. Chen, J. Wang, X.-Y. Liu, Atomistic modeling of Mg/Nb interfaces: shear strength and interaction with lattice glide dislocations, J. Mater. Sci. (2017). doi:10.1007/s10853-017-1703-4.

[297] R.G. Hoagland, R.J. Kurtz, C.H. Henager, Slip resistance of interfaces and the strength of metallic multilayer composites, Scr. Mater. 50 (2004) 775–779. doi:10.1016/j.scriptamat.2003.11.059.

[298] R.G. Hoagland, J.P. Hirth, a. Misra, On the role of weak interfaces in blocking slip in nanoscale layered composites, Philos. Mag. 86 (2006) 3537–3558. doi:10.1080/14786430600669790.

[299] S. Shao, S.N. Medyanik, Interaction of dislocations with incoherent interfaces in nanoscale FCC–BCC metallic bi-layers, Model. Simul. Mater. Sci. Eng. 18 (2010) 55010. doi:10.1088/0965-0393/18/5/055010.

[300] A.S. Sutton, R.W. Balluffi, Interfaces in Crystalline Materials, Oxford University Press, 1995.

[301] Y.W. Mo, D.E. Savage, B.S. Swartzentruber, M.G. Lagally, Kinetic pathway in Stranski-Krastanov growth of Ge on Si(001), Phys. Rev. Lett. (1990). doi:10.1103/PhysRevLett.65.1020.

[302] W.J. Meng, J. Heremans, Y.T. Cheng, Epitaxial growth of aluminum nitride on Si(111) by

reactive sputtering, Appl. Phys. Lett. 59 (1991) 2097–2099. doi:10.1063/1.106092.

[303] W.J. Meng, J. Heremans, Growth of epitaxial aluminum nitride and aluminum nitride/zirconium nitride superlattices on Si(111), J. Vac. Sci. Technol. A Vacuum, Surfaces, Film. 10 (1992) 1610–1617. doi:10.1116/1.578031.

[304] A. Keller, S. Facsko, Ion-induced nanoscale ripple patterns on Si surfaces: Theory and experiment, Materials (Basel). (2010). doi:10.3390/ma3104811.

[305] T. Škereň, K. Temst, W. Vandervorst, A. Vantomme, Ion-induced roughening and ripple formation on polycrystalline metallic films, New J. Phys. (2013). doi:10.1088/1367-2630/15/9/093047.

[306] A. Roy, K. Bhattacharjee, H.P. Lenka, D.P. Mahapatra, B.N. Dev, Surface roughness of ion-bombarded Si(1 0 0) surfaces: Roughening and smoothing with the same roughness exponent, Nucl. Instruments Methods Phys. Res. Sect. B Beam Interact. with Mater. Atoms. (2008). doi:10.1016/j.nimb.2007.10.045.

[307] J.M. Arenas, J.J. Narbón, C. Alía, Optimum adhesive thickness in structural adhesives joints using statistical techniques based on Weibull distribution, Int. J. Adhes. Adhes. 30 (2010) 160–165. doi:10.1016/j.ijadhadh.2009.12.003.

[308] ASTM International, D1002 − 10 Standard Test Method for Apparent Shear Strength of Single-Lap-Joint Adhesively Bonded Metal Specimens by Tension Loading (Metal-to-Metal), (n.d.).

[309] ASTM International, ASTM D3165-07 Standard Test Method for Strength Properties of Adhesives in Shear by Tension Loading of Single-Lap-Joint Laminated Assemblies, (n.d.).

[310] ASTM International, ASTM D3528 Standard Test Method for Strength Properties of Double Lap Shear Adhesive Joints by Tension Loading, (n.d.).

[311] ASTM International, ASTM D897–01 Standard Test Method for Tensile Properties of Adhesive Bonds, (n.d.).

[312] ASTM International, ASTM D2095–96 Standard Test Method for Tensile Strength of Adhesives by Means of Bar and Rod Specimens, (n.d.).

[313] M.J. Jackson, papers contained within Surface Engineering, in: Proc. 5th Int. Surf. Eng. Congr., Seattle, WA, 2006.

[314] S. Zhang, W. Zhu, TiN coating of tool steels: a review, J. Mater. Process. Technol. 39 (1993) 165–177. doi:10.1016/0924-0136(93)90016-Y.

[315] M.F. Othman, A.R. Bushroa, W.N.R. Abdullah, Evaluation techniques and improvements of adhesion strength for TiN coating in tool applications: a review, J. Adhes. Sci. Technol. 29 (2015) 569–591. doi:10.1080/01694243.2014.997379.

[316] J.C. Jiang, W.J. Meng, A.G. Evans, C. V Cooper, Structure and mechanics of W-DLC coated spur gears, Surf. Coatings Technol. 176 (2003) 50–56. doi:10.1016/S0257-8972(03)00445-6.

[317] G.L. Doll, B.K. Osborn, Engineering surfaces of precision steel components, in: 44th Annu. Soc. Vac. Coaters Tech. Conf., Philadelphia, PA, 2001: pp. 78–84.

[318] L.F.M. da Silva, R.D. Adams, Measurement of the mechanical properties of structural adhesives in tension and shear over a wide range of temperatures, J. Adhes. Sci. Technol. 19 (2005) 109–141. doi:10.1163/1568561053148449.

[319] ASTM International, ASTM D4541-17: Standard Test Method for Pull-Off Strength of Coatings Using Portable Adhesion Testers, (2014).

[320] V. Gupta, A.S. Argon, D.M. Parks, J.A. Cornie, Measurement of interface strength by a laser spallation technique, J. Mech. Phys. Solids. 40 (1992) 141–180. doi:10.1016/0022-5096(92)90296-E.

[321] V. Gupta, V. Kireev, J. Tian, H. Yoshida, H. Akahoshi, Glass-modified stress waves for adhesion measurement of ultra thin films for device applications, J. Mech. Phys. Solids. 51 (2003) 1395–1412. doi:10.1016/S0022-5096(03)00057-7.

[322] V. Gupta, J. Yuan, A. Pronin, Recent developments in the laser spallation technique to measure the interface strength and its relationship to interface toughness with applications to metal/ceramic, ceramic/ceramic and ceramic/polymer interfaces, J. Adhes. Sci. Technol. 8 (1994) 713–747. doi:10.1163/156856194X00447.

[323] S.S. V Kandula, C.D. Hartfield, P.H. Geubelle, N.R. Sottos, Adhesion strength measurement of polymer dielectric interfaces using laser spallation technique, Thin Solid Films. 516 (2008) 7627–7635. doi:10.1016/j.tsf.2008.05.033.

[324] W.J. Meng, T.J. Curtis, L.E. Rehn, P.M. Baldo, Temperature dependence of inductively coupled plasma assisted growth of TiN thin films, Surf. Coatings Technol. 120–121 (1999) 206–212. doi:10.1016/S0257-8972(99)00457-0.

[325] Y. Mu, X. Zhang, J.W. Hutchinson, W.J. Meng, Dependence of confined plastic flow of polycrystalline Cu thin films on microstructure, MRS Commun. 6 (2016) 289–294. doi:10.1557/mrc.2016.20.

[326] K. Chen, Y. Mu, W.J. Meng, A new experimental approach for evaluating the mechanical integrity of interfaces between hard coatings and substrates, MRS Commun. 4 (2014) 19–23. doi:10.1557/mrc.2014.3.

[327] E.B. Marin, P.R. Dawson, On modelling the elasto-viscoplastic response of metals using polycrystal plasticity, Comput. Methods Appl. Mech. Eng. 165 (1998) 1–21. doi:10.1016/S0045-7825(98)00034-6.

[328] P.R. Dawson, E.B. Marin, Computational Mechanics for Metal Deformation Processes Using Polycrystal Plasticity, in: Adv. Appl. Mech., 1997: pp. 77–169. doi:10.1016/S0065-2156(08)70320-X.

[329] E.B. Marin, On the formulation of a crystal plasticity model, Livermore, CA, 2006. http://prod.sandia.gov/techlib/access-control.cgi/2006/064170.pdf.

[330] J.D. Schall, G. Gao, J.A. Harrison, Elastic constants of silicon materials calculated as a function of temperature using a parametrization of the second-generation reactive

empirical bond-order potential, Phys. Rev. B. 77 (2008) 115209. doi:10.1103/PhysRevB.77.115209.

[331] M.G. Brik, C.-G. Ma, First-principles studies of the electronic and elastic properties of metal nitrides XN (X=Sc, Ti, V, Cr, Zr, Nb), Comput. Mater. Sci. 51 (2012) 380–388. doi:10.1016/j.commatsci.2011.08.008.

[332] B. Moser, K. Wasmer, L. Barbieri, J. Michler, Strength and fracture of Si micropillars: A new scanning electron microscopy-based micro-compression test, J. Mater. Res. 22 (2007) 1004–1011. doi:10.1557/jmr.2007.0140.

[333] R. Quey, P.R. Dawson, F. Barbe, Large-scale 3D random polycrystals for the finite element method: Generation, meshing and remeshing, Comput. Methods Appl. Mech. Eng. 200 (2011) 1729–1745. doi:10.1016/j.cma.2011.01.002.

[334] R. Quey, L. Renversade, Optimal polyhedral description of 3D polycrystals: Method and application to statistical and synchrotron X-ray diffraction data, Comput. Methods Appl. Mech. Eng. 330 (2018) 308–333. doi:10.1016/j.cma.2017.10.029.

[335] Z. Zhao, S. Kuchnicki, R. Radovitzky, A. Cuitiño, Influence of in-grain mesh resolution on the prediction of deformation textures in fcc polycrystals by crystal plasticity FEM, Acta Mater. 55 (2007) 2361–2373. doi:10.1016/j.actamat.2006.11.035.

[336] M. Kasemer, R. Quey, P. Dawson, The influence of mechanical constraints introduced by $\beta{\$}annealed microstructures on the yield strength and ductility of Ti-6Al-4V, J. Mech. Phys. Solids. 103 (2017) 179–198. doi:10.1016/j.jmps.2017.03.013.

[337] S. Groh, E.B. Marin, M.F. Horstemeyer, H.M. Zbib, Multiscale modeling of the plasticity in an aluminum single crystal, Int. J. Plast. 25 (2009) 1456–1473. doi:10.1016/j.ijplas.2008.11.003.

[338] V. Crupi, G. Epasto, E. Guglielmino, A. Squillace, Influence of microstructure [alpha + beta and beta] on very high cycle fatigue behaviour of Ti-6Al-4V alloy, Int. J. Fatigue. 95 (2017) 64–75. doi:10.1016/j.ijfatigue.2016.10.002.

[339] U. Lienert, T.-S. Han, J. Almer, P.R. Dawson, T. Leffers, L. Margulies, S.F. Nielsen, H.F. Poulsen, S. Schmidt, Investigating the effect of grain interaction during plastic deformation of copper, Acta Mater. 52 (2004) 4461–4467. doi:10.1016/j.actamat.2004.05.051.

[340] R.K. Guduru, K.L. Murty, K.M. Youssef, R.O. Scattergood, C.C. Koch, Mechanical behavior of nanocrystalline copper, Mater. Sci. Eng. A. 463 (2007) 14–21. doi:10.1016/j.msea.2006.07.165.

[341] H. Ichimura, I. Ando, Mechanical properties of arc-evaporated CrN coatings: Part I — nanoindentation hardness and elastic modulus, Surf. Coatings Technol. 145 (2001) 88–93. doi:10.1016/S0257-8972(01)01290-7.

[342] B.D. Cullity, S.R. Stock, Elements of X-ray Diffraction, Third Edition, 3 rd, Prentice-Hall, New York, 2001.

[343] W. Callister, D. Rethwisch, Materials science and engineering: an introduction, 2007.

doi:10.1016/0025-5416(87)90343-0.

[344] D. Hull, D.E. Rimmer, The growth of grain-boundary voids under stress, Philos. Mag. 4 (1959) 673–687. doi:10.1080/14786435908243264.

[345] R. Raj, M.F. Ashby, Intergranular fracture at elevated temperature, Acta Metall. 23 (1975) 653–666. doi:10.1016/0001-6160(75)90047-4.

[346] J.P. Hirth, W.D. Nix, Analysis of cavity nucleation in solids subjected to external and internal stresses, Acta Metall. 33 (1985) 359–368. doi:10.1016/0001-6160(85)90078-1.

[347] E.M. Bringa, S. Traiviratana, M.A. Meyers, Void initiation in fcc metals: Effect of loading orientation and nanocrystalline effects, Acta Mater. 58 (2010) 4458–4477. doi:10.1016/j.actamat.2010.04.043.

[348] S. Shao, H.M. Zbib, I.N. Mastorakos, D.F. Bahr, The void nucleation strengths of the Cu-Ni-Nb-based nanoscale metallic multilayers under high strain rate tensile loadings, Comput. Mater. Sci. 82 (2014). doi:10.1016/j.commatsci.2013.09.036.

[349] S.K. Yadav, R. Ramprasad, J. Wang, A. Misra, X.-Y. Liu, First-principles study of Cu/TiN and Al/TiN interfaces: weak versus strong interfaces, Model. Simul. Mater. Sci. Eng. 22 (2014) 35020. doi:10.1088/0965-0393/22/3/035020.

[350] Y. Huang, J.W. Hutchinson, V. Tvergaard, Cavitation instabilities in elastic-plastic solids, J. Mech. Phys. Solids. 39 (1991) 223–241. doi:10.1016/0022-5096(91)90004-8.

[351] V. Tvergaard, Y. Huang, J.W. Hutchinson, Cavitation instabilities in a power hardening elastic-plastic solid, Eur. J. Mech. A/Solids. 11 (1992) 215–231.

[352] M. Rhee, H.M. Zbib, J.P. Hirth, H. Huang, T. de la Rubia, de la R. T., Models for long-/short-range interactions and cross slip in 3D dislocation simulation of BCC single crystals, Model. Simul. Mater. Sci. Eng. 6 (1998) 467–492. doi:10.1088/0965-0393/6/4/012.

[353] S. Shao, N. Abdolrahim, D.F. Bahr, G. Lin, H.M. Zbib, Stochastic effects in plasticity in small volumes, Int. J. Plast. 52 (2014). doi:10.1016/j.ijplas.2013.09.005.

[354] T.L. Hill, An Introduction to Statistical Thermodynamics, Dover, New York, 1986.

[355] A.F. Whitehouse, T.W. Clyne, Critical stress criteria for interfacial cavitation in MMCs, Acta Metall. Mater. 43 (1995) 2107–2114. doi:10.1016/0956-7151(94)00375-R.

[356] J. Llorca, A. Needleman, S. Suresh, An analysis of the effects of matrix void growth on deformation and ductility in metal-ceramic composites, Acta Metall. Mater. 39 (1991) 2317–2335. doi:10.1016/0956-7151(91)90014-R.

[357] T. Christman, A. Needleman, S. Suresh, An experimental and numerical study of deformation in metal-ceramic composites, Acta Metall. 37 (1989) 3029–3050. doi:10.1016/0001-6160(89)90339-8.

[358] A. Needleman, S.R. Nutt, Title Unknown, in: K. Salama (Ed.), Adv. Fract. Res. (Proc. ICF7), Pergamon Press, Oxford, 1990: pp. 2211–2218.

[359] M. Hauschildt, C. Hennesthal, G. Talut, O. Aubel, M. Gall, K.B. Yeap, E. Zschech, Electromigration early failure void nucleation and growth phenomena in Cu and Cu(Mn) interconnects, in: 2013 IEEE Int. Reliab. Phys. Symp., IEEE, 2013: pp. 2C.1.1----2C.1.6. doi:10.1109/IRPS.2013.6531951.

[360] D.A. Porter, K.E. Easterling, Phase Transformations in Metals and Alloys, Springer US, Boston, MA, 1992. doi:10.1007/978-1-4899-3051-4.

[361] X. Zhang, Y. Mu, M. Dodaran, S. Shao, D. Moldovan, W.J. Meng, Mechanical failure of CrN/Cu/CrN interfacial regions under tensile loading, Acta Mater. 160 (2018). doi:10.1016/j.actamat.2018.08.046.

[362] J.A. Ewing, J.C.W. Humfrey, The Fracture of Metals under Repeated Alternations of Stress, Philos. Trans. R. Soc. A. 200 (1903) 241–250. doi:10.1098/rsta.1903.0006.

[363] M. Dodaran, M.M. Khonsari, S. Shao, Critical operating stress of persistent slip bands in Cu, Comput. Mater. Sci. 165 (2019) 114–120. doi:10.1016/j.commatsci.2019.04.036.

[364] P. Neumann, Low energy dislocation configurations: A possible key to the understanding of fatigue, Mater. Sci. Eng. 81 (1986) 465–475. doi:10.1016/0025-5416(86)90284-3.

[365] J.R. Hancock, J.C. Grosskreutz, Mechanisms of fatigue hardening in copper single crystals, Acta Metall. 17 (1969) 77–97. doi:10.1016/0001-6160(69)90130-8.

[366] G.M. Castelluccio, W.D. Musinski, D.L. McDowell, Computational micromechanics of fatigue of microstructures in the HCF–VHCF regimes, Int. J. Fatigue. 93 (2016) 387–396. doi:10.1016/j.ijfatigue.2016.05.019.

[367] J. Man, K. Obrtlík, J. Polák, Extrusions and intrusions in fatigued metals. Part 1. State of the art and history†, Philos. Mag. 89 (2009) 1295–1336. doi:10.1080/14786430902917616.

[368] J. Man, P. Klapetek, O. Man, A. Weidner†, K. Obrtlík, J. Polák, Extrusions and intrusions in fatigued metals. Part 2. AFM and EBSD study of the early growth of extrusions and intrusions in 316L steel fatigued at room temperature, Philos. Mag. 89 (2009) 1337–1372. doi:10.1080/14786430902917624.

[369] H. Soyama, C.R. Chighizola, M.R. Hill, Effect of compressive residual stress introduced by cavitation peening and shot peening on the improvement of fatigue strength of stainless steel, J. Mater. Process. Technol. 288 (2021) 116877. doi:10.1016/j.jmatprotec.2020.116877.

[370] C.M. Lee, J.P. Chu, W.Z. Chang, J.W. Lee, J.S.C. Jang, P.K. Liaw, Fatigue property improvements of Ti–6Al–4V by thin film coatings of metallic glass and TiN: a comparison study, Thin Solid Films. 561 (2014) 33–37. doi:10.1016/j.tsf.2013.08.027.

[371] S. Bagherifard, I. Fernández Pariente, R. Ghelichi, M. Guagliano, Fatigue properties of nanocrystallized surfaces obtained by high energy shot peening, Procedia Eng. 2 (2010) 1683–1690. doi:10.1016/j.proeng.2010.03.181.

[372] B. Zhang, A. Haghshenas, X. Zhang, J. Zhao, S. Shao, M.M. Khonsari, S. Guo, W.J. Meng, On the failure mechanisms of Cr-coated 316 stainless steel in bending fatigue tests,

Int. J. Fatigue. 139 (2020) 105733. doi:10.1016/j.ijfatigue.2020.105733.

[373] C.-C. Yu, J.P. Chu, H. Jia, Y.-L. Shen, Y. Gao, P.K. Liaw, Y. Yokoyama, Influence of thin-film metallic glass coating on fatigue behavior of bulk metallic glass: Experiments and finite element modeling, Mater. Sci. Eng. A. 692 (2017) 146–155. doi:10.1016/j.msea.2017.03.071.

[374] P.H. Tsai, T.H. Li, K.T. Hsu, J.H. Ke, J.S.C. Jang, J.P. Chu, Coating thickness effect of metallic glass thin film on the fatigue-properties improvement of 7075 aluminum alloy, Thin Solid Films. 677 (2019) 68–72. doi:10.1016/j.tsf.2019.03.021.

[375] Y.L. Su, S.H. Yao, C.S. Wei, W.H. Kao, C.T. Wu, Influence of single- and multilayer TiN films on the axial tension and fatigue performance of AISI 1045 steel, Thin Solid Films. 338 (1999) 177–184. doi:10.1016/S0040-6090(98)00880-3.

[376] Y. Zhou, G.B. Rao, J.Q. Wang, B. Zhang, Z.M. Yu, W. Ke, E.H. Han, Influence of Ti/TiN bilayered and multilayered films on the axial fatigue performance of Ti46Al8Nb alloy, Thin Solid Films. 519 (2011) 2207–2212. doi:10.1016/j.tsf.2010.10.025.

[377] Y.M. Wang, P.F. Zhang, L.X. Guo, J.H. Ouyang, Y. Zhou, D.C. Jia, Effect of microarc oxidation coating on fatigue performance of Ti–Al–Zr alloy, Appl. Surf. Sci. 255 (2009) 8616–8623. doi:10.1016/j.apsusc.2009.06.038.

[378] D. Du, D. Liu, Z. Ye, X. Zhang, F. Li, Z. Zhou, L. Yu, Fretting wear and fretting fatigue behaviors of diamond-like carbon and graphite-like carbon films deposited on Ti-6Al-4V alloy, Appl. Surf. Sci. 313 (2014) 462–469. doi:10.1016/j.apsusc.2014.06.006.

[379] M.. Stoudt, R.. Ricker, R.. Cammarata, The influence of a multilayered metallic coating on fatigue crack nucleation, Int. J. Fatigue. 23 (2001) 215–223. doi:10.1016/S0142-1123(01)00153-0.

[380] H. AKEBONO, J. KOMOTORI, H. SUZUKI, THE EFFECT OF COATING THICKNESS ON FATIGUE PROPERTIES OF STEEL THERMALLY SPRAYED WITH Ni -BASED SELF-FLUXING ALLOY, Int. J. Mod. Phys. B. 20 (2006) 3599–3604. doi:10.1142/S0217979206040052.

[381] M.D. Sangid, H.J. Maier, H. Sehitoglu, A physically based fatigue model for prediction of crack initiation from persistent slip bands in polycrystals, Acta Mater. 59 (2011) 328–341. doi:10.1016/j.actamat.2010.09.036.

[382] F. Roters, M. Diehl, P. Shanthraj, P. Eisenlohr, C. Reuber, S.L. Wong, T. Maiti, A. Ebrahimi, T. Hochrainer, H.-O. Fabritius, S. Nikolov, M. Friák, N. Fujita, N. Grilli, K.G.F. Janssens, N. Jia, P.J.J. Kok, D. Ma, F. Meier, E. Werner, M. Stricker, D. Weygand, D. Raabe, DAMASK – The Düsseldorf Advanced Material Simulation Kit for modeling multi-physics crystal plasticity, thermal, and damage phenomena from the single crystal up to the component scale, Comput. Mater. Sci. 158 (2019) 420–478. doi:10.1016/j.commatsci.2018.04.030.

[383] P. Eisenlohr, M. Diehl, R.A. Lebensohn, F. Roters, A spectral method solution to crystal elasto-viscoplasticity at finite strains, Int. J. Plast. 46 (2013) 37–53. doi:10.1016/j.ijplas.2012.09.012.

[384] P. Shanthraj, P. Eisenlohr, M. Diehl, F. Roters, Numerically robust spectral methods for crystal plasticity simulations of heterogeneous materials, Int. J. Plast. 66 (2015) 31–45. doi:10.1016/j.ijplas.2014.02.006.

[385] R. Pokharel, J. Lind, A.K. Kanjarla, R.A. Lebensohn, S.F. Li, P. Kenesei, R.M. Suter, A.D. Rollett, Polycrystal Plasticity: Comparison Between Grain - Scale Observations of Deformation and Simulations, Annu. Rev. Condens. Matter Phys. 5 (2014) 317–346. doi:10.1146/annurev-conmatphys-031113-133846.

[386] M. Dodaran, J. Wang, Y. Chen, W.J. Meng, S. Shao, Energetic, structural and mechanical properties of terraced interfaces, Acta Mater. 171 (2019). doi:10.1016/j.actamat.2019.04.016.

[387] S. Lavenstein, Y. Gu, D. Madisetti, J.A. El-Awady, The heterogeneity of persistent slip band nucleation and evolution in metals at the micrometer scale, Science (80-.). 370 (2020) eabb2690. doi:10.1126/science.abb2690.

[388] S.B. Palmer, E.W. Lee, The elastic constants of chromium, Philos. Mag. A J. Theor. Exp. Appl. Phys. 24 (1971) 311–318. doi:10.1080/14786437108227390.

[389] H. Do Kweon, J.W. Kim, O. Song, D. Oh, Determination of true stress-strain curve of type 304 and 316 stainless steels using a typical tensile test and finite element analysis, Nucl. Eng. Technol. (2020). doi:10.1016/j.net.2020.07.014.

[390] X. Zhang, Y. Mu, M. Dodaran, S. Shao, D. Moldovan, W.J. Meng, Mechanical failure of CrN/Cu/CrN interfacial regions under tensile loading, Acta Mater. 160 (2018) 1–13. doi:10.1016/j.actamat.2018.08.046.

[391] B. Zhang, M. Dodaran, S. Ahmed, S. Shao, W.J. Meng, K.J. Juul, K.L. Nielsen, Grain-size affected mechanical response and deformation behavior in microscale reverse extrusion, Materialia. 6 (2019). doi:10.1016/j.mtla.2019.100272.

[392] E.B. Marin, On the formulation of a crystal plasticity model., Albuquerque, NM, and Livermore, CA, 2006. doi:10.2172/890604.

[393] S.-T. Tu, X.-C. Zhang, Fatigue Crack Initiation Mechanisms, in: Ref. Modul. Mater. Sci. Mater. Eng., Elsevier, 2016. doi:10.1016/B978-0-12-803581-8.02852-6.

[394] M. Diehl, A spectral method using fast Fourier transform to solve elastoviscoplastic mechanical boundary value problems, TU München, 2010.

[395] J. AHRENS, B. GEVECI, C. LAW, ParaView: An End-User Tool for Large-Data Visualization, in: Vis. Handb., Elsevier, 2005: pp. 717–731. doi:10.1016/B978-012387582-2/50038-1.

[396] A. Fatemi, D.F. Socie, A CRITICAL PLANE APPROACH TO MULTIAXIAL FATIGUE DAMAGE INCLUDING OUT-OF-PHASE LOADING, Fatigue Fract. Eng. Mater. Struct. 11 (1988) 149–165. doi:10.1111/j.1460-2695.1988.tb01169.x.

[397] N. Shamsaei, A. Yadollahi, L. Bian, S.M. Thompson, An overview of Direct Laser Deposition for additive manufacturing; Part II: Mechanical behavior, process parameter optimization and control, Addit. Manuf. 8 (2015) 12–35.

doi:10.1016/j.addma.2015.07.002.

[398] S.M. Thompson, L. Bian, N. Shamsaei, A. Yadollahi, An overview of Direct Laser Deposition for additive manufacturing; Part I: Transport phenomena, modeling and diagnostics, Addit. Manuf. 8 (2015) 36–62. doi:10.1016/j.addma.2015.07.001.

[399] A. Yadollahi, N. Shamsaei, Additive manufacturing of fatigue resistant materials: Challenges and opportunities, Int. J. Fatigue. 98 (2017) 14–31. doi:10.1016/j.ijfatigue.2017.01.001.

[400] R. Molaei, A. Fatemi, N. Sanaei, J. Pegues, N. Shamsaei, S. Shao, P. Li, D.H. Warner, N. Phan, Fatigue of additive manufactured Ti-6Al-4V, Part II: The relationship between microstructure, material cyclic properties, and component performance, Int. J. Fatigue. 132 (2020) 105363. doi:10.1016/j.ijfatigue.2019.105363.

[401] J.W. Pegues, S. Shao, N. Shamsaei, N. Sanaei, A. Fatemi, D.H. Warner, P. Li, N. Phan, Fatigue of additive manufactured Ti-6Al-4V, Part I: The effects of powder feedstock, manufacturing, and post-process conditions on the resulting microstructure and defects, Int. J. Fatigue. 132 (2020) 105358. doi:10.1016/j.ijfatigue.2019.105358.

[402] P.D. Nezhadfar, K. Anderson-Wedge, S. Dandiewicz, N. Phan, S. Shao, N. Shamsaei, Improved High Cycle Fatigue Performance of Additively Manufactured 17-4 PH Stainless Steel via In-Process Refining Micro-/Defect-Structure (Under Review), Addit. Manuf. (2020).

[403] R. Shrestha, J. Simsiriwong, N. Shamsaei, Fatigue behavior of additive manufactured 316L stainless steel under axial versus rotating-bending loading: Synergistic effects of stress gradient, surface roughness, and volumetric defects, Int. J. Fatigue. 144 (2021) 106063. doi:10.1016/j.ijfatigue.2020.106063.

[404] S. Beretta, More than 25 years of extreme value statistics for defects: Fundamentals, historical developments, recent applications, Int. J. Fatigue. 151 (2021) 106407. doi:10.1016/j.ijfatigue.2021.106407.

[405] M. Hamidi Nasab, S. Romano, D. Gastaldi, S. Beretta, M. Vedani, Combined effect of surface anomalies and volumetric defects on fatigue assessment of AlSi7Mg fabricated via laser powder bed fusion, Addit. Manuf. 34 (2020) 100918. doi:10.1016/j.addma.2019.100918.

[406] A. Lingenfelter, Welding of Inconel Alloy 718: A Historical Overview, in: Superalloys 718 Metall. Appl., TMS, 1989: pp. 673–683. doi:10.7449/1989/Superalloys_1989_673_683.

[407] H.-Y. Wan, Z.-J. Zhou, C.-P. Li, G.-F. Chen, G.-P. Zhang, Enhancing Fatigue Strength of Selective Laser Melting-Fabricated Inconel 718 by Tailoring Heat Treatment Route, Adv. Eng. Mater. 20 (2018) 1800307. doi:10.1002/adem.201800307.

[408] K. Yang, Q. Huang, Q. Wang, Q. Chen, Competing crack initiation behaviors of a laser additively manufactured nickel-based superalloy in high and very high cycle fatigue regimes, Int. J. Fatigue. 136 (2020) 105580. doi:10.1016/j.ijfatigue.2020.105580.

[409] M. Muhammad, P. Frye, J. Simsiriwong, S. Shao, N. Shamsaei, An investigation into the

effects of cyclic strain rate on the high cycle and very high cycle fatigue behaviors of wrought and additively manufactured Inconel 718, Int. J. Fatigue. 144 (2021) 106038. doi:10.1016/j.ijfatigue.2020.106038.

[410] M. Tiryakioğlu, J. Campbell, C. Nyahumwa, Fracture Surface Facets and Fatigue Life Potential of Castings, Metall. Mater. Trans. B. 42 (2011) 1098–1103. doi:10.1007/s11663-011-9577-3.

[411] K. Differt, U. Esmann, H. Mughrabi, A model of extrusions and intrusions in fatigued metals II. Surface roughening by random irreversible slip, Philos. Mag. A. 54 (1986) 237–258. doi:10.1080/01418618608242897.

[412] J.-C. Stinville, E. Martin, M. Karadge, S. Ismonov, M. Soare, T. Hanlon, S. Sundaram, M.P. Echlin, P.G. Callahan, W.C. Lenthe, J. Miao, A.E. Wessman, R. Finlay, A. Loghin, J. Marte, T.M. Pollock, Competing Modes for Crack Initiation from Non-metallic Inclusions and Intrinsic Microstructural Features During Fatigue in a Polycrystalline Nickel-Based Superalloy, Metall. Mater. Trans. A. 49 (2018) 3865–3873. doi:10.1007/s11661-018-4780-3.

[413] B.-T. Ma, C. Laird, Overview of fatigue behavior in copper single crystals—I. Surface morphology and stage I crack initiation sites for tests at constant strain amplitude, Acta Metall. 37 (1989) 325–336. doi:10.1016/0001-6160(89)90217-4.

[414] A. Hunsche, P. Neumann, Quantitative measurement of persistent slip band profiles and crack initiation, Acta Metall. 34 (1986) 207–217. doi:10.1016/0001-6160(86)90192-6.

[415] A. Weidner, R. Beyer, C. Blochwitz, C. Holste, A. Schwab, W. Tirschler, Slip activity of persistent slip bands in polycrystalline nickel, Mater. Sci. Eng. A. 435–436 (2006) 540–546. doi:10.1016/j.msea.2006.07.039.

[416] D.L. McDowell, F.P.E. Dunne, Microstructure-sensitive computational modeling of fatigue crack formation, Int. J. Fatigue. 32 (2010) 1521–1542. doi:10.1016/j.ijfatigue.2010.01.003.

[417] D.L. McDowell, K. Gall, M.F. Horstemeyer, J. Fan, Microstructure-based fatigue modeling of cast A356-T6 alloy, Eng. Fract. Mech. 70 (2003) 49–80. doi:10.1016/S0013-7944(02)00021-8.

[418] K. Tanaka, T. Mura, A Dislocation Model for Fatigue Crack Initiation, J. Appl. Mech. 48 (1981) 97–103. doi:10.1115/1.3157599.

[419] J.R. Rice, Dislocation nucleation from a crack tip: An analysis based on the Peierls concept, J. Mech. Phys. Solids. 40 (1992) 239–271. doi:10.1016/S0022-5096(05)80012-2.

[420] M.D. Sangid, T. Ezaz, H. Sehitoglu, I.M. Robertson, Energy of slip transmission and nucleation at grain boundaries, Acta Mater. 59 (2011) 283–296. doi:10.1016/j.actamat.2010.09.032.

[421] G. Martin, N. Ochoa, K. Saï, E. Hervé-Luanco, G. Cailletaud, A multiscale model for the elastoviscoplastic behavior of Directionally Solidified alloys: Application to FE structural computations, Int. J. Solids Struct. 51 (2014) 1175–1187. doi:10.1016/j.ijsolstr.2013.12.013.

[422] A. Cruzado, J. LLorca, J. Segurado, Modeling cyclic deformation of inconel 718 superalloy by means of crystal plasticity and computational homogenization, Int. J. Solids Struct. 122–123 (2017) 148–161. doi:10.1016/j.ijsolstr.2017.06.014.

[423] B. Zhang, M.S. Dodaran, S. Shao, J. Choi, S. Park, W.J. Meng, Understanding of plasticity size-effect governed mechanical response and incomplete die filling in a microscale double-punch molding configuration, Int. J. Mech. Sci. 172 (2020). doi:10.1016/j.ijmecsci.2019.105406.

[424] T. Maiti, P. Eisenlohr, Fourier-based spectral method solution to finite strain crystal plasticity with free surfaces, Scr. Mater. 145 (2018) 37–40. doi:10.1016/j.scriptamat.2017.09.047.

[425] M.S. Dodaran, S. Guo, M.M. Khonsari, N. Shamsaei, S. Shao, A theoretical calculation of stacking fault energy of Ni alloys: The effects of temperature and composition, Comput. Mater. Sci. 191 (2021). doi:10.1016/j.commatsci.2021.110326.

[426] M. Dodaran, J. Wang, Y. Chen, W.J. Meng, S. Shao, Energetic, structural and mechanical properties of terraced interfaces, Acta Mater. 171 (2019) 92–107. doi:10.1016/j.actamat.2019.04.016.

[427] F.. Frank, No Title, in: Rep. Symp. Plast. Deform. Cryst. Solids, Carnegie Institute of Technology, Pittsburgh, PA, 1950.

[428] B.A. Bilby, no title, in: Rep. Conf. Defects Cryst. Solids, London, 1955: p. 124.

[429] J. Wang, R. Zhang, C. Zhou, I.J. Beyerlein, A. Misra, Characterizing interface dislocations by atomically informed Frank-Bilby theory, J. Mater. Res. 28 (2013) 1646–1657. doi:10.1557/jmr.2013.34.

[430] Y. Chen, S. Shao, X.-Y. Liu, S.K. Yadav, N. Li, N. Mara, J. Wang, Misfit dislocation patterns of Mg-Nb interfaces, Acta Mater. 126 (2017) 552–563. doi:10.1016/j.actamat.2016.12.041.